A THEORETICAL AND PRACTICAL STUDY OF THE GUY-TYPE INDUCTOR ALTERNATOR.

A thesis submitted for the degree of
DOCTOR OF PHILOSOPHY.

ANTHONY MICHAEL HIGGINSON.

THE UNIVERSITY OF ASTON IN BIRMINGHAM.

October 1971.

Summary.

The Guy-type Inductor alternator is a variable reluctance machine with slotted structures on both sides of the airgap; the complex airgap geometry and high frequency, tend to magnify distortions and losses to a greater degree than in normal machines. The existing theory of the Guy-type alternator is somewhat empirical and restricted; the lack of detail as to the actual flux distribution on open circuit and on load has led to the underestimation of losses. It is well known that the doubly-slotted structure is not covered by generalised machine theory,[1,2] suggesting that a different approach is needed for the analysis of Guy-machines.

In this thesis a detailed study of flux distribution in the stator and rotor not only leads to a better understanding of the behaviour of the machine, but also allows the losses to be calculated with a greater degree of accuracy than previously achieved.

Before commencing a study of flux distribution, it was necessary to have a good understanding of no-load permeance variations; detailed permeance calculations based upon a simple approximation were compared with Teledeltos plots, and indicated the optimum tooth-slot parameters under open circuit conditions.

A simple method based upon the airgap geometry and the physical movement of the rotor teeth across the stator surface, forms the basis of the theoretical work. Extension of the theory to include the effects of armature reaction and adding a series capacitor on load,

leads to a method of calculating the flux distribution in the stator and rotor. The effects of damping and the calculation of field excitation on load is also discussed. A 3kHz experimental machine, heavily instrumented with search wires, was used throughout the work to verify the theory.

CONTENTS.

Chapter 5. Stator flux distribution under load conditions.

Chapter 7. The calculation of field excitation under load conditions.

Introduction.

After a brief introduction to the Guy-type[3] Inductor alternator to define the various parameters and the principle of operation, a critical survey is made of the existing theories, (chapter 1); the rest of the thesis is concerned with a detailed study of flux distribution in the stator and rotor of a 44.4KVA, 3kHz, Guy-type Inductor alternator.

Before commencing with detailed flux distribution, a study of no-load permeance variations and overall flux distribution in the airgap of Guy-type machines was made, (chapter 2); studies to investigate the effect of d/g and t/λ upon ϵ(1.2.2.1), showed that many of the design criteria were correctly chosen and that there is an optimum value of flux utilisation coefficient on open-circuit for any tooth-slot geometry.

Although Lorenz[4] and Guy-type[3] machines are very different in behaviour (1.2), it was decided to embark on a programme of testing and analysis similar to the one used on Lorenz machines.[5,6,7] Details of the experimental machine are given in chapter 3; a complex array of search wires on the stator and rotor enabled detailed flux measurements to be made under open-circuit and load conditions.

Chapter 4 deals with open-circuit flux distribution in the stator; measurements, especially at the tooth surface, showed the complex nature of the flux distribution.

Analysis of these flux waveforms formed the basis for studying load performance in the stator and rotor. The effects of damping and the calculation of losses is also discussed in this chapter.

Following the basic analysis used in chapter 4, the effects of armature reaction are dealt with in chapter 5; other important factors affecting load flux distribution, e.g. series capacitors and load power factor are also included. The effects of damping and the calculation of losses is also discussed.

From the physical geometry of the airgap region and knowledge of the flux distribution in the stator on open-circuit and on load, the flux waveforms on the rotor were easily calculated, chapter 6; losses were treated in a similar way to the stator, except for the additional loss due to heteropolar flux.

Various methods of calculating field excitation requirements under load conditions are discussed in chapter 7; a major section of the chapter is concerned with work by Bűssing[8], who includes the effects of saturation.

Chapter 8 concludes the thesis with a summary of the conclusions drawn from each chapter; the calculation of flux waveforms and field excitation is demonstrated in two flow-chart diagrams, Figs 96 & 97.

Chapter 1.

An introduction to the machine and the existing theories.

1.1 Historical background.

1.2 The Guy-type Inductor alternator.

1.2.1 Details of Guy-slotting.

.2 Principle of operation.

.2.1 Flux utilisation coefficient.

.2 Flux equations and voltage generation, (open-circuit)

.3 Flux equations on load.

1.3 Survey and discussion of relevant papers.

1.3.1 Walker.

.2 Pohl.

.3 Raby.

.4 Mandl.

.5 Bunea.

Summary.- Chapter 1.

After a brief survey of the history of the Inductor alternator, the chapter is divided into two sections; the first is concerned with the general principles and operation of the machine, and the second with the existing theories.

For high frequency heating applications, the conventional alternator is unsuitable, since the pole pitch becomes impracticable and the windings difficult to retain at 2-pole synchronous speed; at these high frequencies, the modern heteropolar inductor alternator is the most suitable machine. The Lorenz machine is used for frequencies in the range 1-2 kHz; for higher frequencies, use is made of Guy-type machines.

Guy-type slotting and the principles of operation, including simple flux relationships, are discussed in this chapter to introduce the basic ideas and to define some important parameters.

Major contributions to inductor alternator theory, related to the Guy-type machine, are discussed and the relevance of the existing theories to this type of machine and to the work of this thesis is also stated.

1.1 Historical background.

In the early days of the supply industry and wireless, a number of rotating alternating current generators were developed. The principle types are outlined by Laffoon[9] and can be classified as follows:-

(a) Alternators excited by alternating current and connected in cascade to step up the frequency by having the armature of one feeding the field of the next.

(b) The inductor alternator in which the rotating element causes the exciting flux that links the armature coils to either pulsate or alternate.

(c) The reflector type of alternator, which is a combination of the two classes above, and in which the frequency transformations take place in one machine.

The types mentioned in (a) and (c) were developed in the early 1900's and were used mainly in the field of radiotelegraphy. The analysis of type (a) alternators is discussed at some length by Patten[10] and Bethenod[11], and type (c) alternators by Goldschmidt.[12]

The history of the inductor alternator (b) is of particular interest and is dealt with in detail by Lay.[13]

The inductor alternator was developed in the late 1880's and is characterised by having no moving conductors. In 1888 Mordey[14] patented the ' Mordey inductor alternator ' which was used successfully over a decade. The rugged simplicity of the design, coupled with its ability to meet the demands for

greater outputs, formed the basis for its acceptance. Until alternators could be successfully paralleled, there was some delay in the expansion of a.c. power station outputs, but this was overcome by 1894. Before the advent of the steam turbine drive, when prime mover speeds were still low, the inductor alternator type of machine was a rival to the wound pole type, since its construction was favourable to the use of castings. During the early 1890's the steam turbine steadily established its claim to be the most satisfactory prime mover; at these speeds the simplicity of slow speed inductor alternator rotors was lost. These early inductor alternators were eclipsed by the arrival of the steam turbine and were not heard of again until the need for industrial high-frequency arose, (1-10 kHz).

Between 1895 and 1899, experiments were also being carried out in the field of radiotelegraphy. During the next few years a 10,000 Hz alternator was developed by Lamme[15] and a 100,000 Hz alternator by Alexanderson[16]. High frequency alternators having outputs up to 200 KW were subsequently designed by Alexanderson, and employed in numerous high power stations in America and Europe.

The main use of inductor alternators today is for industrial heating. The h.f. power is delivered to a water cooled copper coil surrounding a refractory crucible. An intense alternating magnetic field is generated within the coil causing eddy currents to be induced in the charge.

These currents heat the charge and, in the case of magnetic materials, there is an additional heating effect due to hysteresis. Alternator sets for 500-3000 Hz and later up to 10,000 Hz were designed in the early 1920's. In the early stages many of the machines were of the homopolar type; during recent years, however, modern types of heteropolar inductor alternators have been developed which have been shown to be superior to the homopolar type. Lorenz[4] and Guy-type[3] inductor alternators are used for high-frequency heating applications.

In recent years, the inductor alternator has also been used for special applications in electronics and in spacecraft.

1.2 The Guy-type inductor alternator.

Introduction.

Inductor alternators of the Lorenz or Guy-type are used for generating frequencies in the range 1-10 kHz; at these frequencies the conventional alternator is unsuitable, since the pole pitch becomes impracticable and the windings difficult to retain at 2-pole synchronous speed.

Lorenz type machines have unwound slots on the rotor side of the airgap only, and the a.c. windings are normally single phase, 1 slot/pole. Flux distribution in the Lorenz-type machine has already been analysed in detail by Davies & Lay[5,6,7]. Lorenz type machines are used for frequencies in the range 1-2 kHz; as the rated frequency rises, the pitch of the stator slot falls and use must be made of Guy-slotting (see 1.2.1), which uses unwound slots on both sides of the airgap. Although, at first sight, this seems a modest change, the Lorenz and Guy machines are very different in behaviour. The Lorenz machine has been shown to behave like a normal synchronous machine when allowance is made for the single-phase stator, the reluctance-type rotor and the second order effects caused by the size of the stator a.c. slots.[5,31] On the other hand, the Guy-machine has slotted structures on both sides of the airgap and is not a rotating field machine but a variable reluctance machine.

Both the stator and rotor core are laminated to reduce the losses at these high frequencies; the laminations (0.018cm to 0.04cm) are made from 4% silicon steel and varnished to prevent eddy currents. The simplicity of the construction of the rotor, which consists of a laminated cylinder slotted at the periphery and carrying no windings, permits peripheral speeds up to 100m/sec.

Most heating applications need single phase, which is fortunate, since this is the natural mode of operation of the machine.

1.2.1 Details of Guy-slotting.

For frequencies greater than about 3000 Hz, using a 3000 rev/min machine, the stator slot pitch becomes too small for a practical Lorenz machine to be built.

[e.g. at 10,000 Hz and 3000 rev/min, 200 rotor slots are needed, which gives a rotor slot pitch of 0.635cm for a gap periphery of 127cm(40.5 cm dia.).]

A form of slotting proposed by Guy[3] in 1901 is used for these frequencies; this is shown in Fig 1a. As in the Lorenz machine, the number of rotor slots is decided by the frequency and speed of rotation. The stator of the Guy machine has unwound slots (of the same wavelength as the rotor slots) and larger slots to take the field and a.c. windings. The main teeth A and B, Fig 1a, have the same number of unwound slots at the airgap; these are normally arranged, as shown, with one less slot than the number of teeth - the missing slot can be considered to be made up by two " half slots " due to the fringing at the extremities of each main tooth.

The permeance of main tooth A is arranged so that it varies 180° out of phase with that of main tooth B. Because both main teeth are embraced by the same field coil, the total flux in the pole will divide in the ratio of the two airgap permeances, ignoring the iron circuit. When the rotor moves through half a rotor slot pitch, the flux in main tooth A will change from maximum to minimum and the flux in B from minimum to maximum.

The width of the a.c. and d.c. slots has to be $\lambda(y + \frac{1}{2}) - t$, where y is an odd integer, to obtain the correct permeance phase. Whilst y can take any value, it is normal to use y = 1 for both a.c. and d.c. slot opening, giving $\frac{3s + t}{2}$, as shown.

Each pole pitch then comprises:

2x small teeth	= 2xt
2(x - 1) small slots	= 2(x-1)s
a.c. slot opening	= (3s +t)/2
d.c. slot opening	= (3s +t)/2
total/pole pitch	(2x + 1)λ

(see Fig. 11a and 11b.)

where:-

x= small teeth / main tooth.

t= width of small tooth.

s= width of small slot.

λ = rotor slot pitch = (s + t).

The designer of Guy-type machines does not have a free choice of frequencies, given a speed of rotation. Table 1 shows the possible frequencies in kHz for various values of x and pole numbers at a driven speed of 3000 rev / min.

Table 1.

Frequencies generated (in kHz) for various values of x and pole numbers.

Driven speed 3000 rev/min. Rotor slots= $\frac{\text{frequency in Hz}}{50}$

Teeth main tooth	poles							
	6	8	10	12	14	16	18	24
2	1.5	2.0	2.5	3.0	3.5	4.0	4.5	6.0
3	2.1	2.6	3.5	4.2	4.9	5.6	6.3	8.4
4	2.7	3.6	4.5	5.4	6.3	7.2	8.1	10.8
5	3.3	4.4	5.5	6.6	7.7	8.8	9.9	
6	3.9	5.2	6.5	7.8	9.1	10.4		
7	4.5	6.0	7.5	9.0	10.5			
8	5.1	6.9	8.5	10.2				
9	5.7	7.6	9.5					
10	6.3	9.0	10.5					

It is also possible to design slottings as shown in Fig 1c & 1d, with several a.c. slots for each d.c. slot.

1.2.2 Principle of operation.

Direct current is passed through the field winding producing a steady flux (ϕ) across the d.c. pole pitch, Fig 2. Neglecting the effects of saturation, the steady flux ϕ splits up into the ratio of the airgap permeances; for the rotor tooth position shown in Fig 2, the fluxes in teeth A and B are defined as ϕ_t and ϕ_s respectively, where ϕ_t = flux in a whole stator main tooth for the stator tooth opposite rotor tooth position and ϕ_s = flux in a whole stator main tooth for the stator tooth opposite rotor slot position. When the rotor has moved by half a slot pitch, the permeance condition is reversed, and ϕ_t and ϕ_s are interchanged. The fluxes in teeth A and B are restored to their original values when the rotor has moved by a further half slot pitch. Therefore, alternating flux links the a.c. winding during rotation of the rotor; the frequency of the alternating flux is given by the product of the number of rotor teeth and the number of revolutions/ second.

If single pitch coils are used, as in Fig 1a, the alternating component of flux linking each turn is $(\phi_t - \phi_s)/ 2$.

Instead of the individual coils embracing each main tooth, advantage is taken of the fact that the fundamental permeance variations in main teeth (A and A′) and (B and B′), Fig 2 are in phase, so that ' double pitch coils ' passing from each a.c.

slot to the next can be used to link twice the fundamental flux / main tooth.

To introduce the basic theoretical ideas at this stage, the permeance variation is assumed to vary sinusoidally between the maximum value (tooth opposite tooth) and the minimum value. (In chapter 2, detailed permeance calculations show that permeance harmonics are also present.)

The expression for permeance can be written in the form $\Lambda = \Lambda_o(1 + \epsilon \cos \omega t)$, where ϵ is known as the ' flux utilisation coefficient '.

1.2.2.1 Flux utilisation coefficient (ϵ).

ϵ has been defined by Raby,[18]

$$\epsilon = \frac{\phi_t - \phi_s}{2F\Lambda_o} = \frac{\phi_t - \phi_s}{\phi_t + \phi_s} = \frac{\phi_t - \phi_s}{\phi} = \frac{\phi_{ac}}{\phi}$$

ϵ is obviously a very important design parameter linking ϕ_{ac} , ϕ_t and ϕ_s . With the assumption of sinusoidal variation stated above it is given by

$$\epsilon = \frac{\Lambda_{MAX} - \Lambda_{min}}{\Lambda_{MAX} + \Lambda_{min}}$$

Λ_{MAX} and Λ_{min} can be obtained by Schwarz-Christoffel transformations[19] for the tooth-opposite-tooth and tooth-opposite-slot conditions. Useful contributions to this subject are made by Gibbs[20] and Coe and Taylor.[21]

In practice, an empirical value of 0.9ϵ is used in the design equations. (It will be shown from Teledeltos plots that this 0.9 value follows from the erroneous assumption of sinusoidal permeance variation

and the use of shallow, sloping-sided slots instead of infinitely deep, vertical-sided slots.)

ϵ is dependent on the airgap configuration. It is convenient to plot it in terms of two pairs of dimensionless quantities involving s,g,t and λ. Fortunately, for the values of (t/λ) normally used in these machines (0.37 to 0.44), ϵ is practically constant for a given (s/g), so that a curve of ϵ against (s/g) can be plotted, Fig 3.

1.2.2.2 Flux equations and voltage generation. (open-circuit.)

On open circuit, only the field mmf F is acting,

Maximum flux in a tooth $\phi_t = F\Lambda_o(1 + \epsilon)$

Minimum flux in a tooth $\phi_s = F\Lambda_o(1 - \epsilon)$

If single-pitch coils are used, Fig 1a the alternating component of flux linking each turn is

$(\phi_t - \phi_s) / 2 = \epsilon F\Lambda_o = \epsilon \times$ mean flux.

If double-pitch coils are used, Fig 2

Flux in tooth A $= F\Lambda_o(1 + \epsilon \cos \omega t)$

Flux in tooth A' $= -F\Lambda_o(1 - \epsilon \cos \omega t)$

Total flux linking A + A' $= 2F\Lambda_o\epsilon \cos \omega t$

$= (\phi_t - \phi_s) \cos \omega t,$

i.e. twice the flux embraced by each single pitch coil.

The emf in the total winding, since all the fundamental voltages are in phase, is

$$E = 4.44 f N \phi_{ac} \text{ volts,}$$

where N = total turns in series in the machine.

Because f is high in these machines, the turns are usually small. A.C. windings commonly comprise one to three effective conductors per slot. Parallel paths must be treated with caution as small inequalities in the airgap length produce large differences in path voltages.

1.2.2.3 Flux equations on load.

Under load conditions an additional mmf acts upon the airgap due to armature reaction; the total mmf can be written in the form $\left[F + A\cos(\omega t + \alpha)\right]$, where α is defined as the phase angle between the peak of the load current and the peak permeance. (The angle α defines the amount of overlap of stator and rotor teeth at the moment of maximum applied mmf.)

Simple equations, assuming sinusoidal permeance variation, can be derived for the fluxes linking the a.c. and d.c. windings:-

$$\phi_{ac} = \Lambda_o\left[2F\epsilon\cos\omega t + 2A\cos(\omega t + \alpha)\right] \quad \text{(see 10.4.1)}$$

$$\phi_{d.c} = \Lambda_o\left[2F + A\epsilon\cos\alpha + \frac{A\epsilon}{2}\cos(2\omega t + \alpha)\right]$$

The flux which links the field winding under load conditions contains a second harmonic term due to the interaction of the fundamental permeance variation and the fundamental component of armature reaction. This high frequency flux component linking the field induces a voltage in the field winding which is liable to cause a breakdown of the field insulation, 5.6.2.

Damping windings, consisting of short-circuited turns, are placed either in the top or bottom of the d.c. slots to damp the high frequency flux which links the field winding. The effects of damping on open-circuit and on-load are discussed in subsequent chapters of the thesis, (4.5, 4.7, 5.5 and 5.6.2).

1.3 Survey and discussion of relevant papers.

Walker's papers[22,23] which form a major contribution to inductor alternator theory, and which are well-known in the field of high frequency machines, provide a useful background to the study of high frequency alternators; these papers are discussed briefly in this section with particular reference to the Guy-type inductor alternator.

The major contributions to inductor alternator theory related to the Guy-type machine are presented by Pohl[24], Raby[18], Büssing[8], Mandl[25], and Bunea[26,27]. A detailed survey of each paper is made in this section, except the paper by Büssing. The major part of Büssing's work is concerned with the effects of saturation and the calculation of excitation under load conditions; a critical survey of his work is made in chapter 7, which deals primarily with the calculation of field current on load.

The main difference between existing theories and that presented in this thesis lies in the approach to understanding what actually happens in the machine. Although the majority of the existing theories lead to a useful design technique, they are somewhat empirical and restricted. The lack of detail as to the flux distribution both on open circuit and under load conditions arises because these theories are expressed in overall terms, i.e. 'flux per tooth' or 'ampere-turns for gap and teeth.' In this overall approach no real indication is given as to the actual flux

distribution in the teeth or the core; iron loss calculations based upon assumed flux paths etc, lead in the main to the underestimation of the losses, especially in the small tooth regions.

Throughout this thesis, a combination of experimental work and Teledeltos models has been used to develop expressions for the flux distribution in the teeth and core. Where detailed distribution is discussed, e.g. in the stator tooth surface, little reference is made to the existing theory. However, a limited use can be made of the theory when considering overall aspects, e.g. damping of the fluxes linking a field coil.

Some of the points arising from a survey of the literature are dealt with in appropriate chapters of this thesis; where this occurs, reference is made to the relevant chapter. Other papers which appear in the bibliography and which are not specifically mentioned in this survey or in the thesis were used for background reading, e.g. the papers relating to flux plotting etc.

1.3.1 Walker.[22]

Walker's 1941 paper on the ' Theory of the inductor alternator,' briefly describes the construction of typical homopolar and heteropolar inductor alternators, and presents a theory which is also a practical design technique. The homopolar machine has several disadvantages which are mentioned by Walker and Marchbanks.[28]

Nowadays the homopolar type has almost completely been replaced by the heteropolar machine.

The flux distribution in the airgap and the emf equation is based upon work by F.W.Carter[19]; the equations are based upon simple assumptions which are discussed in chapter 2. To calculate the characteristics of the machine, it is desirable to relate the mean and the alternating fluxes using a flux utilisation coefficient; this is defined by Raby,(section 1.3.3) and is discussed in sections (1.2.2.1 and 2.1).

Walker also discusses main types of armature windings, effects of armature reaction and the necessity of an efficient damping system. Methods of predetermining the field current on open-circuit and on load are indicated and the paper concludes with an investigation of the losses in these alternators. The calculated losses give a false indication of the true loss, since they are based upon simple assumptions which are untrue in practice. Walker comments:-

' The figure of core loss must be multiplied by an empirical constant to allow for the effect of

notching, etc. This constant is of the order of 2 to 3 and is obtained from test results on similar machines.'

The loss calculations are usually based on fundamental flux; the fundamental loss is calculated from design values of flux density and the appropriate loss curve for the material. In subsequent chapters of this thesis, detailed flux measurements, especially in the small teeth, show that harmonic fluxes are present which will influence the loss calculation. Detailed studies in the tooth and core regions, show where these losses occur; the actual loss is then calculated from a simple relationship, i.e. $\text{loss} \propto f^{1.5} B^2$, (see section 4.3).

Walker's second paper, ' High frequency alternators[23],' reviews the various types of alternators available for the generation of frequencies up to 50,000 Hz and shows that for the majority of applications the modern heteropolar inductor alternator is the most suitable machine. After discussing Lorenz and Guy-type machines, single phase machines employing Guy-Lorenz slotting, (Fig 1c&d) and polyphase alternators developed in connection with telecommunication and certain special purpose applications are also mentioned. The electrical characteristics and mechanical construction of these alternators is considered in some detail, with their application to the melting of metals and surface hardening of steel.

1.3.2 Pohl.[24]

In introducing the ' Theory of pulsating field machines,' Pohl shows that electrical machines, as electromagnetic converters of energy can be classified into two main groups:-

> ' The first, that of alternating field machines, which are characterised by a magnetic field of essentially constant permeance and constant flux distribution, alternating relative to the armature windings, due to an alternating mmf. In most of these machines the alternation is brought about through rotation of either the flux or the armature winding. Where a constant field is made to rotate by electrical or mechanical means relative to the a.c. coil, we speak of rotating field machines.
>
> In the second group, the induced emf results from flux pulsations brought about by periodic changes of permeance, generally within a unidirectional, d.c.-excited, heteropolar field. These are the pulsating-field or inductor-type machines. Where the total flux of a d.c. pole, containing side by side two or more a.c. coils in different phases of induction, is kept constant, line cutting has to be imagined as due to lateral swinging of lines out of one coil into another and back again. We may then speak of ' swinging-field machines.'

The paper suggests that instead of attempting to adopt the rotating-field theory to pulsating field machines, it is more satisfactory to employ an independent theory. Pohl shows that if the well-established theory for the first group of machines is applied to the second group, then

> ' it no longer leads to a clear mental picture and a simple theory, but merely creates unnecessary complications. These complications are conducive to misconceptions and they become intolerable when harmonic effects, especially on load have to be investigated.'

Pohl's theoretical approach is based upon being able to find an expression for the pulsating permeance and the total mmf that acts upon that permeance, 7.1.2; this approach is later adopted by Raby (7.1.1) and Büssing (7.2.2.1).

For simple geometries, e.g. tooth-opposite-tooth or tooth-opposite-slot, over a rotor pitch, the airgap permeance is calculated as described in section 1.2.2.1. For the complex geometry of the Guy-machine, the method becomes very tedious and complex. The problem of integration becomes increasingly more involved as the number of corners in the original flux distribution boundary increases; for more than 6 corners the integration leads to elliptic functions.

To obtain expressions for the permeance variation, Pohl makes an approximation to the airgap permeance by using a ' substitute angle' which is claimed to be accurate within 1% for a wide range of s/g values, (10.1 and Fig 4.)

Instead of Carter's coefficient:-

$$c = \frac{2}{\pi}\left[\text{arc tan}(s/2g) - \frac{\log_e (1+ (s/2g)^2)}{s/g}\right]$$

Pohl's method leads to a correction coefficient c' given by

$$c' = \left[1 - \left(2/\beta\right)\frac{\log_e (1 + \beta s/2g)}{s/g}\right]$$

To express the permeance variation over a whole cycle a number of equations have to be used, since there are points of mathematical discontinuity during the permeance cycle, (section 10.3).

The fluxes both on open-circuit and on load are easily calculated by considering the mmfs which act upon this permeance variation, (sections 1.2.2.2 and 7.1.2).

Some important features of the pulsating field machine are mentioned by Pohl which can be summarised as follows:-

(a) <u>open-circuit conditions.</u>

1) The difference ($\phi_t - \phi_s$) is a measure of the flux pulsation and for unsaturated conditions will rise in proportion to the applied ampere-turns. With the commencement of saturation, however, the rate of rise of ϕ_t decreases, while that of ϕ_s remains constant so that ($\phi_t - \phi_s$) now rises less rapidly. Ultimately a point is reached where the slope of ϕ_t equals that of ϕ_s; here ($\phi_t - \phi_s$) reaches its maximum, then decreases with further excitation, Fig 88.

2) The output of pulsating field machines is ultimately limited by the saturation in the iron and the heating of the windings. The limiting saturation is set by the teeth of stator and rotor, since the cores can always be made deep enough to accomodate the tooth flux.

3) As the rotor teeth pass from a position of maximum permeance to a position of minimum permeance, the flux is constrained to enter through a reduced tooth surface where ultimately a very high saturation may be set up. In addition to the high saturation which is possible for certain rotor tooth positions, flux measurements on open-circuit have shown that harmonic fluxes are also present, which cause extra losses in the tooth regions, (section 4.1.2).

(b) On-load.

Pohl also includes the effects of armature reaction:-

' While the maximum ampere-turns producing the flux on load which reach (A + F) greatly exceed F, the stator and rotor teeth may have ceased to face each other, or may do so only over a small angle. In so far as they still overlap, the gap density, and therefore the tooth surface density, reaches much higher values than on open-circuit. The lines of force entering the teeth from the gap at high induction will at once spread out in the iron to make use of its whole width. Despite a low general tooth induction, a very high surface saturation may thus prevail.'

(A mathematical analysis of Pohl's work is given in chapter 7*.)

A close examination of the flux distribution under load conditions, especially in the tooth regions, shows that the flux distribution at the surface is far more complex than that mentioned by Pohl, (chapter 5*); the distortion in small sections of the surface is non-uniform across the surface and is dependent upon a number of factors, e.g. the value of series capacitor,(5.2.7) the tooth-slot geometry and the degree of saturation, (5.5.2).

Under load conditions, the maximum output is limited by field heating , (7.3.6); the maximum output for a given field current is dependent upon the value of series capacitor and load power factor, (7.3.6).

A further important point is discussed in relation to the optimum shape of the teeth. The permeance variation is a function of dimensional ratios only, namely of the ' tooth ratio' (t/λ) and s/g . For a given value of s/g the permeance variation can be plotted for various values of t/λ ; when the curves are analysed for harmonic content, Pohl shows that the optimum value for t/λ approaches 0.4. Chapter 2 shows that this is infact true for a wide range of s/g, but only for open-cicuit conditions. Under load conditions other factors as well as the airgap geometry affect the flux distribution, suggesting that under load conditions a different value of t/λ may have to be chosen to give optimum performance,(5.5.2).

(Chapter 5 and Chapter 7* refer to this thesis.)

1.3.3 Raby.[18]

The property of high-frequency currents whereby the current density at the surface can be many times greater than in the interior of a conductor, makes it possible to heat-treat a piece of steel to produce a relatively thin layer of surface hardening. This important application is discussed in detail by Marchbanks.[28] Two typical applications are mentioned by Raby, namely the pre-heating of rivets and surface hardening of metals. For surface heating applications a demand exists for a.c. supplies at a frequency of 8–10 kHz; the inductor alternator of the Guy-type provides a convenient source of power at these frequencies and is most commonly employed in ratings of 25–250 KW. Raby's paper deals with the principles of operation and the theory for 10 kHz machines of the Guy-type.

In discussing the flux relationships in the machine, two important parameters are defined:-

(a) flux utilisation coefficient (ϵ).

assuming sinusoidal permeance variation, ϵ is defined as $\frac{\phi_t - \phi_s}{\phi_t + \phi_s}$, (1.2.2.1).

(b) 'a' (7.1.1)

'a' is defined as $A/F_o\epsilon$, where

A = peak a.c. ampere turns/pole

F_o = field ampere turns/pole to give rated open-circuit volts

ϵ = flux utilisation coefficient.

For damped conditions the parameter 'a' is modified to $a(1-\epsilon^2/4)$. For 10 kHz machines ϵ is low and leads to a discrepancy of not more than 1.5%. Raby uses these two parameters to develop a simple load theory; this is discussed in detail in chapter 7, which is primarily concerned with the calculation of field excitation under load conditions.

A major part of the paper is concerned with losses in this type of machine. The losses can be classified into three groups:-

(a) losses which are dependent upon uncertain conditions such as the precise quality of the iron, the finish of the punched edges, the amount of machining of the airgap surfaces, etc. In machines of this type the performance is critically dependent upon the length of the airgap. ' Errors in manufacture which are well within the limits of the closest tolerances that can be reasonably specified may still produce discrepancies between observed and predicted performance considerably in excess of those resulting from imperfections in the design procedure.'

(b) loss which can be calculated with a good degree of accuracy, e.g. the copper loss in the a.c. and field windings; this is usually very small compared with the total losses.

(c) The losses in the core and teeth. The losses in the core and teeth are usually calculated from the known flux density, volume of iron and specific loss curves.

Additional losses in the rotor also occur due to heteropolar flux. The conclusions on losses which emerge from the paper are summarised by Raby as follows:-

' The chief requirement is for a theory and straightforward design procedure based on a sound understanding of the fundamental principles of the inductor-type machine. _ _ _ _ _ Until a fundamentally sound theory of the losses has been developed and agreed upon, simultaneous input/output readings at full load should be taken as the sole criteria of efficiency.'

In subsequent chapters of this thesis, the flux distribution in the stator and rotor under open-circuit and load conditions is analysed in detail; with this knowledge of flux distribution, the losses can be calculated with a greater degree of accuracy than previously achieved. A considerable amount of the loss is concentrated in the tooth regions and, although some of the factors mentioned by Raby in (a) will affect the overall loss, the gap between measured and calculated loss is considerably reduced, (4.3, 5.3 and 6.1.4).

1.3.4 Mandl.[25]

This paper is concerned with developing a graphical method of determining the short-circuit current of an inductor alternator, taking into account the effect of a damping circuit which prevents oscillations of the total flux. From the open-circuit and short-circuit characteristics it is shown how an equivalent circuit can be developed which enables the load characteristics to be calculated. The short-circuit current is developed from the magnetic characteristics for maximum and minimum flux. The leakage flux is introduced as a percentage of the minimum flux and a leakage coefficient is defined as the ratio of leakage flux to minimum flux; this coefficient is assumed to be constant and independent of saturation. (Flux measurements on the experimental machine show that there are a number of additional factors which influence leakage flux, (4.2.3 and 5.2.7).

Mandl develops load characteristics from an equivalent circuit, Fig 5a; the terminal voltage, load voltage etc are related by the equation:-

$$E^2 = I^2 \left[(X_L + Z\sin\phi)^2 + (Z\cos\phi)^2 \right]$$

The output is given by

$$I^2 Z = \frac{E^2 Z}{\left[(X_L + Z\sin\phi)^2 + (Z\cos\phi)^2 \right]}$$

Introducing the ratio of output voltage to generated emf, $\frac{V}{E} = \psi$, and the ratio of output current to short-circuit current, $\frac{I}{I_o} = \chi$, a general equation of the load characteristic is obtained:-

$$\psi^2 + \chi^2 + 2\psi\chi \sin\phi = 1$$

From this equation load characteristics are drawn as shown in Fig 5b; these equations are further discussed in chapter 7 of this thesis.

Mandl also discusses capacitor compensation and parallel running; these are summarised as follows:-

Capacitor compensation.

Condensers can be used either in parallel or in series with the machine windings. The parallel condenser increases the open-circuit voltage, but has no effect upon the short circuit current. As a rule it has a very bad effect on the waveform of the output voltage. The series condenser increases the short-circuit current but not the open-circuit voltage. Usually full compensation is not used, since this causes high short-circuit currents.

Compensation of the internal inductive reactance by series condensers for an alternator with constant and variable speed is considered, and the transient and steady voltage changes are investigated. The effects of series capacitor upon flux distribution and load characteristics are discussed in chapters 5,6 and 7.

Parallel operation.

Parallel operation of inductor alternators is also discussed by Mandl:-

' For zero compensation there is no difficulty in synchronising the two machines if they run up simultaneously and their excitations are brought up together either during running up or after, nor does it make any difference whether the load is connected during running up or afterwards._ _ _ _ Experiments proved that it is safe to compensate up to 50% of the internal inductive reactance in order to maintain good parallel operation.

In order to allow for possible variations in the percentage slip between the driving motors, the rating of the combination of alternators should be about 10% less than the sum of their individual ratings. An unusual type of instability arising when paralleling series-compensated alternators is also investigated; this is overcome by the addition of an equalising connection across the machines output terminals.'

1.3.5 Bunea.[26]

In the 'Theory of medium frequency pulsating machines,' Bunea analyses the Guy-type inductor alternator. The theory does not follow the usually accepted approach made by Pohl and Raby; ' the characteristics are traced point by point on the basis of a magnetisation characteristic of the magnetic circuit.' Various equivalent circuits are drawn showing how series capacitors can be used to compensate the load-circuit inductance; the circuit which is normally used, Fig 6a, forms the basis of the thecretical analysis. From this circuit Bunea derives the differential equation for the equivalent circuit and uses this to obtain an expression for the emf v of the armature winding, i.e.

$$\frac{dv}{dx} = (L_a + L_\ell) \omega \frac{d^2 i_a}{dx^2} + (R_a + R_\ell) \frac{di_a}{dx} + \frac{i_a}{\omega C_a}$$

$$v = - W_a A \omega \frac{d}{dx} (B_x - B_{x+\pi})$$

where v= emf of armature winding, x= electrical angle between rotor-tooth and stator-tooth axes, L_a, L_ℓ = inductance of load, leakage inductance of armature winding, ω= angular frequency, i_a= instantaneous armature current corresponding to position x of rotor on load, R_a, R_ℓ= resistance of load, resistance of armature winding, C_a= equivalent capacitance of load, W_a= number of turns on armature winding, A = area of half pole,

B_x = instantaneous magnetic flux density in equivalent airgap at position x of rotor, for a particular running condition.

The airgap in this method is replaced by an equivalent airgap δ_x ; when the equivalent airgap on any half pole is δ_x that on the neighbouring half pole is $\delta_{x+\pi}$. The airgap density B_x is related to F_x by the magnetisation curve, i.e. $F_x = f(B_x)$.

where F_x = mmf in iron magnetic circuit corresponding to B_x . Assuming that the generated emf and the generator current vary sinusoidally as functions of x, the curve relating F_x and B_x is linearised according to the relation,

$$F_x = \frac{a_k}{4\pi} B_x - n_f b_k$$

where a_k = airgap for linearising magnetisation curve, b_k = current for linearising magnetisation curve, n_f = number of conductors in field slot.

With $F_x = f(B_x)$ known from this linearisation process, the characteristics are developed for the machine.

Although the derivation of the equations appears to be sound, the accuracy of this linearisation process is in some doubt and is mentioned by Bunea; ' we are dealing with a limited and progressive linearisation of the magnetisation curve. For synchronous generators, such a linearisation yields unacceptable results._ _ _ _ _ _ _ _ Obviously the wider the range within which the flux density varies, the more inaccurate is the linearisation.

This happens for large and capacitive loads, especially in higher frequency generators,_ _ _ _ _ _ applying the assumption of sinusoidal operation, with

$$F_x = \frac{a_K B_x}{4\pi} - n_f b_K$$

will yield somewhat discontinuous results.'

Some important deviations from Bunea's theory are mentioned which are summarised as follows:-

(a) core packing.

Owing to imperfect packing of the rotor and / or stator core plates, neighbouring laminations may not be perfectly in register, slightly increasing the tooth width. Analysis by Bunea shows that the open-circuit voltage does not decrease significantly, whereas there is a decrease in the short-circuit current. Another consequence of faulty packing is that rotor and stator teeth are not parallel. The effect of this irregularity can be judged by assuming the rotor tooth to have an axial inclination towards the stator tooth. This has the effect of reducing the voltage and the armature current.

(b) Non-uniform gap.

Bunea also discusses the effect of a non-uniform airgap, ' The consequences of a non-uniform airgap may be judged by comparison with a machine having a conical rotor. _ _ _ _ _ _ _ _ A non-uniform gap implies an effective mean gap longer than the minimum measurable one.'

For machines operating in the region of 10 kHz the flux utilisation coefficient falls to 0.2, (2.1.1.1). The unwound slot openings become very small and a large percentage of the flux crosses the gap in the slot regions; to keep ϵ as large as possible very short airgaps are used. ϵ is critically dependent upon s/g and consequently any irregularities in the airgap will influence the output of the machine.

(c) core plate material.

' Another cause of deviation from the theory is the variable quality of the magnetic steel. A magnetisation curve calculated from laboratory tests on a sample seldom agrees with that for the machine as built.'

In a recent paper[27] Bunea completes his theoretical work by considering magnetic skin effects in medium frequency machines. The characteristics of medium frequency alternators for 2-10 kHz can be affected by this phenomenon; the higher the frequency the more pronounced is the skin effect. The phenomenon is well known and has two consequences:-

(a) an increase in the core losses.

(b) modification of the operational characteristics of the machine.

It is well known that the output of medium frequency alternators is limited by magnetic saturation. Saturation makes the operational characteristics exhibit maxima which cannot be

exceeded however much the field current is increased. Due to skin effect, saturation will appear earlier and leads to a decrease of the active power of medium-frequency generators. The analysis follows basically that already outlined in the earlier paper, except that the independent parameter is assumed to be composed of a median density B_K , on which an alternating component is superposed, namely B_{Kox} on open-circuit and B_{KAx} on load. The equations derived for the machine show that:-

(a) there is a decrease in terminal voltage.

(b) there is a backward shift in the phase of this voltage in relation to the voltage if the magnetic skin effect were neglected.

(c) the median flux density B_K is unaffected.

Bunea mentions that for flux densities above 1 Tesla, there is practically no skin effect, suggesting that the descending part of the open-circuit characteristic taking the magnetic skin effect into account coincides with the equivalent part of the characteristic when the skin effect is ignored, Fig 6b. The majority of medium frequency machines operate at flux densities in the region of 1 Tesla, and it is felt therefore that the effects due to magnetic skin effect will be small. Tests carried out by Bunea show this to be true:-

' The measurement on 8 kHz generators under load conditions showed that the magnetic skin effect has negligible effects. _ _ _ _ _ _ _ _ The decrease

in the open-circuit characteristic is due solely to the quality and thickness of the sheet. With good quality sheets, the characteristic at 8-10 kHz is 6-9% lower, and the peak of the open-circuit characteristic falls by 3.5-5.5%. At 2.5 kHz the effect of magnetic skin effect is practically negligible for sheets of this type.'

Chapter 2.

Permeance calculations and overall flux distribution on open-circuit.

2.1 The flux utilisation factor ϵ .

2.1.1 10kHz experiments.

.1.1 Effect of d/g and slope of slot side.

.2 3kHz experiments.

2.2 Permeance variations.

2.2.1 Teledeltos models.

.2 Baillie method.

2.3 Harmonic permeances.

2.3.1 Symmetry.

2.4 Permeance variation in total pole.

2.5 Conclusions.

Summary.- Chapter 2.

Before starting on load performance, it was necessary to have a good understanding of the no-load permeance variations; this chapter compares Teledeltos measurements of permeance through a cycle with the usual assumption of sinusoidal variation between minimum and maximum permeance. The fundamental of the actual variation is shown to compare well with the empirical modification of the sinusoidal approximation. This work was done on a single tooth and slot (for comparison with earlier work) and with the whole of a large stator tooth, which is shown to give a permeance variation closer to measured values from the open-circuit test. A simple approximation (section 2.2.2) for calculating the permeance variations is shown to give good agreement with the measured Teledeltos curves.

Having established the basic variations on open-circuit, measurements were then made of the detailed distribution of flux around the airgap for various positions of the rotor slotting relative to the stator for the whole d.c. pole. These showed that there is sufficient asymmetry between the two main teeth on a pole to cause harmonic flux variations in the field coil on no-load. Although small, these variations would cause substantial voltages, because of the frequency and the large number of turns in the field coils. These variations of flux were verified by test on the actual machine.

2.1 The flux utilisation factor ϵ.

Teledeltos paper provides a simple method for checking and extending knowledge of airgap flux density distributions.

Before commencing with detailed plots over a whole cycle, (2.2) the effects of three practical modifications to the Carter infinitely-deep, vertical-sided slots were measured:

(a) practical slots are shallow and it is obviously advantageous to make them as shallow as possible.

(b) to reduce the mmf drop and iron loss, the teeth should be as wide as possible by tapering the sides cf the slots.

(c) flux concentrations are avoided by making the slot bottoms rounded instead of flat, especially in the shallow slots used at 10kHz.

These experiments did not use the more accurate method of plotting Λ for the whole cycle. It was sufficient to compare the values with the Carter results using $\left[\frac{\Lambda_{MAX} - \Lambda_{min}}{\Lambda_{max} + \Lambda_{min}}\right]$ and measured values of Λ_{MAX} and Λ_{min} which are easily obtained.

2.1.1* 10kHz experiments.

Typical 10kHz values ($t/\lambda = 0.4$ and $s/g = 8$) were chosen for the experiments. The minimum allowable mechanical airgap in these machines is closely related to diameter, so the value of s/g tends to a constant.

* see page 46.

Normal practice is to use a 20° sloping side combined with a circular slot bottom. To minimise the work, the effect of circular slot bottoms with 20° sloping sides only was measured; tests were made at each depth with flat bottomed slots and circular bottomed slots of the same depth. The difference in the two readings was negligible for the useful range of d/g, and was small ($<1\%$) even at d/g =1. Although round bottoms are used in practice, it was decided that there would be no loss of accuracy in doing all the other experiments with flat-bottomed slots, in view of these experiments, with considerable simplification in the slot cutting.

2.1.1.1 Effect of d/g and slope of slot side.

Figure (7a,b,c) [10kHz scales] shows the effect on ϵ of varying d/g and the slope of the slot side. For each slope of side, two models were made: (1) tooth-tooth position, and (2) tooth-slot position. Each was made with a depth of slot approximating to infinity (for parallel sides) and maximum depth (for sloping sides). For each value of d/g, Λ_{max} and Λ_{min} were found and ϵ was calculated from the relationship: $\epsilon = \left[\frac{\Lambda_{max} - \Lambda_{min}}{\Lambda_{max} + \Lambda_{min}}\right]$

Since the permeances are proportional to the measured resistances, it is only necessary to use the resistances directly, without calibration. The value of d/g was changed by cutting off the bottom of the slot with scissors.

It was seen that very little is lost by reducing the slot depth to d/g =4 to 5 and that there is virtually no difference between 0° and 20° sloping side in that region. Too much is lost at 30° slope to recommend it for practical machines.
(compare the $\left[\text{Carter}\,\epsilon\,\text{value} \times 0.9\right]$ of 0.241 for s/g=8 with the value of 0.240 (d/g= 4) from Teledeltos plots.)

2.1.2 3kHz experiments.

The experiments with round-bottomed slots and varying slopes of side were not repeated for 3kHz slotting, but only the normal 20° sloping sides were used. Using s/g = 30, t/λ = 0.4, values of Λ_{MAX} and Λ_{min} were found as for 10kHz slotting and the results plotted in Fig 7d. It will be seen that the optimum value of d/g has now risen to 15. This is the value used for these machines.
(compare the Carter ϵ = 0.635 with value of 0.628 at d/g = 18.)

2.2 Permeance variations.

Since the derivation of ϵ using Λ_{MAX} and Λ_{min} is based on the dubious assumption of sinusoidal variation and gives the wrong answer, and since it was necessary to know the harmonic flux-variations in the iron for other purposes, it was decided to plot the permeance over the whole half cycle as the rotor moves from tooth-opposite-tooth to tooth-opposite-slot.

A new value of ϵ could then be found by harmonic analysis. This was done for typical 3kHz slotting ($d/g = 15$, $s/g = 30$, $t/\lambda = 0.4$).

2.2.1 Teledeltos models.

Eleven models were made representing positions from Λ_{MAX} to Λ_{min} . They were made with 20° sloping sides. The tooth-opposite-tooth condition has simple symmetry as the flux must pass radially across the gap at the centres of the teeth, so it is easy to make these centre-lines the electrodes in an orthogonal plot. Use can also be made of the mid-line of the airgap being an equipotential in practice, i.e. a flow-line in an orthogonal plot.

For the tooth-opposite-slot condition, the only simple places where flux lines can be drawn with certainty are at the centre lines of the slots, but these require long electrodes in an orthogonal plot. After a hand plot to check the accuracy of the approximation, it was found sufficient to join the two corners at each side with electrodes and use an orthogonal plot between these electrodes.

The other nine positions have no simple natural positions for the electrodes. In each position, a short electrode was suitably placed based on knowledge of the flux distributions. For example, where there was no overlap, arguments similar to the tooth-opposite-slot condition were used, except that a whole tooth pitch was used. Where there was reasonable overlap, the mid-point of the overlap was

used as a radial flux line, i.e. an electrode in the orthogonal plot.

In this way, the eleven readings were taken from Λ_{max} to Λ_{min}, and the permeance variation was then analysed to obtain the mean value and the first eight harmonics, as shown in Table 2.

Table 2.

Harmonic analysis of permeance variation for 3kHz slotting.

(t/λ = 0.4, s/g = 30, d/g = 15.)

	← Harmonic order →							
mean value	Fund	2	3	4	5	6	7	8
100	58.6	0.2	2.3	1.1	0.2	0.5	0.3	0.1

The harmonic content is low, which is fortunate since the a.c. coils cannot be short-pitched or spread in these machines, and skewing is extremely delicate as small mechanical angles of skew represent large electrical angles because of the small wavelength of the rotor slots.

The permeance variation for the actual machine geometry, Fig 8, (t/λ = 0.39, s/g = 32.5, d/g = 18.4) was also analysed to obtain ϵ, Table 3.

Table 3.

Harmonic analysis of permeance variation for the experimental machine.

(t/λ = 0.39, s/g = 32.5, d/g = 18.4)

	← Harmonic order →				
mean value	Fund	2	3	4	5
100	52.5	1.3	0.66	0.9	0.13

These Teledeltos plots were all made for a single slot-pitch and are strictly comparable with the Carter method. A series of plots was also made for a whole stator main tooth, containing two small teeth, a small slot and the two adjacent slots, for the whole cycle. The flux utilisation coefficient ϵ increased from 0.525 (single slot) to 0.554. The actual variation, scaled to give the same value of ϕ_t for comparison is shown dotted on Fig 8.

Figure 9 shows the measured open-cicuit curve for the machine together with the calculated curves using the new value of ϵ from the whole large tooth (0.554) and the "single-slot" value of ϵ (0.525). Agreement is much better for the new value of ϵ .

* The experimental work described in sections 2.1.1 → 2.2.1 (except the flux plots over a whole stator main tooth) was carried out at GENERAL ELECTRIC, New York, and has been reproduced by kind permission of E.J.Davies.

2.2.2 Baillie method.

Carter's coefficients for calculating the effective airgap of a slotted structure are well-known. Although the expression can be summarised in the form of a curve or nomograms, it is not suitable for the derivation of permeance variations of the kind discussed in (2.2.1).

In 1909, T.C.Baillie[29] described a simple method for obtaining Carter's curves, which is accurate to better than 1%. The depth of slot is assumed to be 1/5 of its width and the permeance is then calculated as if there were no fringing, Fig 10a, giving the simple expression for Carter's coefficient

$$C = \frac{t+s}{t+\frac{5gs}{5g+s}}$$

which is convenient for slide-rule calculation and economical of computer space.

This method has been used in a French design handbook[30] for the calculation of airgap correction coefficients for simple slots for combinations of stator and rotor slots and for ventilation ducts. It seemed reasonable to apply it to Guy machines to try to calculate the variation of airgap permeance. When applied in a straight-forward way to the Guy airgap geometry between the centre line of the a.c. and d.c. slots, the results were as shown in Fig 11b. It agrees well with the tooth-opposite-tooth position and the error increases to 4% at $\lambda/4$. Thereafter, the divergence

suddenly increases and only returns to a fair approximation at the tooth-opposite-slot position.

The inclusion of the whole of the a.c. and d.c. slots was obviously wrong, from the airgap flux plots already analysed, so it was decided to apply the Baillie method for half a slot pitch on either side of the stator main tooth, i.e. to assume that the a.c. and d.c. slots were only s/2 wide on the stator side, instead of (3s+t)/4 as previously, Fig 10c. The actual tooth-slot configuration at the opening of the a.c. and d.c. slots is as shown in Fig 10b. To allow for the chamfer at the tooth edge, an approximation was made which increased the effective tooth width by 7.5%. The revised calculated points are shown on Fig 11c and will be seen to give good agreement with the Teledeltos plots. The approximation was tested using the other values of s/t, d/g, etc that had been plotted, with equally good results.

With this analytical method available, it is now easy to derive the permeance variations for various values of s/g and t/λ , section 10.3. Permeance curves for typical slottings were obtained, using the Baillie method, (Fig 12 a,b,c & d); similar curves were analysed for mean value, fundamental, 2nd and 3rd harmonics for a practical range of t/λ of 0.3 to 0.45 and for s/g of 28, 30 and 32. The value of ϵ and the harmonic content is shown in Table 4; for s/g = 30, t/λ = 0.4, the Baillie value of ϵ (0.52) can be compared with (Carter $\times$ 0.9) of 0.518.

Table 4.

Computed variation in ϵ and harmonic content of the permeance variation for various values of t/λ and s/g using the Baillie method.

Typical 3kHz slotting.

t/λ	ϵ			% 2nd harmonic flux wrt fundamental			% 3rd harmonic flux wrt fundamental		
	$s/g = 28$	$s/g = 30$	$s/g = 32$	$s/g = 28$	$s/g = 30$	$s/g = 32$	$s/g = 28$	$s/g = 30$	$s/g = 32$
0.3	0.49	0.53	0.53	30	26	27	2	2	2
0.35	0.51	0.54	0.54	15	13	14	2	2	3
0.40	0.50	0.52	0.53	5	4	5	4	6	5
0.45	0.45	0.46	0.47	0.2	1	0.5	8	8	9

In a practical machine, the s/g value is normally made as big as possible by using the minimum airgap. For this value of s/g, the table shows that a small increase in output could be obtained by decreasing the t/λ from its usual value of 0.4 to 0.35, but this would cause a large increase in 2nd harmonic flux content (and the associated losses).

Since the Baillie method is an approximation, the harmonic analysis must be treated with caution. The good agreement of the value of ϵ and of the permeance curves of Fig 11 suggests that considerable confidence can be placed in the fundamental component. The analysis of higher harmonics should not be taken too literally; nevertheless, it is believed that the lower order harmonics shown in Table 4 and their relative values for changes of s/g and t/λ are reasonably accurate.

Figure (12 e,f,g & h) shows the permeance changes for a typical 10kHz slotting, with s/g =8 and t/λ varied over the practical range of 0.3 to 0.45. The ϵ value using Teledeltos (section 2.1.1.1) was 0.24 compared with the Baillie value of 0.2, but it must be remembered that the latter is for a whole stator main tooth and is being compared with a'single-slot' figure. The value of ϵ and the harmonic content is shown in Table 5.

Table 5.

Computed variation in ϵ and harmonic content of the permeance variation for various values of t/λ using the Baillie method. (s/g constant)

Typical 10kHz slotting.

t/λ	ϵ for s/g = 8	% 2nd harmonic flux wrt fundamental	% 3rd harmonic flux wrt fundamental
0.3	0.19	16	6.5
0.35	0.18	13	3
0.40	0.20	6.5	4
0.45	0.19	3.5	4.5

The effect of varying s/g over a wide range, for a constant t/λ is shown in Fig 13, showing that the pu permeance for the tooth-opposite-slot position changes little compared with the tooth-opposite-tooth position.

2.3 Harmonic permeances.

In section 2.2.1 a series of permeance measurements was taken for a whole stator main tooth, containing two small teeth, without considering the distribution of flux in the airgap region. For 8 rotor positions the flux distribution was also determined along the surface of the stator and rotor. Figure 14 shows the flux distribution for these positions, including the two positions of symmetry which occur during a complete cycle (4 and 4a), Fig 14.

2.3.1 Symmetry.

In sections 1.2.2 and 1.2.2.1 the permeance variation was assumed to vary sinusoidally to introduce the basic ideas. Tests have shown that the permeance variation is not sinusoidal. If the permeance variation for a whole stator main tooth is analysed for a mean value and harmonic content over a cycle, i.e. $\phi_t \longrightarrow \phi_s \longrightarrow \phi_t$ position, then the permeance variation can be expressed in the form:-

$$\Lambda_A = \Lambda_o(1 + \epsilon_1 \cos\omega t + \epsilon_2 \cos 2\omega t + \epsilon_3 \cos 3\omega t + \_\_\_\_)$$

$$\Lambda'_A = \Lambda_o(1 + \epsilon_1 \cos(\omega t + \pi) + \epsilon_2 \cos 2(\omega t + \pi) + \epsilon_3 \cos 3(\omega t + \pi) + \_\_\_\_\_)$$

It follows that the a.c. and d.c. flux is given by:-

$$\phi_{ac} = \Lambda_o F(\quad 2\epsilon_1 \cos\omega t + \quad 2\epsilon_3 \cos 3\omega t + \_\_\_\_\_)$$

i.e. only odd harmonics link the a.c. winding.

and

$$\phi_{dc} = \Lambda_o F(2 + 2\epsilon_2 \cos 2\omega t + 2\epsilon_4 \cos 4\omega t + \_\_\_\_)$$

(only even harmonics link the field winding)

Figure 14 shows that during a complete cycle there are two positions of symmetry (4 and 4a) when either a rotor tooth or rotor slot is opposite the centre line of the a.c. slot. The main and leakage fluxes for these two positions are not the same and hence the two halves of the permeance cycle are not symmetrical. To derive expressions for the flux linking the a.c. and d.c. winding it is necessary to consider the two halves of the cycle which will modify the above equations.

Consider teeth A and A' (Fig 2): For the first half of the permeance cycle, i.e. $\phi_t \longrightarrow \phi_s$, the stator main tooth (A) will pass through a position of symmetry, Fig 14 (4), and during the second half of the permeance cycle will pass through the other position of symmetry, Fig 14 (4a). As main tooth (A) passes from $\phi_t \longrightarrow \phi_s$ position, tooth (A') will pass through a position of symmetry, Fig 14 (4a), i.e. (4a) is not a mirror image of (4).

When deriving the expressions for the flux in teeth A and A', the flux utilisation coefficient ϵ cannot be used, since it only applies for a symmetrical variation over a cycle; two coefficients are introduced at this stage, ξ_n and ξ'_n, where

ξ_n = coefficient relating the nth harmonic flux variation and the mmf over a half cycle as tooth A moves from the $\phi_t \longrightarrow \phi_s$ position.

ξ_n' = coefficient relating the nth harmonic flux variation and the mmf over a half cycle as tooth A moves from the $\phi_s \longrightarrow \phi_t$ position.

For the tooth A the flux can be expressed in the form:-

$$\underset{\phi_t \rightarrow \phi_s}{\phi_A} = F\Lambda_o(1 + \xi_1 \cos\omega t + \xi_2 \cos 2\omega t + \xi_3 \cos 3\omega t + \ldots)$$

$$\underset{\phi_s \rightarrow \phi_t}{\phi_A} = F\Lambda_o(1 - \xi_1' \cos\omega t + \xi_2' \cos 2\omega t - \xi_3' \cos 3\omega t + \ldots)$$

for tooth A'

$$\underset{\phi_s \rightarrow \phi_t}{\phi_A'} = F\Lambda_o(1 - \xi_1' \cos\omega t + \xi_2' \cos 2\omega t - \xi_3' \cos 3\omega t \ldots)$$

$$\underset{\phi_t \rightarrow \phi_s}{\phi_A'} = F\Lambda_o(1 + \xi_1 \cos\omega t + \xi_2 \cos 2\omega t + \xi_3 \cos 3\omega t \ldots)$$

From the above expressions it can be seen that the flux linking the d.c. winding will contain even and odd harmonics:

$$\phi_{\text{d.c. pole (teeth A and B)}} = F\Lambda_o\left[2 + (\xi_1 - \xi_1')\cos\omega t + (\xi_2 + \xi_2')\cos 2\omega t + (\xi_3 - \xi_3')\cos 3\omega t + \ldots\right]$$

Similarly the flux variation linking the a.c. winding

$$\phi_{\text{a.c. winding}} = F\Lambda_o\left[(\xi_1 + \xi_1')\cos\omega t + (\xi_2 + \xi_2')\cos 2\omega t + (\xi_3 + \xi_3')\cos 3\omega t \ldots\right]$$

Tests have shown that even and odd harmonic fluxes link the a.c. and d.c. windings under open-circuit conditions. The harmonic fluxes linking the d.c. winding, although small, are of a sufficient high frequency to induce considerable voltages in the d.c. field, Table 6.

Table 6.

Harmonic voltages induced in a field coil.
No damping, Rated open-circuit voltage.

Harmonic order	V peak (volts)
fundamental	90
2	85
3	42.5
4	114
5	5.25

Total peak voltage in one field coil = 326 volts.
In previous papers[5,7] the discussion of high voltages across a field coil has been confined to on-load performance; however, a detailed study of open-circuit permeance variations and measurements across a field coil, have shown that voltages liable to cause a breakdown of the field insulation are also present under open-circuit conditions,(without damping). The need for damping windings on open-circuit is apparent; the effects of damping upon these fluxes and the induced voltages in the field is discussed in subsequent chapters of the thesis.

2.4 Permeance variation in total pole.

Figure 8 is not sinusoidal, nor is it symmetrical about its mean value. The total pole has two such variations, whose fundamentals are 180° out of phase with each other. The total airgap permeance is the sum of these permeances and could be obtained by adding Fig 8 to the same curve moved through 180°. This was done, and showed a variation of the total permeance over a cycle, but was relatively insensitive to fine changes of permeance.

It is important to know the detailed variation of the total permeance, and how the permeance varies in adjacent poles, as the fluxes associated with these permeances link the field and damping windings, so Teledeltos models were made of the total pole (between successive field slots). They were made as large as possible (20 x full size) since the variations in flux linking the field and back of the d.c. slot are small compared with the main fundamental flux. The airgap has to be very accurate in the model; to ensure this, ground key stock (0.635cm) was used to cut and mark the airgap itself.

Measurements were taken over a cycle; the results are plotted in Fig 15a. The peak to peak variation is seen to be about 5% of the mean value. The permeance in two adjacent poles is 180° out of phase so that the resultant permeance, Fig 15c, is given by the difference between Fig 15a and Fig 15b.

From the relationship $\phi = (\text{mmf} \times \Lambda)$, the variation in flux linking the back of the field slots for rated open-circuit voltage was obtained and compared with test results, Fig 15d.

2.5 Conclusions.

This chapter, using Teledeltos plots to examine permeance variations, shows that many of the design criteria (e.g. t/λ , d/g) of practical Guy-type machines are correctly chosen. The new plots have been extended to a whole stator main tooth and to the whole d.c. pole. They show that the permeance variation for the whole stator main tooth is slightly (6%) different from the variation of one stator slot pitch, giving a better prediction of the open-circuit curve of the machine, and that the small asymmetry of the two halves of a pole produce harmonic variations in the field on no load.

A simple approximation, based on Baillie, is shown to give good agreement with flux plots for the values of airgap parameters studied. Whilst it must be used with caution, the method allows the variation of airgap permeance to be calculated easily by hand, or with a small computer programme. The method could be extended to other problems involving overall permeance variations (as opposed to detailed variations at one point in the airgap).

Chapter 3.

The experimental machine.

Chapter 3. The Experimental Machine.

Summary.

This chapter discusses in detail the design and building of the experimental machine. An industrial Guy-type Alternator rated at 44.4 KVA was used for the experimental work.

Minor modifications were made to the normal windings, so that damping currents and voltages in the field windings could be measured.

Search coils were located on the stator and rotor to allow detailed flux measurements to be made.

The design of a series capacitor unit and details of the water cooled load etc, are also given.

3.1. The design of the experimental machine.

The stator frame and punchings used in the experimental machine are exactly the same as used in an Industrial machine rated at 44.4 KVA. The stator and rotor tooth-slot configuration is shown in Fig 16.

General details of the machine are given in Table 7.

Table 7.

General details for the experimental machine.

Voltage	500/250 volts
Current	89/178 amps
Speed	3000 rev/min
D.C. poles	12
Rotor teeth	60
Airgap	0.0317 cm
Stator core length	22.2 cm
Stator i.d.	31.115 cm
rotor slot pitch	1.62 cm
rotor tooth width	o.635 cm
depth of rotor slot	0.583 cm

More detailed information on windings and load field requirements etc, are given in the manufacturers design sheet, Fig 17. From heat run data on a machine of this type,* it was decided that the machine rating could be increased to 55 KVA without overheating. A design for this rating is given in Fig18 .

* see section 7.3.6.1 of this thesis.

3.2 Windings.

The positions of the various windings are shown in Fig 16.

3.2.1 A.C. winding.

The coils for the a.c. winding were preformed from rectangular copper section (6.7 × 1.27)mm. To reduce eddy current losses in the a.c. winding, the conductor in the slot is subdivided; from design curves it is possible to choose an optimum value for the depth of copper in each layer. Six coils, each comprising six conductors (3 effective conductors/slot), were connected in series to give 18 series turns/phase. Tappings across each a.c. coil were brought out of the machine to check the concentricity of the airgap and to allow the two halves of the winding to be connected in series or parallel.

3.2.2 Field windings.

Each of the 12 field coils comprises 143 turns of 0.0812 cm diameter wire. Tappings across two adjacent field coils were brought out of the machine to a main terminal board to allow measurement of the induced voltage in the coils.

3.2.3 Damping windings.

Damping windings (4.5, 5.1.1,& 5.6.2) are usually fitted to inductor alternators of this type to reduce the harmonic fluxes which link the field winding on load; these windings consist of short circuited turns in either the top or the bottom of the d.c. slots.

Short-circuited coils at the back of the d.c. slots have also been used for damping the fluxes which link the field winding.[32] These three types of winding were built into the experimental machine to observe the effects of damping.

The end connections for each damping coil were brought out of the machine so that:-

(a) the effect of each type of damping could be investigated by simply short circuiting the appropriate coils.

(b) the damping currents could be measured.

The core damping windings consist of 7 turns of 0.1648 cm diameter wire; the seven turns were wound around the back of the d.c. slots and anchored to the end-rings. ($R_{CORE} = 0.028\Omega$)

Each coil for the top and bottom damping windings comprises 14 turns of 0.0812 cm diameter wire; these coils and the coils forming the main d.c. winding were all wound on the same former.
(mean length of field, top and bottom damping windings = 84 cm) $R_{TOP} = R_{BOTTOM} = 0.385\Omega$.

3.3 Search coils.

3.3.1 Stator search coils.

The stator was provided with a large number of search wires, Figs 19 & 20, to investigate the flux distribution in the stator core and teeth. A special stator-core packet, 1cm long, was positioned in the middle of the stator core, to enable detailed flux measurements to be made.

The holes to accommodate the search wires were made as small as possible so that their effect upon the fluxes would be negligible; the smallest hole that could be drilled satisfactory was 0.0254 cm diameter, using a drill speed of 18000 rev/min. Due to the shortness of the drill shank, it was necessary to drill each lamination separately. A precision jig was built to drill the matrix of holes in the stator iron; each lamination was accurately located on the jig by a series of ground studs. When the laminations had been drilled, the burrs caused by drilling were carefully removed. The stack was assembled on the jig and riveted together at the back of the core away from the varying fluxes; the holes in individual laminations lined up with each other, since each lamination could be mounted accurately on the jig, (within $\pm$ 0.0013 cm). V shaped grooves were cut in the stator tooth surface to accommodate a 0.0152 cm dimeter wire. Search wires were also positioned on the sides of the d.c. and a.c. slots and at the back of the core. A common connection was made to all the wires at one end of the stack; at the other end of the stack the wires were suitably twisted and led out of the machine to selector switches. At each side of the stator stack the laminations were cut away to accommodate the common connection and the search wire end connections which were led out radially. Each search wire was connected to two 75-way selector switches, enabling any two wires to be connected to form a search coil.

3.3.2 Rotor search coils. Figs, 21 &22.

Search wires on the rotor were placed along the entire core length. The wires were located only on the tooth surface and on the sides of the slots. Shallow V grooves (approximately 0.025 cm wide at the tooth surface), were cut into the tooth surface to accommodate the 0.0152 cm diameter wires. A mixture of Araldite and mica dust was used to hold the search coils in position. A common connection was used on the drive end of the rotor and the wires forming the search coils were led to a terminal block on the end-plate of the rotor core. From this terminal block a multicore screened cable was led out through the shaft to a slip ring assembly coupled to the generator by a flexible coupling.

3.4. Design of the water cooled capacitor.

A water cooled capacitor used to investigate the effects of series compensation was designed to operate over the range 4-40 μF in 4 μF steps. Details of the capacitor unit are given below:-

Water cooled medium frequency capacitor

Type L200, (impregnated in chlorinated diphenyl)

Current carrying capacity 100 amps.

The capacitor unit consists of 6 sections as follows:- 4,8,8,4,8 and 8 μF, making it possible to select any value between 4 and 40 μF in 4 μF steps. All sections singly, or together are capable of operating continuously at 700 volts. Equal sections in either half of the can could also be used in series to provide values of 2,4,-------- 10 μF. (maximum terminal voltage 1400 volts.) The cooling system is adequate for a total loading of 400 KVA_R.

To change over the connections during compensation tests, it was necessary to discharge the capacitors; 150 KΩ 2 watt resistors were connected between each line terminal and the common to reduce the residual voltage across the capacitor to a small value within 1 to 2 minutes.

3.5 Supporting apparatus.

3.5.1 Water cooled load.

The water cooled load consists of a nickel helical resistor mounted on a ceramic core, (2 units each 7.6cm diam x 35.5cm long). The resistance was variable by altering terminal clamps to any point on the helix, (maximum resistance 6 Ω). The unit is suspended in water which can be continuously changed. With full mains water pressure feeding the load tank, (plastic water tank 45.7 x 61 x 38cm), it was possible to dissipate 100 KW. Compared with other methods of dissipating the load, e.g. fan cooled resistors or expanded metal cages, the water cooled load is much smaller and easily controlled.

3.5.2 Drive motor.

G.E.C. Induction motor.
170 h.p.
400/440 volts. 214 amps.
2940 revs/min. B.S. 168 CONT.

Starter. E.A.C. Type 30Q0DSD.
h.p. 170. 400/440 volts, 3 phase.

Chapter 4.

Stator flux distribution on open-circuit.

4.1 Flux distribution at the stator surface.

4.1.1 Theory.

.2 Teledeltos models.

.3 Waveform analysis.

4.2 Experimental work.

4.2.1 Flux waveforms at the surface.

.2 Addition of fluxes at the surface.

.2.1 Fundamental flux.

.2 Second harmonic flux.

.3 Leakage flux waveforms.

4.3 Losses in the small teeth.

4.4 Flux distribution in the stator core (no damping)

4.4.1 Fundamental flux.

.2 Second harmonic flux.

.2.1 Unsaturated conditions.

.2 Saturated conditions.

.3 Second harmonic flux paths (no damping)

4.5 Damping windings and their effect upon flux distribution.

4.5.1 Fluxes linking the a.c. and d.c. windings.

.2 Equivalent circuit for damping winding.

4.6 Experimental work.

4.7 Flux distribution in the core with damping.

4.7.1 Fundamental flux.

.2 Second harmonic flux.

4.8 Conclusions.

STATOR FLUX DISTRIBUTION ON OPEN CIRCUIT.

Summary.

Existing theories related to the open-circuit and load performance of the Guy-machine are based upon simple approximations which are untrue for practical machines, and which lead to considerable errors in calculating the losses in the tooth regions. In the previous chapter detailed permeance calculations showed the necessity to include permeance harmonics and to analyse the permeance variation over a whole stator main tooth.

This chapter considers in detail the open-circuit flux distribution in the stator laminations, the understanding of which is essential before embarking on the calculation of load performance.

The results show that a considerable amount of harmonic flux is present in small sections of the tooth surface; these harmonic fluxes cause additional loss in the tooth surface. In the core region harmonic fluxes are present which link the a.c. and d.c. windings. The voltages induced in the field windings were also investigated in detail for various types of damping, showing the need for damping windings under open-circuit conditions.

4.1 Flux distribution at the stator surface.

4.1.1 Theory.

The flux waveform in a small section of the surface under open-circuit conditions is dependent upon the airgap geometry.

If the tooth surface is divided into m sections, then for any section along the surface the flux will be a maximum for $\left[\frac{t(m-1)360}{m\lambda}\right]$ electrical degrees, Fig 23c. As the rotor tooth moves across the surface, the flux will decrease to a minimum value, and then increase as the next rotor tooth aligns itself with the stator tooth A; the interval for this to take place is given by $\left[(s+\frac{t}{m})\frac{360}{\lambda}\right]$ electrical degrees, Fig 23c.

To fix the shape of the flux waveform, the slope of side of the waveform and the fluxes ϕ_a and ϕ_b have to be calculated, where ϕ_a = maximum flux in a small section of the tooth surface on open-circuit, for a given field current and ϕ_b = minimum flux in a small section of the tooth surface on open-circuit, for a given field current. The rate of decrease or increase of flux is dependent upon the slope of side of the slot and the tooth-slot parameters d/g and t/λ . To determine the slope of side of the flux waveform it is necessary to know the flux distribution in the airgap. Teledeltos models similar to those in chapter2 were used for this purpose. The fluxes for a given field excitation are easily calculated

from the permeances Λ_p and Λ_q , where Λ_p = maximum permeance seen by a small section of the surface and Λ_q = minimum permeance seen by a small section of the surface.

4.1.2 Teledeltos models.

The tooth surface was marked off into seven sections so that results could be correlated directly with the search coil stack. The potential distribution (which can be shown to be analogous to the flux distribution) was measured for each small section of the stator tooth surface over a complete rotor cycle, enabling the flux waveforms to be plotted for each small section, Fig 24. For this particular geometry the slope of the side of the flux waveform was found to be 10°. For machines operating at 3kHz, the d/g and t/λ parameters will be of the same order as the experimental machine; since the slope of side of the slots is usually constant, i.e. 20° for these machines, an angle of 10° (for the slope of side of the flux waveform) may be used with some confidence for 3kHz machines. For other frequencies where t/λ and d/g are substantially different from those used in the experimental machine, flux plots would have to be used to find the slope of side of the flux waveforms, since the time interval for the flux to change from ϕ_a to ϕ_b cannot be determined from the tooth-slot geometry; tests over a wide range of t/λ and d/g would lead to empirical formulae for determining

the slope of side of flux waveforms.

The ratio $\left[\dfrac{\frac{t(m-1)}{m}}{(s+\frac{t}{m})}\right]$ was also verified by Teledeltos, Table 8.

Table 8.

Comparison of slope of side of flux waveform and the ratio $\dfrac{\frac{t(m-1)}{m}}{(s+\frac{t}{m})}$ for measured and calculated results.

3kHz slotting, $t/\lambda = 0.39$, $s/g = 32.5$, $d/g = 18.4$. slope of side of slots $=20^{\circ}$.

	machine parameters	Teledeltos analogue	machine 1 amp field	machine 2.15amps field
$\dfrac{\frac{t(m-1)}{m}}{(s+\frac{t}{m})}$	0.502	0.495	0.51	0.49
slope of side of flux waveform.		10°	10°	10°

The flux waveforms in adjacent small sections are displaced from each other by a time interval, (18.3 μsec, [20° electrical]), Fig 24. This interval which separates each section is associated with the physical movement of a rotor tooth across the stator tooth surface. The shape of the flux waveform in a small section shows that a considerable amount of harmonic flux is present. Previous Teledeltos models (chapter 2) concerned with overall flux variation across the tooth surface, show that it is very nearly sinusoidal. The harmonic fluxes which appear in small

sections of the surface must therefore combine in such a way as not to appear in the resultant flux waveforms across the surface. To relate the flux waveforms in a small section and the waveform across the tooth surface it is convenient to introduce a harmonic reduction factor K_{Dn}, which relates the nth harmonic flux in a small section and the amount of nth harmonic flux in the total surface.

4.1.3 Waveform analysis.

To a good approximation the flux waveform in a small section can be represented by an asymmetrical trapezium, Fig 23d. The harmonic content can be calculated by expressing the waveform as a Fourier series:-

$\phi_{\text{small section}}$ is proportional to

$$\frac{2a\ell}{\alpha\pi^2n^2}\left\{\sum_{n=1}^{\infty}\left[\cos n\frac{(b+\alpha)\pi}{\ell}-\cos n\frac{(b-\alpha)\pi}{\ell}\right]\cos n\frac{\pi x}{\ell}\right\}$$

It follows that the total flux across the surface can be expressed in the form:-

ϕ_{Total} is proportional to

$$\frac{2a\ell_m K_{Dn}}{\alpha\pi^2n^2}\left\{\sum_{n=1}^{\infty}\left[\cos n\frac{(b+\alpha)\pi}{\ell}-\cos n\frac{(b-\alpha)\pi}{\ell}\right]\cos n\frac{\pi x}{\ell}\right\}$$

$$\ell = \lambda/2$$

For accurate results the K_{Dn} value should be calculated for $m\rightarrow\infty$, i.e. K_{Dn} = chord/arc.
The measured fundamental fluxes in small sections of

the tooth surface and in the large teeth are shown in Fig 25, (1 amp field excitation).

$$\text{For } m \to \infty \quad K_{p1} = \frac{\sin m\frac{\sigma}{2}}{\frac{\sigma m}{2}} \quad , \text{ where } \sigma = n\gamma \ .$$

K_{p1} = 0.812 (using theoretical γ angle of 20°).

For tooth (4-11) the average flux in a small section = 50.1 μWb.

Fundamental flux across (4-11) = $7 \times K_{p1} \times 50.1$ μWb

= 285 μWb.

(compare with 276 μWb measured)

For tooth (21-28) the fundamental flux = $7 \times 0.812 \times 48.1$

= 274 μWb.

(compare with 274 μWb measured)

4.2 Experimental work.

4.2.1 Flux waveforms at the surface.

Since the Teledeltos analogue is valid only under non-saturated conditions, initial tests were carried out at a low value of field excitation, (1 amp); at a later stage the field current was increased to observe the effects of saturation, (2.15 amps). The predicted flux waveform (Fig 24) compared favourably with experimental waveforms, Fig 26; the ratio $\left[\frac{\frac{t(m-1)}{m}}{(s + \frac{t}{m})} \right]$ and the slope of side of the measured flux waveform are compared in Table 8, with

the results from Teledeltos and the tooth slot geometry. With the field current increased to 2.15amps, (rated open-circuit voltage of the machine), there is slight distortion of the flux waveform in a small section, but fairly good agreement still exists with the analogue results, Table 8.

Two adjacent search coils on the stator tooth surface were used to measure the phase displacement between the flux waveforms (4-5) and (5-6), Fig 26d; as expected the waveforms are displaced by a time interval associated with the physical movement of the rotor, (20° electrical). The flux waveform was also measured across the total tooth surface, Fig 26e; the waveform shows a considerable reduction in harmonic content compared with a small section. For a small section of the tooth surface the harmonic fluxes were measured using a waveform analyser, and compared with the harmonic analysis obtained from the Teledeltos plots, Table 9. A similar analysis was also conducted over the whole tooth surface, Table 9.

Table 9.

Harmonic content in a small section of the tooth surface and across the total tooth width. I_f=1.0 amp.

conductor and order of harmonic	machine flux readings in μWb 1 amp field.	machine % harmonic wrt fundamental	analogue % harmonic wrt fundamental
Fund(4-5)	41.7	100	100
2nd (4-5)	4.16	10	11.8
3rd (4-5)	8.34	20	25.8
4th (4-5)	3.94	9.45	10
5th (4-5)	2.65	6.36	8.8
Fund(4-11)	230	100	100
2nd (4-11)	5.83	2.54	2.4
3rd (4-11)	2.46	1.06	1.25
4th (4-11)	3.75	1.63	1.7

In both cases good agreement exists between the measured and predicted harmonic content, giving confidence in the Teledeltos plots.

4.2.2 Addition of fluxes at the surface.

To demonstrate the addition of harmonic fluxes at the tooth surface, only the fundamental and second harmonic components are considered in detail. Measurements of the harmonic fluxes in small sections, and across two adjacent sections, enabled vector diagrams to be constructed as shown in Figs 27 and 28.

4.2.2.1 Fundamental flux.

The fundamental fluxes across small sections of the stator tooth surface combine to give a main tooth flux (ϕ_{4-11}) which is given by:-

ϕ_{4-11} = mK_{D1}(fundamental flux in a small section).

The harmonic reduction factor K_{Dn} is analogous to the breadth factor arising from the distribution of a winding in a machine. The displacement between adjacent sections (γ_n electrical degrees) was measured across the surface; from the physical geometry of the machine, these sections should be equally displaced from each other. γ_n angles taken from the vector diagram, Fig 27, varied slightly from the theoretical value due to small errors in measuring the fluxes; the average measured γ_n angle from the vector diagram = 18.5°.

[$\gamma_n = \gamma_1$ for fundamental.]

4.2.2.2 Second harmonic flux. (Fig 28)

The second harmonic fluxes in small sections of the stator tooth surface combine to give a main tooth flux which is given by:-

$\phi_{2(4-11)}$ = mK_{D2}(second harmonic flux in a small section)

K_{D2} is considerably lower than K_{D1} (compare K_{D1} = 0.84 and K_{D2} = 0.169, at rated open-circuit voltage).

The harmonic reduction factors for the other harmonics are also small compared with the fundamental,

resulting in a flux variation across the surface which is nearly sinusoidal, Table 10. For completeness the vector diagrams for the 3rd, 4th and 5th harmonic fluxes are shown in Fig 29.

Table 10.

Comparison of K_{pn} factors from the machine and analogue results.

Harmonic order n.	K_{pn} (machine) 1 amp field.	K_{pn} (machine) 2.15 amps field.	K_{pn} analogue.
1	0.79	0.845	0.8
2	0.2	0.169	0.17
3	0.046	0.037	0.04
4	0.136	0.133	0.13

4.2.3 Leakage flux waveforms.

The flux across (42-32), Fig 19, which does not pass through the small tooth surfaces (4-11) and (21-28) is defined as leakage flux. At the openings of the ac and dc slots the leakage flux was measured across (3-4) and (28-29), Fig 19 and Fig 30; for the small slot in a whole main tooth, the leakage fluxes were measured across (11-13) and (21-29), since the fluxes ϕ (13-15) and ϕ(17-19) are very small under open-circuit conditions, Fig 19 and Fig 30.

For 1.0 amp field excitation the leakage flux waveforms at the tooth surface were measured, Fig 30;

the main tooth surface flux was used as a reference signal so that the phase relationship between the waveforms could be obtained. At the leading and trailing edges of the small tooth (4-11), the leakage flux waveforms are similar in shape to the waveforms 4-5, 5-6, 6-7 etc, since the leakage permeance variation is similar in shape to that for small sections of the tooth surface. When the stator and rotor teeth are opposite, the leakage fluxes at (3-4) and (11-13) are small, since most of the flux passes through the tooth region; as the rotor teeth move into the symmetrical position (4), Fig 14, the leakage flux decreases slightly at the leading edge, as more flux passes through the tooth section and the trailing edge of the stator tooth. For the stator tooth opposite rotor slot position the permeance increases for the leakage paths, resulting in an increase of leakage flux. When the rotor tooth has moved to the second position of symmetry (4a) Fig 14 , the permeance for the leading edge of the tooth is greater than for the trailing edge; the flux at the leading edge reaches a maximum for this condition, while the flux at the trailing edge decreases to its minimum value. The flux waveform across (3-13) was also measured, Fig 30; this flux is in phase with (4-11) and the same magnitude, suggesting that the effects of the leakage flux at the leading and trailing edges of the stator teeth cancel each other out. Flux waveforms for the adjacent small tooth (21-28) are also shown in Fig 30.

4.3 Losses in the small teeth.

In this type of machine, losses are usually calculated using the fundamental component of flux; the fundamental loss is calculated from design values of flux density and the appropriate loss curve for the material. Flux measurements over a small section of the stator tooth surface have shown the presence of harmonic fluxes which will influence the loss calculation. An extra loss factor k is introduced to take account of these harmonic fluxes. The factor k is defined as

$$k = \frac{\text{Total loss}}{\text{fundamental loss}} .$$

If the flux carried by iron in a magnetic circuit is varied, hysteresis and eddy-current losses are produced. Eddy-current loss, under normal conditions, may be expressed to a sufficiently close approximation as $P_e = K_e(B_{MAX} f \Upsilon)^2$ where Υ is the lamination thickness, B_{MAX} the maximum flux density and K_e a proportionality constant whose value depends on the units used, the volume of iron, and the resistivity of the iron. The most commonly used relation for hysteresis loss is $P_h = K_h f B_{MAX}^{\rho}$, where K_h is a proportionality constant, ρ ranges from 1.5 to 2.5.

Loss curves for the core material used in the experimental machine,* (MM262, 0.0178cm grade 1100) are given in Figs 31 and 32. Fig 31 shows the specific

* reproduced by kind permission of E.J.Davies.

loss against frequency for various values of flux-density; if the results are plotted on log-log paper, as shown, the relationship between specific loss and frequency is linear, i.e. loss (for constant B) is proportional to f^n. At 0.20Tesla the slope, $n = 1.41$, i.e. (loss $\propto f^{1.41}$) and at 0.46Tesla, $n = 1.63$, (loss $\propto f^{1.63}$). An average figure of $n = 1.5$ was chosen for calculating the losses in the stator and rotor laminations. Fig 32 shows the specific loss plotted against B (Tesla),for a range of frequencies (1-10 kHz); again the relationship is linear, i.e. loss $\propto B^m$ (for constant f). Over the range 1-10 kHz, m varies between 1.89 and 2.2; for the purpose of calculating losses, m=2.0 was chosen. To a good approximation the losses can be assumed to be proportional to $f^{1.5} B^2$ at these frequencies.

For a small section, the harmonic content is known, and therefore it is possible to calculate the total loss from a knowledge of the fundamental loss and the appropriate K_{Dn} factors.

Example:-

A harmonic analysis of the flux waveform in section (4-5) of the tooth surface, I_f = 1.0 amp, results in the following:-

ϕ_{FUND} = 47.2 μWb, ϕ_2 = 4.5 μWb, ϕ_3 = 9 μWb, ϕ_4 = 4.25μWb, ϕ_5 = 2.82 μWb.

Therefore:-

fundamental loss $\propto 3000^{1.5}(47.2)^2 \propto 3.29\times10^8$

2nd harmonic loss $\propto 6000^{1.5}(4.5)^2 \propto 7.0\times10^6$

3rd harmonic loss $\propto 9000^{1.5}(9)^2 \propto 6.75\times10^7$

4th harmonic loss $\propto 12000^{1.5}(4.25)^2 \propto 5.21\times10^7$

5th harmonic loss $\propto 15000^{1.5}(2.82)^2 \propto 8.9\times10^7$

$$\Sigma \text{ losses} \propto 5.44\times10^8$$

$$k\ (\ 1.0\ \text{amp}\ ) = \frac{5.44\times10^8}{3.29\times10^8} = 1.65,\ (\text{Table 11})$$

For a more accurate determination of k, a different value of m would have to be chosen for each frequency; since m decreases as the frequency increases, Fig 32, the resulting k factor will be slightly lower than when m=constant=2 is chosen.

The actual loss in a small section is found by multiplying the fundamental loss in a small section (obtained from suitable loss curves) by the extra loss factor. For open-circuit conditions extra loss factors calculated at the surface and further back in the tooth are shown in Table 11.

Table 11.

Extra loss factors for the small teeth.

conductor	k(1.0amp)	k(2.15amps)	k(3amps)	k(4amps)
4-5	1.65	1.8	1.8	1.66
21-22	1.62	1.8	1.8	1.67
3-4	1.24	1.34	1.35	1.27
11-12	1.24	1.38	1.38	1.35
1-13	1.0	1.02	1.02	1.05

Extra loss factors calculated for a small distance (0.25cm) away from the tooth surface, quickly approach unity, (section 1-13). An average loss factor for the whole small tooth region was calculated for rated open-circuit voltage and found to be 1.21, which represents a 21% increase in loss compared with the loss based upon fundamental flux.

Under load conditions the fluxes at the surface are further distorted by armature reaction. To obtain a true estimate of the losses, the harmonic fluxes must be taken into account; extra loss factors similar to those described for the open-circuit condition can be used on load to determine the true loss. Losses in the teeth on load are discussed in the next chapter, (section 5.3).

4.4 Flux distribution in the stator core - no damping.

4.4.1 Fundamental flux.

The fundamental flux across the main stator tooth (43-48) was measured for 0→4.0 amps field excitation and was compared with the voltage induced in the a.c. coil linking the search coil area,(AC_{3-4} ,Fig 33). Theoretically the flux linking the a.c. coil AC_{3-4} should be equal to twice the flux linking (43-48), 1.2.2.2; error in estimating the effective core length accounts for the discrepancy between ϕAC_{3-4} and 2ϕ(43-48). The fluxes measured across 43-44,_____48 are in phase, so the phase angles which appear at the tooth surface

are not reflected into the back of the teeth, Fig 25. Most of the fundamental flux passes behind the a.c. slot, Fig 25, resulting in a non-linear flux density distribution across (43-48) and (49-70). The fundamental flux which passes behind the d.c. slots is approximately 2.4% of the main a.c. flux, Fig 33.

4.4.2 Second harmonic flux.

Second harmonic fluxes were measured for various values of field excitation in the following regions:- (a) 43-48, (b) 49-70, (c) 58-67, Fig 34.

4.4.2.1 Unsaturated conditions.

The fluxes passing behind the d.c. and a.c. slots combine to give the flux across the main tooth (43-48). For unsaturated conditions there is no phase angle between ϕ_{49-70} and ϕ_{58-67} . To predict the flux linking the a.c. winding from these measurements it was necessary to assume flux paths for the second harmonic flux, Fig 35a.

From flux measurements for unsaturated conditions, e.g. $I_f = 1.5$ amps, Fig 35b, it was possible to determine the flux paths across a pole pitch B, (search coil area). Initially the same paths were chosen for the adjacent pole A; the resulting flux linking the a.c. winding from these flux paths gave the wrong answer. Since ϕAC_{3-4} was known, the flux linking the a.c. winding in pole A could be calculated; from these results it was obvious that the second harmonic fluxes

behind the a.c. slots are distributed as shown in Fig 35a.

Fig 34 shows the measured a.c. flux ϕAC_{3-4} and the flux linking the a.c. winding from the vector diagram and the assumed flux paths. The close agreement between them gives confidence to the validity of the chosen paths.

4.4.2.2 Saturated conditions.

Under saturation conditions a phase angle is introduced between ϕ_{49-70} and ϕ_{58-67}. Search coil measurements under saturation conditions enabled vector diagrams to be constructed which show how these fluxes combine together. To calculate the flux linking the a.c. winding, it was necessary to consider two adjacent pole pitches and to calculate the flux linking the two main stator teeth, Fig 35. Again good correlation exists between the measured flux linking the a.c. winding and that predicted from vector diagrams.

For unsaturated and saturated conditions, the second harmonic flux linking the a.c. winding is in phase with ϕ_{49-70} and is approximately equal to $2\phi_{49-70}$, Fig 34.

4.4.3 Second harmonic flux paths- no damping.

As the field current is increased from 0 to 4.0amps there is a redistribution of second harmonic flux in the stator core, Fig 35. For unsaturated conditions

($0 \rightarrow 2.0$ amps), the second harmonic fluxes are reasonably well behaved, i.e.

(a) $\phi_{\overline{43\text{-}48}} \simeq \phi_{\overline{58\text{-}67}} + \phi_{\overline{49\text{-}70}}$ ($\phi_{58\text{-}67}$ & $\phi_{49\text{-}70}$ in phase)

($\phi_{58\text{-}67} > \phi_{49\text{-}70}$)

(b) the flux-field current relationship between small sections across 43-48 is approximately linear, Fig 36. At $I_f = 2.5$ amps there is a slight decrease in $\phi_{43\text{-}48}$; beyond this value of field excitation the flux $\phi_{43\text{-}48}$ increases until saturation effects cause a reduction in flux at $I_f = 3.5$ amps. Beyond $I_f = 2.5$ amps ($\phi_{58\text{-}67} < \phi_{49\text{-}70}$) until $I_f = 3.5$ amps where the condition is reversed again and ($\phi_{58\text{-}67} > \phi_{49\text{-}70}$). Although saturation in the stator core may have some effect upon the distribution of flux, the second harmonic flux paths in the core are controlled mainly by what happens in the small tooth regions. The main and leakage fluxes are particularly sensitive to changes in field excitation, and the phase angles which exist at the surface (due to the combination of main and leakage fluxes) are reflected into the back of the small teeth (section 43-48). The non-linear flux distribution across 43-48 results in peculiar saturation curves for the second harmonic components, Fig 36; the dips in the flux curves are due to saturation effects and the redistribution of flux as the field current is altered. Up to approximately 2 amps field excitation, the flux-field current relationship is practically linear, Fig 36; with a further increase in excitation, the fluxes in each of the small sections across 43-48 decrease to

a minimum value and then increase, e.g. $\phi_{45\text{-}46}$ reaches a minimum value at I_f = 2.4 amps. At I_f = 2.5 amps, the second harmonic fluxes in the two small teeth comprising a whole stator main tooth, ($\phi_{3\text{-}13}$ and $\phi_{19\text{-}29}$) are nearly in antiphase, Fig 41; this results in a decrease of flux across 43-48, since $\phi_{\overline{43\text{-}48}} \doteq \phi_{\overline{3\text{-}13}} + \phi_{\overline{19\text{-}29}}$. The magnitude and phase of the second harmonic fluxes across (3-13) and (19-29) depend on how the main tooth surface fluxes and leakage fluxes combine; as the field excitation is increased, the leakage flux in the small slots increases until high values of saturation, e.g. still increasing at I_f = 2.5 amps, (although $\phi_{43\text{-}48}$ is a minimum for this value of I_f , Fig 40 & 41). The magnitude of these fluxes is critically dependent upon the flux waveforms at the surface; saturation effects also influence the calculation. Peculiar flux-field relationships are also present when damping windings are added, 4.7.2. Since the magnitude and phase of these fluxes is critically dependent upon the value of I_f , the calculation for a given field excitation would be extremely tedious, i.e. the flux waveforms across the surface and the leakage flux waveforms would have to be calculated, taking into account their relative phase displacement.

4.5 Damping windings and their effect upon flux distribution.

Damping windings are usually fitted to Guy-machines to reduce the second harmonic flux which links the field

coils under load conditions, 5.1.1. In chapter 2, measurements have shown that harmonic fluxes also link the field winding on open-circuit. These fluxes induce voltages in individual field coils which are liable to cause a breakdown of the field insulation, showing the need for damping windings on open-circuit; at rated open-circuit voltage, the induced voltage in a single field coil = 340 volts (peak), Fig 37.

4.5.1 Fluxes linking the a.c. and d.c. windings and the effects of damping.

If the permeance variation is assumed to be sinusoidal, the fluxes linking the a.c. and d.c. windings under open-circuit conditions (without damping) are given by $2F\Lambda_o\epsilon\cos\omega t$ and $2F\Lambda_o$ respectively, (section 1.2.2.2); when permeance harmonics are introduced, 2.3.1, the a.c. and d.c. fluxes are given by:-

$$\phi_{ac} = \Lambda_o F(2\epsilon_1\cos\omega t + 2\epsilon_3\cos 3\omega t + \_\_\_\_\_)$$

and

$$\phi_{dc} = \Lambda_o F(2 + 2\epsilon_2\cos 2\omega t + 2\epsilon_4\cos 4\omega t + \_\_\_\_\_)$$

Since there are two positions of symmetry over a complete cycle, the above equations have to be modified; the fluxes linking the a.c. and d.c. windings without damping are then given by:-

$$\phi_{dc} = F_c\Lambda_o(2 + (\xi_1 - \xi_1')\cos\omega t + (\xi_2 + \xi_2')\cos 2\omega t + (\xi_3 - \xi_3')\cos 3\omega t \_\_\_\_\_)$$

$$\phi_{ac} = F_c\Lambda_o\left[(\xi_1 + \xi_1')\cos\omega t + (\xi_2 + \xi_2')\cos 2\omega t + (\xi_3 + \xi_3')\cos 3\omega t + \_\_\_\_\_\right] \quad (2.3.1)$$

When damping windings are used, an additional mmf acts upon the airgap permeance. Since harmonic fluxes will link the damping winding, harmonic damping currents will be set up in the damping winding which can be expressed in the form $\sum D_n \cos(n\omega t + \beta_n)$

where D_n = peak value of the damping ampere-turns/pole (nth harmonic),

and β_n = phase angle between the peak of the nth harmonic damping current and the nth harmonic flux component which links the a.c. winding.

The addition of a damping winding results in the following equations for the a.c. and d.c. fluxes:-

The a.c. flux with damping

$$\phi'_{ac} = \Lambda_o \left[F_e \sum (\xi_n - \xi'_n(-1)^n) \cos n\omega t + \sum \frac{D_n}{2} (\xi_n - \xi'_n(-1)^n) \left\{ \cos(2n\omega t + \beta_n) + \cos\beta_n \right\} \right]$$

and the d.c. flux with damping

$$\phi'_{dc} = \Lambda_o \left[2F_e + 2D_n \cos(n\omega t + \beta_n) + F_e \sum (\xi_n + \xi'_n(-1)^n) \cos n\omega t + \sum \frac{D_n}{2} (\xi_n + \xi'_n(-1)^n) \left\{ \cos(2n\omega t + \beta_n) + \cos\beta_n \right\} \right]$$

$$n = 1, 2, 3, \_\_\_\_\_$$

The above equations have been developed for a general damping winding. Obviously the D_n values will be different for each type of damping winding, since the harmonic fluxes which link the damping winding are dependent upon the flux distribution in the core and

the phase angles β_n.

For odd harmonic fluxes $\lesssim(\xi_n+\xi_n'(-1)^n)$ will be very small since $\xi_n \doteq \xi_n'$ e.g. $\xi_1 = 0.554$, $\xi_1' = 0.548$.
The even harmonic fluxes which contain terms in

$\lesssim(\xi_n+\xi_n'(-1)^n)$ will also be small, since for $n>1$ the ϵ values are very small; compare $\xi_2 = 0.006$ with $\xi_1 = 0.554$.

Since the flux terms containing $\left[\xi_n-\xi_n'(-1)^n\right]$ especially for $n>1$, are small compared with the a.c. flux, $F_e\Lambda_o(\xi_n+\xi_n')$ the a.c. flux on open-circuit will not be affected by damping, until high values of saturation, Fig 33,(compare D_1 and D_2 with A_3).
With damping the voltage in a field coil is considerably reduced, i.e. terms in $\left[\xi_n+\xi_n'(-1)^n\right]$ will be very small, Fig 37 and 4.6(b).

4.5.2 Equivalent circuit for damping winding.

Although a general expression has been derived for the flux linking a d.c. coil on open-circuit without damping, 4.5.1, the effectiveness of a particular type of damping winding will also depend on X_{dn} and r_{dn}, where r_{dn} = effective resistance of the damping winding at a frequency f_n and X_{dn} = reactance of damping winding corresponding to a frequency f_n.
The impedance of a damping winding is given by $(r_{dn} + jX_{dn})$; for each type of damping, X_{dn} will vary according to the position of the winding in the d.c. slot and the resistance of each damping winding may be

different, (compare $r_{d(TOP)} = r_{d(BOTTOM)} = 0.385\Omega$ and $r_{d(CORE)} = 0.028\Omega$). When the machine is running on open-circuit (no-damping), harmonic fluxes link the field coils and the damping windings; if the voltage induced in a damping coil due to the nth harmonic flux is V_n , the damping current will be given by:-

$$I_{Dn} = \left| \frac{V_n}{(r_{dn} + j X_{dn})} \right| \quad , \text{ where } \quad I_{Dn} = \text{nth harmonic}$$

damping current.

Although a simple expression can be derived to compare the damping currents in two different windings, e.g.

$$\frac{I_{Dn\,(TOP)}}{I_{Dn(BOTTOM)}} = \left| \frac{(r_{dn} + j X_{dn})_{BOTTOM}}{(r_{dn} + j X_{dn})_{TOP}} \right| ,$$

(V_n same for top and bottom damping windings)

it is necessary to see how each damping winding affects the total voltage across a field coil before assessing the most effective type of damping winding, 4.6. Although the reactances are difficult to calculate, some qualitative results follow from measurements taken in section 4.6.

Clearly the top damping winding is the most effective for damping the harmonic fluxes which link the field winding, Table 12; to demonstrate why certain types of damping are more effective, it is convenient to compare the reactances of the various damping windings. For top and bottom damping windings, $r_{d(TOP)} = r_{d(BOTTOM)} = 0.385\Omega$; since $r_d \ll X_{dn}$, the value of I_{Dn} will depend on the value of X_{dn} for each winding,

i.e. $$\frac{I_{pn}\,(\text{top})}{I_{pn}\,(\text{bottom})} \simeq \frac{X_{dn}\,(\text{bottom})}{X_{dn}\,(\text{top})}$$

To compare fundamental and second harmonic reactances, V_n and I_{pn} were measured for various values of field excitation, Fig 38; the reactance for a particular frequency and field current was calculated from the relationship $X_{dn} = \frac{V_n}{I_{pn}}$.

Without damping, the open-circuit voltage was measured for various values of field current, (0→ 2.75 amps) [I_f limited to 2.75 amps to prevent possible breakdown of the field insulation] ; the resulting curves for fundamental and second harmonic components are shown in Fig 38. The induced voltage in both cases, which bears a non-linear relationship to the field mmf, is dependent upon the flux distribution in the core region; the effects of field mmf on flux distribution have already been discussed in sections (4.4.1, 4.4.2 and 4.4.3).

Damping currents in top and bottom damping windings were also measured for various values of field excitation, Fig 38; throughout these tests a non-inductive shunt was used for measuring I_{pn} .

Since I_{pn} and V_n vary with field excitation and bear a non-linear relationship to each other, the reactance of a damping winding will also depend on the value of field excitation, Fig 38.

Fundamental damping currents for top and bottom damping windings are practically equal and therefore X_{d_1} (top) $\simeq X_{d_1}$ (bottom).

$$X_{d_1}\,(\text{top})_{2\cdot0\,\text{Amps}} = \frac{V_n}{I_{D_n}} = \frac{14}{0.235} = 59.5\,\Omega$$

$$X_{d_1}\,(\text{bottom})_{2\cdot0\,\text{Amps}} = \frac{14}{0.22} = 63\,\Omega$$

$$\text{i.e.}\quad \frac{X_{d_1}\,(\text{bottom})}{X_{d_1}\,(\text{top})} = \frac{63}{59.5} = 1.06 = \frac{I_{D_1}\,(\text{top})}{I_{D_1}\,(\text{bottom})}$$

Second harmonic reactances (for top and bottom damping windings) were also calculated; for a field current of 2.0 amps:-

$$X_{d_2}\,(\text{top}) = \frac{18}{0.17} = 106\,\Omega$$

$$X_{d_2}\,(\text{bottom}) = \frac{17}{0.034} = 495\,\Omega$$

$$\text{i.e.}\quad \frac{X_{d_2}\,(\text{bottom})}{X_{d_2}\,(\text{top})} = 4.66 = \frac{I_{D_2}\,(\text{top})}{I_{D_2}\,(\text{bottom})}$$

Since $X_{d_2}(\text{top}) < X_{d_2}(\text{bottom})$, $I_{D_2}\,(\text{top})$ will be greater than $I_{D_2}\,(\text{bottom})$, i.e. top damping winding will be the most effective for damping the second harmonic fluxes; (compare ϕ_2 linking field with top damping $= 1.8\,\mu$Wb and ϕ_2 linking field with bottom damping $= 1.93\,\mu$Wb, Table 12.)

Since for all n, $X_{d_n}(\text{bottom}) > X_{d_n}(\text{top})$, top damping windings will be the most effective for damping the fluxes which link a field coil, Table 12.

Fundamental and second harmonic reactances were also compared for bottom and top damping.

For top damping, $\frac{X_{d_2}}{X_{d_1}} = \frac{106}{59.5} = 1.78$ (2.0 amps)

This ratio varies with field excitation, i.e.

compare $\frac{X_{d_2}}{X_{d_1}} = 1.0$ ($I_f = 1.5$ amps) and

$\frac{X_{d_2}}{X_{d_1}} = 1.67$ ($I_f = 2.75$ amps)

For bottom damping, $\frac{X_{d_2}}{X_{d_1}} = \frac{495}{63} = 7.85$ ($I_f = 2.0$amps)

This ratio also varies with field excitation, i.e.

compare $\frac{X_{d_2}}{X_{d_1}} = 3.36$ ($I_f = 1.0$ amp) and

$\frac{X_{d_2}}{X_{d_1}} = 10.6$ ($I_f = 2.5$ amps).

If the system were linear, then $\frac{X_2}{X_1} = 2$; for most values of field excitation $\frac{X_{d_2}}{X_{d_1}}$ diverges substantially from this ideal ratio. Two factors regarding flux distribution are obviously connected with these results:-

(a) saturation (especially at the tooth surface) affects the flux distribution, i.e. non-linear system.

(b) second harmonic fluxes are particularly sensitive to different types of damping and changes in field excitation; (peculiar flux-field relationships which occur in the core region are discussed in sections 4.4.1⟶4.4.3.) In view of these results and the fact that values of reactance are difficult to check theoretically, measurements of V_n and I_{Dn} were repeated; over the full range of field excitation, close agreement was obtained between the two sets of results giving confidence to the measured values of reactance.

4.6 Experimental work.

Tests were carried out to determine:-

(a) the flux which links the d.c. winding for various types of damping,

(b) the voltages which are induced in the field winding,

(c) the damping currents which appear in bottom and top damping windings.

(a) Harmonic fluxes linking the d.c. winding for the different types of damping were measured, Table 12.

Table 12.

Harmonic fluxes linking the back of the d.c. slots for different types of damping.

Type of Damping	Harmonic fluxes in μWb.				
	Fund	2nd	3rd	4th	5th
No Damping	59.6	6.96	3.5	4.24	0.186
Bottom Damping	11.75	1.93	0.67	0.33	0.017
Top Damping	10.2	1.8	0.52	0.29	NOT MEASURABLE.
Core Damping	16.8	2.55	0.83	0.56	0.09

The effectiveness of a damping winding depends on how the damping currents affect the fluxes linking the field winding; for each harmonic, the top damping winding reduces the voltages induced in a field coil (expressed as fluxes in Table 12) to a minimum.

A similar analysis to that described in section 4.5.2 can be used to compare the reactances of core and bottom damping windings. For the core damping winding, the reactance is different from $X_{dn(BOTTOM)}$, since part of the winding links the core and part links the airspace behind the core. Core damping windings are seldom used, since they are difficult to wind and they are not as effective as bottom or top damping windings; e.g. at rated open-circuit voltage, the core damping winding reduces the induced voltage in a field coil to about 13% of the peak value without damping, whereas the top damping winding reduces the induced voltage to about 1.6% of the voltage without damping.

(b) The high frequency fluxes which link the field winding without damping, although they may be small, induce high voltages in the field winding. Fig 37 shows the peak voltage induced in a single field coil when no damping windings are used; the peak voltage in the field coil for rated open-circuit voltage is 340 volts, which is a voltage high enough to cause a possible breakdown of the insulation. This voltage which appears in a single field coil is not apparent if the voltage is measured across the total field winding. The voltages induced in individual field coils tend to cancel each other out, resulting in a very small residual induced voltage across the total winding; the sum of all modulations across the total winding = 1.4% of the voltage induced in one field coil.

This can be shown theoretically by considering the fluxes linking two adjacent field coils. Taking into account permeance harmonics, the flux linking a field coil (A) is given by

$$\Lambda_o F \left\{ 2 + \sum (\xi_n + (-1)^n \xi_n') \cos n\omega t \right\}$$

(section 2.3.1)

hence,

$$E_n(A) = 4.44 f_n N_{dc} \Lambda_o F \left\{ 2 + \sum (\xi_n + (-1)^n \xi_n') \right\}$$

where:- E_n = nth harmonic voltage induced in a field coil and N_{dc} = number of series turns in a field coil.

In the adjacent pole, the flux linking the field coil (B) is given by

$$-\Lambda_o F \left\{ 2 + \sum (\xi_n + (-1)^n \xi_n') \cos n\omega t \right\}$$

If the d.c. winding has m poles, then the total effective voltage induced in the field winding is given by

$$E_{n\,(\text{TOTAL})} = 4.44 f_n N_{dc} \frac{m}{2} \left\{ \left[2 + \sum (\xi_n + (-1)^n \xi_n') \right] - \left[2 + \sum (\xi_n + (-1)^n \xi_n') \right] \right\}$$

$$= 0.$$

The same effects as mentioned above are also exhibited in the Lorenz-type machine.[5]

For three different types of damping, the peak voltages were measured across a field coil, Fig 37. The top damping winding is very effective in damping the induced voltage, the peak voltage with top damping

being only 1.5% of the peak voltage without damping.

(c) Since fundamental and second harmonic flux components have been considered in detail, fundamental and second harmonic damping currents were measured for top and bottom damping windings and plotted against field current, Fig 38. The fundamental and second harmonic currents are small as suggested by the theory; with these small damping currents the I^2R loss in the damping windings will be negligible compared with the total losses in the machine. The fundamental damping currents are difficult to calculate with any confidence, since small changes in airgap around the periphery affects $(\xi_1 - \xi_1')$; measurements on the experimental machine showed a slight variation in I_{D1} for various poles. This variation was particularly marked for 2nd harmonic components which are sensitive to small changes in airgap. Although readings over a pole pitch indicate the flux patterns, absolute measurements taken over a pole pitch must be treated with caution, since they may not represent exactly what is happening in other poles. Calculation of the damping currents is inherently difficult due to the complex nature of the flux distribution and requires:-

(a) the accurate calculation of fluxes linking a damping coil when open-circuited- hence voltage V_{dn}.

(b) the accurate calculation of the reactance of the damping winding.

Under load conditions the damping currents increase considerably; these are discussed in section 5.6.2.

4.7 Flux distribution in the core with damping.

4.7.1 Fundamental flux.

The fundamental flux linking a whole stator main tooth (43-48) was measured for bottom and top damping windings at various values of field excitation, and the resulting fundamental flux linking the a.c. winding is shown in Fig 34. For unsaturated conditions there is very little difference between top, bottom and no damping, as suggested by the theory. Under saturation conditions where the flux distribution changes in the core region, the fundamental flux density does not saturate quite as quickly as when there is no damping.

4.7.2 Second harmonic flux.

The distribution of second harmonic flux has already been shown to be complicated when no damping is used, (section 4.4.2). With the addition of a damping winding, it is even more complex. For no damping, the second harmonic flux patterns are as shown in Fig 39a; the fluxes shown here are for a field excitation of 2.5 amps. The fluxes in teeth A and B are given by the following relationships:-

$$\overline{\phi_A} = \overline{4.5} + \overline{2.5}$$
$$\overline{\phi_B} = \overline{4.5} - \overline{2.5}$$

where $\overline{4.5}$ is the measured flux in μWb passing behind the field slots for I_f = 2.5 Amps,
and $\overline{2.5}$ is the measured flux in μWb passing behind the

a.c. slot for I_f = 2.5 Amps.

The a.c. flux is given by $\overline{\phi_A} - \overline{\phi_{B'}}$ as shown in the vector diagram, Fig 39c.

When a damping winding is added , in this case a bottom damping winding, the vector diagram has to be modified. Measurements have shown that the second harmonic fluxes behind adjacent field slots are equal under damped conditions, and it was therefore assumed that the total flux due to the damping winding ($2\phi_D$) would split up in the way shown in Fig 39b. The a.c. flux was calculated from the following relationships which exist when I_f = 2.5 amps:-

flux linking tooth A with damping $\quad \overline{\phi_A} = \overline{4.5} + \overline{2.5} - \overline{\phi_D}$

flux linking tooth B with damping $\quad \overline{\phi_B} = \overline{4.5} - \overline{2.5} - \overline{\phi_D}$

a.c. flux with damping $\quad \overline{\phi_{ac}} = \overline{\phi_A} - \overline{\phi_{B'}}$

The a.c. flux for various values of field excitation was calculated from a series of vector diagrams and compared with the actual second harmonic flux linking the a.c. winding, Fig 34.

Good correlation between actual measurements and those predicted from the vector diagrams gives confidence in the flux paths chosen. The redistribution of flux in the core due to saturation and the effects of damping, both of which are difficult to calculate for a given field excitation, produces peculiar

flux/field excitation curves as shown in Fig 34. With bottom damping (I_f 0 $\longrightarrow$ 2.5 amps), $\phi_{58\text{-}67} < \phi_{49\text{-}70}$; beyond this value of field current $\phi_{58\text{-}67} > \phi_{49\text{-}70}$, Fig 40. Across (43-48) as the field current is increased from 0 to 2.0 amps, the flux increases linearly with field excitation; at 2.5 amps the flux decreases to quite a low value and then increases with additional field excitation. Phase angles between the fluxes in two small adjacent teeth are present for all values of excitation; for I_f = 2.5amps the two fluxes are nearly in anti-phase.

The second harmonic leakage fluxes are also quite large and are comparable with or larger than the small tooth surface flux, Fig 41. In the small tooth regions there is very little difference between the second harmonic flux components for top or bottom damping.

The second harmonic paths are critically dependent upon the value of field excitation, Fig 41; this makes the calculation of second harmonic fluxes extremely difficult.

4.8 Conclusions.

It has been shown by experiment and from theory that although the flux variation across the total surface of a small tooth is approximately sinusoidal, flux waveforms in small sections of the tooth surface contain considerable harmonic content. These harmonic fluxes can easily be predicted from the tooth-slot geometry and Teledeltos plots. Extra loss factors derived for small sections of the tooth surface enable an estimate to be made of the extra loss at the surface due to these harmonic fluxes and the total loss in the tooth. Harmonic fluxes are also present in the core region, their patterns being determined by the tooth-slot geometry and the amount of saturation in various parts of the core; second harmonic flux components are particularly sensitive to changes in field excitation. Measurements across a field coil (without damping) show that harmonic fluxes cause high voltages to be induced in a field coil; the voltages which appear in each coil cancel each other out and do not appear across the total winding. Various types of damping were investigated and it was shown that top damping windings (which have a lower reactance than either bottom or core damping windings) are the most effective in reducing the voltages induced in a field coil.

Chapter 5.

Stator flux distribution under load conditions.

5.1 Theoretical analysis.

5.1.1 Fluxes linking the a.c. and d.c. windings on load.

.1.1 Simple analysis.

.1.2 Effect of permeance harmonics and damping currents on ϕ_{ac} and ϕ_{dc}.

.2 Flux waveforms at the tooth surface.

.3 Phase relationship between the flux waveforms at the leading and trailing edges of a small stator tooth.

.4 Effects of armature reaction.

.5 Effects of damping.

5.2 Experimental work.

5.2.1 Flux waveforms at the tooth surface under load conditions.

.1.1 Fundamental and second harmonic fluxes at the surface.

5.2.2 δ angles.

.3 Comparison of calculated and measured flux waveforms on load.

.4 Flux density distribution across the tooth surface.

.5 Flux waveforms in a small stator tooth, (C= 12 μF).

.6 Flux waveforms at the surface (no C).

.7 Effects of varying the value of series capacitor.

.8 Addition of fluxes at the tooth surface.

.9 ψ angles.

5.2.10 K_{Dn} factors.

5.3 Losses under load conditions.

5.3.1 Extra loss factors.

.2 Overall extra loss factor and total loss in a small tooth.

5.4 Machine on short-circuit.

5.4.1 Flux waveforms at the tooth surface, (no series capacitor).

.2 Flux waveforms at the tooth surface ($C=12\mu F$).

.3 Addition of fundamental fluxes under short-circuit conditions.

.3.1 No series capacitor.

.2 $C= 12\mu F$.

.4 Flux density distribution in the stator tooth surface.

5.5 Additional comments and conclusions.

5.5.1 optimum value for series capacitor.

.2 Choice of tooth-slot parameters.

5.6 Flux distribution in the stator core under load conditions.

5.6.1 Harmonic fluxes.

.2 Voltages induced in a field coil and the effects of damping.

.2.1 Voltages in a field coil.

.2 Damping currents.

.3 Factors affecting I_D.

Summary. - Chapter 5

Under load conditions an additional mmf due to armature reaction acts upon the airgap permeance, resulting in a non-uniform distribution of flux across the tooth surface.

The mmf acting upon the airgap permeance, assuming sinusoidal load current, is given by $\left[F + A\cos(\omega t+\alpha)\right]$ ampere-turns, where α is the phase angle between the peak permeance and the peak current. The angle α defines the amount of overlap of stator and rotor teeth at the moment of maximum applied mmf.

An extension of the results obtained from open-circuit tests leads to a method of predicting the flux waveforms at the tooth surface under load conditions and also for the short-circuit condition. The distortion in a given section is shown to depend upon the angle α and upon the magnitude of the armature reaction. Although saturation effects have been neglected in the analysis, good correlation exists between measured and calculated results giving confidence in the method used.

From the flux waveforms across the surface it is possible to derive extra loss factors for the small sections and thus determine the true loss in the stator teeth under load conditions. The extra loss factors are shown to be dependent upon the value of series capacitor. With this understanding of the flux distribution at the tooth surface it is now possible to discuss the effects upon losses when the power factor or series capacitor is altered, for any tooth-slot geometry.

5.1 Theoretical analysis.

5.1.1 Fluxes linking the a.c. and d.c. windings on load.

.1 Simple analysis.

Neglecting permeance harmonics and the asymmetry of the permeance variation over a cycle, the fluxes linking the a.c. and d.c. windings under load conditions (without damping) are given by:-

$$\phi_{ac} = \left[2F\epsilon\cos\omega t + 2A\cos(\omega t + \alpha)\right]\Lambda_o$$

$$\phi_{dc} = \left[2F + A\epsilon\cos\alpha + A\epsilon\cos(2\omega t + \alpha)\right]\Lambda_o$$

(section 10.4.1)

The flux which links the field winding under load conditions contains a second harmonic term due to the interaction of the fundamental permeance variation and the fundamental component of armature reaction. This high frequency flux component linking the field induces high voltages in the field winding which are liable to cause breakdown of the field insulation. Damping windings situated either in the top or the bottom of the d.c. slots are used to damp the fluxes which link the field winding. To calculate the ampere-turns required to damp the second harmonic flux component, a term $D\cos(2\omega t + \beta)$ is introduced into the equations, where D is the peak mmf of the damping winding and β is the phase angle between the peak permeance and the peak mmf of the damping winding. Although the above expression has neglected the fact that terms in $D_1\cos\omega t$ and higher order harmonic damping

currents will be present, (5.1.1.2) the analysis gives a good approximation to the ampere-turns required to damp the second harmonic flux.

With damping:-

$$\phi_{ac} = \Lambda_o\left[2A\cos(\omega t + \alpha) + \epsilon 2F\cos\omega t + D\epsilon\cos(\omega t + \beta)\right]$$

and

$$\phi_{dc} = \Lambda_o\left[2F + A\epsilon\cos\alpha + A\epsilon\cos(2\omega t + \alpha) + 2D\cos(2\omega t + \beta)\right]$$

(section 10.4.2)

For complete damping of the second harmonic flux linking the field winding:-

$$D = -\frac{A\epsilon}{2} \quad \text{and} \quad \beta = \alpha$$

Then

$$\phi_{ac} = \Lambda_o\left[2A(1-\frac{\epsilon^2}{4})\cos(\omega t + \alpha) + 2F\epsilon\cos\omega t\right]$$

and

$$\phi_{dc} = \Lambda_o\left[2F + A\epsilon\cos\alpha\right]$$

The mmf of the damping winding also modifies the flux due to armature reaction to $2\Lambda_o A(1-\frac{\epsilon^2}{4})\cos(\omega t + \alpha)$.

5.1.1.2 Effect of permeance harmonics and damping currents on ϕ_{ac} and ϕ_{dc}.

The effect of permeance harmonics adds considerably to the complexity of the problem; with an assumed permeance variation of the form

$$\Lambda_o(1 + \epsilon_1\cos\omega t + \epsilon_2\cos 2\omega t + \_\_\_\_\_),$$

the d.c. flux without damping is given by:-

$$\phi_{dc} = \Lambda_o\left[2F + F\Sigma\epsilon_n(1 + (-1)^n)\cos n\omega t + \Sigma A\epsilon_n(1 - (-1)^n)\cos(n\omega t + \alpha)\cos n\omega t\right]$$

(section 10.4.3)

$$\phi_{dc} = \Lambda_o\Big[2F + A\epsilon_1\cos(2\omega t + \alpha) + A\epsilon_1\cos\alpha + 2F\epsilon_2\cos 2\omega t + 2F\epsilon_4\cos 4\omega t + A\epsilon_3\cos(4\omega t + \alpha) + A\epsilon_3\cos(2\omega t - \alpha) + \text{----------}\Big]$$

The additional terms which contain ϵ_2, ϵ_3 and ϵ_4 etc, do not have a marked effect upon ϕ_{dc} since these ϵ_n values are small compared with the fundamental and second harmonic terms, but the expression does indicate that harmonic fluxes will link the field and damping winding. Harmonic damping currents will flow in the damping windings setting up mmfs in opposition to the harmonic fluxes which link the winding.

To see how these harmonic damping currents affect the fluxes ϕ_{ac} and ϕ_{dc}, it is necessary to take into account:-

(a) the asymmetry of the permeance variation over a cycle.

(b) permeance harmonics.

(c) a term $D_m\cos(m\omega t + \beta_m)$, m=1,2,3,4---------

The resulting expressions for ϕ_{ac} and ϕ_{dc} are given by:-

$$\phi_{dc} = \Lambda_o\Big[2F + 2\Sigma D_m\cos(m\omega t+\beta_m) + \Sigma F(\xi_n + (-1)^n\xi_n')\cos n\omega t + \Sigma A_n(\xi_n - (-1)^n\xi_n')\cos n\omega t\cos(n\omega t + \alpha_n) + \Sigma D_m(\xi_n + (-1)^n\xi_n')\cos(m\omega t+\beta_m)\cos n\omega t\Big]$$

and

$$\phi_{ac} = \Lambda_o\Big[2\Sigma A_n\cos(n\omega t + \alpha) + \Sigma F(\xi_n - (-1)^n\xi_n')\cos n\omega t + \Sigma A_n(\xi_n + \xi_n'(-1)^n)\cos n\omega t\cos(n\omega t + \alpha_n) + \Sigma D_m(\xi_n - (-1)^n\xi_n')\cos n\omega t\cos(m\omega t + \beta_m)\Big]$$

The second harmonic flux (ϕ_2) linking a d.c. coil is given by:-

$$\phi_2 = 2D_2\cos(2\omega t + \beta_2) + F(\xi_2 + \xi_2')\cos 2\omega t + \frac{A_1}{2}(\xi_1 + \xi_1')\cos(2\omega t + \alpha) + \frac{D_1}{2}(\xi_1 - \xi_1')\cos(2\omega t + \beta_2)$$

For practical calculations, terms in $(\xi_1 - \xi_1')$ and $(\xi_2 + \xi_2')$ can be neglected, i.e.

$$\phi_2 = 2D_2\cos(2\omega t + \beta_2) + \frac{A_1}{2}(\xi_1 + \xi_1')\cos(2\omega t + \alpha)$$

To damp the second harmonic flux completely,

$$\alpha = \beta_2 \quad \text{and} \quad D_2 = -\frac{A_1(\xi_1 + \xi_1')}{4}$$

(compare $\alpha = \beta$ and $D = \frac{-A\epsilon}{2}$ for simple analysis, 5.1.1.1)

Fundamental damping currents will also be present, i.e.

$$\phi_1 = 2D_1\cos(\omega t + \beta_1) + F(\xi_1 - \xi_1')\cos\omega t + \frac{D_2}{2}(\xi_1 - \xi_1')\cos(\omega t + \beta_1)$$

since $\frac{D_2}{2}(\xi_1 - \xi_1')$ is very small compared with $F(\xi_1 - \xi_1')$,

$$2D_1\cos(\omega t + \beta_1) = -F(\xi_1 - \xi_1')\cos\omega t.$$

To damp the fundamental flux completely,

$$\beta_1 = 0 \quad \text{and} \quad D_1 = \frac{F(\xi_1 - \xi_1')}{2}$$

The theoretical analysis although giving an expression for the flux linking a whole stator main tooth, the d.c. and the a.c. windings, does not give any indication of what the flux distribution is like at the tooth surface. To obtain a true understanding of the flux distribution at the tooth surface it is necessary to look at small sections across the surface and to calculate the distortion caused by armature reaction.

5.1.2 Flux waveforms at the tooth surface.

In the present section, the angle α will be treated as a known quantity; the calculation of α is dealt with in detail in chapter 7.

The shape of the open-circuit flux waveform in a small section of the tooth surface, neglecting saturation effects, is associated with the tooth slot geometry and has been shown to be proportional to

$$\frac{2a\ell}{\alpha\pi^2 n^2}\sum_{n=1}^{\infty}\left[\cos n\frac{(b+\alpha)\pi}{\ell}-\cos\frac{(b-\alpha)\pi}{\ell}\right]\cos n\omega t, \quad (4.1.3)$$

It follows that the flux on open-circuit is given by:-

$$\Lambda_R F - \frac{2\ell}{\alpha\pi^2 n^2}(\Lambda_P-\Lambda_R)\sum_{n=1}^{\infty}\left[\cos n\frac{(b+\alpha)\pi}{\ell}-\cos n\frac{(b-\alpha)\pi}{\ell}\right] F\cos n\omega t$$

where:- Λ_R is the mean permeance as seen by a small section of the surface,

Λ_P is the maximum permeance seen by a small section of the surface.

From design sheet data it is possible to calculate the flux passing through a whole small tooth for the stator tooth opposite rotor tooth position. Static tests have shown that the flux is uniformly distributed across the tooth surface for this position, thus enabling the maximum flux in a small section to be calculated. The maximum nth harmonic flux is given by:-

$$\Lambda_R F - \frac{2\ell}{\alpha\pi^2 n^2}\left[\Lambda_P-\Lambda_R\right]\left[\cos n\frac{(b+\alpha)\pi}{\ell}-\cos n\frac{(b-\alpha)\pi}{\ell}\right] F$$

The flux in a small section for the stator tooth

opposite rotor slot position ($\Lambda_q F$) is not easily calculable, since the flux is not evenly distributed across the tooth surface. Either a simple hand flux plot or Teledeltos model is needed to obtain the flux in one of these small sections.

From the tooth-slot geometry the shape of the flux waveform in a small section of the stator tooth surface is known. For any section along the surface the maximum flux level is constant.

The minimum flux level will vary for each section due to the fringing effect of the flux at the tooth edges. A scale diagram can be drawn of the flux waveform in a small section with these levels marked on the diagram. The mean flux level can be obtained by using a planimeter. Before introducing the effects of armature reaction it is necessary to know the phase relationship of the fluxes across the surface for open-circuit conditions.

5.1.3 Phase relationship between the flux waveforms at the leading and trailing edges of a small stator tooth.

At Fig 42a the flux in (4-5) has just reached its maximum value. The flux remains constant until the stator and rotor small teeth are opposite, Fig 42b. The time interval over which the flux is constant in (4-5) is associated with the displacement of the stator and rotor teeth in electrical degrees, i.e.

$x = \frac{6}{7} \times 140^{\circ}$ ($t = 140^{\circ}$ electrical for our particular tooth-slot geometry).

At tooth position (b), section (10-11) has just reached its maximum value, which remains constant until the tooth position shown in Fig 42c. The flux waveforms $\phi(4\text{-}5)$ and $\phi(10\text{-}11)$ are related as shown in Fig 42d.

5.1.4 Effects of armature reaction.

Under load conditions the peak value of the load current waveform is displaced from the maximum permeance position (b) by an angle α . To relate the load current waveform to any particular section across the tooth surface it is necessary to define an angle 'δ' which relates the peak value of the load current and the centre line of the maximum flux level period in the appropriate small section. For a given displacement 'β_c' from this centre line, the armature reaction mmf acting is $A\cos(\delta_q \pm \beta_c)$ where q is the qth section across the surface, i.e.

$$\delta_1 = \delta_{4\text{-}5} \ , \ \delta_2 = \delta_{5\text{-}6} \text{ ----------}$$

The flux on load for the qth section across the surface is given by:-

$$\left[F + A\cos(\delta_q \pm \beta_c)\right]\left[\Lambda_R - \frac{(\Lambda_p - \Lambda_R)2l}{\alpha\pi^2 n^2}\left\{\cos n\frac{(b+\alpha)\pi}{l} - \cos n\frac{(b-\alpha)x}{l}\right\} \cos n\omega t\right]$$

5.1.5 Effects of damping.

The equation for the flux waveform in a small

section will be modified when damping is taken into account, resulting in the following:-

$$\phi_{\substack{\text{WITH}\\\text{DAMPING}}} = \left[F + A\left(1-\frac{\epsilon^2}{4}\right)\cos(\delta_q \pm \beta_c)\right]\left[\Lambda_R - \frac{(\Lambda_p - \Lambda_R)2l}{\alpha\pi^2 n^2}\left\{\operatorname{cosn}\frac{(b+\alpha)\pi}{l} - \operatorname{cosn}\frac{(b-\alpha)\pi}{l}\right\}\operatorname{cosn}\omega t\right]$$

For F = 390 ampere-turns/pole, A= 188 ampere-turns/pole,

$$\frac{\left[F + A\left(1-\epsilon^2/4\right)\right]}{\left[F + A\right]} = \frac{566}{578} = 0.98$$

i.e. % error in neglecting damping = $\frac{12\times100}{566}$ = 2.1%

The effects of damping have been neglected in the work following, since the percentage error is likely to be small enough not to introduce any appreciable error in the predicted load waveform. It can be seen however, that where the armature reaction assists the d.c. field, then the predicted flux levels will be reduced slightly compared with the predicted flux levels without damping. Similarly where the armature reaction is opposing the d.c. field then the flux levels in that region will be slightly higher than if damping were neglected. Comparison with measured and predicted waveforms (without damping effects) show that if damping effects had been taken into account it would have improved the correlation between measured and calculated results, but only by a small amount.

5.2 Experimental work.

5.2.1 Flux waveforms at the tooth surface under load conditions.

For rated output of the machine and with a capacitor connected in series with the alternator, flux measurements were made at the tooth surface. Figs (43 & 44) show the flux waveforms across the tooth surface for two small teeth comprising a stator main tooth; the load current waveform is also displayed for each section showing whether the armature reaction is magnetising or demagnetising. At (4-5) and (21-22), where there is a large demagnetising component of armature reaction for the maximum permeance condition for the section, the flux is reduced considerably from its open-circuit value at the same field excitation. Further across the surface the open-circuit flux waveform is distorted by an amount depending on the angle $(\delta_q \pm \beta_c)$. At (10-11) and (27-28) and a maximum permeance condition for this section, there is a magnetising component which increases the flux in the small section.

The distortion in each section affects the mean flux density. At the leading edge of the small stator tooth (defined as section 4-5), the armature reaction is demagnetising for the maximum permeance condition reducing the peak flux level on load to a lower value than on open-circuit. The mean flux and hence the mean flux density was calculated using a planimeter. The mean density on the leading edge is

reduced to 0.63 Tesla compared with 0.76 Tesla on open-circuit. At the trailing edge of the tooth (10-11), the mean density only varies by 2.6% (0.76 Tesla open-circuit to 0.78 Tesla on load.)

Since the flux waveforms in other sections across the surface are known, it is easy to calculate the mean density for each section across the surface. From the leading to the trailing edge there is an increase in mean density of 18%. The variation in mean density depends upon the value of series capacitor and load power factor which control the magnitude of the angle α ; the mean density in (4-5) for an 8μF series capacitor is less than the mean density in (4-5) when a 36μF series capacitor is used, (constant power factor), Fig 45. At the trailing edge of the stator tooth the mean density is little affected by changing the value of the series capacitor. For a given power factor the mean density across the tooth surface will increase as the amount of compensation decreases.

5.2.1.1 Fundamental and second harmonic fluxes at the surface.

Fundamental and second harmonic fluxes were measured at the tooth surface with and without a series capacitor, Fig 46. The distortion of the flux in each section leads to a non-uniform flux distribution across the tooth surface; at the leading edge of the stator tooth the armature reaction is demagnetising for the maximum permeance condition and at the trailing

edge the armature reaction is magnetising for the same permeance condition. For C=0 & C= 12μF, the fundamental fluxes in teeth A and B are in phase, Fig 46. Second harmonic flux distribution is more sensitive to changes in field current for a given output; when a series capacitor is added to give rated output, there is a substantial increase in second harmonic flux at the tooth surface. The magnitude of these fluxes will alter for different values of series capacitor, since the value of series capacitor controls the α angle and the distortion of flux in the small sections.

Total flux measurements were also made in the tooth regions for the two load conditions, (C=0 and C= 12μF) Fig 46e&f. The main difference between the fluxes for these two conditions is the amount of leakage at the leading edge of the stator teeth; for no series capacitor the leakage flux is approximately twice that for C= 12μF. This is to be expected since the overlap of the teeth for maximum applied mmf (C=12μF) is greater than for C = 0, [the α angle determines the amount of overlap of the teeth for maximum applied mmf.] At the trailing edge of the stator teeth A and B changes in α angle have very little effect upon the flux waveforms and hence the leakage fluxes are approximately equal for the two conditions.

5.2.2 δ angles.

From a given α^* it is possible to calculate the δ angles (section 5.1.4) for each section along the tooth surface. For C = 16μF comparison between measured and calculated δ angles is given in Table 13, for the small tooth (4-11).

Table 13.

Comparison of measured and calculated δ angles for C= 16μF.

* (α angle from Table 27, $\alpha = 134^\circ$)

Conductor	δ (Calculated) electrical degrees	δ (Measured) electrical degrees
4-5	196	190
5-6	176	174
6-7	155	152
7-8	134	129
8-9	114	115
9-10	93	90
10-11	72	70

5.2.3 Comparison of calculated and measured flux waveforms on load.

For sections (4-5), (7-8) and (10-11), the flux waveforms on load were calculated using the actual open-circuit flux waveform, Figs (47, 48 & 49). The theoretical approach which assumes a trapezoidal open-circuit waveform was also used to check certain

points on the curve; some error is introduced in the slot region due to the approximation made in the theoretical approach. From theory it was possible to calculate the mean flux under load conditions for any particular section across the tooth surface. To compare the measured waveforms with the calculated results, it was necessary to use the theoretical mean flux as a reference for the measured results, since the mean level was not indicated on the measured waveform. The measured flux waveform (calibrated in μWb) was then suitably scaled to compare its shape with the calculated results. The measured and calculated flux waveforms were analysed for harmonic content, Table 14.

Table 14.

Harmonic content of flux waveforms at the tooth surface under load conditions.

Series capacitor C= 16μF.

(Harmonic fluxes are expressed as a percentage of the fundamental flux, i.e. fundamental flux taken as reference (100%)).

Cond.	2nd harmonic flux		3rd harmonic flux		4th harmonic flux		5th harmonic flux	
	meas.	cal.	meas.	cal.	meas.	cal.	meas.	cal.
4-5	14.8	19.9	34.6	38.3	10	12.1	4.9	5.4
7-8	18.0	23.5	14.0	19.9	9	11.2	6.9	7.2
10-11	20.0	31.0	17.9	16.5	8	12.2	4.9	6.0

For sections (4-5) and (7-8) good correlation exists between the measured and calculated harmonics,

since the saturation effects are negligible. At (10-11) where armature reaction assists the main field, the calculated maximum flux is 7% greater than the measured flux, the discrepancy being due to neglect of saturation effects in the theoretical analysis. The shape of the flux waveforms on load is particularly sensitive to the second harmonic flux terms, i.e. a slight variation in shape can have a marked effect upon the harmonic content. The main sources of error in predicting the waveforms on load are due to small errors in calculation of the α angle, and to saturation effects which distort the calculated flux waveforms.

5.2.4 Flux density distribution across the tooth surface.

To obtain the flux density distribution across the tooth surface for various rotor positions, it was necessary to determine the flux in each small section at a certain instant of time; this was done by dividing the load current waveform into suitable intervals, Fig 50. The rotor position is directly related to these points on the load current waveform. For position B where the stator and rotor teeth are opposite, the flux density is appreciably constant across the tooth surface. As the rotor tooth moves across the stator tooth surface, the flux density on the trailing edge of the stator tooth increases as more flux is passed through a decreasing permeance path, until at D, a high flux density B=1.55 Tesla

exists at the trailing edge. At F where the rotor slot is opposite the stator tooth, the flux density is appreciably constant along the tooth surface, except at the edges of the tooth where the permeance is larger than at the centre of the tooth.

5.2.5 Flux waveforms in a small stator tooth (C=12μF).

With C= 12μF and for rated output of the machine, flux waveforms in the small tooth (4-11) were recorded as shown in Fig 51. The flux waveforms in small sections of the tooth surface are far from being sinusoidal. When the flux waveforms across the tooth surface are added together, taking into account their relative phase angles, then the resulting waveform across the tooth surface is approximately sinusoidal. The overall flux waveform, without the knowledge of the flux distribution in small sections of the tooth surface, gives a false picture of what is really happening at the tooth surface. The harmonic fluxes which appear in small sections of the tooth surface will produce surface loss which is discussed in section 5.3. A small distance away from the tooth surface,(0.25cm) flux waveforms in sections across the tooth width are reasonably sinusoidal, suggesting that these harmonic fluxes are mainly confined to the tooth surface, although it has been observed that the distortion at the tooth surface does influence the harmonic content further back in the teeth, i.e. at (43-48), section 5.6. Changes in series capacitor

and power factor will influence the harmonic content in the back of the teeth, since both these factors affect the distortion at the tooth surface. The flux distribution further back in the teeth, and the fluxes linking the damping windings under load conditions are discussed in section 5.6.

5.2.6 Flux waveforms at the surface (no series capacitor).

To achieve the rated output of the machine without a series capacitor, the field current is increased considerably, i.e. (I_f = 4.05 amps compared with 3.05 amps for C = 16μF). It was felt that the field current needed to give rated output without a series capacitor would cause the field winding to overheat when running a series of tests for various sections of the tooth surface. After recording the flux waveforms at the surface for rated output , Fig 52, and comparing the flux waveform in section (10-11) with the calculated waveform, Fig 53 tests were carried out for a lower output rating, (30 KW) to reduce the possibility of overheating the field winding. The measured and calculated flux waveforms at the leading and trailing edge of the tooth surface are shown in Figs 54 & 55. For rated output , section (10-11) and sections [(4-5) and (10-11), 30 KW] fairly good correlation exists between the measured and calculated results, except where saturation has prevented the flux from rising to the calculated value.

The harmonic analysis for sections (4-5) and (10-11) is given in Table 15.

Table 15.

Harmonic analysis of load flux waveforms (no series capacitor.)

Harmonic fluxes are given as a percentage of the fundamental flux, which is taken as reference (100%).

(output rating of the machine 30 KW.)

cond	2nd harmonic flux		3rd harmonic flux		4th harmonic flux		5th harmonic flux	
	meas.	cal.	meas.	cal.	meas.	cal.	meas.	cal.
4-5	8.0	12.2	34	37.5	2.34	2.25	10.9	12.7
10-11	19.2	22.5	19.4	21.4	7.41	8.03	3.8	5.66

The good agreement which exists between calculated and measured results for the above condition and also when a series capacitor is added, gives confidence in the method used. The results obtained from harmonic analysis (from calculated flux curves) must however be treated with caution where the flux densities are high, and where saturation effects can have a marked effect upon the load flux waveform.

5.2.7 Effects of varying the value of series capacitor.

Altering the value of series capacitor for a given output and power factor of the machine causes the α angle to change its value. The effects upon the flux distribution in a small tooth are summarised as follows:-

(a) The load flux waveforms in small sections of the stator surface will alter as α alters, resulting in a variation of harmonic content for each section, Fig 56.

(b) The variation in α will affect the distribution of flux in the tooth, i.e. the leakage and main tooth fluxes are dependent upon the angle α .

For rated output of the machine (44.4 KVA) fundamental fluxes were measured for various values of series capacitor, Table 16.

Table 16.

Main and leakage fluxes (fundamental) for various values of series capacitor. (constant power factor)

(all fluxes in μWb, total core length.)

cond.	36μF	28μF	20μF	16μF	8μF
4-11 (main flux)	540	540	518	518	582
3-4 (leakage flux)	102	95	82	74	15.8
11-13 (leakage flux)	194	190	190	190	184
3-13 (main flux)	495	495	520	520	585
3-11 (main flux)	470	450	426	426	560

Considering the leakage flux at the leading edge of the stator tooth (3-4), the flux decreases from 102μWb to 15.8μWb as the compensation is increased from 0.2 to 0.9 pu, i.e. the leakage flux increases as the angle

α decreases. [As α decreases the permeance increases for the leakage flux path.] (1 pu compensation is defined for condition where $(a + X_L) = X_c$)

Altering the α angle also affects the amount of distortion in the small sections across the surface, and will therefore influence the main tooth surface flux in magnitude and phase, since the main tooth surface flux is calculated by adding vectorially the fluxes in the small sections. As the amount of compensation is increased, there is a slight decrease in the main tooth surface flux until high levels of compensation, where the tooth surface flux increases. In Fig 56, for C = 8μF, the fundamental flux in (4-5) is less than the fundamental flux in (4-5) C=12μF due to the shape of the flux waveform.

These facts suggest that there must be an optimum value of series capacitor, which for a given output, keeps the main tooth density to a minimum; this is discussed in section 5.5.1.

For each value of series capacitor and therefore a given α (for constant power factor), the peak of the total flux waveform across the surface is displaced from the peak of the load current waveform by an angle defined as $\measuredangle$. $\measuredangle$ angles for various values of series capacitor are given in Table 17.

Table 17.

$\angle$ angles for various values of series capacitor.

(constant power factor)

C μF	$\angle_{4-11}$	$\angle_{21-28}$	α	$\alpha - \angle$
36	103.5	104	145	41
28	98.4	99	141	42
20	92.6	93	135	42
16	89.5	90	129	39
8	65.5	62	112	50

For a wide range of compensation (0.2-0.7 pu), the angle $\angle$ is related to α by the following relationship:-

$$\alpha - \angle = 41^{\circ} \text{ (average)}$$

As the compensation is increased further up to 0.9 pu this relationship breaks down and

$$\alpha - \angle = 50^{\circ}.$$

Usually machines do not run at these high levels of compensation; for normal operating conditions the value of series capacitor and the power factor of the machine control the angle between the peak load current and the peak of the main tooth flux.

5.2.8 Addition of fluxes at the tooth surface.

Using the search coil stack it was possible to form vector diagrams of how the harmonic fluxes combine at the tooth surface; for rated output of the machine the vector diagram of the fundamental flux is

shown in Fig 57. Tests were carried out at four levels of excitation to see what effect saturation had upon the vector diagram.

The fundamental flux under load conditions in small sections of the tooth surface combine to give a main tooth flux which is given by:-

K_{p1} (arithmetic sum of the fundamental fluxes through the small sections across the surface)

The vector diagram under load conditions is very similar to the open-circuit diagram, except that the fundamental fluxes in each section are not equal, due to the distortion caused by armature reaction. For unsaturated and saturated conditions the total tooth flux ϕ_{3-15} is displaced by a constant angle from the main tooth flux at the surface. On open-circuit the fluxes in sections (3-15) and (4-11) are in phase, since the leakage fluxes are small compared with the main tooth flux. Under load conditions, the leakage fluxes are much larger than on open-circuit, leading to a phase displacement between the main tooth surface flux and the total tooth flux. Since the value of series capacitor affects the magnitude of the main and leakage fluxes, it is to be expected that varying the value of series capacitor will vary this angle between the main tooth surface flux and the total tooth flux.

5.2.9 ψ angles.

The phase displacement between sections along the tooth surface are defined as ψ_1 , ψ_2 , ψ_3 etc, where

ψ_1 is the phase angle between section (4-5) and (5-6)

ψ_2 is the phase angle between section (5-6) and (6-7)

ψ_6 is the phase angle between section (9-10) and (10-11).

The phase displacement for fundamental flux and for the harmonic fluxes was measured and compared with calculated results in Table 18. Although the phase displacement was found to vary considerably between sections, the average measured angles corresponded closely to the calculated results.

Table 18.

ψ angles for open-circuit and load conditions.

ψ	open-circuit I_f = 2.75 amps					on-load C=12μF, I_f = 2.75 amps.				
	fund	2nd	3rd	4th	5th	fund	2nd	3rd	4th	5th
ψ_1	24	40	60	85	90	27	27	70	100	88
ψ_2	17	41	58	80	92	27	34	46	82	98
ψ_3	23	54	53	73	95	30	40	55	77	98
ψ_4	21	46	52	67	95	12	29	69	75	88
ψ_5	16	33	56	80	84	13	41	45	75	95
ψ_6	18	39	69	80	90	22	30	22	76	88
AVERAGE ψ MEASURED	19	40	58	78	91	19	34	51	81	93
ψ THEORETICAL	20	40	60	80	100	20	40	60	80	100

5.2.10 K_{Dn} factors. (4.1.3 and 4.2.2)

From these results it was possible to calculate K_{Dn} factors for the load condition and to compare these factors with the open-circuit K_{Dn} factors for a given excitation, Table 19.

Table 19.

K_{Dn} factors for open-circuit and load conditions.

I_f = 2.75 amps.

K_{Dn}	open-circuit	on-load, C=12μF
K_{D1}	0.794	0.79
K_{D2}	0.148	0.49
K_{D3}	0.035	0.085
K_{D4}	0.129	0.134
K_{D5}	0.186	0.155

For C = 12μF the K_{Dn} factors are very similar to the open-circuit condition except for the second harmonic term which is approximately three times as large as the open-circuit K_{Dn} factor; this only applies for C = 12μF, since the K_{Dn} factors on load will vary according to the value of series capacitor. Since the losses at the surface are dependent upon the amount of harmonic flux, the losses will be a function of K_{Dn}.

5.3 Losses under load conditions.

The harmonic fluxes which are present at the tooth surface produce surface losses. Data from test curves show that the losses are proportional to $f^{1.5}B^2$ at the

frequencies that we are considering, 4.3. To obtain the loss at the tooth surface it is convenient to define an extra loss factor $k = \frac{\text{Total loss}}{\text{fundamental loss}}$.

Under open-circuit conditions it is easy to calculate an overall extra loss factor, and hence to calculate the true loss in the teeth simply by multiplying the fundamental loss (calculated by standard techniques) by the overall loss factor. Under load conditions the problem is more complex due to the distortion across the tooth surface. Extra loss factors quickly approach unity at a small distance away from the tooth surface. Depending on the values of k for a given tooth-slot geometry it is possible to estimate an area [depth d into the iron from the tooth surface] where these loss factors can be used to calculate the extra losses under load conditions. To find the total loss in the shaded section, Fig 58, it is necessary to calculate the following:-

(a) the fundamental flux across (4-11) under load conditions.

(b) the fundamental flux distribution across the surface (analyse the fundamental component in each section of the surface).

(c) the fundamental loss for a given small section.

(d) extra loss factor for each small section across the surface.

(e) multiply (c) by the appropriate extra loss factor.

(f) the total loss in the shaded region- compare with loss based upon fundamental flux- hence K_o .

(g) multiply actual fundamental loss (W/mm^3) by K_o to obtain true loss.

In general terms:-

Fundamental loss in each section = a,b,c,d_____

K factors for respective sections = K_a, K_b, K_c_____

Actual loss on load for shaded region

$$= K_a a + K_b b + K_c c + \_\_\_\_\_$$

Total loss based upon fundamental flux

$$= a + b + c + d \_\_\_\_\_$$

Overall loss factor $K_o = \dfrac{K_a a + K_b b + K_c c + \_\_\_\_\_}{a + b + c + d \_\_\_\_\_}$

5.3.1 Extra loss factors.

Extra loss factors at the tooth surface were calculated for rated output and for various values of series capacitor as shown in Table 20.

Table 20.

Extra loss factors for various values of series capacitor (rated output).

conductor	$K_{8\mu F}$	$K_{12\mu F}$	$K_{36\mu F}$
4-5	3.22	3.16	2.2
3-4	2.04	2.39	1.56
10-11	1.53	1.58	1.5
11-12	1.3	1.22	1.26
1-13	1.27	1.03	1.02
3-2	1.02	1.03	1.22
21-22	2.73	2.9	2.15
24-25	1.54	1.77	1.74
27-28	1.43	1.49	1.4
28-29	1.22	1.28	1.25
19-31	1.02	1.03	1.09
31-30	1.04	1.09	1.03
30-29	1.02	1.02	1.0

5.3.2 Overall extra loss factor and total loss in a small tooth.

For the machine running on load at rated output (C = 12μF), the extra loss factors for small sections across the surface are given in Table 21.

Table 21.

K factors for small sections of the tooth surface and the total loss for rated output, C = 12μF.

section	K factor	fundamental flux μWb	fundamental loss $\propto f^{1.5}B^2$ $\propto \phi^2$	total loss $\propto K\phi^2$
4-5	3.16	61	3700	11700
5-6	2.80	79	6120	17100
6-7	2.50	95	9000	22500
7-8	2.28	110	12000	27500
8-9	2.0	126	16000	32000
9-10	1.76	140	19500	34500
10-11	1.58	155	24000	38000
			$\Sigma_{\text{loss}}^{\text{fund}}$ $\propto 90320$	Σ total loss $\propto 183300$

Overall extra loss factor $K_o = \frac{183300}{90320} = 2.03.$

In the rest of the tooth section (1) an approximation to the extra loss factor can be made, leading to an overall loss factor for the tooth.

Example:-

For rated output and C = 12μF, the tooth region can be divided up into a series of squares to form a mesh, Fig 58. With the extra loss factors known for the tooth surface and further back in the tooth, it is possible to estimate an extra loss factor

for the tooth region.

Calculated fundamental loss in a whole tooth = 248watts

average extra loss factor K_A = 1.28

Total loss in whole tooth = 320 watts.

The harmonic fluxes at the surface introduce surface losses which increase the total loss in the tooth by 28%. From the table of loss factors for various values of series capacitor it will be seen that the loss factors decrease as the amount of compensation is reduced; at these lower values of compensation the field current increases considerably. In reducing the losses in the teeth and increasing the field winding losses, a compromise must be sought which ensures that the field does not overheat and yet which keeps the losses in the small teeth to a reasonable level.

5.4 Machine on short-circuit.

5.4.1 Flux waveforms at the tooth surface.

(no series capacitor)

On short circuit, without a series capacitor, the angle α approaches 180°. Fig 59 shows the flux waveforms across the tooth surface for a short circuit current equal to the rated load current, (88.8 amps). The measured α angle was found to be 174°. This increase in α as the machine changes from on load to a short circuit condition, further distorts the fluxes at the tooth surface, i.e. on short circuit there is a substantial amount of harmonic flux present at the surface.

5.4.2 Flux waveforms at the tooth surface, (C=12μF).

To obtain the rated load current under short circuit conditions with a series capacitor, the field current is reduced considerably; (compare I_f = 2.87amps [No C] with I_f = 1.19 amps [C= 12μF], see Fig 60. With the machine running under short circuit conditions, flux waveforms were recorded at the tooth surface, Fig 61. Adding a series capacitor has little effect upon α , but the flux waveforms are distorted more than on load without a series capacitor, since the field ampere-turns are much less with C for a given armature reaction mmf. At this value of field excitation the field and armature reaction mmfs are practically the same; at certain points across the surface the flux density is reduced to quite a low level due to the cancelling of the main flux by armature reaction, Fig 61.

5.4.3 Addition of fundamental fluxes under short circuit conditions.

Vector diagrams showing the combination of fundamental fluxes in small sections of the tooth surface (under short-circuit conditions) are shown in Fig 62.

5.4.3.1 No series capacitor.

The vector diagram is similar in form to the on-load diagram, except that the additional distortion in each section increases the average γ angle to 28.6° (electrical); compare with γ = 18.5°(under load conditions.)

5.4.3.2 With series capacitor, C = 12μF.

With C = 12μF, the vector diagram becomes very distorted from the open-circuit diagram as the fluxes in the centre of the tooth are reduced to fairly low values, and the fluxes at the edges tend to be much larger due to leakage flux. The average γ angle is reduced from 28.6° to 26.6° and K_D increases nearly to the same value as under normal load conditions, (K_D = 0.722).

5.4.4 Flux density distribution in the stator tooth surface.

For various rotor-tooth positions the flux density distribution across the stator tooth surface was calculated, Fig 63. For the rotor-tooth opposite stator-tooth position, the flux is approximately uniform across the tooth surface. The flux density for a given rotor tooth position depends on the magnitude of field and armature reaction mmf and the angle α.

5.5 Additional comments and conclusions.

Analysis and practical tests have shown that for a given tooth-slot configuration and load condition, it is possible to calculate the flux distribution across the tooth surface and also the losses in the teeth. The distortion at the surface has been shown to be dependent on the value of series capacitor and load power factor. In choosing a series capacitor the

following factors have to be taken into account:-

(a) saturation caused by F_{pu} .

(b) losses and heating in small teeth.

(c) field heating due to F_{pu} .

(d) cost of capacitor KVA_R .

A typical set of curves showing the relationship between F_{pu} and the pu compensation is shown in Fig 64. The field F_{pu} increases as the pu compensation is reduced, and as the power factor changes from a leading to a more lagging power factor, for a given value of compensation, the field current increases. For a given load power factor the angle α determines the amount of distortion in the tooth surface, and therefore controls the losses. As the compensation increases the angle α decreases, and for the particular tooth-slot geometry under consideration, the distortion in the surface increases. In choosing a series capacitor a balance must be found between a suitable field current, and an α angle which will keep the losses in the tooth region to a reasonable level.

5.5.1 Optimum value for series capacitor.

From the search coil stack it was possible to measure the fundamental flux across the tooth surface for various values of compensation. The fundamental flux with C = 36μF was taken as a reference (1 pu), hence the pu fundamental loss in each section for various values of series capacitor. For five different values of compensation an overall loss factor was

found for the tooth surface, which enabled the total loss in the tooth surface to be calculated, Fig 65. For minimum loss in the tooth surface the pu compensation = 0.44; this corresponds to 1.47 F_{pu}.

5.5.2 Choice of tooth-slot parameters.

When the machine is running under load conditions, armature reaction distorts the fluxes in the teeth; this distortion is also dependent upon the value of series capacitor, load power factor and the degree of saturation. Altering the ratio t/λ will also affect the distortion in the teeth and the field current required for a given output. To find the optimum t/λ it is necessary to calculate the following for each tooth-slot geometry:-

(a) flux waveform in a small section on open-circuit.
(b) load flux waveforms for various values of series capacitor.
(c) plot the field-compensation curves for the required load conditions.
(d) plot tooth loss-compensation curves.
(e) decide from the sets of curves the optimum performance for a given load condition, i.e. compare field current and losses for each value of t/λ.

Since the optimum value of t/λ under load conditions is dependent upon the value of series capacitor and the load power factor, the value of t/λ may be different from the open-circuit value; (optimum

t/λ for open-circuit conditions = 0.4), Tables 4&5, section 2.2.2.

An optimum value of t/λ (on-load) can only be calculated for a particular power factor and series capacitor; if the machine is designed to operate over a range of power factor, e.g. (0.9lag to 0.9lead), then an average value for t/λ would have to be chosen.

Since the calculations outlined in sections (a)_____(e) (5.5.2) are tedious, especially for varying C and power factor, the effect of altering t/λ has not been analysed in detail. One of the main problems concerns the harmonic analysis of flux waveforms across the surface; for a given power factor and series capacitor, 100 points are needed for harmonic analysis of the flux waveform in each section to give a reasonably accurate analysis up to the 5th harmonic. (700 points across the surface.)

From detailed measurements already made (for constant power factor and varying C), it is difficult to make any general statements as to the optimum value for t/λ ; a complete analysis of the problem (i.e. calculation of optimum value of t/λ for varying C and power factor is needed.)

The calculation of the optimum tooth-slot parameters on load could provide an interesting line to be followed in future work, and would undoubtedly prove useful for design calculations.

5.6 Flux distribution in the stator core under load conditions.

5.6.1 Harmonic fluxes.

Under load conditions two additional factors influence the flux distribution at the stator surface and across the whole stator main tooth (43-48), (a) armature reaction mmf and (b) the angle α .

For rated output (44.4 KVA), and two values of compensation, fundamental, second and third harmonic fluxes were measured in the core region, Fig 66; most of the odd harmonic fluxes pass behind the a.c. slots, resulting in a non-linear flux density distribution across (43-48) and (49-70). When a 12μF capacitor is connected in series with the alternator, the fundamental flux across (43-48) increases by about 24% for rated output; the flux across (43-48) can be calculated from a consideration of the fluxes at the tooth surface, i.e. $\phi_{43\text{-}48} = \phi_{4\text{-}11} + \phi_{21\text{-}28}$.

The second harmonic flux paths, already discussed in sections 4.4.2.1, 4.4.3 and 4.7.2 (open-circuit), are further complicated by the fact that armature reaction mmfs act upon the airgap permeance; detailed measurements across (43-48) for two values of compensation are shown in Fig 67. As for open-circuit conditions, the flux across (43-48) depends on the flux distribution at the surface and the leakage fluxes, e.g. Fig 46c&d shows the increase in 2nd harmonic flux at the surface when a series capacitor

is added under load conditions. Calculation of these fluxes for a given excitation is difficult, since different types of damping and variations in field excitation also affect the flux distribution.

Although there is a considerable amount of harmonic flux in the teeth under load conditions, the harmonic content in the core region is fairly low, Fig 66; consequently losses in the core region can be calculated with a reasonable degree of confidence by considering the loss due to fundamental flux.

5.6.2 Voltages induced in a field coil and the effects of damping.

Taking into account permeance harmonics and assuming that the mmf due to damping can be written in the form $D_m \cos(m\omega t + \beta_m)$, the flux linking the d.c. winding is given by :-

$$\phi_{dc} = \Lambda_o \Big[2F + 2\sum F\epsilon_n \cos n\omega t + 2\sum \epsilon_n A_n \cos n\omega t \cos(n\omega t + \alpha_n) + 2D_m \cos(m\omega t + \beta_m) + 2\sum \epsilon_n D_m \cos n\omega t \cos(m\omega t + \beta_m) \Big]$$

$$\begin{Bmatrix} n=2,4,6 \\ m=1,2,3 \end{Bmatrix}$$

(section 10.5)

5.6.2.1 Voltages in a field coil.

If the machine is run on load without damping windings, then the voltage induced in a field coil may be large enough to cause a breakdown of the

insulation; this voltage is produced mainly by the flux component $A\epsilon_1\Lambda_0\cos(2\omega t + \alpha)$, since the other second harmonic fluxes contain terms in ϵ_2, ϵ_3, etc, which are small compared with ϵ_1.

Without damping windings, the machine was run on load, and the field excitation adjusted to a low value, to avoid possible breakdown of the insulation; at I_f = 1.0 amp, the peak voltage in a field coil =260v. If it is assumed that the voltage induced in a field coil increases linearly with excitation, which is reasonable from Fig 68, then the induced voltage for rated output = 1040 volts (peak). The second harmonic flux linking the winding is given by $\Lambda_0\epsilon_1 A\cos(2\omega t + \alpha)$; the voltage due to this flux can be calculated easily from the following expression:-

$$E_{fc} = 4.44 f_2 N_{fc} \Delta\phi$$

where E_{fc} = voltage induced in a single field coil on load without damping.

f_2 = second harmonic frequency

N_{fc} = number of turns in a single field coil

$$\Delta\phi = \Lambda_0 \epsilon_1 A \mu_0 l_1 \frac{\text{pole pitch}}{\text{rotor slot pitch}}$$

for $l_1 = 0.225$; $\mu_0 = 4\pi.10^{-7}$; $f_2 = 6000$; $N_{fc} = 129$;
$\Lambda_0 = 15.16$; $\epsilon_1 = 0.554$; $A = 188$,

E_{fc} = 700 volts (RMS) = 970 volts(peak).
(compare with 1040 volts(peak)- measured.)

Damping windings are very effective for damping these fluxes; top damping windings are the most effective. The peak voltage across a field coil with

top damping is approximately 1.4% of the voltage induced without damping, Fig 68.

5.6.2.2 Damping currents.

To damp the second harmonic fluxes which link the field coil completely:-

$$D_2 = -\frac{\epsilon_1 A_1}{2} \quad \text{and} \quad \beta = \alpha$$

For rated output, i.e. I_L = 88.8 amps, V_L = 500 volts

$$D_2 = 52 \text{ AT/pole (peak)}$$

(compare D_2 = 54 AT/pole (peak)- measured)

The damping currents on load are larger than on open-circuit, but they are still small and the I^2R loss is negligible compared with the other losses in the machine.

5.6.2.3 Factors affecting I_D.

Two factors affect I_D , (a) the type of damping and (b) the value of series capacitor.

Damping current waveforms for various values of series compensation and for two types of damping, are shown in Fig 69; for a wide range of compensation and one type of damping, the waveform shape remains appreciably constant, but there is a difference in the value of I_D for each value of series capacitor as shown in Fig 70.

From the equations developed for ϕ_{dc} and ϕ_{ac}, (section 5.1.1.2) the phase angle between I_L (peak) and I_{D_2} (peak) is given by $(\beta_2 - \alpha)$; since α depends on the value of series capacitor, the angle $(\beta_2 - \alpha)$ will alter for various values of C. [β_2 constant = 145° (electrical), Fig 69. (top damping)]
As the pu compensation increases, the angle $(\beta_2 - \alpha)$ will increase, (compare $\beta_2 - \alpha = 0$ at C=36μF and $\beta_2 - \alpha = 33°$ at C=8μF.)
In fig 69 the load current waveform was taken as reference, and shows the phase displacement between I_D (peak) and I_L (peak) for various values of C; for top damping, the second harmonic damping current is predominant and the angles $(\beta_2 - \alpha)$ can easily be taken from the diagrams shown in Fig 69. For bottom damping, the second harmonic damping current would have to be separated from the total I_D waveform to give a true picture of the displacement between I_{D_2} and I_L.

For top and bottom damping, the damping current increases as the pu compensation increases. The reactance of each damping winding controls the magnitude of the damping current for a given series capacitor; for the experimental machine, the ratio $I_{D(Top)} / I_{D(Bottom)}$ is approximately 2:1, Fig 70.

Chapter 6. Rotor flux distribution.

6.1 Rotor flux distribution under open-circuit conditions.

6.1.1 Theory.

.1.1 Flux waveforms.

.1.2 Harmonic fluxes in the rotor teeth.

6.1.2 Experimental work.

.2.1 Flux waveforms at the rotor tooth surface.

.2.2 Flux density distribution across the rotor tooth surface.

.2.3 Harmonic content of flux waveforms at the tooth surface and at the tooth root.

.2.4 Losses.

6.2 Flux distribution under load conditions.

6.2.1 Theory.

.2 Experimental work.

.2.1 Flux waveforms under load conditions.

.2.2 Harmonic analysis of flux waveforms.

.2.3 Distortion of flux waveforms for different values of series capacitor.

.3 Losses under load conditions.

.3.1 Losses in the rotor teeth.

.3.2 Losses in the core region.

6.3 Rotor flux distribution under short-circuit conditions.

6.4 Conclusions.

Summary. - Chapter 6

To investigate the rotor flux distribution, search wires were set in shallow slots along the entire rotor tooth surface and brought out of the machine to a slip-ring assembly, enabling any two conductors to be connected to form a search coil. Flux measurements, made under open-circuit, load and short-circuit conditions, showed the similarity between stator and rotor flux waveforms over a rotor pitch, and the nature of the heteropolar flux which links the rotor teeth and core. For any given load condition, the flux waveforms on the rotor can easily be determined by relating a search coil on the rotor to a given reference on the stator surface. From an understanding of the flux distribution at the tooth surface and at the tooth root, it was possible to estimate the losses in the rotor teeth and in the core.

6.1 Rotor flux distribution under open-circuit conditions.

6.1.1 Theory.

.1.1 Flux waveforms.

From a consideration of the physical geometry of the airgap region and the detailed flux measurements on the stator, it is possible to predict the flux waveforms in the rotor teeth.

As the rotor tooth A, Fig 71a, moves across a pole pitch, the flux in tooth A will vary according to the position of the rotor tooth relative to the stator surface; in addition, the rotor tooth is subjected to heteropolar flux, due to the reversal of the mean flux component under successive d.c. poles. This reversal takes place at a frequency determined by the speed of rotation and the number of d.c. poles. For the experimental machine, the heteropolar frequency is 300 Hz, since there are 12 d.c. poles and the speed of rotation of the rotor is 3000 rev/min. In previous work on Lorenz type machines[6], it was shown that the overall flux variation across the rotor tooth surface is proportional to the heteropolar flux wave, whereas a search coil comparable to the armature slot opening in width will also sense the slot opening. In the Guy-machine, where the rotor tooth width is comparable to the stator-slot openings, a search coil embracing the whole tooth surface can be expected to sense these slot openings, giving a waveform of the shape shown in Fig 71b.

Flux waveforms in small sections of the tooth surface will also sense these slot openings, Fig 71c. From the tooth slot geometry, Z/Y = a.c. slot width / small slot width, Figs 71b and 71c. By analogy with the flux waveform in a small section of the stator tooth surface, the rotor flux waveform for a similar section will also have approximately the same shape, Fig 71d. These waveforms can be added together taking into account their relative displacement, to obtain the total flux variation over a rotor pitch, Fig 72. The position of the rotor tooth with respect to the stator surface is easily obtained, Figs 72 & 73, allowing the flux density distribution to be plotted for various rotor tooth positions. If the stator tooth (4-11) is taken as reference, Fig 74, then under open-circuit conditions, the flux linking a search coil on the leading edge of the rotor tooth (12-13) will reach a maximum at the same instant as the search coil (4-5 stator), Fig 74a, and the flux linking coil (6-7 rotor) will reach a maximum value at the same instant as coil (10-11 stator), Fig 74a. Over a d.c. pole pitch the flux waveforms in (6-7 rotor) and (12-13 rotor) are related as shown in Fig 74b. As the rotor tooth A passes teeth A and B on the stator, the flux waveforms in (4-5 stator) and (12-13 rotor) will be in phase, Fig 74c. Similarly (ϕ 6-7 rotor) and (ϕ 10-11 rotor) will also be in phase, Fig 74d. When the rotor tooth A passes teeth C and D on the stator, there will be a phase displacement between

the rotor and stator flux waveforms of 180°, due to the necessary permeance variation across the pole pitch, Fig 74c&d.

6.1.1.2 Harmonic fluxes in the rotor teeth.

Slot ripples in the open-circuit emf waveform of salient pole synchronous machines,[34,35] caused by the interaction of rotor permeance harmonics with those set up by the stator slot-openings, are very similar to the patterns shown in Fig 71; although a slightly different problem is being dealt with for the Guy-machine, use can be made of the well established theory for synchronous machines.[34]

A brief summary of slot ripples is made by Say[35]:- ' If the main flux wave were assumed to be rectangular (as in a salient pole machine without fringing) and the ripple flux a pure sine wave superimposed on it _ _ _ _ _ _ _, the frequency of flux pulsation would correspond to the rate at which the slots cross the pole face. This pulsation may be regarded as two waves of fundamental space distribution rotating at angular velocity, one forwards and one backwards; the component fields will have velocities of $(2g \pm 1)\omega$ relative to the armature winding, and will generate emfs of frequency $(2g \pm 1)f$ Hz, where g=slots/pole.' A detailed mathematical analysis is given by Walker.[49]

By analogy with these results, the harmonics in the rotor teeth of a Guy-machine can be predicted. Consider Fig 71: as the rotor tooth A moves across

a pole pitch, the flux waveform across the tooth surface has the form shown in Fig 71b, (i.e. the ripples superimposed on the heteropolar flux wave are caused by the stator slot openings.)

The frequencies induced in the rotor teeth, at the surface, (assuming that the ripple flux is purely sinusoidal) will be given by:-

$$f_{RS} = (\ 2 \text{ rotor slots/pole} \pm 1\ ) f_h$$

where f_h = heteropolar frequency.

Since the a.c. slot width is greater than the small slot width s, the resulting ripple flux is not sinusoidal; this distortion of the ideal ripple flux, produces further harmonic fluxes, (i.e. 3rd and 7th harmonic fluxes for the experimental machine, Table 22.)

For the Guy-machine simple relationships can be derived for f_{RS} :-

A d.c. pole comprises (2x + 1) rotor slot pitches,

where x = number of small teeth/main tooth, (1.2.1)

$$\therefore f_{RS} = \left[2(\ 2x + 1\ ) \pm 1 \right] f_h$$

number of rotor teeth = $(\ 2x + 1\ ) P_{dc}$

where P_{dc} = number of d.c. poles

Since $f_{MACHINE}$ = 50 (number of rotor teeth),

$$f_{MACHINE} = 50(\ 2x + 1\ ) P_{dc} = 50(2x + 1) \frac{2f_h}{50} = 2f_h(\ 2x + 1\ )$$

The main frequencies induced in the rotor teeth are given by $\left[\frac{f_{MACHINE}}{f_h} \pm 1 \right] f_h = \left[f_{MACHINE} \pm f_h \right]$

Harmonics which are produced by asymmetry of the tooth ripple waveform, will also be present in the experimental machine, (i.e. the frequencies induced in the rotor surface are given by:-

$\left[f_{MACHINE} \pm f_h\right]$ and the harmonic frequencies due to asymmetry of the ripple waveform.

For the experimental machine, frequencies of $3f_h$ and $7f_h$ are present in addition to the main frequencies, Table 22.

(i.e. frequencies induced in the rotor tooth surface are $\left[f_{MACHINE} \pm f_h\right]$, f_3 and f_7)

where $f_{MACHINE} = 3000Hz.$

$f_3 = 3f_h$

$f_7 = 7f_h$

The magnitude of the harmonic fluxes which link the rotor tooth surface can be obtained theoretically by using a simple approximation outlined in Appendix 10.7.

6.1.2 Experimental work.

To verify the theory, search coil signals were integrated and results compared with the theoretical analysis.

6.1.2.1 Flux waveforms at the rotor tooth surface.

If two adjacent search coils on the rotor surface are chosen, namely (6-7) and (7-8), the flux variation is as shown in Fig 75a. Due to the scaling of the waveforms, the phase displacement between them is not detectable. The search coil signals at the leading and trailing edges of the rotor tooth surface were expanded giving a display of the flux variation over a d.c. pole pitch, Fig 75b. The display was expanded further to investigate the shape of the waveform in a small section, Fig 75d; these waveforms are similar in shape to the open-circuit waveforms on the stator. Flux waveforms in sections (6-7) and (7-8), Fig 75a, also demonstrate the nature of the heteropolar flux variation as the rotor tooth A moves under successive d.c. poles. The phase relationship between coils (4-5 stator, 10-11 stator) and coils at the leading and trailing edges of the rotor tooth surface, Fig 76a&b, show the 180° phase displacement as tooth A passes under teeth C and D. If a search coil is formed from conductors at each side of the rotor tooth surface, (coil 6-13) the coil is sensitive to the heteropolar flux wave

and the slot openings, Fig 76c. The phase relationship of the flux linking coil (6-13) is shown related to the total flux passing through the stator tooth surface (4-11); again the 180° phase change is apparent after the rotor tooth has moved across the a.c. slot. Leakage flux waveforms at the leading and trailing edges of the rotor tooth are also sensitive to the heteropolar flux and the stator slot openings, Fig 76d&e.

6.1.2.2 Flux density distribution across the rotor tooth surface under open-circuit conditions.

The flux density distribution, Fig 77, which shows the open-circuit and load flux density variation, was easily obtained from calibrated flux waveforms across the tooth surface. For the condition where the rotor and stator teeth are opposite, the flux density is appreciably uniform across the tooth surface. Close agreement between open-circuit and load flux density distribution for the rotor tooth positions where the armature reaction mmf is zero, gave an added degree of confidence to the analysis.

6.1.2.3 Harmonic content of flux waveforms at the tooth surface and the tooth root.

The flux waveform across the total tooth surface (6-13) was analysed for harmonic content, considering the heteropolar frequency (300 Hz) as the fundamental component. Waveforms were also analysed

at various depths in the tooth to investigate the effects leakage flux may have upon the harmonic fluxes entering the root of the teeth, Table 22.

Table 22.

Harmonic analysis of the total flux variation in a rotor tooth.

open-circuit rated voltage (500 volts), I_f =2.15amps.
Top damping windings connected.
All fluxes in μWb (total core length).
Fundamental flux taken as f_h, i.e. 300 Hz.

Harmonic order	coil 6-13 ϕ	% HARMONIC wrt Fund.	coil 5-14 ϕ	coil 4-15 ϕ	coil 2-17 ϕ	% HARMONIC wrt Fund.
Fund	730	100	890	930	970	100
3rd	380	52	280	290	290	30
7th	245	34	270	270	270	28
9th	300	41	310	300	300	31
11th	180	25	200	200	200	21

The harmonic content at the surface is considerable, and the harmonic fluxes which are present at the surface are still of the same order of magnitude at the tooth root; the fundamental flux entering the root of the tooth is 25% greater than at the surface, due to leakage flux.

The main rotor frequencies are given by $\left[f_{MACHINE} \pm f_h\right]$, (6.1.1.2) i.e. the 9th and 11th harmonics, where f_h is taken as the fundamental flux and $f_{MACHINE}$ = 3000 Hz.

3rd and 7th order harmonic fluxes are also present, Table 22, and are of the same order as the 9th and 11th harmonic fluxes. (see section 6.1.1.2 and appendix 10.7.)

6.1.2.4 Losses.

Usually the loss in the rotor is calculated taking into account the following components:-

(a) 3000 Hz loss in the rotor teeth.

(b) 300 Hz heteropolar loss in the rotor teeth.

(c) 3000 Hz loss in the rotor core.

(d) 300 Hz heteropolar loss in the rotor core.

The losses in the teeth and core calculated from the above will be in considerable error, since:-

(1) the harmonic fluxes are neglected.

(2) there is no 3000 Hz frequency in the rotor; harmonic frequencies of $\left[\left(f_{MACHINE} \pm f_h\right), f_3 \text{ and } f_7\right]$ are superimposed on the heteropolar flux wave.

(3) an additional loss due to the surface saturation effect must also be taken into account.

At these frequencies the losses are proportional to $f^{1.5} B^2$, (4.3); using this simple relationship it is possible to calculate the total loss in the tooth, and to compare this value with the loss calculated from the normal assumptions. Neglecting the harmonic fluxes which link the teeth, and assuming that the loss in the teeth and core occurs due to frequencies of 3000 Hz and 300 Hz, leads to an underestimation of the losses in the teeth, but gives

a reasonably accurate value for loss in the core region as shown by the following calculations.

(1) Rotor teeth.

normal loss calculation:-

Taking 3000 Hz loss as 1pu; 300 Hz loss = 0.138pu.

new loss calculation:-

From analysis of the flux waveform (6-13) the total loss = 1.6pu.

Extra loss due to the surface saturation effect=0.21pu.

$\therefore$ Total loss = 1.81pu.

The ratio $\frac{\text{Total loss}}{(3000\text{Hz} + 300\text{Hz})\text{loss}} = 1.59 = K_{RT}$

From this calculation the true loss in the teeth is shown to be approximately 60% greater than that calculated by only considering the 3000 Hz and 300 Hz loss, (which is not present at the rotor surface).

(2) Losses in the rotor core.

No experimental data has been obtained for the rotor core, but from analysis of the flux variation in the root of the rotor teeth, it is reasonable to assume that part of the core will also be subjected to harmonic fluxes, causing additional loss to that normally calculated.

Since the harmonic content of the flux waveform at the root of a rotor tooth is known, i.e. (2-17), it is possible to estimate the harmonics present across P-Q, Fig 78, by adding the flux waveforms in

two adjacent rotor teeth, taking into account their relative phase displacement.

The flux waveform in section (2-17) can be expressed in the form:-

$$\phi\ (2\text{-}17) = A\sin\theta + B\sin3\theta + C\sin7\theta + D\sin9\theta + \_\_\_\_\_$$

ϕ in adjacent rotor tooth

$$= A\sin(\theta + \chi_R) + B\sin3(\theta + \chi_R) + C\sin7(\theta + \chi_R) + \_\_\_\_\_$$

where χ_R = phase angle between ϕ (2-17) and ϕ in adjacent rotor tooth.

$$\phi\ (\text{P-Q}) = A\ (1 + \cos\chi_R)\sin\theta + A\cos\theta\sin\chi_R$$
$$+ B\ (1 + \cos3\chi_R)\sin3\theta + B\cos3\theta\sin3\chi_R$$
$$+ C\ (1 + \cos7\chi_R)\sin7\theta + C\cos7\theta\sin7\chi_R$$
$$+ \_\_\_\_\_$$

ϕ (P-Q) can be written in the form:-

$$A'\sin(\theta + \phi_1) + B'\sin(3\theta + \phi_3) + \_\_\_\_\_$$

For open-circuit conditions the harmonic analysis of the total flux waveform across P-Q is shown in Table 23.

Table 23.

Harmonic content of flux waveform across P-Q.

Rated open-circuit voltage (500 volts) I = 2.15 amps.

[f_h = 300 Hz, taken as fundamental flux.]

Harmonic	% Harmonic wrt fundamental	loss.
Fund	100	$\propto$ 5170
3rd	16	$\propto$ 690
7th	15	$\propto$ 2090
9th	33	$\propto$ 16000
11th	16	$\propto$ 5100

The actual total loss was compared with the losses calculated on the basis of 3000 Hz and 300 Hz loss in a similar way to the rotor teeth.

$$K_{RC} = 1.12 \quad \text{where } K_{RC} = \frac{\text{Total loss in core}}{(3000\text{Hz} + 300\text{Hz}) \text{ loss}}$$

In the core region the K factor is much smaller than the K factor in the teeth; the losses based upon the (3000Hz and 300Hz)loss account for 89% of the losses in the core region.

It is felt that the calculation of losses from a consideration of the total flux variation is far more realistic for the tooth and core regions, and may in conjunction with the new approach to calculating losses in the stator teeth, reduce the large discrepancy between measured and calculated losses in this class of machine.

6.2 Flux distribution under load conditions.

6.2.1 Theory.

For open-circuit conditions the phase relationship between the flux waveform in a small section of the rotor surface and a particular reference coil on the stator surface can be calculated as shown in section 6.1.1; under load conditions two additional factors are needed to predict the load flux waveforms:-

(a) the magnitude of the armature reaction mmf.

(b) the angle α .

Under load conditions the load current waveform is stationary with respect to the flux waveforms (4-5 stator) and (10-11 stator), its phase displacement being dependent upon the angle α, Fig79b. The rotor positions shown in Fig 79a denoted by A,B,C_____H are for a particular load condition, i.e. C= 16μF, (α = 134°); for other values of α , A,B,C_____H will represent different rotor positions. Since the rotor flux waveforms under open-circuit conditions are related in phase to the stator flux waveforms, it follows that the load current waveform will also remain stationary with respect to the flux waveforms (12-13 rotor) and (6-7 rotor), Fig 79c. The angle α can be transferred directly to the rotor, enabling the magnitude of the armature reaction mmf to be determined for any rotor position. The distortion in each section of the rotor surface can be analysed in a similar way to the stator, enabling an extra loss factor to be calculated. The distortion at the tooth surface is dependent on the value of series capacitor and load power factor.

6.2.2 Experimental work.

6.2.2.1 Flux waveforms under load conditions.

The flux variation across the total tooth surface (6-13 rotor), Fig 80a, shows the relationship between ϕ (6-13) and the flux variation across the stator tooth surface (4-11); the nature of the heteropolar flux and the 180° phase shift as the rotor

tooth A moves across the a.c. slot opening is apparent.

The load waveforms (6-7) and (12-13), Fig 80(b,c,d&e), show (a) the nature of the heteropolar flux variation and (b) the relationship between the associated stator flux waveforms. In each case the 180° phase change is apparent as the rotor tooth A moves across an a.c. slot width. At the trailing edge of the rotor tooth (6-7), the armature reaction mmf assists the main field, whereas at the leading edge of the rotor tooth (12-13), the armature reaction opposes the main field causing a considerable reduction in flux. The distortion across the tooth surface is shown in Fig 81; these waveforms are very similar to the stator flux waveforms, (chapter 5).

6.2.2.2 Harmonic analysis of flux waveforms under load conditions.

The flux variation across the surface (6-13) and in various sections of the tooth was analysed for harmonic content, Table 24.

Table 24

Harmonic analysis of flux waveforms in a rotor tooth.
Rated output: 44.4 KVA. series capacitor C = 16μF.
Fluxes in μWb (total core length).

FREQUENCY.	ϕ 6-13	%HARMONIC wrt fund (6-13)	ϕ 5-14	ϕ 4-15	ϕ 2-17	%HARMONIC wrt fund (2-17)
300Hz	840	100	1000	1100	1200	100
900Hz	460	49	560	580	600	50
2100Hz	280	33	280	280	280	23
2700Hz	320	38	310	310	310	26
3300Hz	210	30	220	220	230	19

The harmonic content across the total rotor tooth surface under load conditions is very similar to the open-circuit condition; due to more leakage flux under load conditions, there is a 30% increase in the fundamental flux in the root of the tooth. (compare 25% increase on open-circuit.)

6.2.2.3 Distortion of flux waveforms for different values of series capacitor.

The effect of altering the value of series capacitor was investigated for three different values of compensation:-

(a) no series capacitor.

(b) 36μF (0.206pu compensation.)

(c) 8μF (0.93pu compensation.)

At the trailing edge of the rotor tooth surface there is no marked effect in the flux variation as the value of the series capacitor is altered, (compare with stator section (10-11) , 5.2.7) whereas at the leading edge (12-13) there is quite a marked effect in the distortion, (compare with stator (section 4-5), 5.2.7), Fig 82.

6.2.3 Losses under load conditions.

6.2.3.1 Losses in the rotor teeth.

The harmonic content of the flux waveform across the total tooth surface is practically identical for open-circuit and load conditions. Since the surface

loss in the rotor and stator teeth are of the same order, it can be concluded that under load conditions, the true loss in the rotor teeth is approximately 60% greater than normally calculated using the simple assumption that the rotor teeth are only subjected to a 3000Hz and 300Hz loss.

6.2.3.2 Losses in the core region.

The harmonic content of the total flux waveform across (P-Q) under load conditions is shown in Table 25.

Table 25.

Harmonic content of flux waveform across P-Q under load conditions.

Rated output: 44.4 KVA. C= 16μF.

Hz	Harmonic	% Harmonic wrt fundamental	loss
300	Fund	100	$\propto$ 5170
900	3rd	26.6	$\propto$ 1820
2100	7th	12.2	$\propto$ 1340
2700	9th	27.7	$\propto$ 11,500
3300	11th	15.4	$\propto$ 4400

$$\frac{\text{Total loss}}{\text{3000Hz + 300Hz loss}} = 1.15$$

From the above figures, the true core loss is 15% greater than normally calculated from assuming that the losses in the core are due to frequencies of 3000 and 300 Hz.

6.3 Rotor flux distribution under short-circuit conditions.

The flux distribution was analysed for

(a) short-circuit- no series capacitor.

(b) short-circuit with series capacitor (C=16μF).

With the machine running on short-circuit (I_{sc} =rated load current) the flux variation was displayed for the whole tooth surface, and for the leading and trailing edges of the tooth. For both conditions the total flux variation across the surface and in the tooth was analysed as shown in Table 26.

Table 26.

Harmonic analysis of flux waveforms across sections of the rotor tooth under short-circuit conditions.

all fluxes in μWb (total core length). I_{sc} = 88.8amps.

(a) no series capacitor.

freq.	Ø 6-13	% HARMONIC wrt fund (6-13)	Ø 5-14	Ø 4-15	Ø 2-17	% HARMONIC wrt fund (2-17)
300Hz	750	100	980	980	1000	100
900Hz	380	51	470	500	510	51
2100Hz	200	26.6	200	190	180	18
2700Hz	160	21.4	140	110	100	10
3300Hz	70	9.3	10	12	29	2.9

(b) series capacitor C = 16μF.

freq.	Ø 6-13	% HARMONIC wrt fund (6-13)	Ø 5-14	Ø 4-15	Ø 2-17	% HARMONIC wrt fund (2-17)
300Hz	340	100	460	510	540	100
900Hz	160	47	210	220	230	42.6
2100Hz	52	15.4	44	38	33	6.1
2700Hz	16	4.7	53	74	92	17
3300Hz	56	16.5	110	130	150	27.8

The third harmonic component remains approximately 50% of the fundamental flux at the surface for all conditions, whereas the higher order harmonics are considerably reduced compared with the open-circuit and load conditions. For C = 16μF, there is a 37% increase in tooth flux at the tooth root, due to leakage flux effects; for different values of compensation, the leakage flux will alter due to the change in α . Flux waveforms at the leading and trailing edges of the tooth surfaces for these two conditions are shown in Figs 83 and 84, with their corresponding waveforms on the stator surface.

6.4 Conclusions.

The flux distribution across the rotor tooth surface under open-circuit, load and short-circuit conditions is very similar to the flux distribution on the stator surface over a rotor pitch, and can be predicted from a knowledge of the stator flux waveforms. The magnitude of the load or short-circuit current and the appropriate α angle, enables the flux density to be plotted across the rotor tooth surface. A loss calculation for the rotor teeth can be made, taking into account the surface loss and the harmonic fluxes seen by the rotor teeth; these losses calculated for the tooth region are about 60% greater than the normal calculated losses. The losses in the core region are a little more difficult to calculate accurately, since the harmonic fluxes entering the tooth root are different from the harmonic fluxes at the surface, due to leakage fluxes. Usually it is sufficient to consider the harmonic content at the surface for the core loss calculation, especially for normal values of compensation where the leakage fluxes will not have a significant effect upon the flux entering the tooth root.

Chapter 7.

The calculation of field excitation under load conditions.

7.1 On load analysis (Raby and Pohl)

7.1.1 Raby.

.2 Pohl.

.3 Calculation of I_f under load conditions for various values of series capacitor.

7.2 Büssing.

7.2.1 open-circuit analysis (part 1)

.1.1 Permeance calculations.

.1.2 Fluxes linking the a.c. and d.c. windings under open-circuit conditions.

.1.3 Voltage generated in the a.c. winding.

7.2.2 On load analysis (part 1)

.2.1 Fluxes linking the a.c. and d.c. windings under load conditions.

.2.2 Main and leakage fluxes.

7.2.3 On load analysis (part 2).

.3.1 Main and leakage fluxes.

.3.2 Calculation of I_f under load conditions.

7.2.4 Fluxes linking the a.c. and d.c. windings under load conditions, taking into account permeance harmonics.

7.2.5 Calculation of I_f from main and leakage fluxes.

7.2.6 Conclusions.

7.3 Calculation of α and field excitation using the concept of saturated synchronous reactance.

7.3.1 Saturation factor k_s and synchronous reactance.

.2 Load vector diagrams using the concept of saturated synchronous reactance.

.2.1 unsaturated conditions.

.2.2 Saturated conditions.

7.3.3 Maximum power and load angle.

7.3.4 Load angle for the Guy-machine (θ_g)

.4.1 θ_g for zero compensation.

.4.2 θ_g for series compensation.

7.3.5 Experimental work.

7.3.6 Choice of rating for the experimental machine.

.6.1 Temperature measurements on load.

7.3.7 Comparison of calculated and measured results for various load conditions using the concept of saturated synchronous reactance.

.7.1 Constant impedance test.

.7.2 Alternator supplying a variable impedance load, I_f constant.

.7.3 V load constant (variable load and field current).

Summary. - Chapter 7.

In design work it is important to be able to calculate the field excitation requirements under load conditions. The calculation of field excitation for unsaturated conditions is considered by Raby[18] and Pohl[24]; these theories are based upon simple assumptions which give reasonable results for non-saturated conditions, but which are considerably in error at high values of saturation. These theories are discussed at the beginning of this chapter to introduce some of the basic ideas and problems.

The major contribution to load theory is presented by Büssing[8] who attempts to include the effects of leakage flux and saturation; in this section a survey is made of Büssing's analysis with calculations for the experimental machine.

A simple method of obtaining the field requirements from the open-circuit and short-circuit curves, taking saturation into account, is also given.

Chapter 7.

The calculation of field excitation under load conditions.

7.1 On load analysis (Raby and Pohl).

7.1.1 Raby.[18]

Under load conditions two mmfs (neglecting damping), act upon the airgap permeance,

(a) the field mmf, F

(b) the mmf due to armature reaction, A.

Assuming that the load current is sinusoidal, the total mmf acting upon the airgap permeance is given by $(F + A\cos\omega t)$ ampere-turns.

If permeance harmonics are neglected, the permeance variation can be expressed in the form:-

$$\Lambda_o(1 + \epsilon \cos(\omega t + \alpha))$$

where Λ_o = mean permeance,
ϵ = flux utilisation coefficient,
α = phase angle between the instants of peak current and peak permeance.

The flux which is given by the product of mmf and permeance can be expressed in the following form:-

$$\phi = \Lambda_o\left[F + \tfrac{1}{2}A\epsilon\cos\alpha\right] \quad \text{(constant flux)}$$
$$+\Lambda_o\left[F\epsilon\cos(\omega t+\alpha) + A\cos\omega t\right] \quad \text{(fundamental flux)}$$
$$+\Lambda_o\left[\tfrac{1}{2}A\epsilon\cos(2\omega t+\alpha)\right] \quad \text{(second harmonic flux)}$$

The fundamental a.c. flux can be represented by a vector diagram, Fig 85(a).

At this stage it is convenient to express the fluxes in pu terms to eliminate Λ_o. If the machine

were running under open-circuit conditions and excited to give rated voltage, then the fundamental flux would be given by $\epsilon F_o \Lambda_o \cos\omega t$. If this value is taken as our unit of alternating flux and F_o as the unit of field excitation, ϕ_{ac} = emf numerically, and it follows that $\Lambda_o = 1/F_o\epsilon$. The vector diagram can therefore be drawn in pu terms, Fig 85b&c.

If damping windings are added, the value of 'a' is modified to $a(1 - \epsilon^2/4)$. ('a' is an important parameter and is defined by Raby, section 1.3.3*) For 10kHz machines, ϵ is of the order of 0.2 and hence $a(1 - \epsilon^2/4) \triangleq 0.99a$; for 3kHz machines where the ϵ value is much higher, the value of 'a' is modified to approximately 0.94a.

Since damping has little effect upon the value of 'a', the change in the a.c. flux with damping will be small; for the experimental machine the increase in a.c. fundamental flux with damping is approximately 2.6%.

In this simple theory which neglects saturation, it is necessary that α, 'a' and ϕ_{ac} are known before the field excitation can be calculated.

7.1.2 Pohl[24]

A further extension to the theory is presented by Pohl who takes into account permeance harmonics. The permeance variation can be written in the form:-

$$\Lambda_o\left[1 + \epsilon_1\cos(\omega t + \alpha) + \epsilon_2\cos(2\omega t + 2\alpha) + \epsilon_3\cos(3\omega t + 3\alpha) + \text{----------}\right]$$

where $\epsilon_v = \Lambda_v/\Lambda_o$.

* section 1.3.3 refers to chapter 1 of this thesis.

Flux expressions are derived similar to the analysis presented by Raby:-

$$\phi = \Lambda_o\left[F + \tfrac{1}{2}\epsilon_1 A\cos\alpha\right]$$
$$+\Lambda_o\left[F\epsilon_1\cos(\omega t+\alpha) + A\cos\omega t + \underline{\frac{A\epsilon_2}{2}\cos(2\alpha+\omega t)}\right]$$
$$+\Lambda_o\left[\underline{F\epsilon_2\cos(2\omega t + 2\alpha)} + \frac{A\epsilon_1}{2}\cos(2\omega t + \alpha)\right.$$
$$\left. + \underline{\frac{A\epsilon_3}{2}\cos(2\omega t + 3\alpha)}\right]$$

Terms underlined, e.g. $\underline{F\epsilon_2\cos(2\omega t + 2\alpha)}$ are the components that are added when permeance harmonics are included. For t=0, a simple vector diagram can be drawn which combines the amplitudes of the three fundamental flux components to form ϕ_1 (fundamental component of ϕ), Fig 85d.

If $A\epsilon_2\Lambda_o/2$ is small compared with the other fundamental components, then it can be neglected, resulting in the same vector diagram as Raby.
(For the experimental machine $\epsilon_2 \triangleq 0.025\,\epsilon_1$ and therefore the term $A\epsilon_2\Lambda_o/2$ will be approximately 1% of $F\epsilon_1\Lambda_o$, and can be neglected for practical purposes.) The extra terms introduced by Pohl are not important for practical calculations, since they are small compared with the main flux components.

7.1.3 Calculation of I_f under load conditions for various values of series capacitor.

To calculate the field requirements on load, it is convenient to work in the pu system, and to use a vector diagram similar to that used for

synchronous machines. Two conditions are considered,

(a) machine on load- zero compensation and

(b) machine on load with series compensation, Fig86a&b.

If the reactances X_l and 'a' are known, then the voltage E_{oc} is easily obtained from the vector diagram;

(a) $\overline{E_{oc}} = \overline{V} + \overline{X_l} + \overline{a}$ (I_L = 1pu) [No C.]

(b) $\overline{E_{oc}} = \overline{V} + \overline{X_l} + \overline{X_c} + \overline{a}$ (I_L = 1pu) [with C.]

The field current (I_f) corresponding to E_{oc} is obtained from the open-circuit saturation curve.

The experimental machine was run to give rated output for various values of series compensation; the field current and α angle were measured and compared with calculated results, Table 27.

A typical calculation for α and I_f when a 16μF capacitor is connected in series with the alternator is given below; the corresponding vector diagram is shown in Fig 86c.

Rated load current = 88.8 amps = 1pu current.
load voltage = 500 volts = 1pu voltage.
1pu resistance = 5.62Ω.

From design sheet data:-

X_l = 0.078pu and a = 1.23pu.

For cos ϕ = 0.962, E_{oc} is easily found from the relationship:-

$$\overline{E_{oc}} = \overline{V} + \overline{X_l} + \overline{X_c} + \overline{a}$$

V	=	0.962 + j0.270
X_l	=	j0.078
X_c	=	-j0.59
a	=	j1.23
E_{oc}	=	0.962 + j0.988

$$\left|E_{oc}\right| = \sqrt{1.91} = 1.38 \text{ pu} \longrightarrow 395 \text{ AT/pole}$$

(from o.c. saturation curve)

($I_f = 3.1$ amps.)

$$\tan \psi_L = \frac{0.988}{0.962} \quad ; \quad \psi_L = 45^\circ\ 42'$$

$$\alpha = \psi_L + 90^\circ = \underline{135^\circ\ 42'}$$

Table 27.

Comparison between measured and calculated values of field current and α angle for various values of series compensation. Rated output, $I_L = 88.8$ amps.

compensation $C\mu F$	α° (measured)	α° (calculated)	field amps (measured)	field amps (calculated)
8	111	116	2.4	2.25
12	126	132	2.75	2.8
16	134	135° 42'	3.05	3.1
28	141	144	3.5	4.3
36	145	145	3.6	5.0
No C	150	148° 30'	4.05	5.5

For the calculation of field current, the synchronous reactance given by (a $+X_\ell$) is assumed to be constant. For field excitations up to 3 amps where this condition is satisfied, Fig 87b, the analysis gives results which compare favourably with measured values of field current, (max error 6%). For further increases in field current, i.e. decreasing compensation to achieve rated output, the value of X_s

decreases due to saturation. If the value of X_s is assumed to be constant, then the calculated field current will be larger than the measured value, Fig 87a&b; at zero compensation the percentage error between measured and calculated results is 37%.

Small changes in synchronous reactance due to saturation will not have a very marked effect upon the α angle as shown in Fig 87a; for the whole range of compensation the calculated values of α compared favourably with measured values (max error 5%).

Two main conclusions result from this analysis:-

(a) The method gives reasonable results for unsaturated conditions when a series capacitor is used to give rated output.

(b) It is obvious from measured and calculated results that, at low values of compensation and at rated output, the effects of saturation must be taken into account to obtain a reasonably accurate estimate of the field excitation; this problem is dealt with in some detail by Büssing, (section 7.2).

7.2 Büssing.[8]

In his theoretical analysis of the Guy-machine, Büssing includes the effects of leakage flux and saturation. A method analogous to that used in synchronous machine theory is also developed to calculate the field excitation under load conditions.

7.2.1 Open-circuit analysis (Paper 1)

7.2.1.1 Permeance calculations.

The magnetic permeance is calculated for the tooth opposite tooth and tooth opposite slot positions using the substitute angle method, (section 10.1) resulting in the following:-

$$\Lambda_t = t/g + (2.3/\beta)\log(1 + \beta s/g)$$

and

$$\Lambda_s = \frac{s-t}{g + \beta\frac{(s-t)}{2}} + \frac{9.2}{\beta}\log\left(\frac{1 + \beta s/2g}{1 + \beta\frac{(s-t)}{2g}}\right)$$

The total permeance per d.c. pole half is obtained by multiplying the values of Λ (which correspond to unit core length and one rotor slot pitch) by $k = \mu_o \ell_1 Z_2$

where μ_o = absolute permeability,
ℓ_1 = effective length of the core,
Z_2 = number of stator teeth per dc pole half.

In the initial stages of the analysis it is assumed that the permeance variation is sinusoidal; for the two main teeth A and B, Fig 88a the permeance

variation can be expressed in the form:-

$$\Lambda_A = \Lambda_o(1 + \epsilon \cos \omega t)$$

and $\Lambda_B = \Lambda_o(1 + \epsilon \cos(\omega t + \pi)) = \Lambda_o(1 - \epsilon \cos \omega t)$

7.2.1.2 Fluxes linking the a.c. and d.c. windings under open-circuit conditions.

The fluxes in teeth A and B are given by:-

$$\phi_A = F_e \Lambda_A = F_e \Lambda_o(1 + \epsilon \cos \omega t)$$

$$\phi_B = F_e \Lambda_B = F_e \Lambda_o(1 - \epsilon \cos \omega t)$$

The flux linking the a.c. winding = $\phi_A + \phi_B'$

$$\phi_{ac} = F_e \Lambda_o \{1 + \epsilon \cos \omega t\} - F_e \Lambda_o \{1 - \epsilon \cos \omega t\}$$

$$= \underline{2 F_e \Lambda_o \epsilon \cos \omega t}$$

Similarly the flux linking the d.c. winding is given by $\phi_a + \phi_B$

$$\phi_{dc} = F_e \Lambda_o \{1 + \epsilon \cos \omega t\} + F_e \Lambda_o \{1 - \epsilon \cos \omega t\}$$

$$= \underline{2 F_e \Lambda_o}$$

7.2.1.3 Voltage generated in the a.c. winding.

The induced voltage E is found by differentiating the a.c. flux wrt time, i.e.

$$E = 4.44 f \omega_a \Delta\phi$$

where ω_a = series turns in the a.c. winding

$\Delta\phi$ = resultant flux linking the a.c. winding.

$(\Delta\phi = 2 \Lambda_o \epsilon (F_1 + F_2) \mu_o l_1 Z_2)$

If the specific fluxes in the d.c. pole halves A and B are calculated at the airgap then $\phi_A = \Lambda_t F_1$ and $\phi_B = \Lambda_s F_1$, where F_1 = mmf at the airgap. With these fluxes and with the mmf F_z at the stator and rotor teeth, the flux ϕ is given by

$$\phi = f(F_1 + F_z), \text{ Fig 88b.}$$

At a certain value of excitation the voltage reaches a maximum due to saturation of the teeth; this maximum occurs where the tangent to ϕ_A is parallel to ϕ_B .

From design sheet data E was calculated for I_f = 2.15 amps, (500 volts- measured).

$$E = 4.44 f \omega_a \Delta\phi$$

with $f = 3000$; $\omega_a = 18$; $\mu_o = 4\pi .10^{-7}$; $\ell_1 = 0.22$m;
$Z_2 = 2$; $\Lambda_o = 15.16$; $\epsilon = 0.554$; $(F_1 + F_z) = 260$,

$E_{CALCULATED}$ = 510 volts, compare 500 volts(measured)

(2% error)

7.2.2 On load analysis (part 1)

7.2.2.1 Fluxes linking the a.c. and d.c. windings under load conditions.

Under load conditions an additional mmf acts upon the airgap permeance due to armature reaction; this mmf can be represented by $A\cos(\omega t + \alpha)$,

where A= peak a.c. ampere turns/pole

α = phase angle between the peak of the load current and the peak permeance.

Initially, if damping is neglected, the following equations result for ϕ_A and $\phi_{B'}$, Fig 88.

$$\phi_A = \Lambda_o(1 + \epsilon \cos \omega t)(F_e + A\cos(\omega t + \alpha))$$

$$\phi_{B'} = \Lambda_o(1 - \epsilon \cos \omega t)(-F_e + A\cos(\omega t + \alpha))$$

The a.c flux is given by $\phi_A + \phi_B'$

$$\phi_{ac} = 2\Lambda_o A\cos(\omega t + \alpha) + 2\Lambda_o \epsilon F_e \cos \omega t$$

ϕ_{dc} is given by $\phi_A - \phi_{B'}$

$$\phi_{dc} = \Lambda_o\left\{2F_e + \epsilon A\cos\alpha + \epsilon A\cos(2\omega t + \alpha)\right\}$$

These results are summarised by Büssing:-

'The above equations show that for an assumed harmonic change of permeance, change of the fluxes effective in the a.c. winding are purely harmonic; while in the d.c. winding a flux of double synchronous frequency boosts the d.c. flux.'

Harmonic fluxes are also considered by Büssing, (section 7.2.4); a detailed discussion of these fluxes is given in chapter 5 of this thesis (section 5.6).

7.2.2.2 Main and leakage fluxes.

In addition to the airgap fields, the a.c. current also excites leakage fields across the a.c. slots and around the end-winding. These fields are associated with reactance and can be calculated by known methods.

Büssing extends the results outlined in section 7.2.2.1 by splitting the a.c. flux into main and leakage fluxes. Initially, the a.c. flux is split into two components, namely ϕ_{as} and ϕ_h,

where ϕ_{as} = leakage flux
ϕ_h = main flux.

The split of ϕ_{ac} into two components is based upon the following assumptions:-

(a) under short-circuit conditions, the angle α approaches 180°.

(b) for $\alpha = 180°$ and $A = F\epsilon$, the a.c. flux in the machine is reduced to zero.

(c) if $F = A$, $\alpha = 180°$, the flux in the machine is leakage flux, whose peak amplitude is given by $2(1 - \epsilon)\Lambda_o A$.

At this stage, it was decided to examine these assumptions (by comparing them with experimental data

from the test machine) before proceeding with any calculations for field excitation based on ϕ_h and ϕ_{as} , (section 7.2.3.2).

(a) <u>under short-circuit conditions, the angle α approaches 180°.</u>

Measurements on short-circuit (no series capacitor) showed that the α angle = 174°, (section 5.4.1). Tests also showed that α is little affected by the value of series capacitor on short-circuit. The assumption that $\alpha = 180°$ on s.c., which is also used by Pohl[24], seems to be reasonable.

(b) <u>for $\alpha = 180°$ and $A = F\epsilon$, the a.c. flux in the machine is reduced to zero.</u>

Measurements on open-circuit and on-load (chapters 4 and 5) have shown that the overall equations for ϕ_{ac} and ϕ_{dc} must be treated with caution, and do not give any indication of the flux distribution at the surface and in the small teeth.

If $A = F\epsilon$ and $\alpha = 180°$ is substituted into the equation for ϕ_{ac} (without damping), then

$$\phi_{ac} = 2\Lambda_o A \cos(\omega t + 180°) + 2\Lambda_o A \cos \omega t$$
$$= -2\Lambda_o A \cos \omega t + 2\Lambda_o A \cos \omega t = 0.$$

With the experimental machine running on short-circuit (no series capacitor), the flux distribution at the tooth surface and across (43-48) is shown in Fig 59.

[For I_{sc} = 88.8 amps, $\alpha \triangleq 180^{\circ}$ and $A \triangleq F\epsilon$,
i.e A = 188AT/pole and $F\epsilon$ = 200AT/pole.]

The distortion at the tooth surface is greater than on load, but the fluxes in small sections of the surface are still comparable with fluxes under load conditions, (compare Figs 59 and 56). The fluxes at the surface combine with the leakage fluxes to give $\phi_{43\text{-}48}$; $\phi_{43\text{-}48}$ is considerably less than on load, (compare $\phi_{43\text{-}48}$ (peak) on s.c. = 337μWb and $\phi_{43\text{-}48}$ (peak) on load = 1680μWb). The flux linking the a.c.winding is given by $\phi_{43\text{-}48}$ (Fig 59) added to a similar waveform moved through 180° (electrical); it can be seen from Fig 59 that, when these two waveforms are added together, the resulting a.c. flux will be very small, (practically zero for the condition shown in Fig 59). Although the assumption made by Büssing is not based upon the actual flux distribution, the overall equations do give a correct value for ϕ_{ac} on short-circuit (for the particular conditions stated).

(c) <u>if F= A, α = 180°, the flux in the machine is leakage flux, whose peak amplitude is given by $2(1-\epsilon)\Lambda_o A$.</u>

Büssing extends the ideas expressed in (a) and (b) by substituting F=A and α = 180° into the expression for ϕ_{ac}:-

i.e. $\phi_{ac} = 2\Lambda_o A\cos(\omega t + 180^{\circ}) + 2\Lambda_o A\epsilon \cos\omega t$

$= -2\Lambda_o A\cos\omega t(1-\epsilon)$

This flux is defined as leakage flux (ϕ_{as}) whose peak amplitude is given by $2(1 - \epsilon)\Lambda_o A$.

Büssing includes this term in the expression for the a.c. flux by rewriting ϕ_{ac} in the form:-

$$\phi_{ac} = \phi_{as} + \phi_h ,$$

i.e.

$$\phi_{ac} = 2\epsilon\Lambda_o\left[F_e \cos\omega t + A\cos(\omega t + \alpha)\right] + 2(1 - \epsilon)\Lambda_o A\cos(\omega t + \alpha)$$

Although Büssing gives no reasons for this initial split [(c) does not follow directly from (a) and (b)], the calculation of I_f based upon this equation, does give reasonable results as shown in 7.2.3.2, Table 28.

From the above expression, Büssing assumes that the peak amplitude of the fundamental leakage flux is given by $2(1 - \epsilon)\Lambda_o A$, i.e. independent of power factor and series capacitor. Measurements on load, (Table 16, chapter 5) show that although the fundamental leakage flux is practically constant for the trailing edge of the teeth for various values of series capacitor, the leakage fluxes decrease with increasing compensation at the leading edge. Leakage flux waveforms also contain a considerable amount of harmonic flux, Fig 51; obviously these harmonic fluxes must be taken into account when considering the relationship between main and leakage fluxes,

[Compare $\frac{\phi_{43\text{-}48}}{\phi_{LEAKAGE}}$ = 2.05 (C= 12μF)- Fig 46

with $\frac{\phi_{43\text{-}48}}{\phi_{LEAKAGE}}$ = 1.67 (No C) (Total fluxes)]

Using the argument below, Büssing proceeds to split the a.c. flux into three components, namely ϕ_{ahg}, ϕ_{as}, and ϕ_{hm}; calculation of I_f (discussed in 7.2.3.2) shows that this further split gives the wrong answer.

'At the instant $\omega t = 0$, the main fluxes in the a.c. and d.c. windings are of equal value. At other instants the two main fluxes do not correspond with one another, due to the d.c. winding having a flux component with a frequency not corresponding to the windings.'

To obtain equality of the main fluxes, Büssing splits the a.c. main flux into a main and leakage flux.

The a.c. flux is then given by $\phi_{hm} + \phi_{ahg} + \phi_{as}$

where ϕ_{hm} = main a.c. flux

and ϕ_{ahg}, ϕ_{as} = leakage fluxes.

ϕ_{ac} is then written in the form:-

$$\phi_{ac} = 2\epsilon\Lambda_o\left\{F_e\cos\omega t + \tfrac{1}{2}A\cos(\omega t + \alpha)\right\} + \epsilon\Lambda_o A\cos(\omega t + \alpha) + 2(1-\epsilon)\Lambda_o A\cos(\omega t + \alpha)$$

Büssing associates these fluxes with reactance and proceeds to calculate the various components from the open circuit saturation curve. Measurements discussed in 7.2.3.2, show that the leakage reactance given by $X_{ahg} + X_s$ is incorrect, (compare $X_{ahg} + X_s = 1.13$pu and X_s (measured) = 0.76 pu).

The calculation of these fluxes, using a complicated graphical solution, is also mentioned by Büssing, but no detailed calculations are given. Büssing concludes his first section by suggesting that the graphical

solution is too complex for normal calculations:-

'The calculation of these fluxes is not dealt with in any detail, since the method is very complicated, especially for determining the necessary field current for a given terminal voltage and load current_____ ____It is obvious that this method is unsatisfactory and lengthy.'

7.2.3 Part 2. (Büssing)

In this section Büssing presents an analysis based on synchronous machine theory.

7.2.3.1 Main and leakage fluxes.

The fluxes in teeth A and B are given by:-

$$\phi_A = \Lambda_o F_A + \Lambda_o \epsilon F_A \cos\omega t$$
$$\phi_B = \Lambda_o F_B - \Lambda_o \epsilon F_B \cos\omega t$$

where $F_A = (F + A\cos(\omega t + \alpha))$

$F_B = (-F + A\cos(\omega t + \alpha))$

$$\phi_{ac} = (\Lambda_o F_A - \Lambda_o F_B) + (\epsilon\Lambda_o F_A + \epsilon\Lambda_o F_B)\cos\omega t.$$

Assuming that the permeance changes harmonically for each saturation condition, the a.c. flux can be expressed in the following form:-

$$\phi_{ac} = \tfrac{1}{2}\Lambda_t F_A + \tfrac{1}{2}\Lambda_s F_A - \tfrac{1}{2}\Lambda_t F_B - \tfrac{1}{2}\Lambda_s F_B$$

which reduces to

$$\tfrac{1}{2}(\Lambda_t - \Lambda_s)F_A - \tfrac{1}{2}(\Lambda_t - \Lambda_s)F_B + 2\Lambda_s A\cos(\omega t + \alpha)$$

(see section 10.6)

The term $2\Lambda_s A\cos(\omega t + \alpha) \equiv \underbrace{2\Lambda_o(1-\epsilon)A\cos(\omega t+\alpha)}_{\phi_{as}}$

If Λ_s is assumed to be constant, then the leakage reactance will be independent of saturation.

The a.c. main flux $= \phi_{ac} - \phi_{as}$

$= (\Lambda_o F_A - \Lambda_o F_B)+(\epsilon\Lambda_o F_A + \epsilon\Lambda_o F_B)\cos\omega t - 2\Lambda_o(1-\epsilon)A\cos(\omega t+\alpha)$

This reduces to

$2F_e\epsilon\Lambda_o\cos\omega t + 2\epsilon\Lambda_o A\cos(\omega t+\alpha)$, (see section 10.6)

(same result as obtained in 7.2.2.3)

and similarly ϕ_{dc}

$= (\Lambda_o\epsilon F_A - \Lambda_o\epsilon F_B)\cos\omega t + (\epsilon\Lambda_o F_A + \epsilon\Lambda_o F_B) + 2\Lambda_s F_e$

$(2\Lambda_s F_e = 2(1-\epsilon)\Lambda_o F_e)$

Two important conclusions arise from this analysis:-

(a) the leakage flux is independent of saturation, i.e. only contains terms in Λ_s.

(b) the main flux which contains $\epsilon\Lambda_o$ terms is affected by saturation.

7.2.3.2 Calculation of I_f under load conditions.

Following standard synchronous machine theory a simple method is obtained for calculating the field excitation under load conditions. With a given terminal voltage U, the internal voltage $\mathcal{S}$ is obtained from a vector diagram, Fig 89 where R= resistance of the a.c. winding and X_s' = leakage reactance.

From the open-circuit saturation curve, the field current to give $\mathcal{S}$ on open-circuit is found. The required field current(I_e) under load conditions is given by adding vectorially the currents I_μ and J, where J= load current, I_μ = field excitation to give $\mathcal{S}$ referred to the a.c. winding, I_e = field excitation on load referred to the a.c. winding. (compare with synchronous machine vector diagram, Fig 89b)

Initially calculations for I_f(on load) were made, assuming that the leakage reactance $X_s' = X_{ahg} + X_s$ (i.e. $\phi_{ac} = \phi_{ahg} + \phi_{hm} + \phi_{as}$).

For C=0, I_f (Büssing) = 5.25 amps,

(compare I_f = 4.05 amps-measured [% error 29.6%])

For C=16μF, I_f (Büssing) = 3.38 amps.

(compare I_f = 3.05 amps-measured [% error 10.8%])

For C = 16μF there is reasonable correlation between measured and calculated results; at zero compensation where the amount of saturation is greater than for C= 16μF to achieve rated output, the discrepancy between measured and calculated results increases to 29.6%.

The value of field current is critically dependent upon the value of X_s'. For various values of compensation, the angle α and field excitation were measured; from a vector diagram, the leakage reactance was calculated and compared with X_s' (Büssing), where $X_s' = (X_{ahg} + X_s)$. Over the whole range of compensation ($0 \rightarrow 0.93$ pu), the variation in leakage flux was approximately 4%, which suggests that for all practical purposes the value of leakage reactance can be assumed to be independent of saturation. (This agrees with the analysis given in 7.2.3.1) The average leakage reactance was found to be 0.76 pu, (compare X_s' (Büssing) = 1.13 pu).

If the flux component ϕ_{ahg} is considered to be part of the main a.c. flux, i.e. $X_s' = X_s$ ($\phi_{ac} = \phi_h + \phi_{as}$), then $X_s' = 0.722$ pu, which corresponds closely with the measured value. If the a.c. flux is split up into ($\phi_h + \phi_{as}$), then a correct value for X_s' is obtained, and gives correct answers for I_f on load; assuming that $X_s' = X_s$, the field current and α angle were calculated for various values of compensation, Table 28.

Table 28.

Comparison of calculated and measured values of α and I_f for rated output. (assuming $\phi_{ac} = \phi_h + \phi_{as}$)

$C\mu F$	$\alpha°$ * (calculated)	$\alpha°$ (measured)	I_f * (calculated)	I_f (measured)
36	143	145	3.4	3.6
28	140	141	3.3	3.5
16	132	134	2.9	3.05
12	124	126	2.57	2.75
8	109	111	2.26	2.4

(maximum error in α = 1.84%, maximum error in I_f=0.56%)

[* calculated from Büssing.]

From Table 28 it can be seen that very good correlation is obtained between I_f (measured) and I_f (calculated) when X_s' is equal to X_s . Measurements on the experimental machine have also shown that the correct value of X_s' is obtained by splitting the a.c. flux into ϕ_h and ϕ_{as}.

7.2.4 Fluxes linking the a.c. and d.c. windings under load conditions, taking into account permeance harmonics.

Throughout Büssing's analysis the permeance variation is assumed to be sinusoidal. Permeance harmonics will however be present, and are discussed by Büssing in an appendix. The equations for ϕ_{ac} and ϕ_{dc} which result are not suitable for calculating the

performance characteristics, but they indicate the complex nature of the flux linking the a.c. and d.c. windings when permeance harmonics are present, (section 10.4.4).

7.2.5 Calculation of I_f from main and leakage fluxes. (based on theoretical and practical work-chap 5)

The methods already described for calculating I_f are based upon overall equations which neglect the distortion in the tooth-surface and the actual flux distribution in the teeth, whereas detailed flux measurements have shown that the flux linking the a.c. winding under load conditions is mainly dependent upon the distortion at the surface; although these methods are simple and give reasonable results, it is felt that a more realistic approach would result from a calculation based upon the actual flux distribution.

The distortion in each section of the tooth surface depends on the angle α ; for the calculation outlined in this section, it is assumed that α is known.

The flux linking ϕ_{43-48} depends on the flux distribution in the stator teeth, i.e. upon the distortion at the tooth surface and the leakage fluxes, ($\overline{\phi_{43-48}} = \overline{\phi_{4-11}} + \overline{\phi_{21-28}} + \overline{\phi_{LEAKAGE}}$).
For normal operating conditions, the leakage fluxes at the leading and trailing edges of the stator teeth have little effect upon the main tooth flux, which suggests that for practical purposes the flux across (43-48) can be calculated from ϕ_{4-11} and ϕ_{21-28} . The distortion at the tooth surface depends on the ratio A/F and the angle α ; if A is assumed to be constant, i.e. the armature reaction mmf corresponding to the required load current, and various values of I_f are

chosen, then a series of flux waveforms (on load) can be drawn for each section of the surface. For each value of I_f, the flux waveform in ϕ_{4-11} and ϕ_{21-28} can be calculated by adding the flux waveforms together; from ϕ_{4-11} and ϕ_{21-28}, ϕ_{43-48} is easily calculated.

For a given load voltage, load current, power factor and series capacitor, the terminal voltage of the machine can be calculated from a simple vector diagram. The field current to give I_L is then obtained when ϕ_{43-48} (from flux waveforms) = ϕ_{43-48} (to give terminal voltage of the machine).

For the experimental machine and C= 16μF, (Rated output) terminal voltage of the machine = 510 volts (ϕ_{43-48} = 1065μWb).

To demonstrate the principle, the flux across ϕ_{43-48} was calculated for the measured value of field current (3.05 amps), instead of a series of values; [Compare ϕ_{43-48} calculated from flux waveforms =1100μWb with ϕ_{43-48} = 1065μWb from actual measurements.] I_f calculated from flux waveforms will be very close to I_f(measured), since there is only 4% difference in the fluxes.

Although this calculation gives some degree of confidence to the method, there are two main disadvantages:-

(a) the calculation of flux waveforms at the surface is tedious.

(b) for different values of series capacitor and power

factor, α alters, and the calculations have to be repeated for each section.

As a first approximation, I_f can be calculated from one of the methods already described, thus reducing the number of values of I_f to be used in the analysis.

7.2.6 Conclusions. (Büssing and 7.2.5)

From experimental data it was shown that for a wide range of compensation, the leakage reactance is independent of saturation; the measured value of X_s' corresponds closely to the X_s value calculated from Büssing, i.e. the a.c. flux can be split up into a main and leakage flux given by:- $\phi = \phi_h + \phi_{as}$. The reactance X_s can be calculated from the parameters of the machine, and the field current and α angle from a vector diagram similar to that used in synchronous machine theory. A method of calculating the field excitation based upon the actual flux distribution is also discussed; the method is tedious, but the correlation for only one value of series capacitor, suggests that the method will give a good approximation to the field current.

7.3 Calculation of α and field excitation using the concept of saturated synchronous reactance.

7.3.1 Saturation factor k_s and synchronous reactance.

It is well known that the effects of magnetic saturation are important in modifying the operating characteristics of synchronous machines. When a synchronous machine is loaded, magnetic conditions are determined by the combined influence of field and armature mmfs. The treatment of saturation under these circumstances is inherently a difficult problem requiring the use of judiciously chosen simplifying assumptions for its solution. The effects of saturation under load conditions can be taken into account with good accuracy by use of a saturation factor determined from the open circuit characteristic. The degree of saturation can be described in terms of a saturation factor k_s defined as

$$k_s = \frac{E_r \text{ (air gap)}}{E_r \text{ (o.c. curve)}}$$

For unsaturated conditions $x_{\phi ag} = x_{s(ag)} - x_\ell$

where x_ℓ = leakage reactance

$x_{\phi ag}$ = unsaturated value of magnetising reactance

$x_{s(ag)}$ = unsaturated value of synchronous reactance.

Because of the effects of saturation, the reluctance of the magnetic circuit is k_s times its unsaturated value, and the component fluxes are reduced to $1/k_s$

times their unsaturated values. Under saturation conditions

$$x_\phi = \frac{x_{\phi ag}}{k_s} = \frac{x_{s(ag)} - x_l}{k_s}$$

$$\text{and } x_s = x_l + \frac{x_{s(ag)} - x_l}{k_s}$$

This saturated value of synchronous reactance is easily calculated from the open and short circuit characteristics.

The same approach can be applied to Guy-type machines, provided that the open and short circuit characteristics are known or can be accurately calculated. In previous chapters good correlation has been obtained between the measured and calculated open-circuit curve by using a new value of ϵ based upon a whole stator main tooth. On short-circuit the pu field excitation is given by (a +X_ℓ); Fig 60 shows the calculated and measured short-circuit curves for the experimental machine. It follows that X_s can be calculated in a similar way to that described for cylindrical rotor synchronous machines; the reactance (X_s) is shown in Fig 90. As saturation increases, the value of X_s decreases fairly rapidly; for the experimental machine the decrease in X_s bears a linear relationship to the field excitation. The relationship between X_s and I_f is dependent upon the shape of the open-circuit and short-circuit curves and will not necessarily decrease linearly with an increase in field excitation. For the same tooth-slot

geometry and different airgap (0.0406 cm), X_s decreases fairly rapidly as saturation increases, but the relationship between X_s and I_f is not linear. (X_s[airgap = 0.0406cm] from o.c. and s.c. test curves on 44.4 KVA machine- A.E.I.)

7.3.2 Load vector diagrams using the concept of saturated synchronous reactance.

For zero compensation and neglecting armature resistance, the vector diagram for the machine can be drawn as shown in Fig 89.

The induced voltage is given by:-

$$E = \sqrt{I^2X_s^2 + V^2 + 2VIX_s \sin\phi}$$

7.3.2.1 Unsaturated conditions.

The field current is related to the voltage E by $E = KI_f$ and hence

$$I_f = \sqrt{\frac{I^2X_s^2 + V^2 + 2VIX_s \sin\phi}{K^2}}$$

7.3.2.2 Saturation conditions.

For saturation conditions E and X_s are functions of I_f ; the simplest way of dealing with this situation is to find E and IX_s graphically, Fig 91. For a given V and I, IX_s can be drawn for various values of X_s , i.e. IX_1 , IX_2 , etc; the correct value of E and I_f is obtained from the vector diagram when X_s for the induced voltage E and the volt drop IX_s are equal.

7.3.3 Maximum power and load angle.

For synchronous machines an angle θ_L is introduced which is called the 'load angle'; this is the angle between the induced emf and the terminal voltage. The power output is given by

$$mUI\cos\phi,$$

where U= phase volts
I= phase amps
m= number of phases.

The maximum power is delivered when $\sin\theta_L = 1$

$$\text{i.e. } N_{P_{MAX}} = \frac{mVE}{X}$$

where N_P = power output.

If a Guy-machine is supplying power to a load impedance Z, the following relationships result:-

$$E^2 = I^2\left[(X_S + Z\sin\phi)^2 + (Z\cos\phi)^2\right]$$

E^2 can also be written in the form:-

$$\frac{V^2}{E^2} + \frac{I^2}{I_{sc}^2} + \frac{2IV\sin\phi}{I_{sc}E} = 1$$

If $\gamma_P = \frac{V}{E}$ and $\chi_P = \frac{I}{I_{sc}}$ then

$$\gamma_P^2 + \chi_P^2 + 2\gamma_P\chi_P\sin\phi = 1$$

Maximum output is achieved when $\gamma_P = \chi_P = \frac{1}{\sqrt{2(1+\sin\phi)}}$

i.e. maximum output given by $\frac{E^2}{2X_S(1+\sin\phi)}$

For constant power factor, the maximum output is dependent on E and X_s. (Heating of the field windings is discussed in section 7.3.6.)

For unsaturated conditions, X_s remains constant, Fig 90; under these conditions the power output can be obtained from the following expression:-

$$\text{Power output} = I^2Z = \frac{E^2Z}{X_s^2 + Z^2 + 2X_sZ\sin\phi}$$

[For I_f = 2.5 amps, E = 565 volts, X_s = 7.21Ω , Z = 5.6Ω , $\sin\phi$ = 0.276: Power output = 17 KVA.
Compare power output = 17.4 KVA-measured (Fig 93).]

If X_s remained constant for saturated conditions (i.e. $I_f > 3$ amps for the experimental machine), then the maximum output would be given by $\frac{E_{MAX}^2}{2X_s(1+\sin\phi)}$.

(Maximum power at field excitation corresponding to E_{MAX})

From Fig 90 it can be seen that, for $I_f > 3$ amps, the value of X_s decreases with increasing field current; under these conditions, the power output can be obtained from $\frac{E^2Z}{X_s^2 + Z^2 + 2X_sZ\sin\phi}$. [I_f = 3.5 amps, power output = 33 KVA (compare 34 KVA- measured)]

For I_f = 5.25 amps (E_{MAX}), the calculated power output = 56.2 KVA. (compare 61 KVA - measured)

For $I_f > 5.25$ amps, the power output increases and is still increasing at I_f = 6.0 amps.* (I_f limited to 6.0 amps to prevent overheating of the field winding.)

From these results it can be seen that, although the maximum output depends on E, it does not necessarily coincide with E_{MAX} , since X_s also influences the maximum power output.

* see Fig 93.

With the addition of a series capacitor, the output can be increased still further (see 7.3.6 and Fig 93).

7.3.4 Load angle for the Guy-machine.

7.3.4.1 Load angle - zero compensation.

For zero compensation the load angle is given by $\theta_g = (\gamma_L - \phi)$, Fig 92a.

7.3.4.2 Load angle - series compensation.

For series compensation the load angle is given by $\theta_g = (\gamma_L + \beta_P)$, Fig 92b&c.

For the Guy-machine, the factors which affect the load angle are:-

(a) X_s

(b) power factor

(c) series capacitor.

Compare with synchronous machine running under normal conditions, where θ_L is dependent upon (a) and (b). [If a synchronous machine had a series capacitor, then θ_L would also depend on (c).]

7.3.5 Experimental work.

From the calculated open-circuit and short-circuit curves, the value of X_s was determined for various values of field excitation and compared with the results obtained from actual measurements on the machine, Table 29.

Table 29.

Comparison between calculated and measured values of synchronous reactance for various values of field current.

AT/pole	I_f amps	← measured →			calculated
		V_{pu}	$I_{sc\,pu}$	$X_{s\,pu}$	$X_{s\,pu}$
100	0.775	0.34	0.265	1.26	1.29
200	1.55	0.7	0.54	1.28	1.29
300	2.32	1.05	0.81	1.28	1.29
355	2.75	1.24	0.96	1.29	1.29
400	3.1	1.38	1.07	1.29	1.28
500	3.89	1.58	1.35	1.14	1.17
600	4.65	1.68	1.62	1.07	1.03

Good correlation exists between X_s (calculated) and X_s (measured); maximum error 4%, even for high values of saturation; the correlation is dependent upon being able to predict accurately the open-circuit and short-circuit curves. Using the concept of saturated synchronous reactance it was possible to calculate the field current and the α angle for a wide range of compensation and to compare results with measured values, Table 30.

Table 30.

Calculated and measured values of α and I_f for various values of series compensation.

(Rated output)

$C\mu F$	I_f amps (cal)	I_f amps (meas)	%error in I_f	α (meas)	α (cal)	%error in α .
No C	4.4	4.05	8.6	150	145	3.4
36	3.8	3.6	5.5	145	142	2.1
28	3.6	3.5	2.85	141	141	0
16	3.1	3.05	1.7	134	136	1.5
12	2.7	2.75	1.8	126	128	1.6
8	2.35	2.4	2.1	111	113	1.7

For zero compensation the error in calculating I_f is a maximum (8.6%); at this value of field excitation the saturation is considerable and any small errors in the calculation of X_s can lead to errors of this order. In practice a series capacitor is used to reduce the field current for a given output; at a reasonable level of compensation, i.e. about 50%, the errors are quite small, (2.5%). From the vector diagrams used in the above analysis, it was possible to calculate the load angles for various degrees of compensation, Table 31 and to compare them with measured angles.

Table 31.

Measured and calculated load angles for various values of compensation. (constant power factor).

(Rated output)

$C\mu F$	load angle θ_g (measured) (electrical deg)	load angle θ_g (calculated) (electrical deg)
8	64	66
12	63	65° 12′
16	62	62° 24′
28	54	53
36	53	52° 30′
No C	44	39

7.3.6 Choice of rating for the experimental machine.

During load tests it was obvious that the experimental machine could deliver a much higher output than its rating of 44.4 KVA without overheating; the measured output against field excitation is shown in Fig 93, for zero compensation and C = 16μF. The simple theory using the concept of saturated synchronous reactance was used to predict the field current required for these outputs; output/field current curves are shown in Fig 93. For zero compensation the theory gives good correlation up to 36% more output than the design value, and for C=16μF

where the saturation effects are not so marked, the theory gives good correlation up to 80% more output. For these large outputs the problem of heating becomes apparent and it may be impossible to run these machines for long periods.

7.3.6.1 Temperature measurements on load.

To monitor the temperatures in the windings and stator iron, thermocouples were placed in the following regions:-

(a) at the back of the core

(b) small teeth (near surface) and

(c) a.c. end-winding.

The temperature in the field winding was measured by the resistance method.

Since a) the air flow between the stator core and the outer frame is restricted considerably in the experimental machine due to the end-windings and damping connections and b) the field slot is not used to the best advantage, (26% increase in field AT/pole when only 1 damping winding used), the recorded temperatures are expected to be higher than in a standard machine of the same rating.

At 44.4 KVA (rated output), the maximum temperature rise in the field winding is 67.2°C, (C= 28μF). The temperature rise decreases when the pu compensation is increased; (47.2°C rise at 0.93pu compensation).

Maximum temperature rise in the a.c. winding is 40°C and in the core and teeth, 35°C. These temperature rises are well within the specified limits set out in BS2613. With the alternator delivering 55 KVA output, similar temperature measurements were taken, Fig 94. The core and tooth temperature rises are still reasonably low (max 45°C); the minimum temperature rise occurs at 0.45 pu compensation which corresponds to the calculated minimum overall loss in the teeth, Fig 65. For this value of compensation the temperature rise in the field and a.c. winding is within the required limits; these results show that the machine can deliver at least 25% more than its rated output without overheating. If full use is made of the d.c. slots then the temperature rise is much lower, Fig 94c; at higher values of pu compensation, the temperature rise is reduced still further. Obviously at these higher values of compensation the s.c. current will increase and adequate protection must be incorporated into the system.

Two important conclusions arise from the analysis:-

(a) A saturated value of synchronous reactance as used in normal synchronous machine theory, can be applied to the Guy-type inductor alternator. Good correlation is obtained between measured and calculated values of field current over a wide range of conditions, provided that the open-circuit and short-circuit curves are known accurately.

(b) The theory can be applied to a new design or an existing machine to see whether the machine is correctly rated. For the experimental machine the output can be increased to about 60 KW (C= 16μF) without any appreciable overheating of the field winding. The current density at this output (6.2A/mm^2) is not much higher than for rated output (5.5A/mm^2). For (C= 16μF), the machine is capable of generating 100 KVA (Fig 93), current density 10A/mm^2, and could be run at this output, provided the field coils could be kept cool.

7.3.7 Comparison of calculated and measured results for various load conditions using the concept of saturated synchronous reactance.

7.3.7.1 Constant impedance test.

Measurements of terminal voltage were taken when the machine was supplying a constant impedance load; for a range of field current values, load current and terminal voltage were measured. For various values of load current and terminal voltage, the theory was used to calculate the field current, Fig 95B.

7.3.7.2 Alternator supplying a variable impedance load, I_f constant.

(For two values of compensation, 9.6μF and 12μF)

Readings of load voltage and load current were recorded when the machine was supplying a variable

impedance load and the field current constant at 1 amp, Fig 95C&D.

7.3.7.3 V load constant (variable load and field current) 9.6μF compensation.

Readings of load current and field current were recorded while the load voltage was kept constant, Fig 95A.

In each of these three tests, good correlation exists between the calculated and measured results giving confidence in the theory.

Chapter 8.

General conclusions and comments.

Chapter 8.

General conclusions and comments.

The main objectives under consideration were:-

(a) to obtain an understanding of the flux distribution in the stator and rotor on open-circuit and on load, theoretically and by measurement.

(b) to relate this to the loss distribution in the machine.

(c) to produce a load theory for the machine.

(d) to investigate the effects of series capacitors on load.

(e) to investigate damping windings in this class of machine.

Each of these aspects is considered in detail in chapters 2-7; at each stage, experimental results are compared with the theoretical analysis.

Existing theories are somewhat empirical and restricted; the lack of detail as to the flux distribution both on open-circuit and on load, arises because these theories are expressed in overall terms. By considering the physical movement of a rotor tooth across the stator surface, a simple method was developed for predicting the flux distribution at the surface; this approach led not only to a better understanding of the behaviour of the machine, but also enabled the losses to be calculated with a greater degree of accuracy than previously achieved.

The calculation of the fluxes on open-circuit and on load is summarised in Figs 96 and 97.

At the commencement of the research programme, a detailed study was made of permeance variations in the airgap region; Teledeltos plots were made for a single slot pitch and extended to a whole stator main tooth. The derivation of ϵ using Λ_{MAX} and Λ_{MIN} is based on the dubious assumption of sinusoidal permeance variation and gives the wrong answer; a correct value for ϵ is obtained from a harmonic analysis of the actual permeance variation. The value of ϵ obtained from a whole stator main tooth gives a better prediction of the open-circuit curve; it is important that a correct value of ϵ is chosen, since it is used for calculating damping currents and the field excitation on load. The value of ϵ is dependent on the airgap configuration; experiments on 10kHz and 3kHz slotting showed that for

(a) <u>10kHz slotting,</u>

for d/g = 4 to 5 the ϵ value is a maximum and practically constant; in this region there is virtually no difference between 0° and 20° sloping side. Too much is lost at 30° slope to recommend it for practical purposes.

(b) <u>3kHz slotting</u>,

optimum value for d/g =15.

A simple approximation to the airgap permeance variation, based on Baillie, was shown to give good

agreement with Teledeltos plots; this method allows the permeance variation to be calculated easily by hand, or with a small computer programme. With this analytical method available, it is easy to derive the permeance variations for various values of s/g and t/λ . For typical 3kHz slotting a small increase in output can be obtained by decreasing t/λ from its usual value of 0.4 to 0.35, but this causes a large increase in 2nd harmonic flux content (and the associated losses). For a constant t/λ and varying s/g, the pu permeance for the tooth-opposite-slot position changes little compared with the tooth-opposite-tooth position. The Baillie method could be extended to other problems involving overall permeance variations (as opposed to detailed variations at one point in the airgap).

Without damping, large voltages are induced in a field coil on open-circuit; these voltages are caused by asymmetry of the permeance variation over a cycle, and show the need for damping windings on open-circuit.

Analysis of the flux distribution at the stator tooth surface on open-circuit, showed that a considerable amount of harmonic flux is present in small sections of the surface; these fluxes cause additional losses in the tooth surface. The harmonic fluxes can be predicted from the tooth-slot geometry and Teledeltos plots. For 3kHz machines, the slope of side of the flux waveform is 10°.

The harmonic fluxes which appear in each section of the surface, combine in such a way that the harmonic content over the total tooth surface is small; the addition of these fluxes using a harmonic reduction factor K_{Dn}, is analogous to the breadth factor arising from the distribution of a winding in a machine.

Since losses at these frequencies are proportional to $f^{1.5}B^2$, the losses in a small section of the surface can be calculated and compared with the fundamental loss. An average extra loss factor derived for the stator teeth, enables the true loss in the teeth to be calculated. For the experimental machine, the true loss in the teeth is 21% greater than the loss based upon fundamental flux.

Harmonic fluxes are also present in the core region, their pattern being determined by the tooth-slot geometry and the amount of saturation in various parts of the core. Fundamental fluxes are reasonably well behaved; most of the fundamental flux passes behind the a.c. slots, resulting in a non-linear flux distribution across the whole stator main teeth. The fundamental flux which passes behind the field slots is small, (approximately 2.4% of the main a.c. flux). Second harmonic flux components are particularly sensitive to changes in field excitation; assumed flux paths for the second harmonic components, (verified by experimental results) can be used to predict the second harmonic fluxes linking the a.c. and d.c. windings.

Without damping, large voltages are induced across a field coil; these voltages tend to cancel each other out around the machine, resulting in a small induced voltage across the total winding. Damping windings are very effective in damping these voltages; top damping windings which have a lower reactance than either bottom or core damping windings are the most effective, and for the experimental machine, reduce the induced voltage in a field coil to approximately 1.5% of the voltage without damping.

For unsaturated conditions the flux linking the a.c. winding is not affected by damping, and the damping currents required to damp the fluxes linking the field winding are small.

The detailed analysis of flux distribution on open-circuit, coupled with experimental results, gave confidence to the theory, and formed the basis for analysing the flux distribution in the stator on-load, and in the rotor.

Under load conditions, the flux waveform in a small section of the surface is distorted from its open-circuit shape, due to the effects of armature reaction; the amount of distortion is dependent upon the angle α and upon the ratio A/F.

The distortion in each section of the surface is different, since each small section across the surface is displaced by an angle $(\delta_q \pm \beta_c)$ from the load current waveform; [for a particular instant of time, the armature reaction mmf acting on the airgap permeance

for each small section is different.] At the leading edge of the stator tooth, the armature reaction is demagnetising for the maximum permeance condition, and at the trailing edge, the armature reaction is magnetising. The mean flux density is affected by the distortion; at the leading edge, the mean density is reduced by approximately 17%, whereas the mean density at the trailing edge remains substantially constant, (true for varying C). The addition of fluxes at the tooth surface is more complex than on open-circuit, since the harmonic flux components in each section are different in magnitude; K_{pn} factors on-load are dependent upon the value of series capacitor and load power factor. Extra loss factors for the teeth can be calculated from the flux waveforms at the surface; as the amount of compensation is reduced, the loss factors also decrease, but the field current increases considerably. In reducing the losses in the teeth and increasing the field winding losses, a compromise must be sought which ensures that the field does not overheat, and yet which keeps the losses in the small teeth to a reasonable level. Calculation of the total losses in the teeth for various values of series compensation enable an optimum value of series capacitor to be chosen. If the ratio t/λ is altered, this will also affect the distortion at the tooth surface; since the distortion is also dependent upon the value of series capacitor and load power factor, the optimum value of $t/\lambda = 0.4$ may not be the optimum

value on load, (section 5.5.2).

Detailed flux measurements in the stator core showed the complex nature of the flux distribution; although calculations for the harmonic fluxes are difficult and tedious, overall equations can be used to predict damping currents and the induced voltage in a field coil without damping.

Although there is a considerable amount of harmonic flux in the teeth under load conditions, the harmonic content in the core region is fairly low; losses in the core region can be calculated with a good degree of accuracy from a consideration of the fundamental loss.

If the machine is run on-load without damping windings, a large voltage is induced across a field coil (for the experimental machine, V (peak)=1040volts at rated output). Damping windings are very effective on load and reduce the peak voltage across a field coil to approximately 1.4% of the voltage induced without damping; top damping windings are the most effective. The damping currents on load are larger than on open-circuit, but the I^2R loss is negligible compared with the other losses in the machine.

On short-circuit, without a series capacitor, the angle α approaches 180°. With a series capacitor the flux at certain points on the tooth surface is reduced to a low level, due to the cancelling of the

main flux by armature reaction. For no series capacitor, vector diagrams of how the fluxes combine at the surface are similar to the no-load diagrams; with a series capacitor the diagrams become very distorted.

Using the detailed knowledge of flux distribution on the stator, and relating sections on the rotor tooth surface to a given reference on the stator, the flux waveforms on the rotor surface can be calculated. Theoretical and measured results showed the similarity between stator and rotor flux waveforms under open-circuit, load and short-circuit conditions.

The rotor is subjected to heteropolar flux, due to the reversal of the mean flux component under successive d.c. poles; frequencies of ($f_{MACHINE} \pm f_h$), $3f_h$ and $7f_h$ are also superimposed on this waveform due to the slot openings. Analysis of the flux waveform across the total tooth surface, coupled with an approximation for the surface loss, leads to a more accurate estimation of the rotor losses than previously achieved. On open-circuit, the true loss is approximately 60% greater than the normal calculated loss.

Although no experimental data was available for the rotor core, an estimation of the losses can be made by considering the flux distribution over two adjacent rotor teeth. Results showed that previous loss calculations based upon a 3000Hz and 300Hz component, account for about 90% of the true loss in the core.

On-load and open-circuit waveforms across the total tooth surface are very similar in shape; due to the increase in leakage flux on-load, there was approximately a 30% increase in fundamental flux in the root of the teeth. Flux waveforms in the rotor are affected by the value of series capacitor and load power factor. For each α angle, the rotor flux waveforms and the rotor tooth position can be related to the stator surface, enabling the flux density variation to be plotted for various rotor positions.

To obtain the correct answers in design work, the total calculated losses are usually multiplied by a factor K_L , where $K_L \triangleq 1.3\text{-}1.4$; for the experimental machine $K_L \triangleq 1.26$ (average value for various values of C). Flux measurements and analysis, have showed the presence of harmonic fluxes and their effect upon the losses; the above figures suggest that, a loss calculation based upon an understanding of the flux distribution, will lead to a loss figure which will give results comparable to the actual loss.

The calculation of field current under load conditions can be considered under four main headings:-

(a) Simple theory based upon the work of Raby and Pohl.

For the calculation of field current, the synchronous reactance is assumed to be constant; for values of field excitation where this condition holds true, the analysis gives good results which compare favourably with measured values. For further increases

in field current, (decreasing compensation to achieve rated output) the value of X_s decreases due to saturation. If X_s is assumed to be constant for these values of field current, then errors of about 40% can be expected between measured and calculated values. A small change in X_s has little effect upon the angle α; for a wide range of series compensation (0-93%) the analysis provided a simple method for calculating this angle.

(b) Büssing.

Büssing's analysis includes the effects of leakage flux and saturation. For the whole range of compensation the leakage reactance is independent from saturation. The leakage reactance can be calculated from the parameters of the machine; the field current and angle is then obtained from a vector diagram similar to that used in synchronous machine theory.

(c) Flux waveforms.

The value of I_f can also be calculated from the flux waveforms at the surface provided α and ϕ_{43-48} is known. The method is tedious, but gives a good approximation to the field current.

(d) Saturated synchronous reactance.

If the open-circuit and short-circuit characteristics are known accurately, the synchronous reactance for varying I_f can be calculated; the field current and α angle is then calculated from a vector

diagram. The theory can be applied to a new design or an existing machine, to see whether the machine is correctly rated.

Chapter 9.

References and Acknowledgments.

9.1 Symbols.

9.2 Bibliography.

9.3 Acknowledgments.

9.1 List of symbols.

ϕ_t - flux defined in a whole stator main tooth for the stator tooth opposite rotor tooth position. (Wb)

ϕ_s - flux defined in a whole stator main tooth for the stator tooth opposite rotor slot position. (Wb)

ϕ - constant d.c. flux across a pole pitch. (Wb)

C - Carter coefficient.

s - width of small slot. (cm)

g - airgap. (cm)

c' - correction coefficient, (Pohl).

β - fictitious angle of sides of rectangular slots,(Pohl)

t - width of small tooth. (cm)

λ - rotor slot pitch. (cm)

ϵ - flux utilisation coefficient.

f - frequency. (Hz)

v - peripheral speed of the rotor, (m/sec)

λ_p - pole pitch, (cm)(Raby).

ϕ_{ac} - a.c. flux. (Wb)

A - peak a.c. ampere turns/pole.

F_o - field ampere-turns to give rated open circuit volts.

a - defined as $A/F_o\epsilon$.

E - terminal voltage. (volts)

I - load current. (amps)

y - odd integer.

x - small teeth/main tooth.

Λ - total permeance variation.

Λ_o - mean permeance.

F - field mmf. (ampere-turns)

N - total number of series turns in high frequency winding.

Λ_{max} - maximum permeance (rotor and stator teeth opposite)

Λ_{min} - minimum permeance (rotor tooth opposite stator slot)

d - depth of slot. (cm)

ω - angular frequency. (radians/sec)

Λ_n - nth harmonic permeance.

ϵ_n - Λ_n/Λ_o.

ξ_n - coefficient relating the nth harmonic flux variation and the mmf over a half cycle as tooth A moves from the $\phi_t \rightarrow \phi_s$ position.

ξ'_n - coefficient relating the nth harmonic flux variation and the mmf over a half cycle as tooth A moves from the $\phi_s \rightarrow \phi_t$ position.

θ - angle between the centre line of a small stator tooth and the centre line of a rotor tooth. (electrical deg)

v - harmonic voltage (peak) in a field coil for rated open circuit voltage. (volts)

m - number of sections in the tooth surface.

θ_s - slope of side of the slots. (degrees)

σ - $n\psi$.

n - harmonic order.

ψ - phase displacement between sections on the tooth surface. (degrees)

K_{dn} - harmonic reduction factor.

a, b, α - parameters for waveform analysis.

k - extra loss factor.

B - flux density. (Wb/m^2)

D_m - peak value of the damping ampere turns/pole, mth harmonic.

β_m - phase angle between the peak of the mth harmonic damping current and the peak permeance. (electrical degrees).

ϕ'_{ac} - a.c. flux with damping. (Wb)

ϕ'_{dc} - d.c. flux with damping. (Wb)

$2\phi_D$ - damping flux. (Wb)

α - phase angle between the peak permeance and the peak current. (electrical deg)

Λ_R - mean permeance as seen by a small section of the surface.

Λ_q - minimum permeance as seen by a small section of the surface.

Λ_p - maximum permeance seen by a small section of the surface.

'x' - displacement of the stator and rotor teeth, (electrical degrees).

δ - phase angle between the peak value of the load current and the centre line of the maximum flux level period in the appropriate small section. (electrical deg)

β_c - displacement in electrical degrees from the centre line of the maximum flux level period in a particular section on the surface.

$\angle$ - phase angle between the peak of the total flux waveform across the surface and the peak of the load current waveform.(electrical deg)

a, b, c, d ----- - fundamental loss in each section of the tooth surface. (watts)

K_a, K_b ------ - loss factors under load conditions for the respective sections.

K_o - overall loss factor for the tooth surface under load conditions.

K_A - overall loss factor for the small tooth region under load conditions.

$K_{D_{sc}}$ - harmonic reduction factor for short circuit.

X_l - slot leakage reactance. (ohms)

V - load voltage. (volts)

E_{oc} - voltage on open circuit with field excitation applied to give rated load current. (volts)

$\cos\phi$ - power factor.

ψ_L - angle between E and I. (degrees)

X_S - synchronous reactance. (ohms)

F_R - resultant field due to F and A. (ampere-turns)

k_S - saturation factor.

$x\phi_{ag}$ - unsaturated value of magnetising reactance. (ohms)

x_{sag} - unsaturated value of synchronous reactance. (ohms)

x_S - saturated value of synchronous reactance. (ohms)

θ_L - load angle for synchronous machines. (elect deg)

U - phase volts. (volts)

m_p - number of phases.

N_p - power ($m_p VE \sin\theta_L / X$). (watts)

Z - load impedance. (ohms)

ψ_p - V/E .

x_p - I/I_{sc} .

V_T - terminal voltage of the machine. (volts)

θ_g - load angle for the Guy-machine. (elect deg)

β_p - phase angle between terminal voltage of the machine and the load current I. (degrees)

x_a - leakage reactance (synchronous machine).(ohms)

x_A - fictitious reactance which replaces the effect of armatute reaction. (ohms)

X_S - ($x_a + x_A$) , synchronous machine. (Ohms)

E'_a - open circuit voltage corresponding to the excitation F on the open circuit curve. (volts)

r - resistance of a.c. winding,(synchronous machine)

E_{fc} - voltage induced in a single field coil on load, without damping. (volts)

N_{fc} - number of turns in a single field coil.

K_L - total loss factor for the machine.

ϕ_a - maximum flux in a small section of the tooth surface on open circuit, for a given value of field excitation. (Wb)

ϕ_b - minimum flux in a small section of the tooth surface on open cicuit, for a given value of field excitation. (Wb)

q - slots/pole.

f_h - heteropolar frequency. (Hz)

f_{RS} - frequency of fluxes at the rotor tooth surface.(Hz)

P_{dc} - number of d.c. poles.

List of symbols. (applied particularly to Büssing)

μ_o - absolute permeability. (H/m)

l_1 - effective length of the core.(cm)

Z_2 - number of stator teeth per d.c. pole half.

$\Delta\phi$ - resultant flux linking the a.c. winding. (Wb)

ω_a - series turns in a.c. winding.

ϕ_{hm} - main a.c. flux. (Wb)

ϕ_{ahg}, ϕ_{as} - leakage fluxes. (Wb)

U - terminal voltage. (volts)

R - resistance of the a.c. winding. (ohms)

J - load current. (amps)

$\mathcal{E}$ - internal voltage. (volts)

I_μ - field excitation corresponding to $\mathcal{E}$. (amps)

I_e' - field excitation under load conditions referred to the a.c. winding. (amps)

Z_{na} - number of conductors/a.c. slot.

N_z - number of a.c. slots.

g - $\sqrt{2}\, Z_{ne} / Z_{na}$.

F_1 - mmf at the airgap. (ampere-turns)

F_z - mmf at the stator and rotor teeth. (ampere-turns)

X_{hm}, X_{ahg} } reactances. $\left(K Z_{na}^2 (\Lambda_t - \Lambda_s)/2.\right)$ (ohms)

X_s - reactance given by $K Z_{na}^2 2\Lambda_s$. (ohms)

X_s' - $X_s + X_{ahg}$. (ohms)

I_e - field excitation under load conditions. (amps)

9.2 Bibliography.

1. GIBBS W.J. 'Electric machine analysis using matrices', Pitman.

2. O'KELLY D., SIMMONS S. 'Introduction to generalised electrical machine theory', Mc GRAW-HILL.

3. British patent No 18027, (1901).

4. German patent DRP 303321.

5. DAVIES E.J., LAY R.K. 'Stator flux distributions in Lorenz-type medium frequency inductor alternators', Proc I.E.E., vol 113, No 12, Dec 1966, p2023-2030.

6. DAVIES E.J., LAY R.K. 'Rotor surface flux distributions in Lorenz-type medium frequency inductor alternators', Proc I.E.E., vol 114, No 9, Sept 1967, p1251-1259.

7. DAVIES E.J., LAY R.K. 'Performance of Lorenz-type medium frequency inductor alternators on load', Proc I.E.E., vol 115, No 12, Dec 1968, p1791-1800.

8. BÜSSING N. 'Das Betriebsverhalten Der Guy-Maschine', Elektrotechnik und Maschinenbau, No 9, vol 76, 1959, p199-203; No 10, vol 76, p219-223.

9. LAFFOON C.M. 'H-F alternators', Electric Journal, vol 21, 1924, p416.

10. PATTEN F.J. 'Special types of alternator', Elect World and Engineer, vol 33, 1899, p648-649.

11. BETHENOD J. 'High frequency alternators and their regulation', Soc. Franc. Elect, Bull.9 p161-176, March 1919; Rev Gen.d'El.5, p787-793, May 1919.

12. GOLDSCHMIDT R. 'High frequency alternator for radiotelegraphy', Elektrotech. Zeitschr.(32), p 54-56, 1871; (66), p 744-746, Feb 1911.

13. LAY R.K. 'The history and changing fortunes of the inductor alternator', Paper read before the South Midland, the Mersey and North Wales,and the Sheffield Graduate and Student Sections of the I.E.E. 1966/67.

14. CHUBB L.W., ALLCOTT C.T. 'The foundations of modern radio', Electric Journal, vol 18, p120, 1921.

15. LAMME B.G. 'Data and tests on a 10,000 Hz alternator', Trans A.I.E.E., vol 23, 1904, p417.

16. ALEXANDERSON E.F.W. 'Alternator for 100,000 Hz', Trans A.I.E.E., vol 28, pt1, 1909, p399.

17. British patent No 554827 (1941).

18. RABY K.F. 'Inductor alternators for 10kHz', Students Quarterly Journal, I.E.E. Sept 1950,p15.

19. CARTER F.W. 'Magnetic field of the dynamo-electric machine', J.I.E.E., vol 64, 1926, p1115-1138.

20. GIBBS W.J. 'Conformal transformations in electrical engineering', Chapman and Hall,1958.

21. COE R.T., TAYLOR H.W. 'Some problems in electrical machine design involving elliptic functions', Phil.Mag., 6 (1928) p100-145.

22. WALKER J.H. 'The theory of the inductor alternator', J.I.E.E. pt1, 1942, p227-241.

23. WALKER J.H. 'High frequency alternators', J.I.E.E., pt2, 1946, p67.

24. POHL R. 'Theory of pulsating field machines', J.I.E.E., vol 93, 1946, p37-47.

25. MANDL A. 'Short-circuit characteristics and load performance of inductor type alternators', J.I.E.E., vol 94, 1947, p102-117.

26. BUNEA V. 'Theory of medium frequency pulsating field machines', Proc I.E.E., vol3, 1964, p1324-1332.

27. BUNEA V. 'Magnetic skin effects in medium frequency machines', Proc I.E.E. vol 117, No 7, July 1970,p1303-1308.

28. MARCHBANKS M.J. 'High frequency generators for induction furnaces', J.I.E.E. (93) p 520. 1946.

29. BAILLIE T.C. 'A diagram of correction coefficients for airgap reluctances', The Electrician, Oct 1908-April 1909, vol LXII,p494-5.

30. DAVID R. 'Calcul des machines electriques tournantes ', Ecole Superieure d'Electricite, 1954, p56-59.

31. LAY R.K. 'A theoretical and practical study of the Lorenz-type inductor alternator', PhD Thesis, April 1967.

32. ASZTALOS P. 'Sudden short-circuit current of inductor alternators', Periodica Polytech., Elect Engng.(Hungary), vol 8, No 3,p275-91., March 1964.

33. BS 2613, 1957, 'The electrical performance of rotating electrical machinery'.

34. WALKER J.H. 'Slot ripples in alternator emf waves', J.I.E.E. vol 96, 1949, p81-92.

35. SAY M.G. 'The performance and design of alternating current machines.' Pitman.

36. HELE-SHAW H.S., HAIG A., POWELL P.H., 'Hydrodynamical and electromagnetic investigations regarding the magnetic flux distribution in toothed core armatures', J.I.E.E. vol XXXIV, 1904-05, p 21-50.

37. WALL T.F. 'The reluctance of the airgap in dynamo Machines', J.I.E.E., vol 40, 1907-08, p 550-76.

38. VITKOVITCH D. 'Experimental and computational analysis', Van Nostrand, 1966.

39. ROSS D.S., QURESHI I.H. 'The conducting paper analogue and its application to the solution of the Laplace's and Poisson's equations', J. Scientific Inst. vol 40, Nov 1963,p513-518.

40. LIEBMANN G. 'Electrical analogues', British Journal Applied Physics, vol 4, 1953, p193-197.

41. BINNS K.J. 'Calculation of some basic flux quantities in induction and other doubly-slotted electrical machines', Proc I.E.E. 1964, III, No 11, p1847.

42. Mc CURLEY E.T. 'High frequency inductor alternators', (abstract of paper read before east Midland section on 17th Feb 1953).

43. ALEXEVA M.M. 'Advanced calculation for machine generators', 'Energy' Lenningrad section.

44. KOUBA C.C. 'Magnetic force unbalance and flux distribution in inductor alternators', Intersociety energy conversion engineering conference 3rd, Colorado. 1968 vol 13-17 Aug, I.E.E.E. New York.

45. ALPER N.Y., TERZYAN A.A. 'Steady-state processes in inductor machines having pulsating fluxes', Elektrotekhnika (USSR) 1966, No 9, (In Russian).

46. ALPER N.Y., TERZYAN A.A. 'Taking saturation into account with pulsating flux inductor machines', Elektrotekhnika (USSR) 1967, No 1, (In Russian).

47. ROBERTSON B.L. 'Analytical determination of magnetic fields', Trans Amer, Inst Elec Engineers, 1929 (48) , p1242.

48. APSIT V.V. 'Contactless electrical machines', Riga, USSR. (In Russian).

49. WIESMAN R.W. 'Graphical determination of magnetic fields', Trans A.I.E.E. 1927 (46) p141.

50. STEVENSON A.R. , PARK R.H. 'Graphical determination of magnetic fields', Trans A.I.E.E. 1927, (46) p112.

51. AHAMED S.V., ERDELYI E.A., HOPKINS R.E., 'Non linear theory of heteropolar electrical machines', I.E.E.E. Trans Aerospace, 1965, AS-3, No 2, p32-39.

9.3 Acknowledgments.

Firstly the author wishes to acknowledge the continuous advice and encouragement given by Professor E.J. Davies, Professor in Electrical Engineering, the University of Aston in Birmingham, who has supervised the work from which this thesis is drawn.

The author also wishes to thank the following:-

Mr E.Beedham (A.E.I. Rugby) for helpful discussion at the design stage.

Mr C Partridge for invaluable work in connection with assembling and instrumenting the experimental machine; in particular for producing the search coil stack on the stator.

Chapter 10. Appendices.

10.1 Pohl's approximation to airgap permeance variation.

10.2 Waveform analysis.

10.3 Permeance calculations- Baillie.

10.4 Fluxes linking the a.c. and d.c. windings on load.

10.4.1 No damping.

.2 With damping.

.3 No damping (including permeance harmonics).

.4 Including permeance harmonics-Büssing.

10.5 Damping currents under load conditions.

10.6 Main and leakage fluxes- Büssing.

10.1 Pohl's approximation to airgap permeance variation.

For the position of coincidence of the tooth axes, i.e. x=0, the specific airgap permeance is given by:-

$$\Lambda_t = t/g + \frac{2.3}{\beta} \log(1 + \beta s/g)$$

For the position of coincidence of stator-tooth and rotor-slot axes, i.e. for x= (s + t)/2

$$\Lambda_s = \frac{s-t}{g + \beta\frac{(s-t)}{2}} + \frac{9.2}{\beta} \log \frac{(1 + \beta s/2g)}{(1 + \beta\frac{(s-t)}{2g})}$$

There are in principle four kinds of field area, A,B,C, D, not necessarily all present at a given moment, Fig 4. The area A is bordered by peripheral iron surfaces and the length of flux path is constant; the permeance is (t- x)/g. The two areas B are bordered by one peripheral and one radial surface. Their combined permeance is given by:-

$$2\int_0^x \frac{dr}{g + \beta r} = \frac{2}{\beta} \log\left[\frac{g + \beta x}{g}\right]$$

The two areas C, bordered only by radial surfaces, similarly supply a logarithmic function as their contribution to the permeance, namely

$$2\int_x^{s/2} \frac{dr}{g + \beta r + \beta(r-x)} = \frac{1}{\beta} \log\left[\frac{g + \beta(s-x)}{g + \beta x}\right]$$

The part D, bordered by radial surfaces at opposite sides has, like A, a constant length of flux path,

namely $\beta(s-x)$ and contributes

$$\int_{s/2-x}^{s/2} \frac{dr}{g+\beta(s-x)} = \frac{x}{g+\beta(s-x)}$$

The permeance equations for the half cycle are given below:-

For $0 \leq x \leq s/2$

$$\bigwedge = \frac{t-x}{g} + \frac{4.6}{\beta}\left[\log \frac{g+\beta x}{g} + \tfrac{1}{2}\log \frac{g+\beta(s-x)}{g+\beta x}\right] + \frac{x}{g+\beta(s-x)}$$

For $s/2 \leq x \leq t$

$$\bigwedge = \frac{t-x}{g} + \frac{4.6}{\beta}\left[\log \frac{g+\beta s/2}{g} + \log \frac{g+\beta s/2}{g+\beta(s-x)}\right] + \frac{s-x}{g+\beta(s-x)}$$

For $t \leq x \leq \frac{s+t}{2}$

$$\bigwedge = \frac{4.6}{\beta}\left[\log \frac{g+\beta s/2}{g+\beta(x-t)} + \log \frac{g+\beta s/2}{g+\beta(s-x)}\right] + \frac{s-x}{g+\beta(s-x)} + \frac{x-t}{g+\beta(x-t)}$$

(compare with simple equations given by Baillie method, 10.3)

10.2 Waveform analysis.

The harmonic content of experimental waveforms was analysed using a main computer program (AMH1) and a Fourier subroutine program taken from ' Fortran- Engineering Applications. '

Details of main computer program (Fortran)

C WAVEFORM ANALYSIS AMH1 14 8 69

```
      INTEGER N2,POINTS
      REAL F(100),F0,A0,A(50),B(50)
      COMMON/X1/N2,F,F0,A0,A,B
      N=25
    2 READ(1,100)N2
      POINTS=2*N-1
      READ(3,101)F0,(F(K),K=1,POINTS)
      CALL FOURN
      PAUSE 1
      READ(1,102)XDASH
    3 READ(1,102)X
      IF(X.LT.0.0)GOTO 2
      XD=X/XDASH
      ARG=6.2831853*XD
      Y=A0*.5
      I=N2-1
      DO 4 K=1,I
      RK=K
    4 Y=Y+A(K)*COS(RK*ARG)+B(K)*SIN(RK*ARG)
      WRITE(2,103)X,Y
      GOTO 3
  100 FORMAT(12)
  101 FORMAT(F8.3)
  102 FORMAT(F6.4)
  103 FORMAT(3H X=,F6.4,5H     Y=,F8.3)
      END
```

10.3 Permeance calculations. - Baillie

For a single-slot pitch the permeances Λ_{MAX} and Λ_{min} can be calculated easily from Carter or Pohl. Between these two symmetrical positions one has to distinguish three sections with different equations for the permeance variation, because they meet at points of mathematical discontinuity; these sections are defined as (a) $0 \leq x \leq s/2$, (b) $s/2 \leq x \leq t$ and (c) $t \leq x \leq (s+t)/2$. If the permeance variation is taken over a whole stator main tooth and account is taken of the chamfer at the tooth edge, then 6 equations are necessary. The equations for an airgap geometry similar to that for the experimental machine are given below and were used to predict the curves in Figs12 and 13.

It is convenient to express the permeance equations in terms of m and K where $m=s/g$ and $K=s/t$.

Regions for permeance calculation defined as:-

(a) $0 \leq x \leq 0.15t$	$x=0$ corresponds to Λ_1
(b) $0.15t \leq x \leq s/2$	$x=0.15t$ corresponds to Λ_2
(c) $s/2 \leq x \leq t$	$x=s/t$ corresponds to Λ_3
(d) $t \leq x \leq t+0.15t$	$x=t$ corresponds to Λ_4
(e) $t+0.15t \leq x \leq \frac{s+t}{2}$	$x=t+0.15t$ corresponds to Λ_5
	$x=\frac{s+t}{2}$ corresponds to Λ_6

Permeance equations.

$$\Lambda_1 = m/K \left[2.0+0.3/(1+0.2m)+(2K-0.3)/(1+0.4m)\right]$$

$$\Lambda_2 = m/K \left[1.85+0.6/(1+0.2m)+(2K-0.45)/(1+0.4m)\right]$$

$$\Lambda_3 = m/K \left[2.15-K+2K/(1+0.2m)+(K-0.15)/(1+0.4m)\right]$$

$$\Lambda_4 = m/K \left[0.15+4/(1+0.2m)+(2K-2.15)/(1+0.4m)\right]$$

$$\Lambda_5 = m/K \left[4.45/(1+0.2m)+(2K-2.3)/(1+0.4m)\right]$$

$$\Lambda_6 = m/K \left[4.3/(1+0.2m)+(2K-2.3)/(1+0.4m)\right]$$

The calculation of permeance for varying s/g and t/λ is made easy by the use of a simple computer program.

'Focal' program for Λ_3.

```
C    PERM 3
1.1    T  "  M        P3     "!
1.2  ASK  K,MMIN,DM,MAX
1.3  FOR  M=MMIN,DM,MMAX;DO 2
1.4  QUIT
2.1 SET P3=(m/K)*<[2.15-K]+2*K/[1+0.2m]
     +[K-0.15]/[1+0.4m]>     (same line as 2.1 )
2.2  T  %2.00,M,"    ",P3,!
2.3  RETURN.
```

10.4 Fluxes linking the a.c. and d.c. windings on load.

10.4.1 Neglecting damping.

$$\phi_A = \Lambda_o\left[F + A\cos(\omega t + \alpha)\right]\left[1 + \epsilon\cos\omega t\right]$$

$$\phi_B = \Lambda_o\left[-F + A\cos(\omega t + \alpha)\right]\left[1 - \epsilon\cos\omega t\right]$$

$$\phi_A = \Lambda_o\left\{F + F\epsilon\cos\omega t + A\cos(\omega t + \alpha) + \frac{A\epsilon}{2}\cos\alpha + \frac{A\epsilon}{2}\cos(2\omega t + \alpha)\right\}$$

$$\phi_B = \Lambda_o\left\{-F + F\epsilon\cos\omega t + A\cos(\omega t + \alpha) - \frac{A\epsilon}{2}\cos\alpha - \frac{A\epsilon}{2}\cos(2\omega t + \alpha)\right\}$$

ϕ_{Dc} is given by $\phi_A - \phi_B$

$$= \Lambda_o\left[2F + A\epsilon\cos\alpha + A\epsilon\cos(2\omega t + \alpha)\right]$$

$$\phi_{ac} = \phi_A + \phi_B$$

$$= \Lambda_o\left[2F\epsilon\cos\omega t + 2A\cos(\omega t + \alpha)\right]$$

10.4.2 With damping.

$$\phi_A = \Lambda_o\left\{F + A\cos(\omega t + \alpha) + D\cos(2\omega t + \beta)\right\}\left\{1 + \epsilon\cos\omega t\right\}$$

$$\phi_B = \Lambda_o\left\{-F + A\cos(\omega t + \alpha) - D\cos(2\omega t + \beta)\right\}\left\{1 - \epsilon\cos\omega t\right\}$$

$$\phi_A = \Lambda_o\left\{F + F\epsilon\cos\omega t + A\cos(\omega t + \alpha) + \frac{A\epsilon}{2}\cos\alpha + \frac{A\epsilon}{2}\cos(2\omega t + \alpha) + D\cos(2\omega t + \beta) + \frac{D\epsilon}{2}\cos(3\omega t + \beta) + \frac{D\epsilon}{2}\cos(\omega t + \beta)\right\}$$

$$\phi_B = \Lambda_o\left\{-F + F\epsilon\cos\omega t + A\cos(\omega t + \alpha) - \frac{A\epsilon}{2}\cos\alpha - \frac{A\epsilon}{2}\cos(2\omega t + \alpha) - D\cos(2\omega t + \beta) + \frac{D\epsilon}{2}\cos(3\omega t + \beta) + \frac{D\epsilon}{2}\cos(\omega t + \beta)\right\}$$

neglecting terms above 2nd harmonic:-

$$\phi_{Dc} = \Lambda_o\left[2F + A\epsilon\cos\alpha + A\epsilon\cos(2\omega t + \alpha) + 2D\cos(2\omega t + \beta)\right]$$

$$\phi_{ac} = \Lambda_o\left[2A\cos(\omega t + \alpha) + 2F\epsilon\cos\omega t + D\epsilon\cos(\omega t + \beta)\right]$$

10.4.3 Analysis with permeance harmonics.

(assuming sinusoidal load current)

$$\phi_A = \Lambda_o\left[F+A\cos(\omega t+\alpha)\right]\left[1+\sum \epsilon_n \cos n\omega t\right] \qquad n=1,2,3\_\_\_\_\_$$

$$\phi_B = \Lambda_o\left[-F+A\cos(\omega t+\alpha)\right]\left[1+\sum \epsilon_n (-1)^n \cos n\omega t\right] \qquad n=1,2,3\_\_\_\_\_$$

$$\phi_{DC} = \Lambda_o\left[2F + F\sum \epsilon_n(1+(-1)^n)\cos n\omega t + \sum A\epsilon_n(1-(-1)^n)\cos n\omega t \cos(n\omega t+\alpha)\right]$$

and

$$\phi_{ac} = \Lambda_o\left[2A\cos(\omega t+\alpha) + F\sum \epsilon_n(1-(-1)^n)\cos n\omega t + \sum A\epsilon_n(1+(-1)^n)\cos n\omega t\cos(n\omega t+\alpha)\right]$$

10.4.4 Load analysis- Büssing.

$$\Lambda_t = \Lambda_o(1+\epsilon_1\cos\omega t + \epsilon_2\cos 2\omega t + \epsilon_3\cos 3\omega t\_\_\_\_\_)$$

$$\Lambda_s = \Lambda_o(1-\epsilon_1\cos\omega t + \epsilon_2\cos 2\omega t - \epsilon_3\cos 3\omega t\_\_\_\_\_)$$

$$\phi_t = \Lambda_o\left[F_e + A_1\cos(\omega t+\alpha_1) + A_3\cos(3\omega t+\alpha_3)\_\_\_\_\_\right]\left[(1+\epsilon_1\cos\omega t + \epsilon_2\cos 2\omega t + \epsilon_3\cos 3\omega t\_\_\_\_)\right]$$

$$\phi_s = \Lambda_o\left[F_e - A_1\cos(\omega t+\alpha_1) - A_3\cos(3\omega t+\alpha_3)\_\_\_\_\_\right]\left[(1-\epsilon_1\cos\omega t + \epsilon_2\cos 2\omega t - \epsilon_3\cos 3\omega t\_\_\_\_)\right]$$

$$\phi_{ac} = \phi_t - \phi_s$$

$$= \Lambda_o\left[(1+\sum \epsilon_n\cos n\omega t)(F_e + \sum A_m\cos(m\omega t+\alpha_m))\right] - \Lambda_o\left[(1+\sum (-1)^n\epsilon_n\cos n\omega t)(F_e - \sum A_m\cos(m\omega t+\alpha_m))\right]$$

$n=1,2,3,4\_\_\_\_$ $\quad m=1,3,5,7\_\_\_\_$

$$\phi_{DC} = \phi_t + \phi_s$$

$$= \Lambda_o(1 + \sum \epsilon_n \cos n\omega t)(F_e + \sum A_m \cos(m\omega t + \alpha_m)$$

$$+ \Lambda_o(1 + \sum (-1)^n \epsilon_n \cos n\omega t)(F_e - \sum A_m \cos(m\omega t + \alpha_m)$$

$$\phi_{ac} = \Big[\Lambda_o 2\epsilon_1 \left[F_e \cos\omega t + A_1 \cos(\omega t + \alpha_1) \right]$$
$$+ 2(1-\epsilon_1)\Lambda_o A_1 \cos(\omega t + \alpha_1)$$
$$+ \Sigma_1 + \Sigma_1'$$
$$+ 2\Lambda_o \epsilon_3 F_e \cos 3\omega t + A_3 \cos(3\omega t + \alpha_3)$$
$$+ 2(1-\epsilon_3)\Lambda_o A_3 \cos(3\omega t + \alpha_3)$$
$$+ \Sigma_3 + \Sigma_3' \text{ ---------- } \Big]$$

where $\Sigma_v = \sum \Lambda_n A_m \cos \left[(m-n)\omega t + \alpha_m \right]$

$\Sigma_v' = \sum \Lambda_n A_m \cos \left[(m+n)\omega t + \alpha_m \right]$ $\quad |n-m| = v$

$$\phi_{DC} = \Big[\Lambda_o \left[2F_e + \epsilon_1 A_1 \cos\alpha_1 + \epsilon_1 A_1 \cos(2\omega t + \alpha_1) \right]$$
$$+ 2\Lambda_o F_e \sum \epsilon_n \cos n\omega t$$
$$+ \Lambda_o \sum A_m \epsilon_m \cos\alpha_m$$
$$+ \Lambda_o \sum A_m \epsilon_m \cos(2m\omega t + \alpha_m) \text{ ---------- } \Big]$$

(compare with simple theory):-

$$\phi_{ac} = 2\epsilon\Lambda_o \left[F_e \cos\omega t + A\cos(\omega t + \alpha) \right]$$
$$+ 2(1-\epsilon)\Lambda_o A\cos(\omega t + \alpha)$$

$$\phi_{DC} = \Lambda_o \left[2F_e + \epsilon A\cos\alpha + \epsilon A\cos(2\omega t + \alpha) \right]$$

10.5 Damping currents under load conditions.

$$\phi_A = \Lambda_o(1+\Sigma\epsilon_n \cos n\omega t)(F_e + \Sigma A_n \cos(n\omega t + \alpha_n) + D_m \cos(m\omega t + \beta_m))$$

$$\phi_B = \Lambda_o(1+\Sigma\epsilon_n(-1)^n \cos n\omega t)(-F_e + \Sigma A_n \cos(n\omega t + \alpha_n) - D_m \cos(m\omega t + \beta_m))$$

$$\phi_{DC} = \phi_A - \phi_B$$

$$= \Lambda_o \Big[F_e + \Sigma A_n \cos(n\omega t + \alpha_n) + D_m \cos(m\omega t + \beta_m) + F_e \Sigma \epsilon_n \cos n\omega t$$
$$+ \Sigma \epsilon_n A_n \cos n\omega t \cos(n\omega t + \alpha_n) + \Sigma \epsilon_n D_m \cos n\omega t \cos(m\omega t + \beta_m)$$
$$+ F_e - \Sigma A_n \cos(n\omega t + \alpha_n) + D_m \cos(m\omega t + \beta_m) + \Sigma F_e \epsilon_n (-1)^n \cos n\omega t$$
$$- \Sigma \epsilon_n A_n (-1)^n \cos n\omega t \cos(n\omega t + \alpha_n) + \Sigma \epsilon_n (-1)^n \cos n\omega t D_m \cos(m\omega t + \beta_m) \Big]$$

$$= \Lambda_o \Big[2F_e + 2\Sigma F_e \epsilon_n \cos n\omega t + 2\Sigma \epsilon_n A_n \cos n\omega t \cos(n\omega t + \alpha_n)$$
$$+ 2D_m \cos(m\omega t + \beta_m) + 2\Sigma \epsilon_n D_m \cos(m\omega t + \beta_m) \cos n\omega t \Big]$$

$$\phi_{DC} = \Lambda_o \Big[2F_e + 2F_e \epsilon_2 \cos 2\omega t + 2D_2 \cos(2\omega t + \beta_2)$$
$$+ 2D_1 \cos(\omega t + \beta_1) + 2\epsilon_2 D_1 \cos 2\omega t \cos(\omega t + \beta_1)$$
$$+ 2\epsilon_2 D_2 \cos 2\omega t \cos(2\omega t + \beta_2)$$
$$+ 2\epsilon_1 A_1 \cos\omega t \cos(\omega t + \alpha_1)$$
$$+ 2\epsilon_3 A_3 \cos 3\omega t \cos(3\omega t + \alpha_3) \_\_\_\_\_ \Big]$$

2nd harmonic terms:-

$$2D_2 \cos(2\omega t + \beta_2) + \epsilon_1 A_1 \cos(2\omega t + \alpha_1) + 2F_e \epsilon_2 \cos 2\omega t$$

For complete damping of the second harmonic flux,
(neglecting $2F\epsilon_2 \cos 2\omega t$, since ϵ_2 small compared with ϵ_1)

$$\alpha_1 = \beta_2 \quad \text{and} \quad D_2 = -\frac{\epsilon_1 A_1}{2}$$

$$\phi_{ac} = \phi_A + \phi_B$$

$$= \Lambda_o \left[2A_n \cos(n\omega t + \alpha_n) + \sum F_e \epsilon_n \cos n\omega t \left(1-(-1)^n\right) \right.$$

$$+ \sum \epsilon_n A_n \cos n\omega t \cos(n\omega t + \alpha_n) \left(1+ (-1)^n\right)$$

$$\left. + \sum \epsilon_n D_m \cos n\omega t \cos(m\omega t + \beta_m) \left(1-(-1)^n\right) \right]$$

for $n=2,4,6,8\ldots$ terms in $\left(1- (-1)^n\right) = 0$

$\therefore$ $n= 1,3,5,7\ldots$ and $m = 1,2,3,4,5\ldots$

$$\phi_{ac} = \Lambda_o \left[2A_n \cos(n\omega t + \alpha_n) + 2\sum F_e \epsilon_n \cos n\omega t \right.$$

$$+ 2\sum \epsilon_n A_n \cos n\omega t \cos(n\omega t + \alpha_n)$$

$$\left. + 2\sum \epsilon_n D_m \cos n\omega t \cos(m\omega t + \beta) \right]$$

$$\phi_{ac} = \tfrac{1}{2}\Lambda_t F_A + \tfrac{1}{2}\Lambda_s F_A - \tfrac{1}{2}\Lambda_t F_B - \tfrac{1}{2}\Lambda_s F_B$$

$$= \tfrac{1}{2}\Lambda_t F_A - \tfrac{1}{2}\Lambda_t F_B - \tfrac{1}{2}\Lambda_s F_A + \Lambda_s F_A - \Lambda_s F_B + \tfrac{1}{2}\Lambda_s F_B$$

$$= \tfrac{1}{2}(\Lambda_t - \Lambda_s)F_A - \tfrac{1}{2}(\Lambda_t - \Lambda_s)F_B + \Lambda_s\left[F_e + A\cos(\omega t+\alpha) + A\cos(\omega t+\alpha) - F_e\right]$$

$$\phi_{ac} = \tfrac{1}{2}(\Lambda_t - \Lambda_s)F_A - \tfrac{1}{2}(\Lambda_t - \Lambda_s)F_B + 2\Lambda_s A\cos(\omega t+\alpha)$$

where

$$2\Lambda_s A\cos(\omega t+\alpha) \equiv 2\Lambda_o(1-\epsilon)A\cos(\omega t+\alpha) = \phi_{as}$$

a.c. main flux. $= \phi_{ac} - \phi_{as}$

$$= (\Lambda_o F_A - \Lambda_o F_B) + (\epsilon\Lambda_o F_A + \epsilon\Lambda_o F_B)\cos\omega t - 2\Lambda_o(1-\epsilon)A\cos(\omega t+\alpha)$$

$$= \Lambda_o F_A - \Lambda_o F_B + (\epsilon\Lambda_o F_A + \epsilon\Lambda_o F_B)\cos\omega t - \Lambda_s(F_A - F_B)$$

$$= \Lambda_o F_A - \Lambda_o F_B + (\epsilon\Lambda_o F_A + \epsilon\Lambda_o F_B)\cos\omega t - (1-\epsilon)\Lambda_o(F_A - F_B)$$

$$= (\epsilon\Lambda_o F_A + \epsilon\Lambda_o F_B)\cos\omega t + \epsilon\Lambda_o(F_A - F_B)$$

$$= 2F_e\epsilon\Lambda_o\cos\omega t + 2\epsilon\Lambda_o A\cos(\omega t+\alpha)$$

$$\phi_{DC} = \Lambda_o F_A + \Lambda_o\epsilon F_A\cos\omega t + \Lambda_o F_B - \Lambda_o\epsilon F_B\cos\omega t$$

$$= \left(\Lambda_o\epsilon F_A - \Lambda_o\epsilon F_B\right)\cos\omega t + \Lambda_o\left(F_A + F_B\right)$$

$$= \left(\Lambda_o\epsilon F_A - \Lambda_o\epsilon F_B\right)\cos\omega t + \left(\epsilon\Lambda_o F_A + \epsilon\Lambda_o F_B\right) + 2\Lambda_s F_e$$

$$\left(\ 2\Lambda_s F_e = 2(1-\epsilon)\Lambda_o F_e\ \right)$$

10.7 Fourier analysis of flux waveform at the rotor tooth surface.

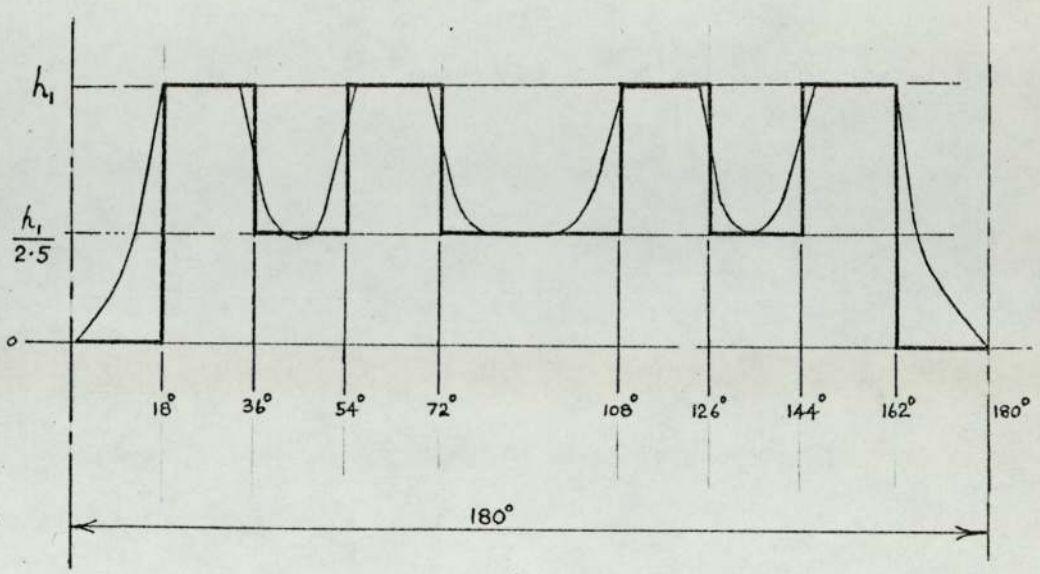

$$f(x) = \text{mean value} + \sum B_n \sin(n\omega t)$$

$$B_n = \frac{h_1 K}{n}\left[\int_{18°}^{36°}\sin nx.dx + \frac{1}{2.5}\int_{36°}^{54°}\sin nx.dx + \int_{54}^{72}\sin nx.dx + \frac{1}{2.5}\int_{72}^{108}\sin nx.dx + \int_{108°}^{126°}\sin nx.dx + \frac{1}{2.5}\int_{126°}^{144°}\sin nx.dx + \int_{144°}^{162°}\sin nx.dx\right]$$

$B_1 = 1.26$; $B_3 = 0.76$; $B_7 = 0.4$; $B_9 = 0.44$; $B_{11} = 0.27$.

Comparison of measured and calculated values:-

harmonic	calculated	measured
Fund	100%	100%
3rd	60	52
7th	32	34
9th	35	41
11th	21.5	25

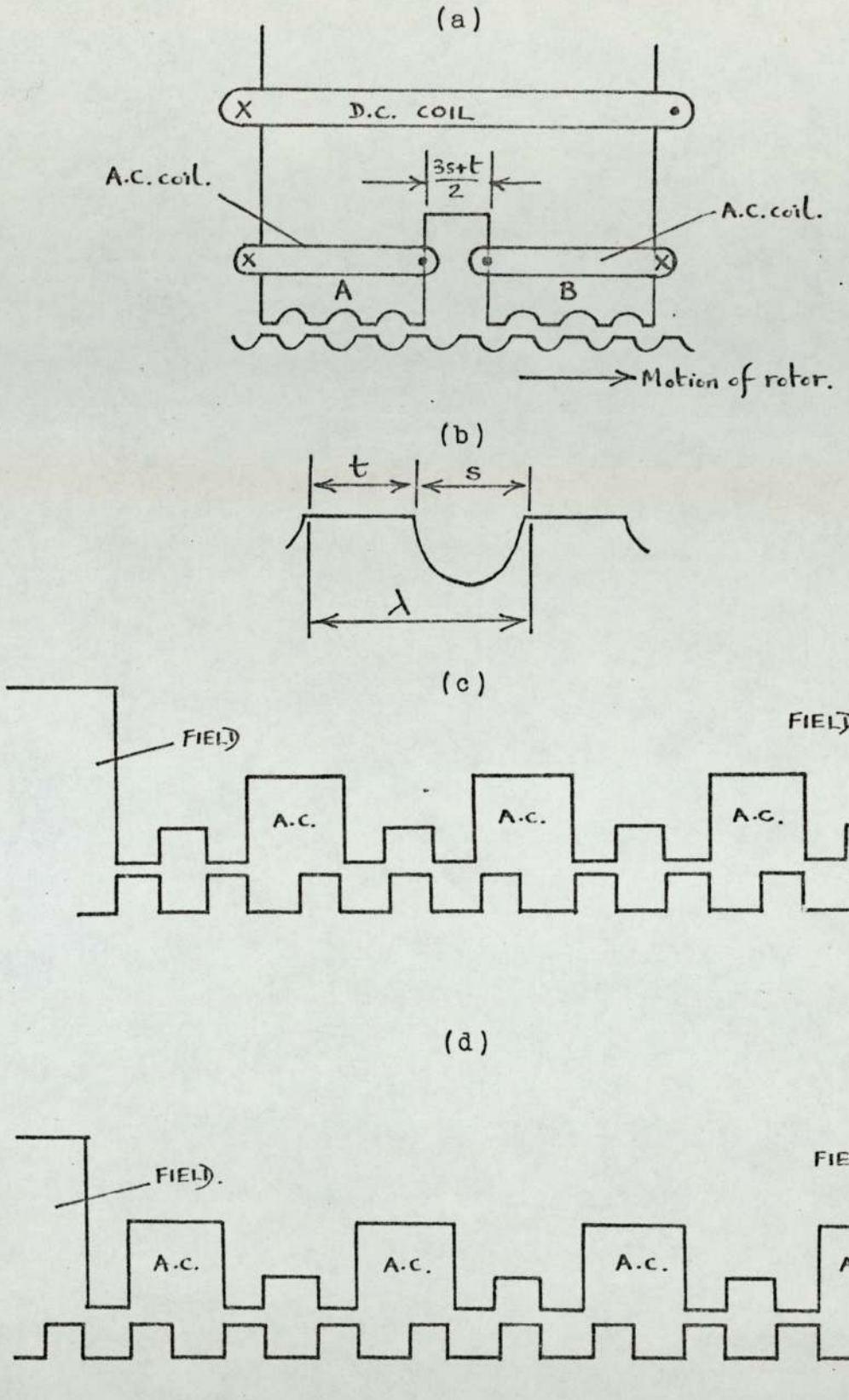

Fig.1

Typical slotting arrangements.

(a) Simple form of guy slotting.
(b) Tooth slot parameters, t=tooth width, s=slot width.
(c) Guy-Lorenz slotting, odd ac slots dc pole.
(d) Guy-Lorenz slotting, even ac slots dc pole.

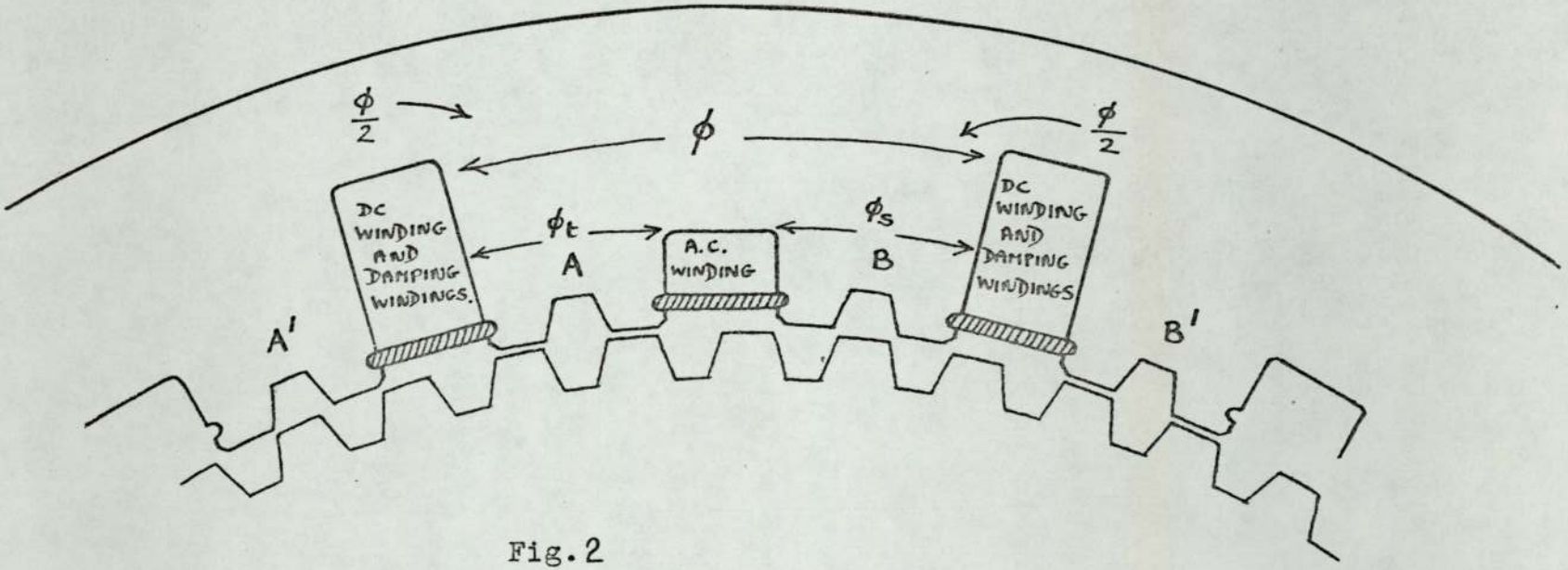

Fig.2

Slotting arrangement for the experimental machine.

ϕ = DC flux. For simple analysis ϕ_{dc} assumed to be constant, i.e. $\leq \Lambda$ (over a d.c. pole pitch) = constant. In practice $\leq \Lambda \neq$ constant, (2.4).

ϕ_t = flux defined in a whole stator main tooth for the stator tooth-opposite rotor tooth position.

ϕ_s = flux defined in a whole stator main tooth for the stator tooth opposite rotor slot position.

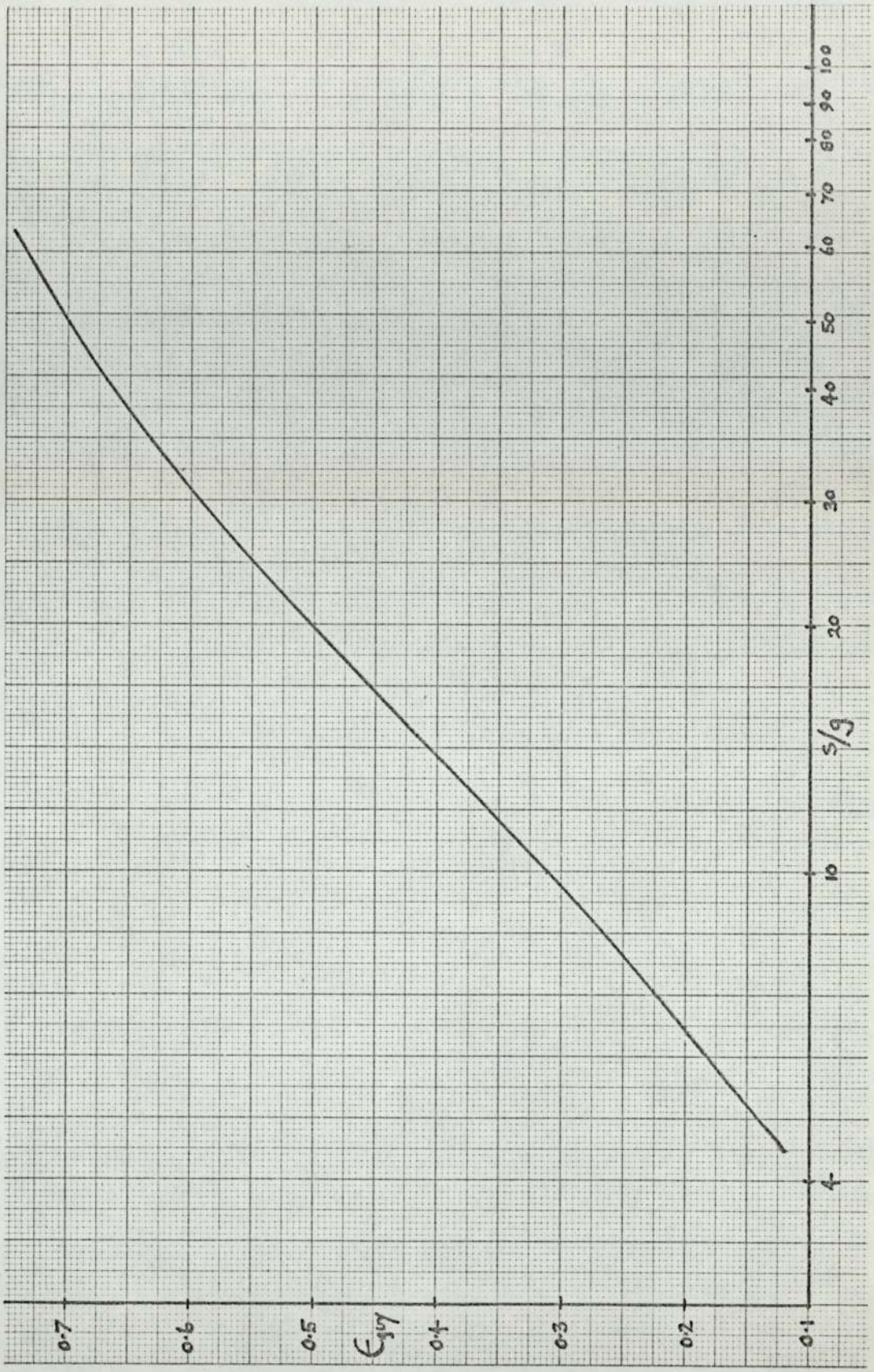

Fig.3

Variation of flux utilisation coefficient ϵ with s/g .

The ϵ values shown are (ϵ carter x0·9). The curve is valid for ($0{\cdot}37 \leq t/\lambda \leq 0{\cdot}44$.)

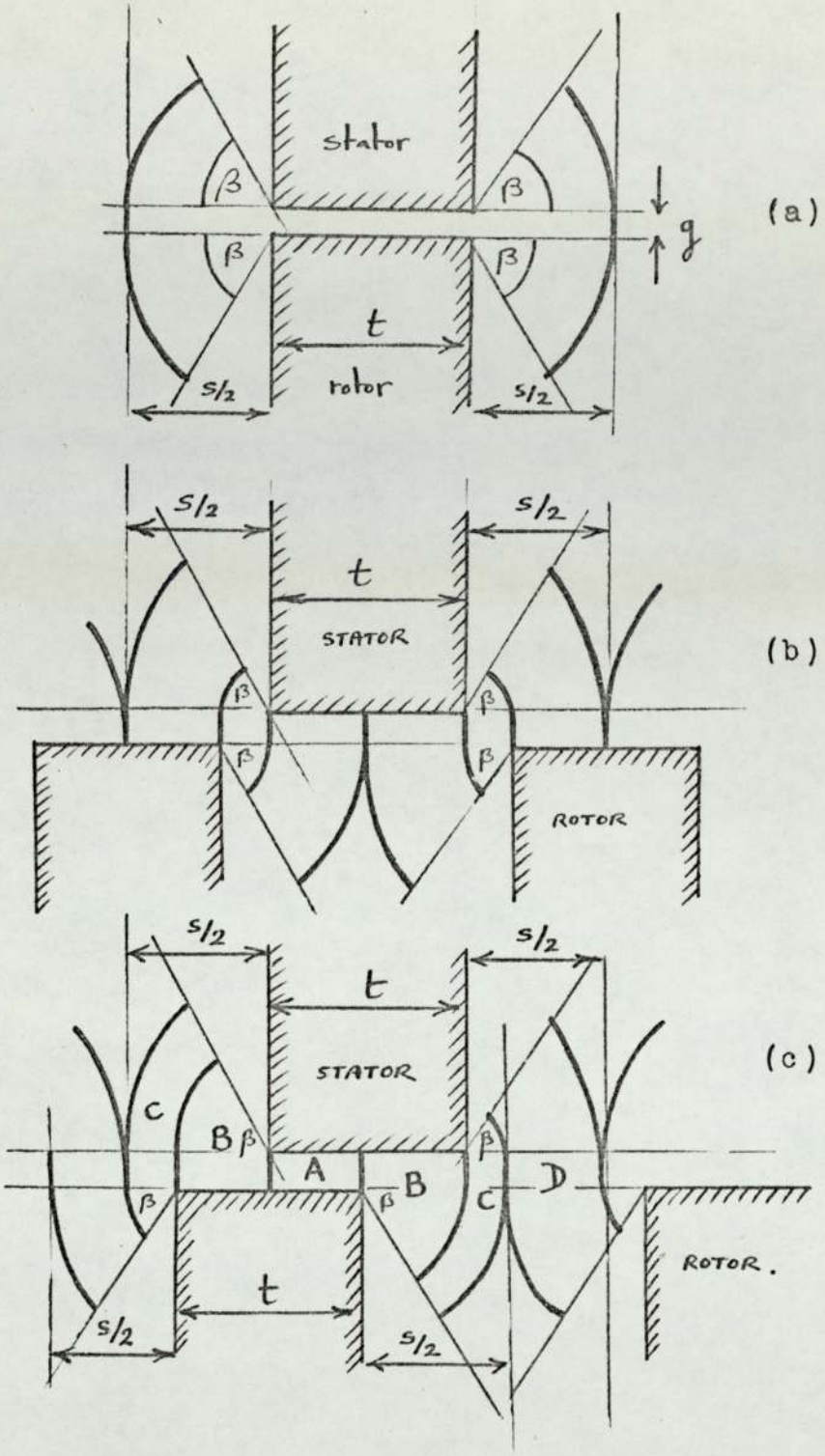

Fig. 4

Approximations to airgap permeance, (Pohl).

(a) $x = 0$, i.e. rotor and stator teeth opposite.

(b) $x = \frac{s+t}{2}$ i.e. stator tooth opposite rotor slot.

(c) $0 \leq x \leq s/2$ (Λ = A+2B+2C+D).

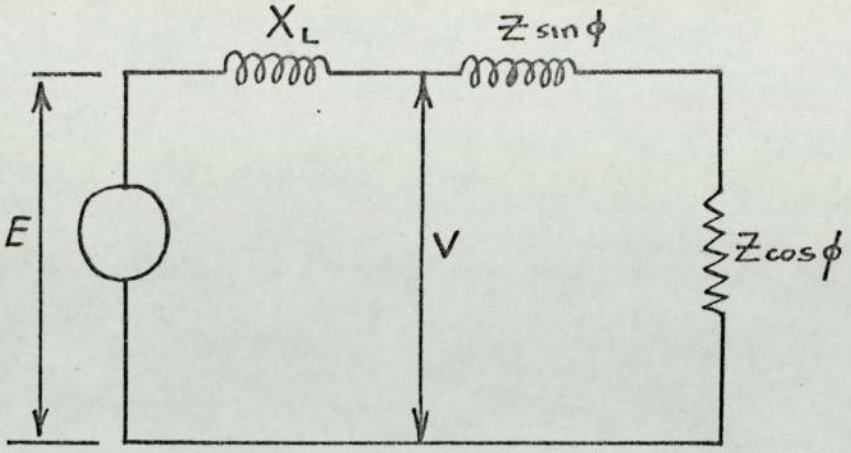

(a)

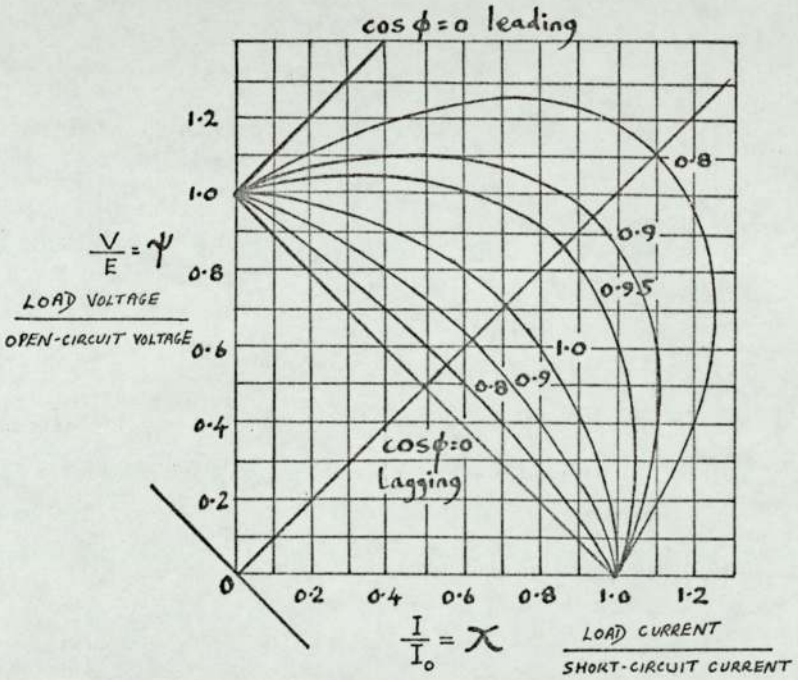

(b)

Fig.5

(a) Equivalent circuit of Inductor Alternator (Mandl)

(b) General load characteristics for various power factors.

E- open-circuit voltage, V-terminal volts of alternator, I, I_o ,-load, short-circuit current, Z- load impedance, X_L-internal reactance.

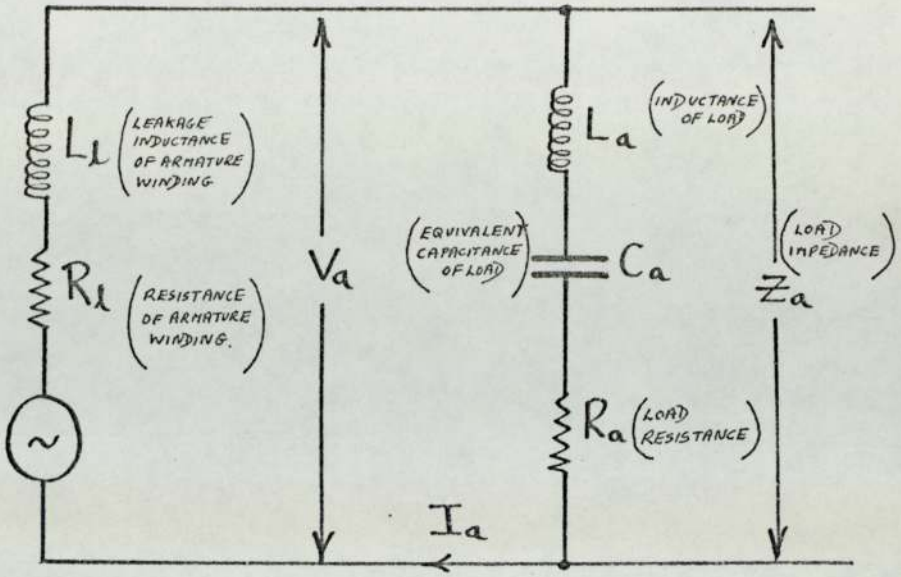

(a)

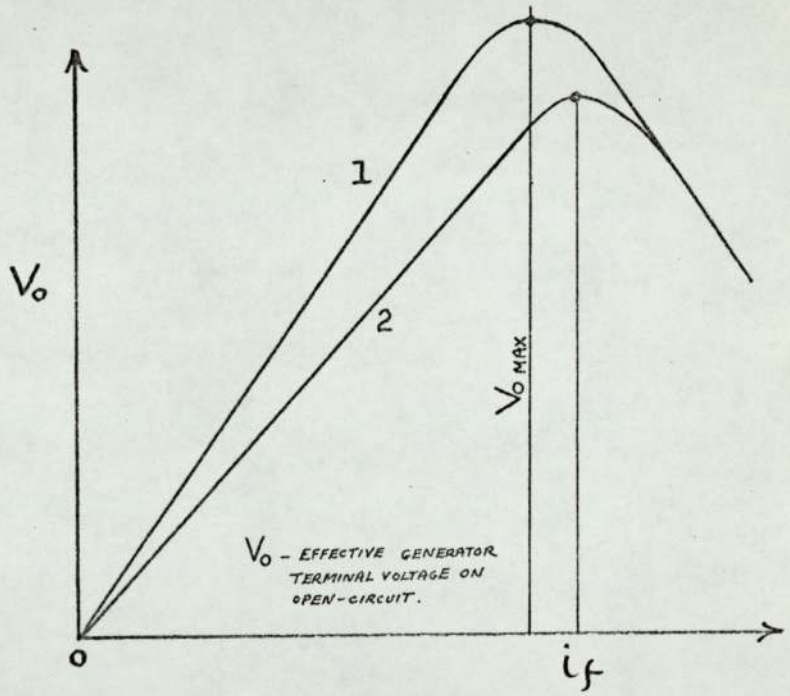

(b)

Fig.6

(a) Equivalent circuit of Inductor Alternator (Bunea)

(b) Open circuit characteristics of medium frequency alternator.

(1) Neglecting magnetic skin effect.
(2) Taking account of magnetic skin effect.

Fig.7

Variation of ϵ with d/g and slope of the side of the slot.

10khz slotting.

(a) 0° (b) 20° (c) 30°

for (a),(b) and (c) $t/\lambda = 0{\cdot}4$;

$s/g = 8$;

3khz slotting.

$t/\lambda = 0{\cdot}4$; $s/g = 30$;

$$d/g = \frac{\text{depth of slot}}{\text{airgap}}$$

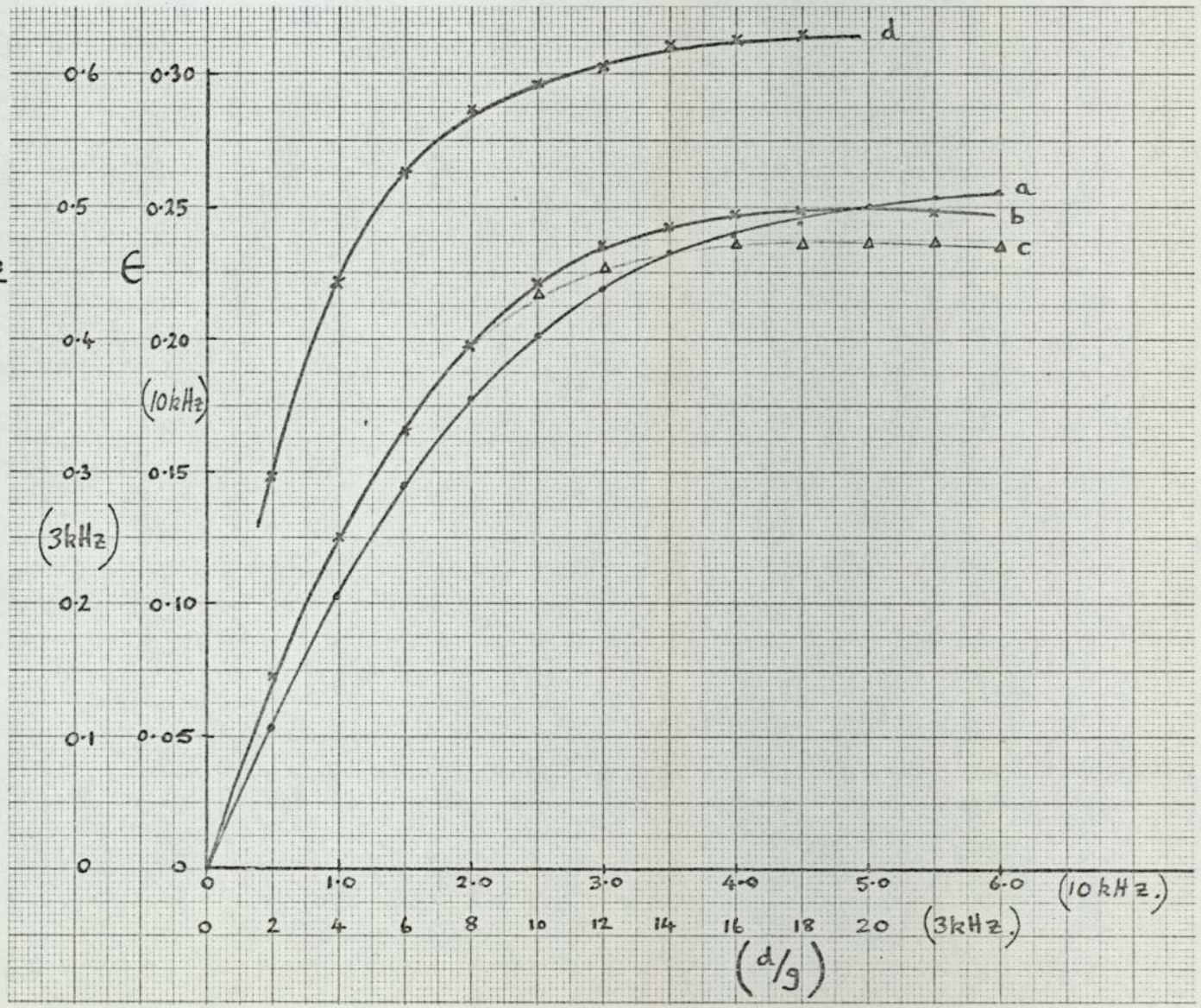

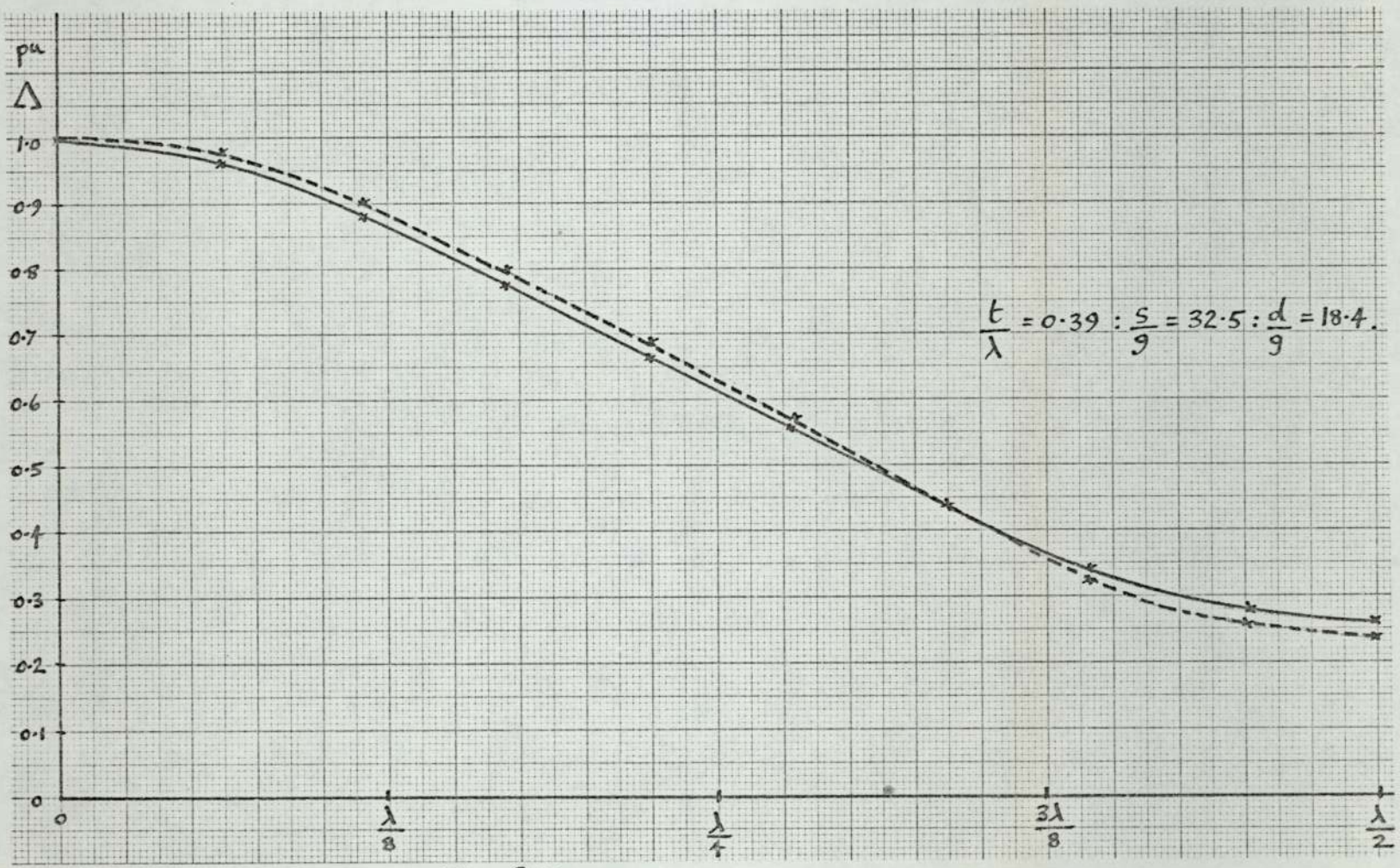

Fig.8 Permeance curves.
Permeance variation over a half cycle for the actual machine.

Dotted curve shows the permeance variation over a half cycle as seen by a whole stator main tooth.

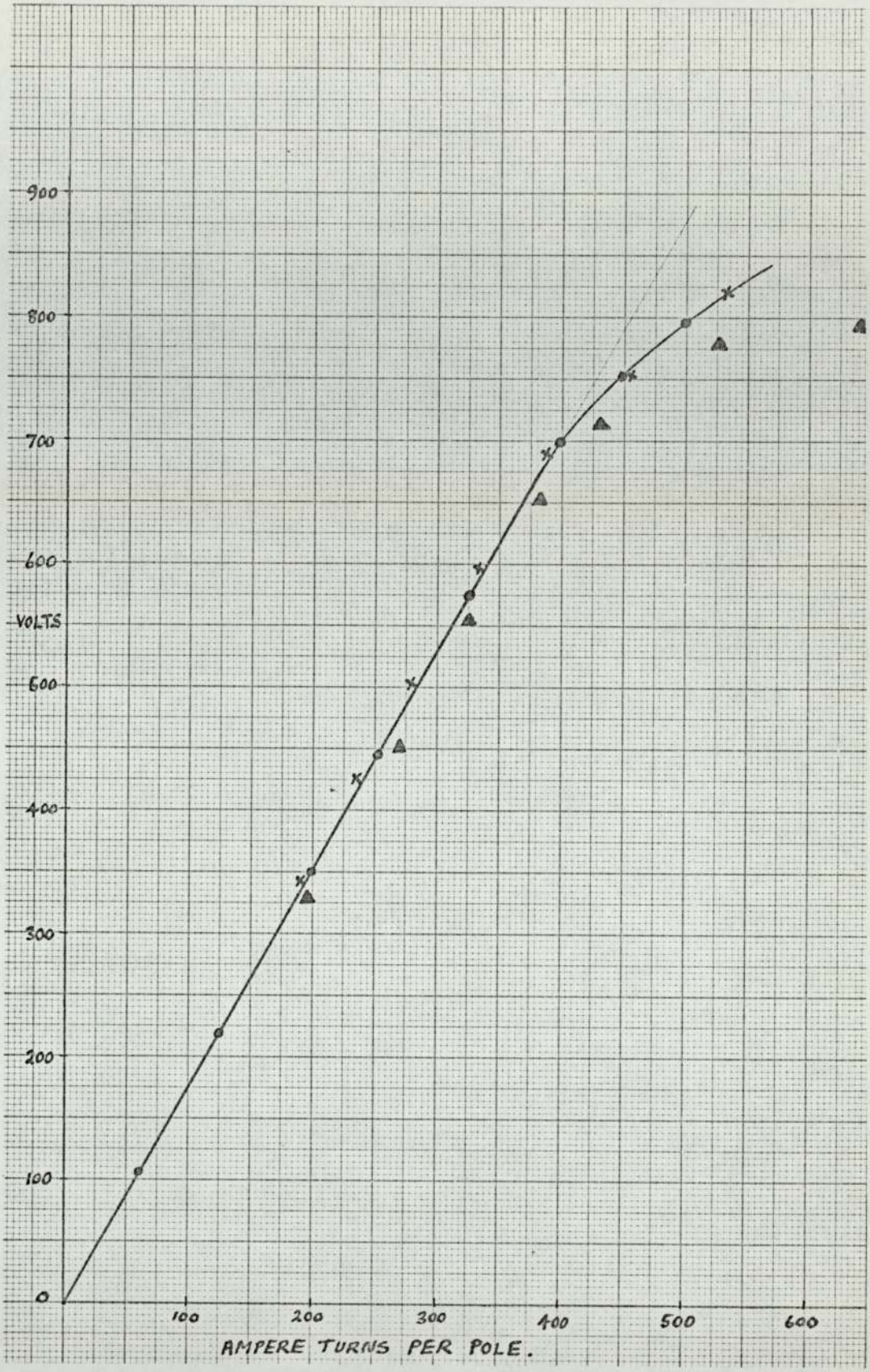

Fig. 9

Open circuit voltage curve for the machine.

- test o.c. curve on actual machine.
- ▲ calculated using value of $\epsilon = 0{\cdot}525$.
- X calculated using value of $\epsilon = 0{\cdot}554$.

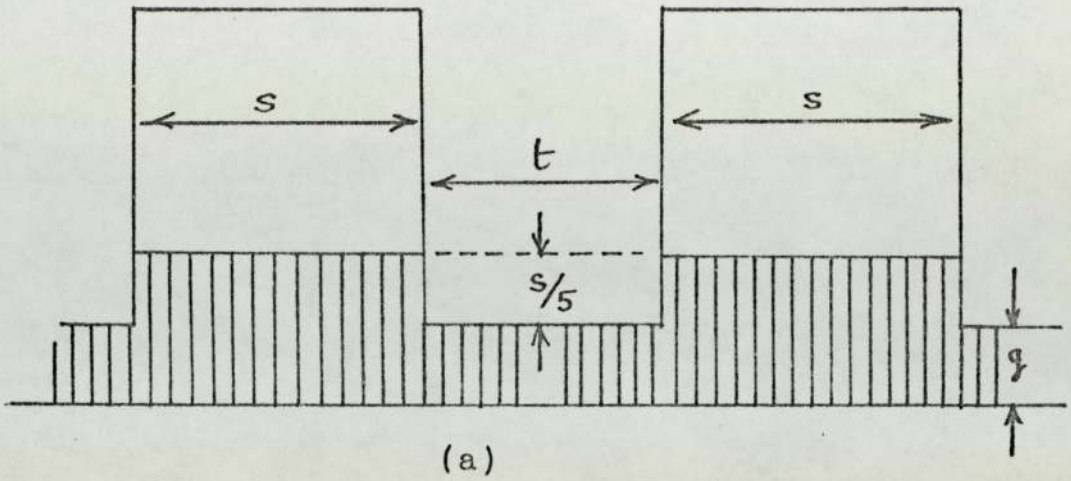

(a)

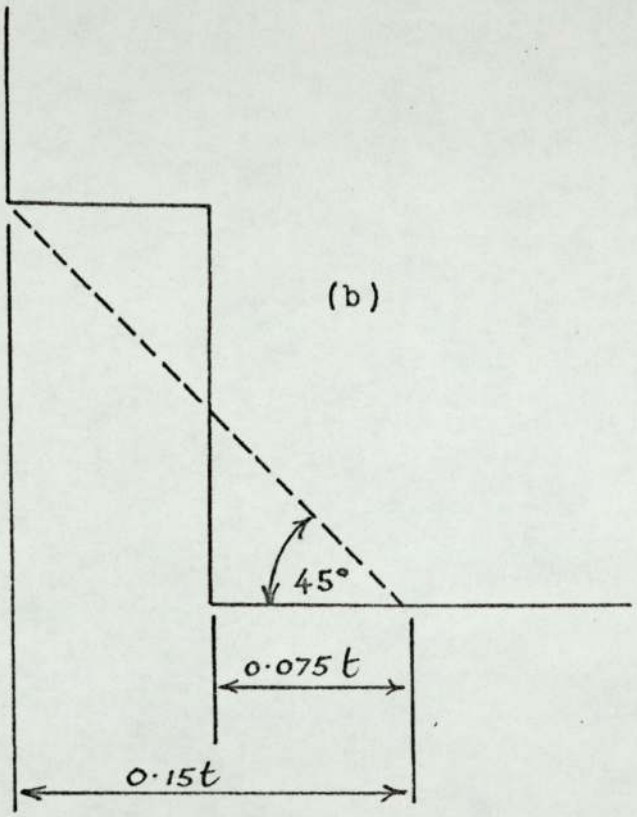

Fig.10

Approximations to airgap permeance.

(a) Baillie approximation to airgap permeance.

(b) _ _ _ _ _ _ _ actual chamfer.

——————— Approximation to chamfer at tooth edge.

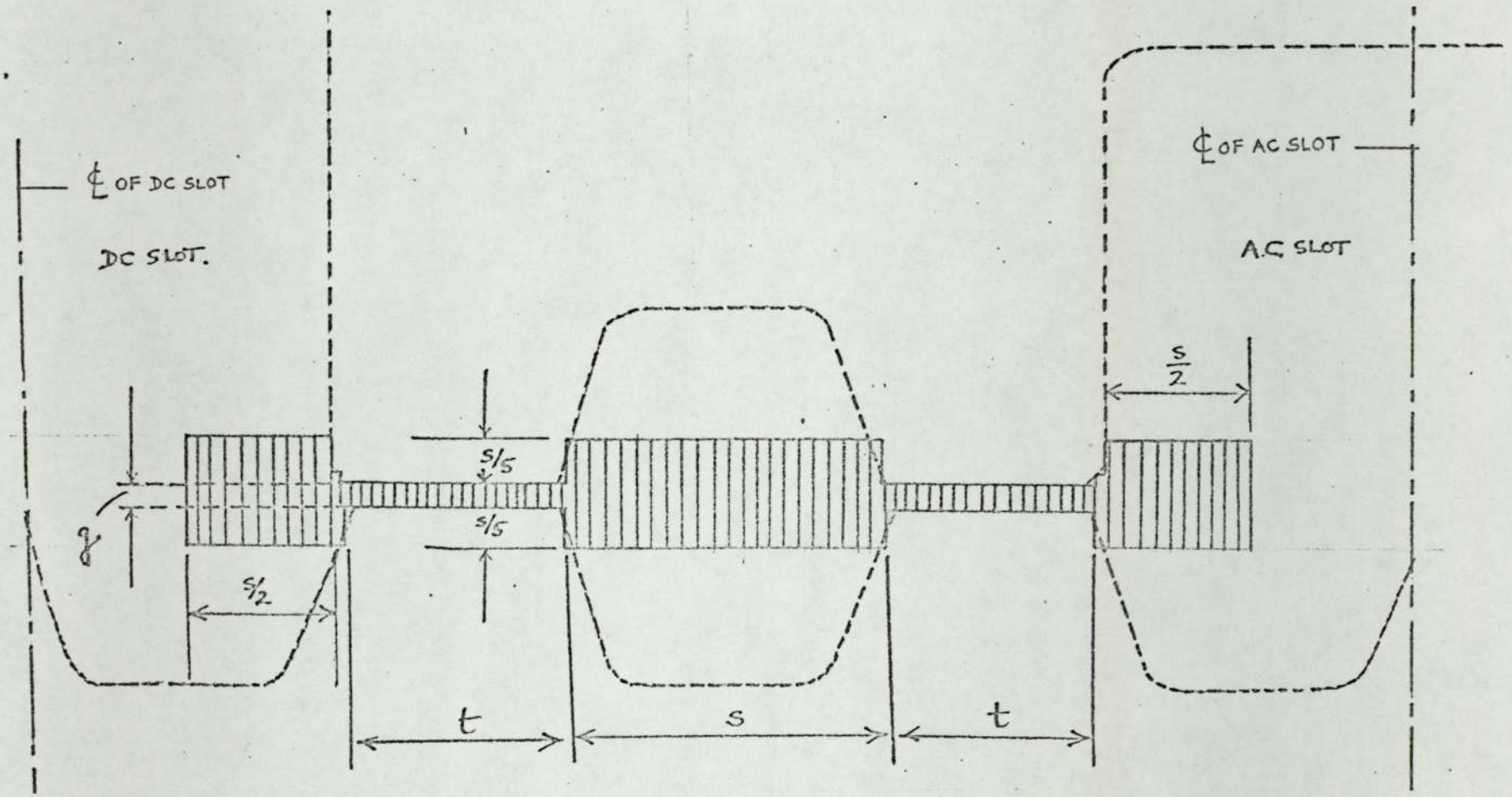

Fig.10c

Authors approximation for the actual machine.

Fig.11

Permeance curves.

(a) Permeance variation over a whole cycle for a whole stator main tooth from a teledeltos plot.
$t/\lambda = 0{\cdot}39 : s/g = 32\ 5 : d/g = 18{\cdot}4$.

(b) Permeance variation over a half cycle derived from a straightforward application of Baillie.

(c) Permeance variation over a half cycle using the approximations shown in fig(10b) & (10c).

The angle 'θ' represents the angle between the centre line of a small stator tooth and the centre line of a rotor tooth.

1pu permeance taken for θ=0 i.e. Tooth-opposite tooth position.

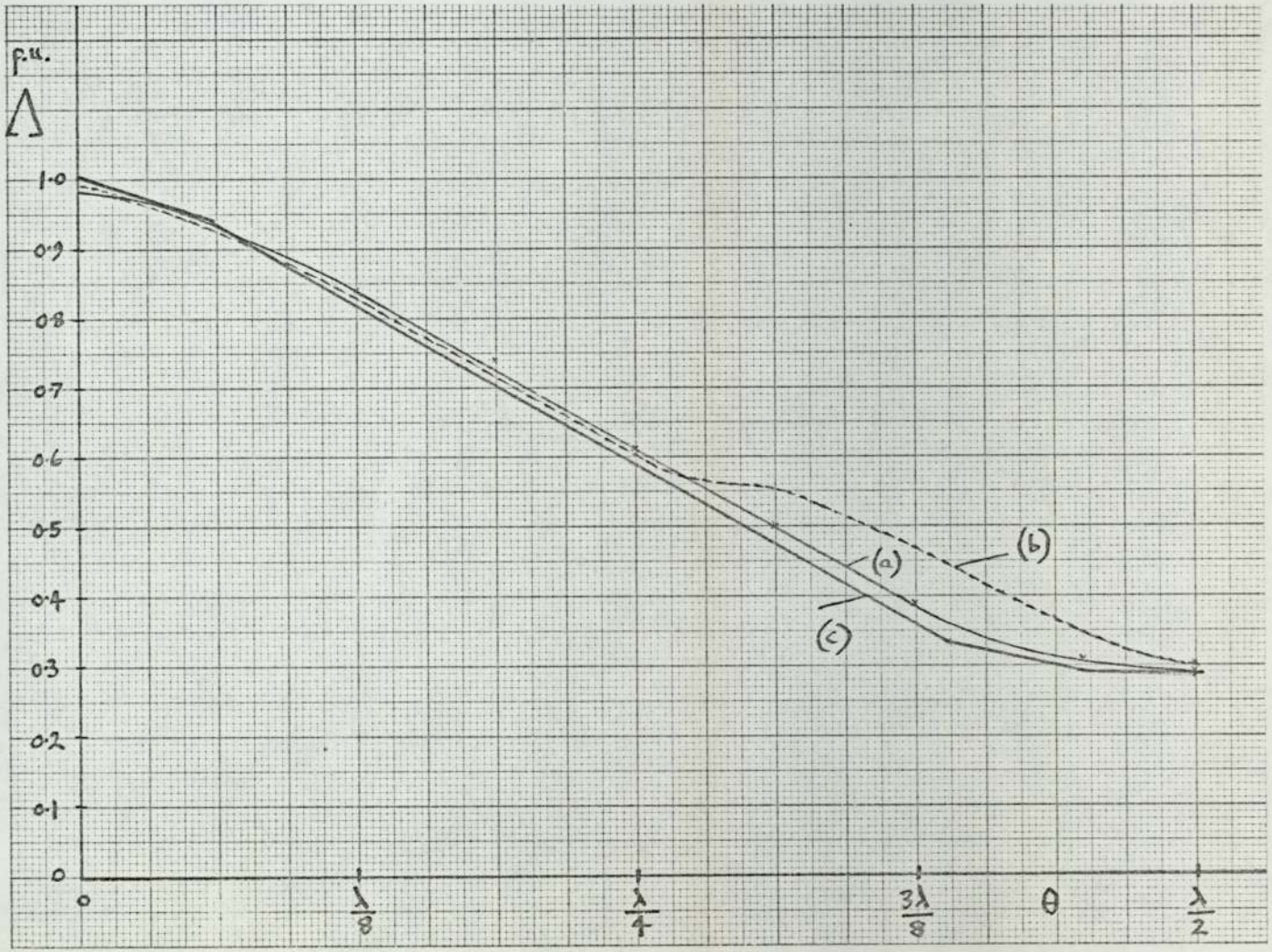

Fig.12

Permeance curves predicted from modified version of Baillie, showing the effects of altering t/λ for typical 3khz and 10khz slotting.

1pu permeance taken for $s/g = 30$: $t/\lambda = 0{\cdot}4$; $\theta = 0$.

$\theta = 0$: stator tooth opposite rotor tooth.

$\theta = \frac{\lambda}{2}$: stator tooth opposite rotor slot.

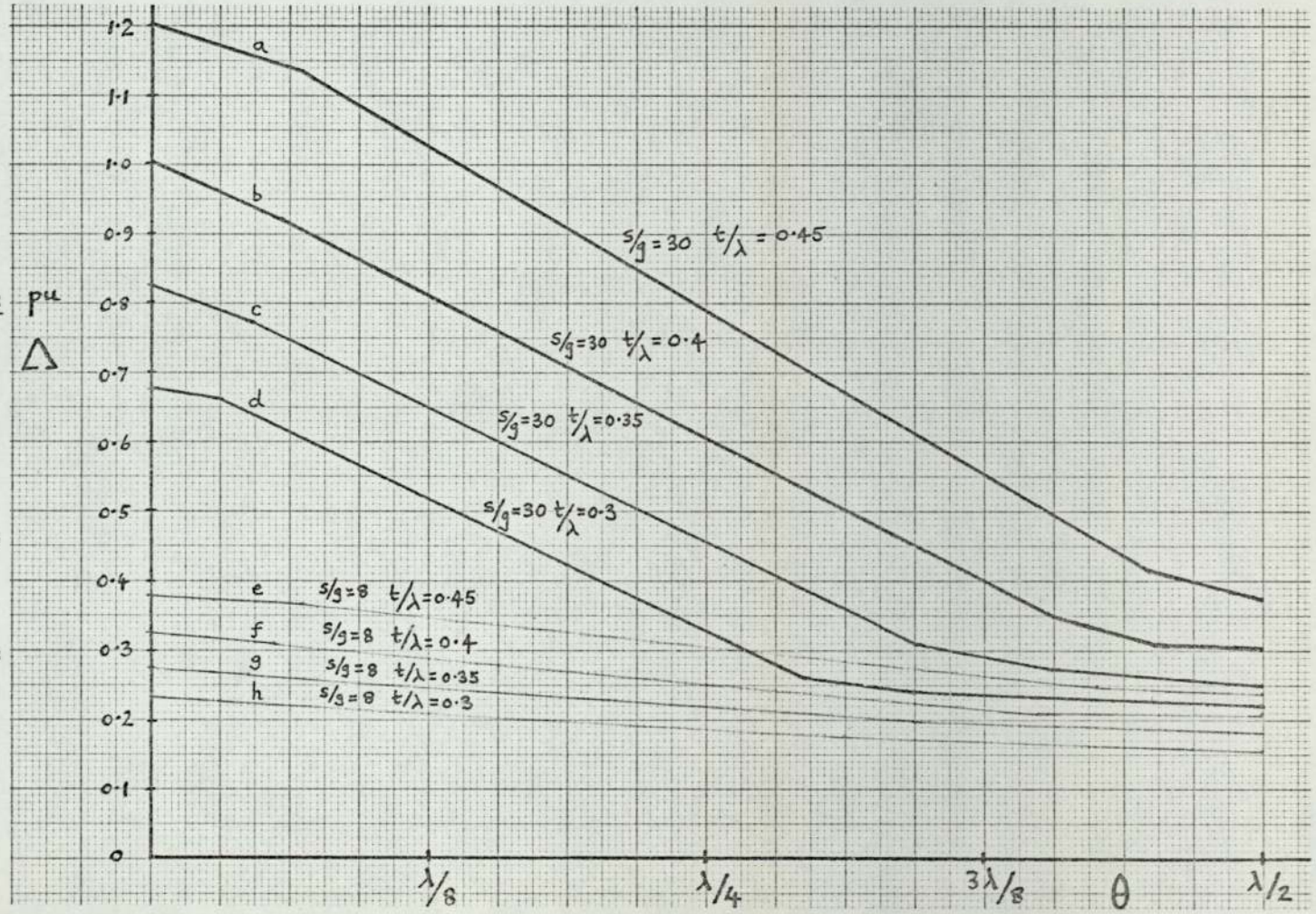

Fig.13

Permeance curves predicted from modified version of Baillie showing the effects of altering s/g for a constant $t/\lambda = 0{\cdot}4$.

1pu permeance taken for $s/g = 30$.

$t/\lambda = 0{\cdot}4$; $\theta = 0$.

$\theta = 0$: stator tooth opposite rotor tooth.

$\theta = \frac{\lambda}{2}$; stator tooth opposite rotor slot.

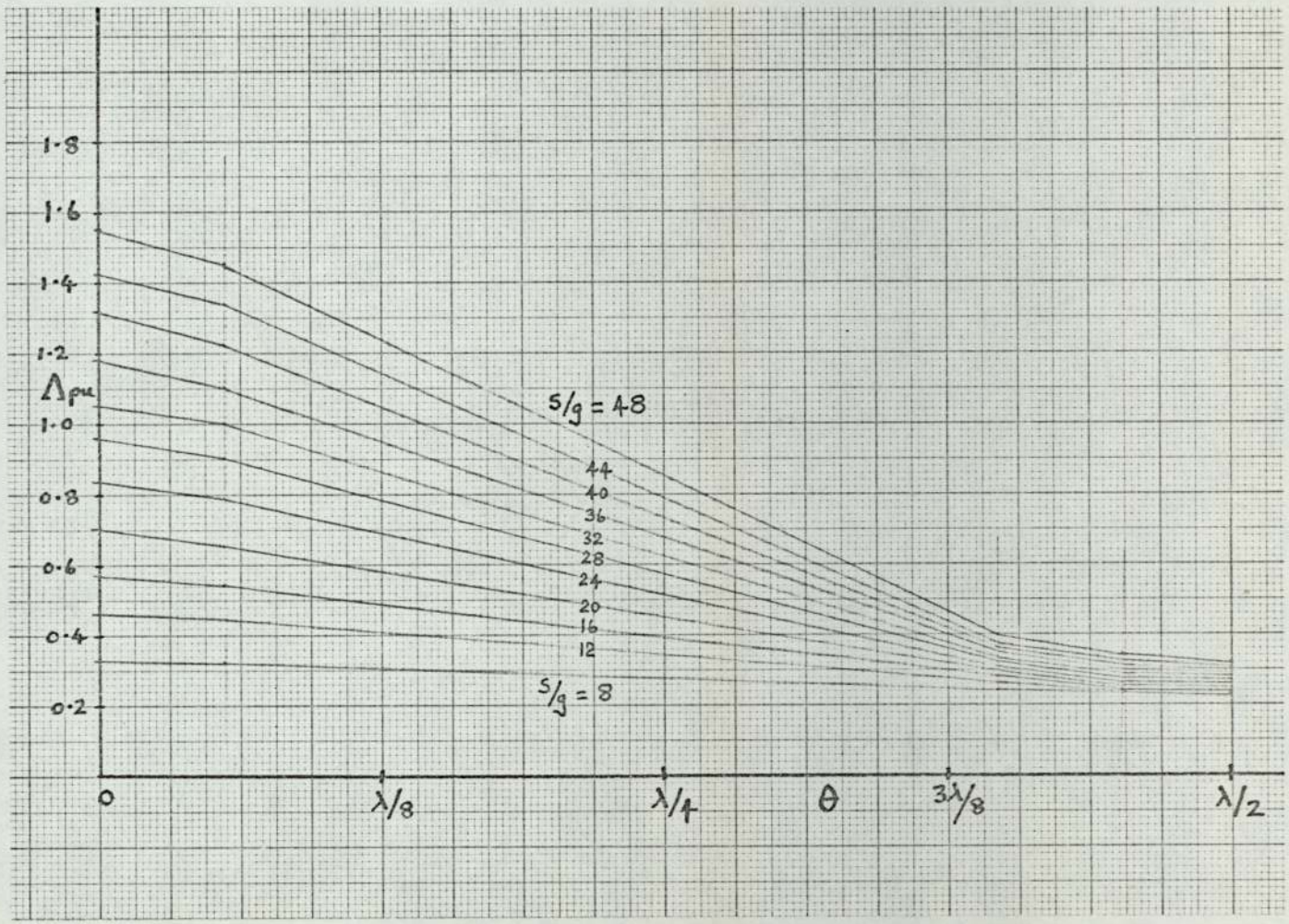

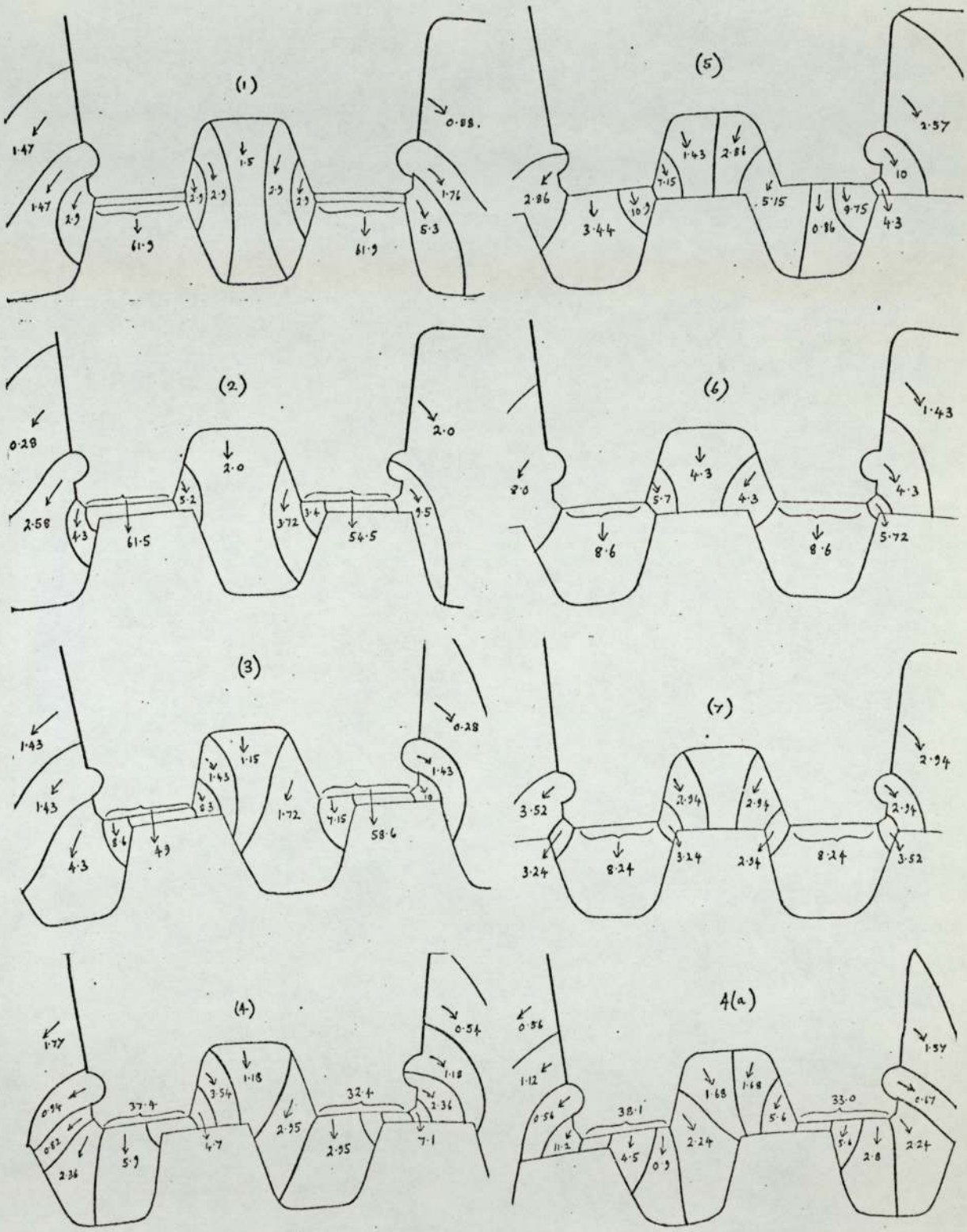

Fig.14

Flux distribution for various rotor positions.

(4) and (4a) - positions of symmetry.

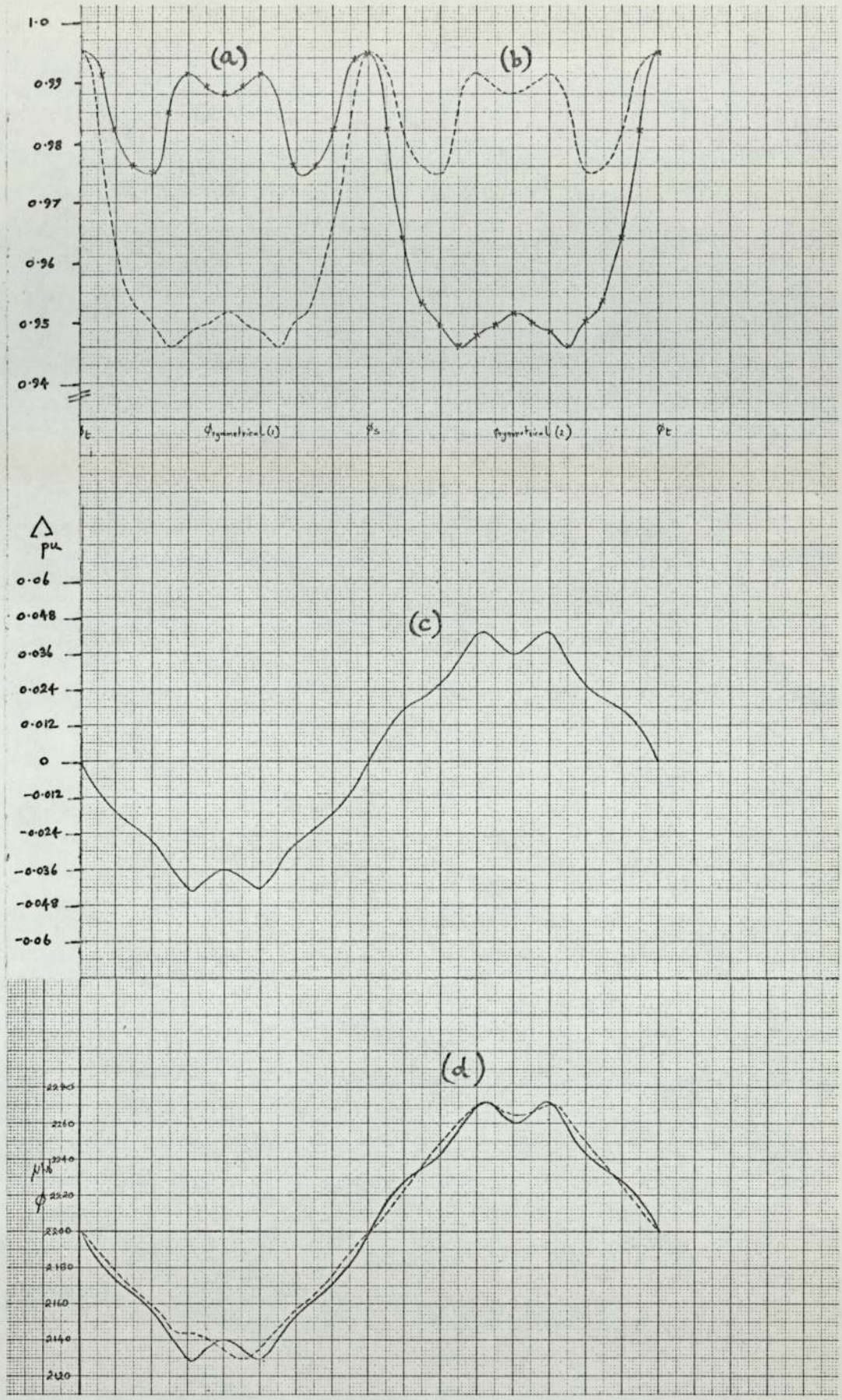

Fig. 15

(a) Permeance variation across a total pole pitch.
(b) Permeance variation in adjacent pole.
(c) Resultant permeance variation behind the field slots.
(d) Flux variation behind the field slots. 500v.o.c.

———— teledeltos ---------- measured.

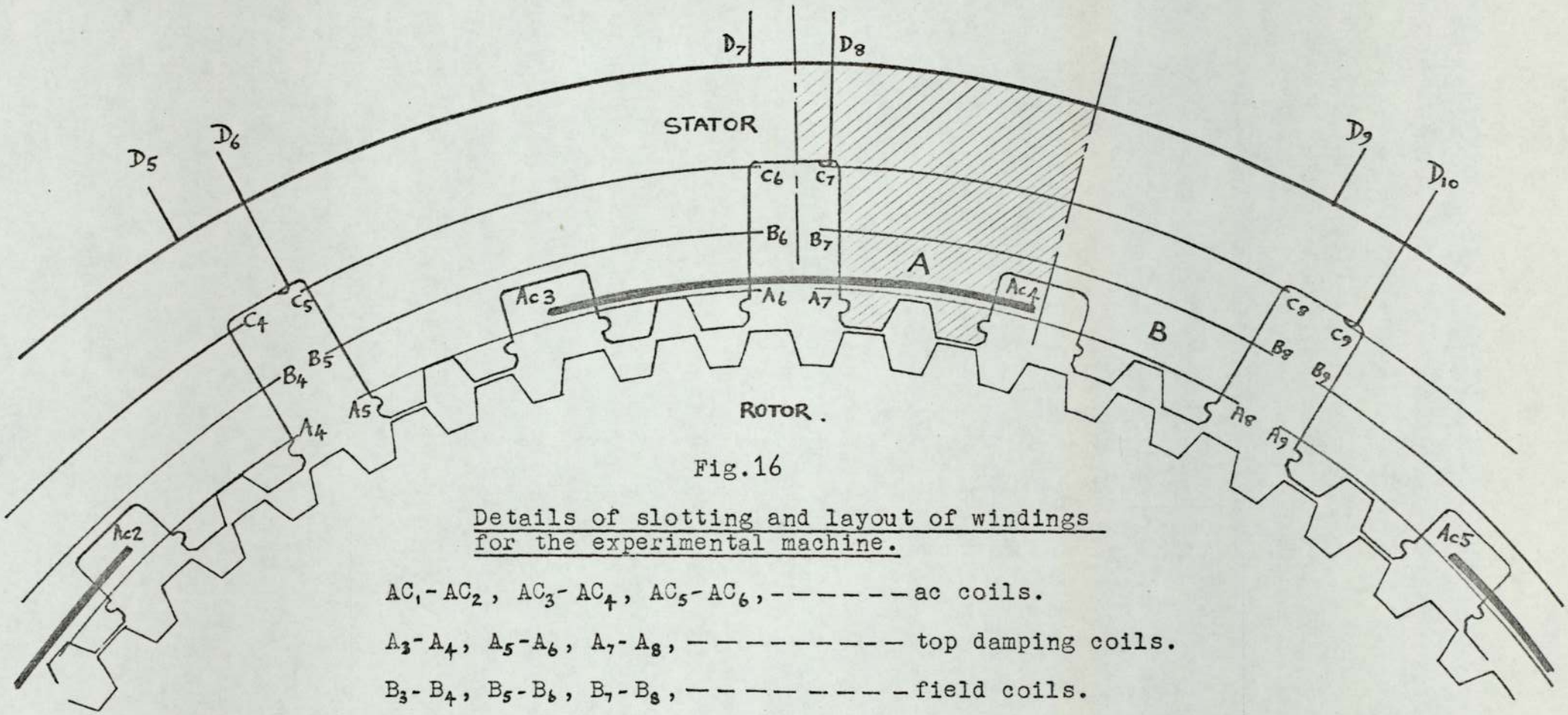

Fig.16

Details of slotting and layout of windings for the experimental machine.

AC_1-AC_2, AC_3-AC_4, AC_5-AC_6, ------- ac coils.

A_3-A_4, A_5-A_6, A_7-A_8, ---------- top damping coils.

B_3-B_4, B_5-B_6, B_7-B_8, ---------- field coils.

C_3-C_4, C_5-C_6, C_7-C_8, ---------- bottom damping coils.

D_5-D_6, D_7-D_8, D_9-D_{10}, ---------- core damping coils.

Shaded area represents the search coil stack section for the stator.

Date ..... Ds. No. .....

SYNCH AHS 3000 Hz MEA./A.C./S.O. No. ..... No. off. .....

CUSTOMER 3000 rpm 40 KW Ex/Q/Req. No. .....

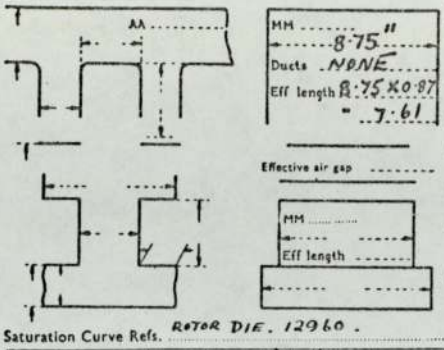

Saturation Curve Refs. ROTOR DIE. 12960.

	Section	Density ϕ_t	AT/in ϕ_{dc}	Length	AT
Stator Core DC / AC			12·4		
Stator Teeth (1) / B max Km(2)	7·61 / 3·96	43·4 / 83·4	13·7 / 26·0		
Air Gap C 2·12 kδ Leff 8·78	5·31	58·8		0·016	295
Rotor Teeth	3·96	83·4	26		
Pole Body					
Spider DC / AC			11·2		
ATg = α = 1·092 SCR =			AT₀		

Specn. ..... Enclosure .....

Drive ..... Fans .....

kVA 44·4 Connection S.P. P. Speed 9430

Cos φ 0·9 Volts per phase 500(s) Pole Pitch 3·206

kW h.p. 40 Amp. per phase 88·8 Pole Arc ..... = ... %

G = ... G_1 = ... Leakage Co-eff ..... Eff. P.A. ..... = ... %

Flux = $\frac{500}{4{\cdot}44 \times 3000 \times 18 \times 2} \times 10^2 = 0{\cdot}1045$ mgl. Field Flux = ... mgl.

$AT_{AR} = \frac{\sqrt{2} \times 88{\cdot}8 \times 3}{2} = 188{\cdot}1$ per inch

$\frac{kVA}{D^2L.N.} = 1{\cdot}126 \times 10^{-3}$ B. mean = 14·65 A.C. per slot .....

A.C. per Inch .....

$\phi_t = 0{\cdot}33$.

STATOR WINDING $\phi_{DC} = 0{\cdot}4035$ FIELD WINDING

Cond. Insn. I.S. asb		Turn Insn. SW. 39 YY2.		Ext. Turns I.S.	Turn Insn. F.F.
Type of Winding		chain	DC. wdg	Type of Winding	
No. of Slots	Total	12	12	No. of Poles	12 DC.
	per phase			Poles in parallel	
	Eff. per ph.	12		Turns per pole	14·3.
2 Wires. Conductors per Slot	Total	6	286	d. bare	Damping
	Effec.	3	286	d. insul.	
	d. bare	0·26 X 0·65	0·032	Cross Secn.	Windings see
	d. insul	0·275 X 1·65	0·035	Current Density	separate sheet.
	"mf Cr. Secn	0·129	0·000804	Mean L. of Turn	
Insulation	Sides	0·09	0·068	Total cu. Secn.	
	T. and B.	0·255	0·27	Ind. Volts per layer	
Total Copper Secn.		0·928	2·76	Res. at 75°C	58·2.
Current Density		3440	3090	" 100°C	63·75.
Mean L. of Turn		31	33		
Turns in Series/ph		18	1716		
Res./ph. at 75°C		0·0178	= ..... %		
" " 100°C		0·0194	= ..... %		

SQUIRREL CAGE WINDING

Bars ..... □"

Rings/Segs .....

λr ..... λs ..... $\frac{\lambda r}{\lambda s}$ = ...

	AT	A	V	kW
N.L. 500 Volts	295	2·06	129·5	0·267
FL (PF = 1·0)	325	2·28	143	0·326
LAG xFL (PF = 0·9)	355	2·48	156	0·386
LEAD xFL (PF = 0·9)	265	1·85	116	0·215
xFL (PF =)				

0·078
0·040
0·099
0·135
0·1910
0·5436

P_1 = 0·5436

x_1 = 2π 3000 3·29 · 12 { 1·15 · 8·75 + 0·543 + 0·135 = 0·4425 Ω / 0·079 % + 0·524 + 0·46

Iron Losses { Core + 0·148 / Teeth + 0·268 + 0·288 } = 0·984 = 0·684

Surface Loss Heteropolar Loss. = 0·132

TOTAL Loss = 1·800

S/g = 23·8 $\frac{t}{\lambda}$ X = 1·46 $\frac{t}{\lambda}$ = 0·4 { K = 1·3 Total = 2·34.

LOSSES	Cos φ = 0·9 LAG / LEAD			
	1 F.L. UPF	0·9 pf X.F.L.	0·9 pf X.F.L.	X.F.L.
Windage Bearing	2·26	2·26	2·26	
Core –	2·34	2·34	2·34	
I^2R Stator 100 75°C	0·123	0·151	0·15	
Eddy 0·45 / Load 0·65	0·0554 / 1·52	0·068 / 1·52	0·068 / 1·52	
I^2R Field 100 75°C	0·326	0·386	—	
Exciter –				
Total –	6·624	6·724	6·338	
Output –	40·0	40·0	40·0	
Input –	46·624	46·724	46·338	+ 10% on LOSSES.
% Efficiency –	85·45	85·5	= 46 96	
Guarantee/Offer		62·7 HP.		

POLE DIES

Face Clip .....

Piercing .....

Blanking .....

Base Clip .....

WINDING HEATING

Stator Watts/sq. in. ..... Slot T. Drop ..... °C

Field Surface ..... Watts/Sq. in. .....

K = " ..(mod.) ..... (at °C) ..... °C (res)

REGULATION, etc.

At F.L. (PF =) = ... %

" " (PF =) = ... %

Max. Output = ... x h.p.

P_o at ..... PF = ... x kVA

WR^2 Rotor 35 lb ft².

WR^2 Flywheel .....

Nat. Frequency .....

H Rotor .....

~~WEIGHTS~~

S. Copper .....

F. Copper $\phi_t = 0{\cdot}33$ mgl.

Sq. C. Bars $B\phi_t = 1{\cdot}325$ Tesla.

Sq. C. Rings .....

S. Punchings $B\phi_s = 0{\cdot}342$ Tesla.

R. Punchings .....

Exciter Size .....

Rectifiers .....

Des. by AMH / EB / EJ. ..... Appd. by .....

C optimum Compensation. 15·7 μF

Use 12 μF $X_c = 4{\cdot}425\ \Omega = 0{\cdot}79$ pu. % comp. 67%.

For Duplicate Machines and Test Results, see over

Form 583/X

Fig.17

Design sheet data for the experimental machine.

Rating: 44·4 KVA. 500/250 volts. cos φ = 0·9.

Date..... Ds. No.....

SYNCH ..... MEA./A.C./S.O. No..... No. off.....

CUSTOMER ..... Ex/Q/Req. No.....

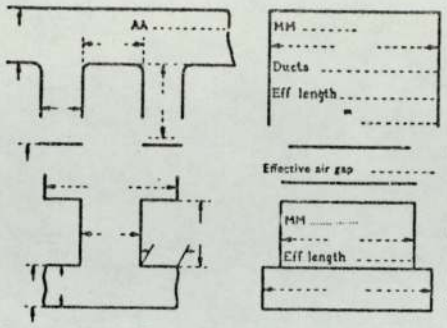

Specn. ..... Enclosure .....

Drive ..... Fans .....

kVA 55 Connection ..... P. Speed .....

Cos ϕ 0·9 Volts per phase 550 Pole Pitch .....

kW h.p. 49·5 Amp. per phase 100 Pole Arc ..... = ... %

G = ... G_1 = ... Leakage Co-eff ..... Eff. P.A. = ... %

$\text{Flux} = \frac{\times 10^2}{444 \times} = 0{\cdot}117$ mgl. Field Flux = ... mgl.

$AT_{AR} = \frac{}{} = 212$ ..... per inch .....

$\frac{kVA}{D^2L.N.} = \text{.....} \times 10^{-3}$ B. mean = 16·4 A.C. per slot .....

A.C. per inch .....

$\epsilon = 0{\cdot}518$ · $\Phi_t = 0{\cdot}343$ $\Phi_{oc} = 0{\cdot}451$

STATOR WINDING FIELD WINDING

Saturation Curve Refs. .....

	Section	Density	AT/in.	Length	AT
Stator Core					
Stator Teeth B max ... K_m					
Air Gap C ... $k\delta$ ... L_{eff}	5·31	64·5			320
Rotor Teeth					
Pole Body					
Spider					
α AT_{si} = 1·26 SCR = $\Phi_L = 0{\cdot}66 AT_0$					

	AT	A	V	kW
N.L. 550 Volts	325	2·27	142·5	0·324
FL(PF=1·0)	346	2·42	152·0	0·318
lag xFL(PF=0·9)	388	2·72	171·0	0·465
lead xFL(PF=0·9)	316	2·21	138·5	0·306
xFL(PF=)				

Cond. Insn. I.S.	Turn Insn. SW.	Ext. Turns I.S.	Turn Insn. F.F.
Type of Winding		Type of Winding	
No. of Slots: Total		No. of Poles	
per phase		Poles in parallel	
Eff. per ph.		Turns per pole	
Conductors per Slot: Total		d. bare	
Effec.		d. insul.	
d. bare		Cross Secn.	
d. insul.		Current Density	
"mf Cr. Secn.		Mean L. of Turn	
Insulation: Sides		Total cu. Secn.	
T. and B.		Ind. Volts per layer	
Total Copper Secn.		Res. at 75°C	
Current Density 3860	3090	" " °C	
Mean L. of Turn		SQUIRREL CAGE WINDING	
Turns in Series/ph		Bars	□"
Res./ph. at 75°C ..... = ... %		Rings/Segs	
" " " °C ..... = ... %		λr ..... λs ..... $\frac{\lambda r}{\lambda s}$ = ...	

P_s = ... = { ω

x_l = ... = { %

Iron Losses { Core ..... } { ..... = ... Teeth ..... } { ..... =

Surface Loss ..... =

Loss ..... =

S/g = f_s = Total =

LOSSES	Cos ϕ =	0·9 lag	0·9 lead	
	F.L. OFF	X.F.L.	X.F.L.	X.F.L.
Windage Bearing	2·26	2·26	2·26	2·26
Core –	2·5	2·5	2·5	2·5
I^2R Stator 100 75°C	0·194	0·239	0·239	0·239
Eddy Load	1·57	1·58	1·58	1·58
I^2R Field 100 75°C	0·368	0·465	0·306	–
Exciter –	6·89			
Total –	↓	7·04	6·88	6·42
Output –				49·5
Input –				55·9
% Efficiency –			+10%	
Guarantee/Offer			≥ 75·5HP	

POLE DIES	WINDING HEATING
Face Clip	Stator Watts/sq. in. ..... Slot T. Drop ..... °C
Piercing	Field Surface ..... Watts/Sq. in. .....
Blanking	" ..... (mod.) ..... (at °C) ..... °C (rest)
Base Clip	K =

REGULATION, etc.	WEIGHTS
At F.L. (PF=) = ... %	S. Copper .....
" " (PF=) = ... %	F Copper ..... $B\phi_e$ = 1·37 Tesla.
Max. Output = ... x h.p.	Sq. C Bars .....
P_o at ..... PF = ... x kVA	Sq. C Rings .....
WR^2 Rotor	S. Punchings ..... $B\phi_s$ = 0·357 Tesla.
WR^2 Flywheel	R. Punchings .....
Nat. Frequency	Exciter Size .....
H Rotor	Rectifiers .....

Des. by AMH/EB/E.J.D. ..... Appd. by .....

(Series Capacitor see "Compensation" Details) For Duplicate Machines and Test Results, see over

Form 583/X

Fig.18

Design sheet data for the experimental machine.

Rating increased to 55KVA. 550 volts, 100 Amps, cosϕ = 0·9.

(a) (approximately 2×full size)

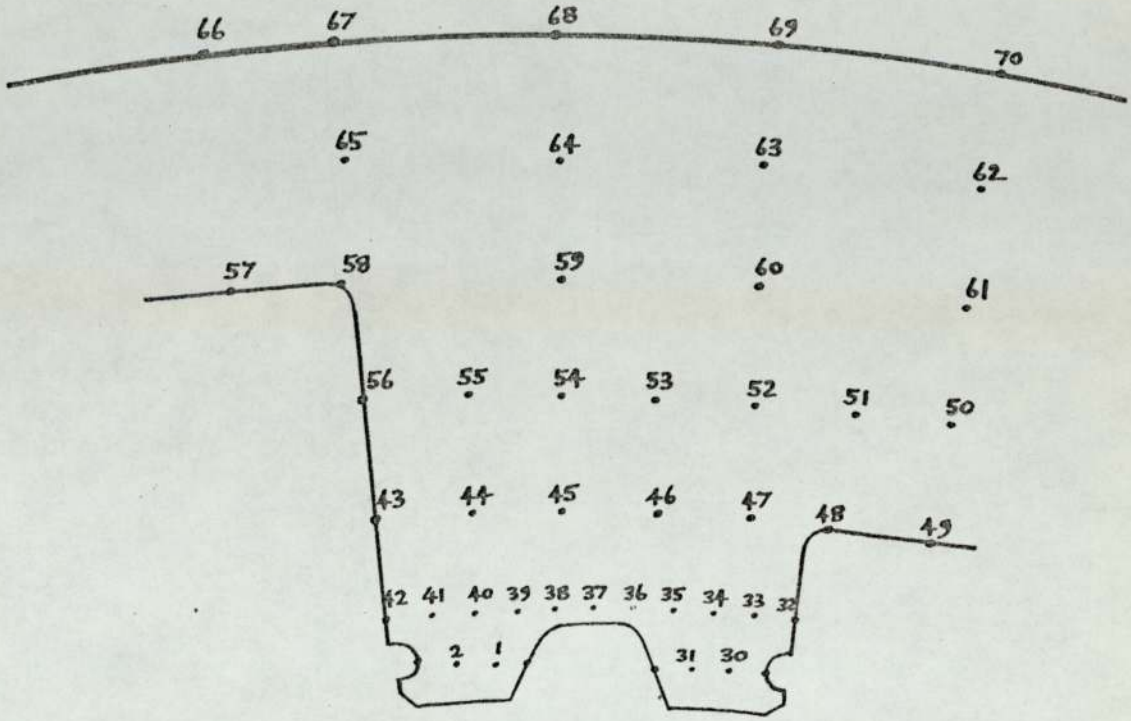

(b) (approximately 3.5×full size)

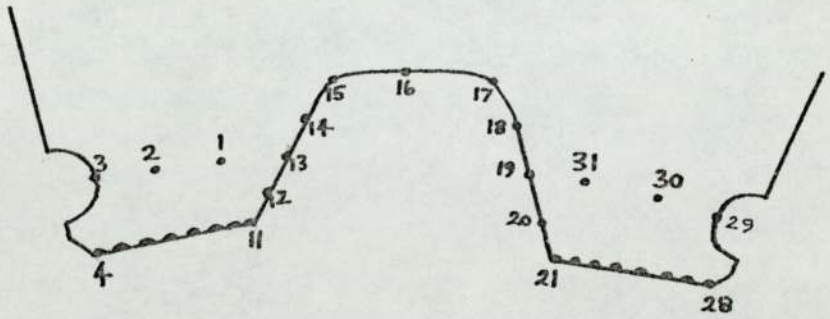

Fig.19

STATOR SEARCH COILS.

(a) Search coils in the stator core and teeth.

(b) Search coil arrangement for the small teeth.

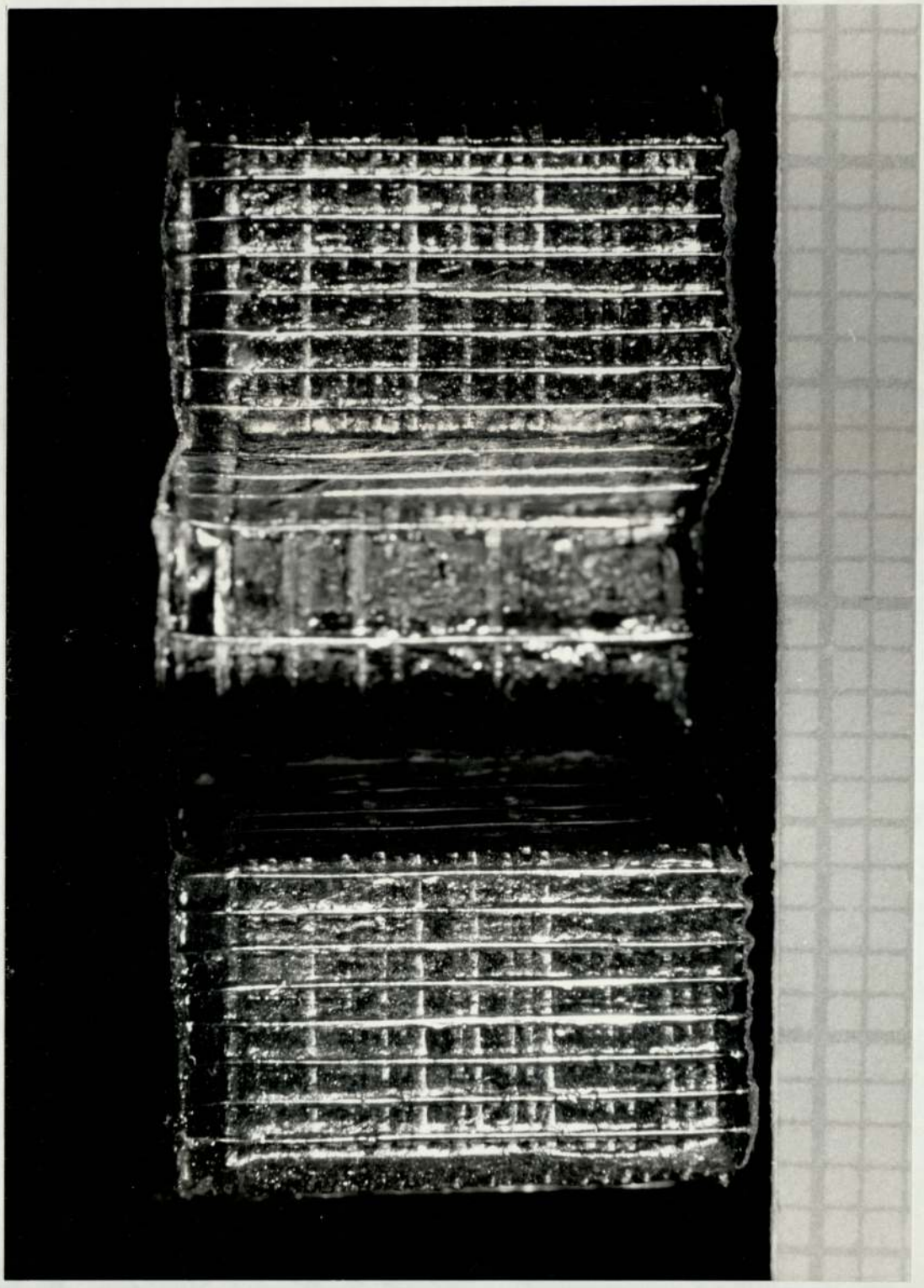

Fig 20.

Search coils on the surface of the stator teeth.

(grid markings - mm graph paper)

Approximate scale - 7x full size.

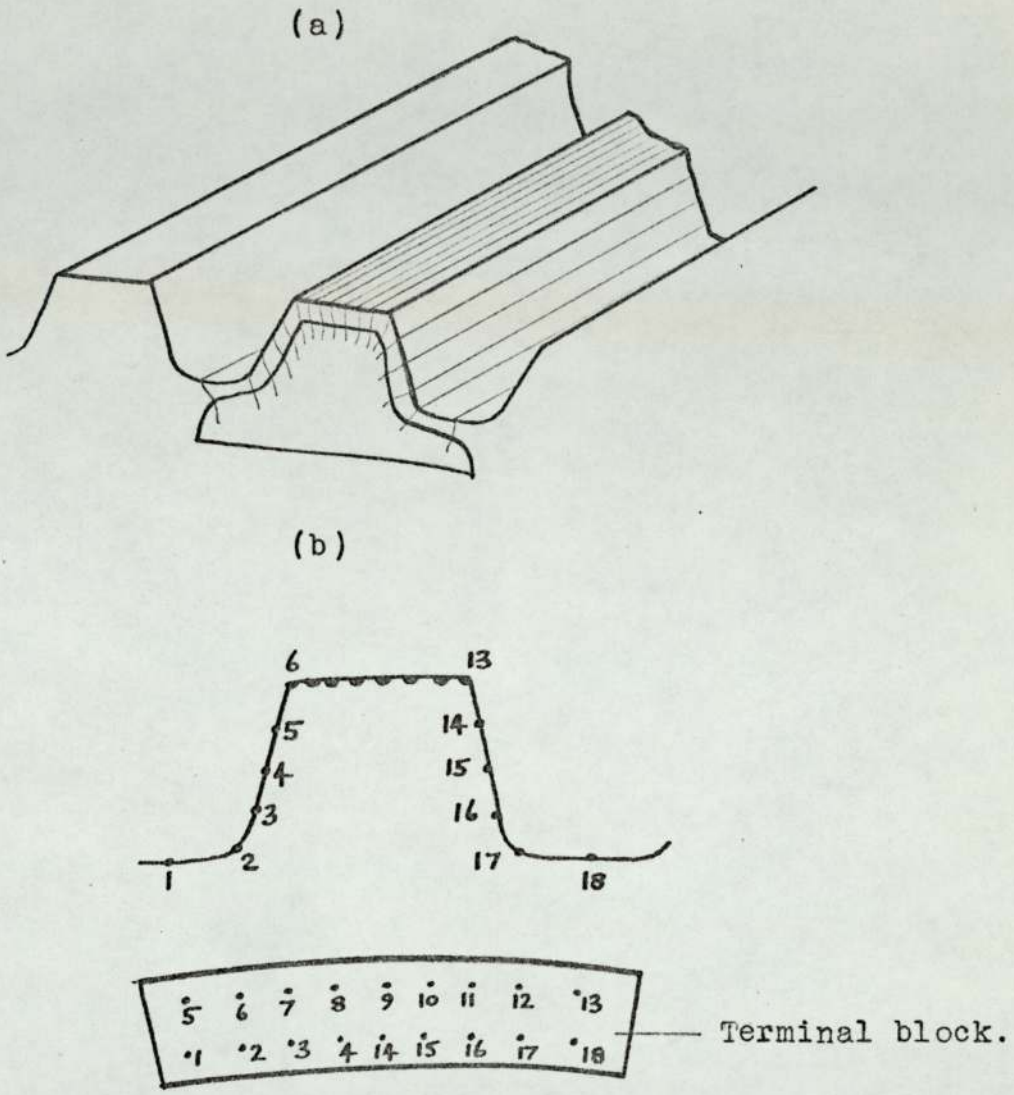

Fig. 21

Rotor search coils.

(a) General view of rotor search coils showing the common connection on the drive end of the machine.

(b) Numbering system for search wires and the terminal block. (non-drive end)

Fig 22.

Rotor search coils and terminal block connections on the non-drive end.

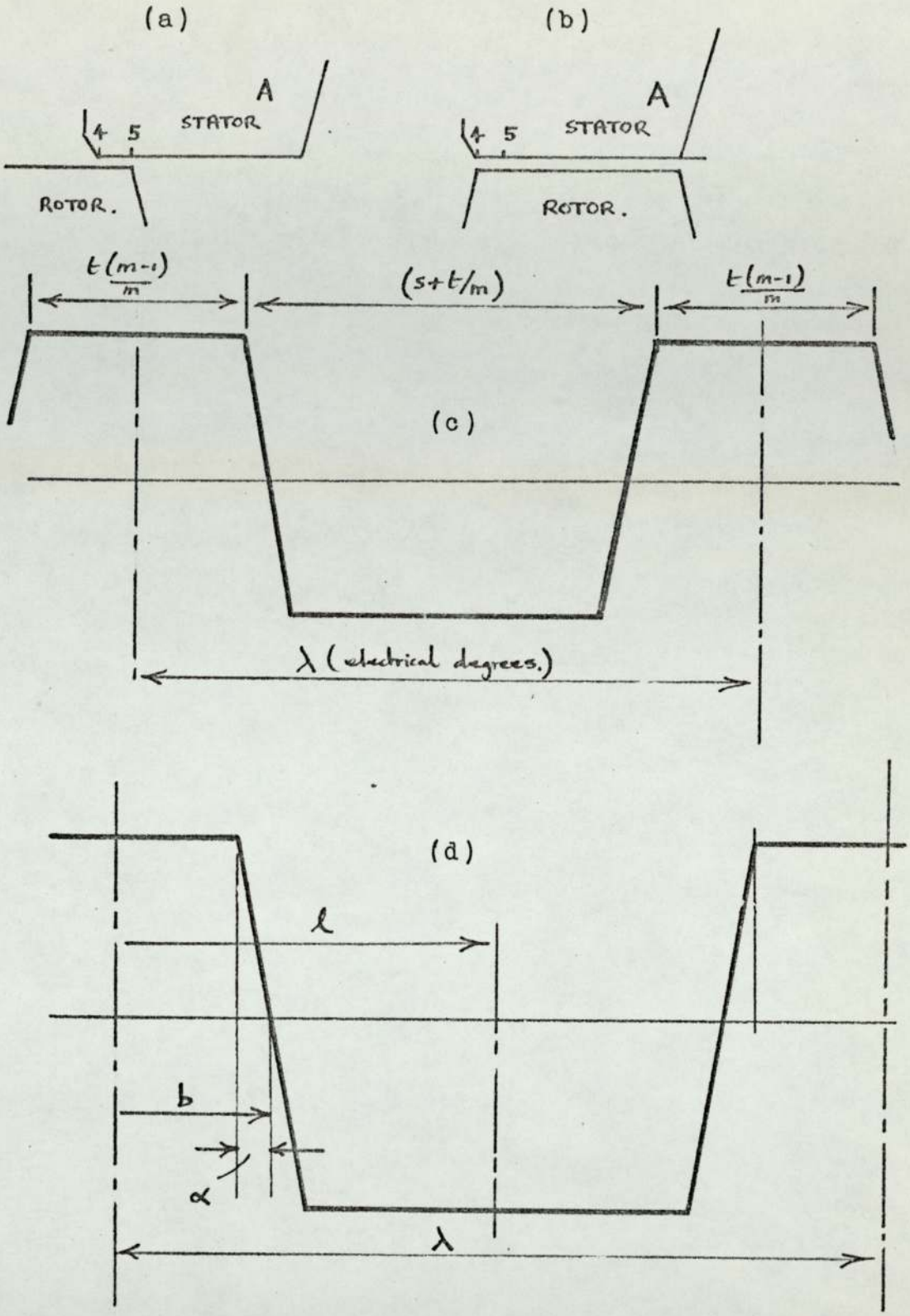

Fig.23

Flux waveforms in a small section of the tooth surface.

(a) Flux in section 4-5 (just reached a maximum.)

(b) Flux waveform still a maximum in 4-5, just about to decrease.

(c) Flux waveform in a small section for the experimental machine.

(d) Approximation to flux waveform, (section 4.1.3).

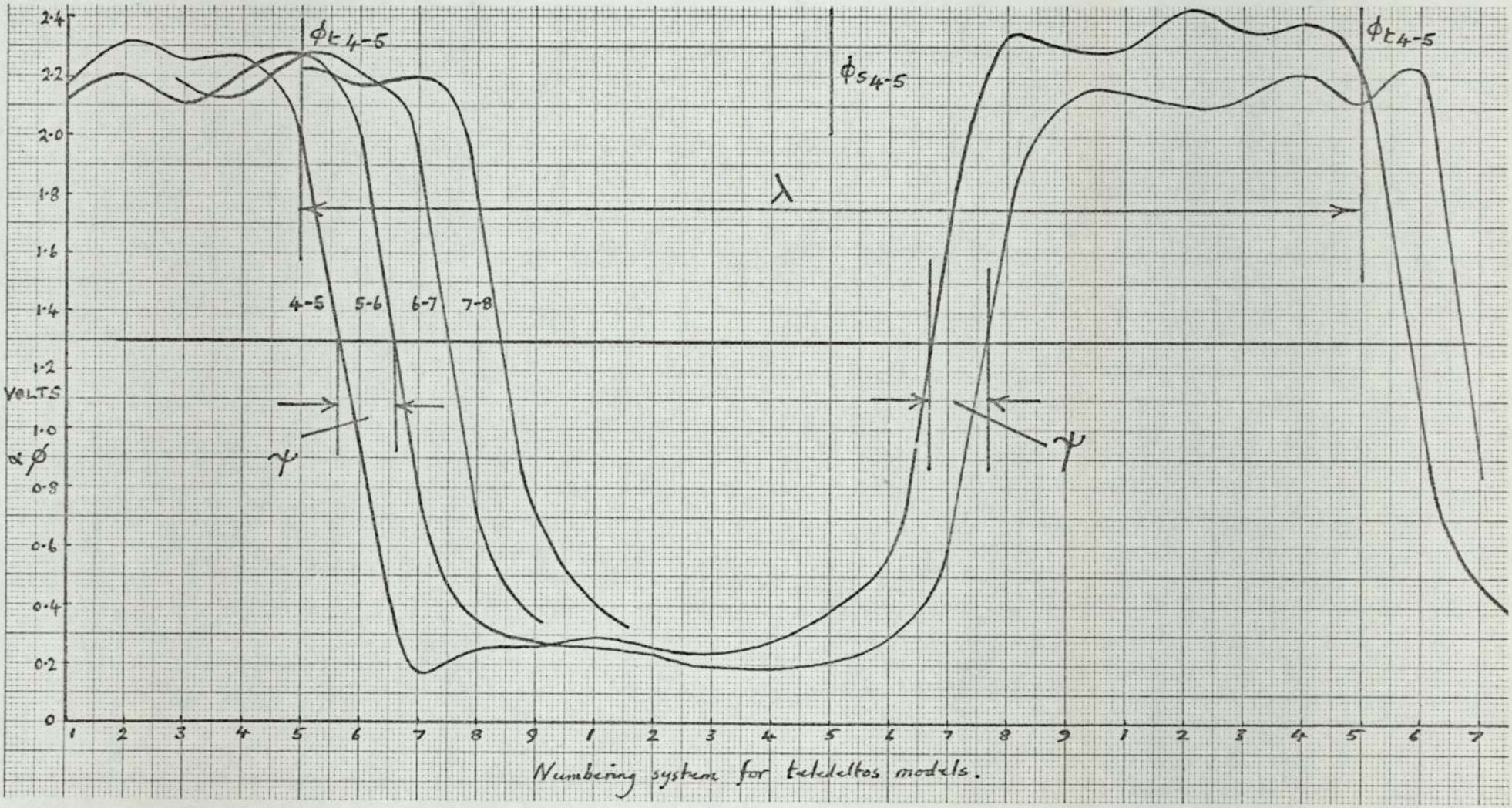

Fig. 24
Flux waveforms at the tooth surface from teledeltos plots.

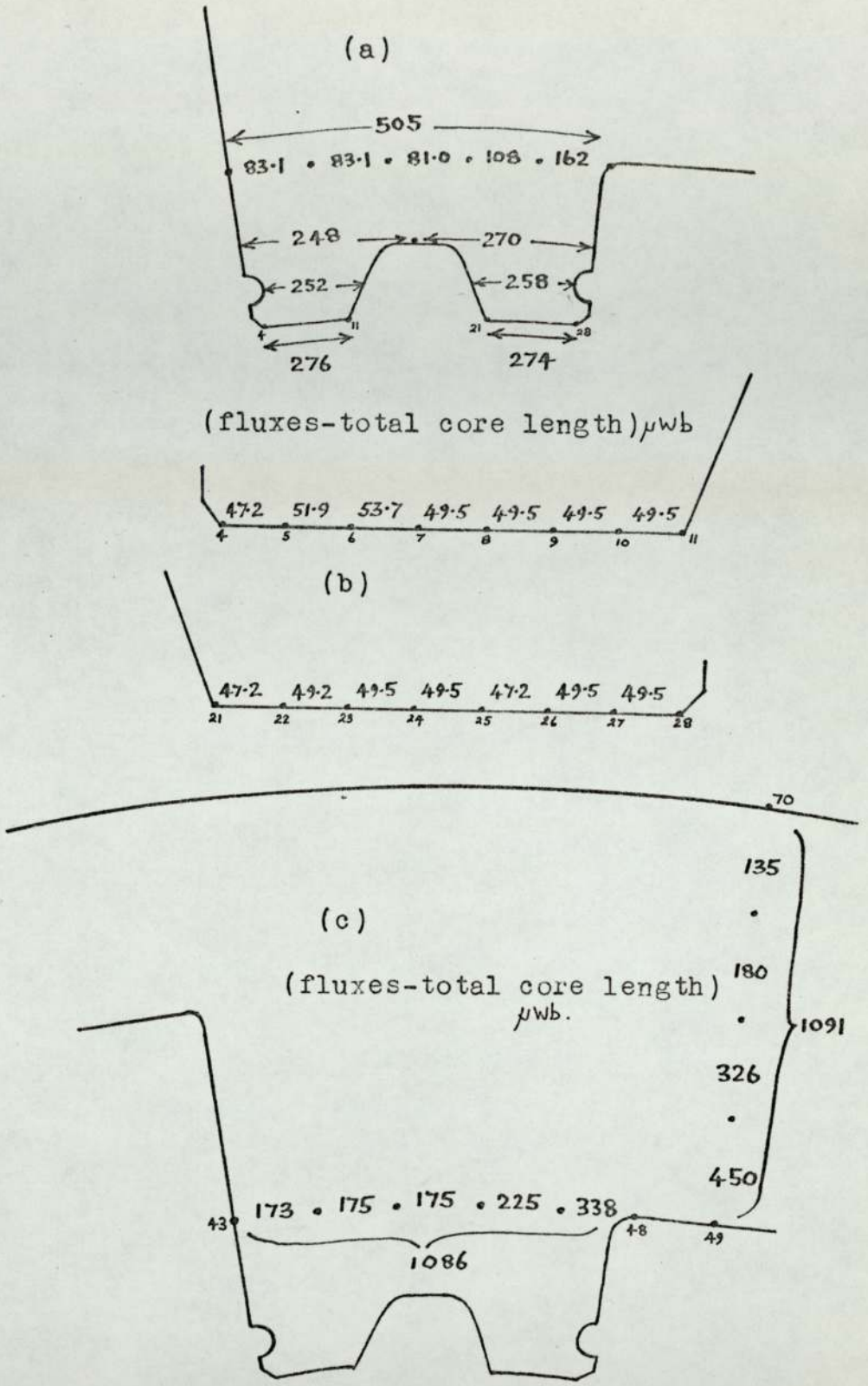

Fig.25

Fundamental flux distribution in the core and teeth.
(open-circuit.)

(a) fundamental fluxes in the core and teeth (lamp field.)
(b) fundamental fluxes at the tooth surface (lamp field.)
(c) fundamental fluxes in the core, (2·15 amps field.)

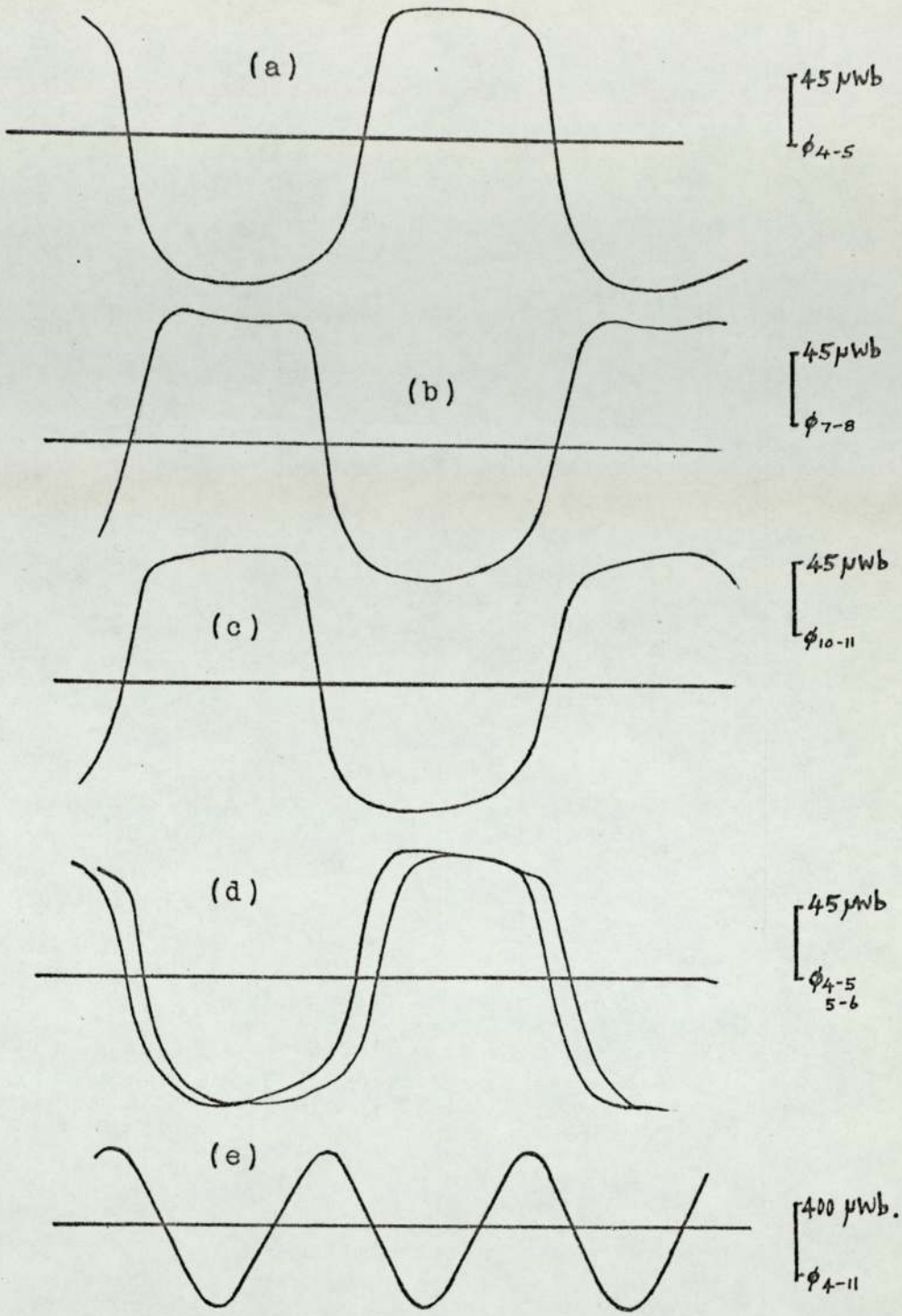

Fig. 26

Measured flux waveforms at the tooth surface.
(1·0amp field excitation.)

(a) flux waveform in section 4-5.
(b) flux waveform in section 7-8.
(c) flux waveform in section 10-11.
(d) phase displacement between (4-5) and(5-6).
(e) flux waveform across the total tooth surface.

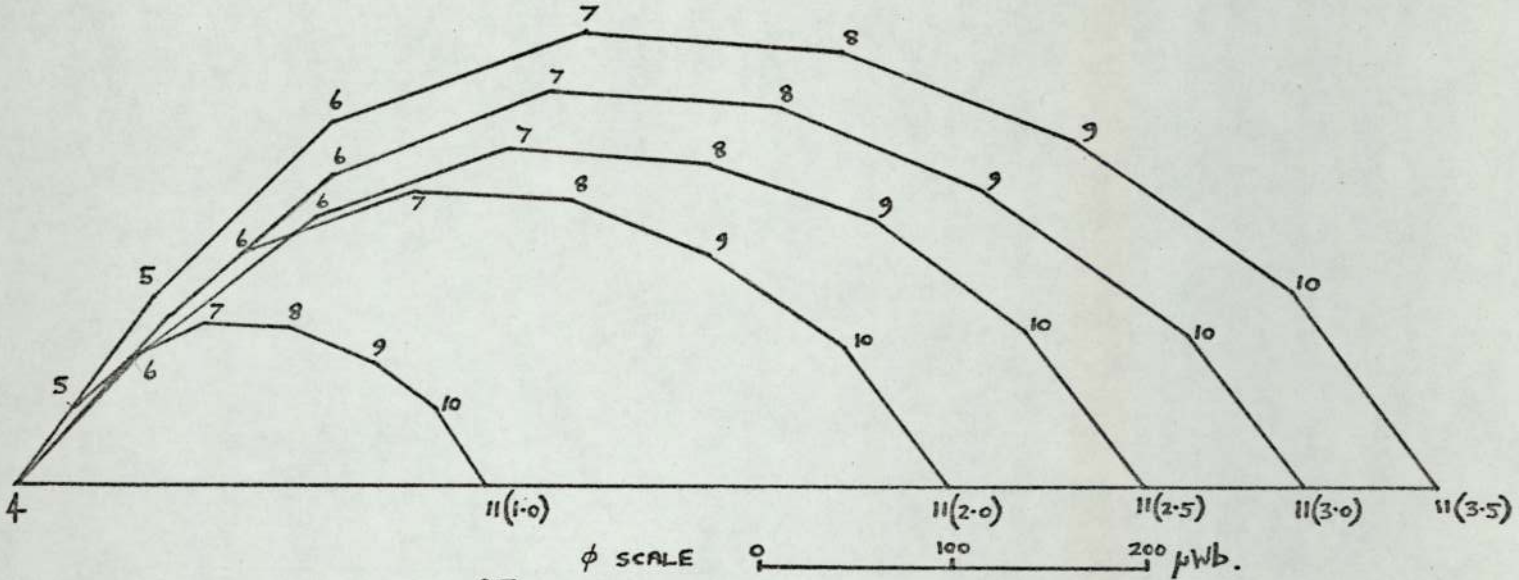

Fig.27

Addition of fundamental fluxes in small sections of the tooth surface.

ϕ (4-5,5-6,6-7,-------10-11) fluxes in small sections of the tooth surface.

ϕ_{4-11} total flux through the surface,(fundamental)

(1·0), (2·0), etc denotes the field excitation in amps.

Fig. 28

Addition of second harmonic fluxes in small sections of the tooth surface.

4-5,5-6,6-7,----10-11- fluxes at the tooth surface.

ϕ_{4-11} flux across the total tooth surface.

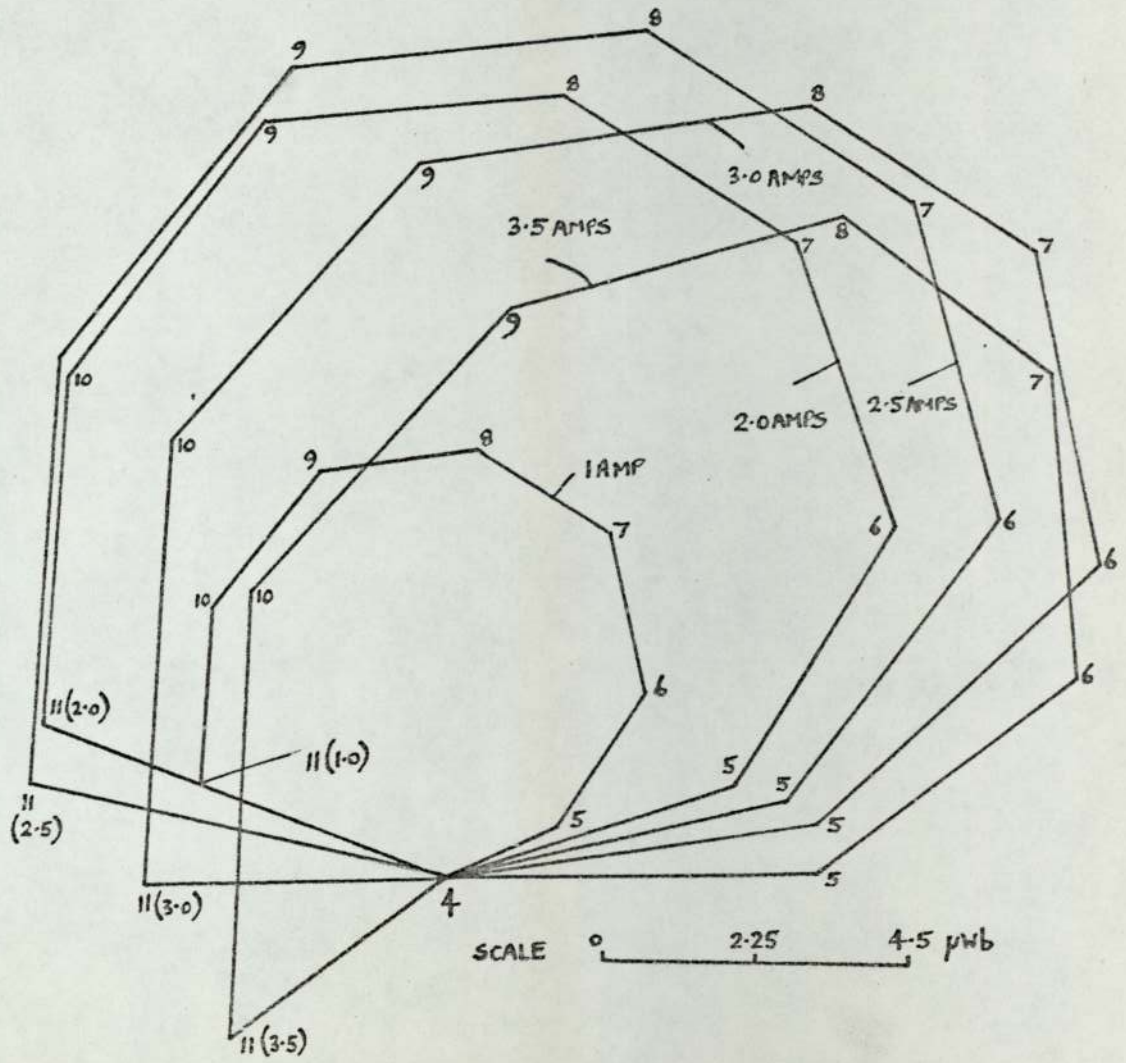

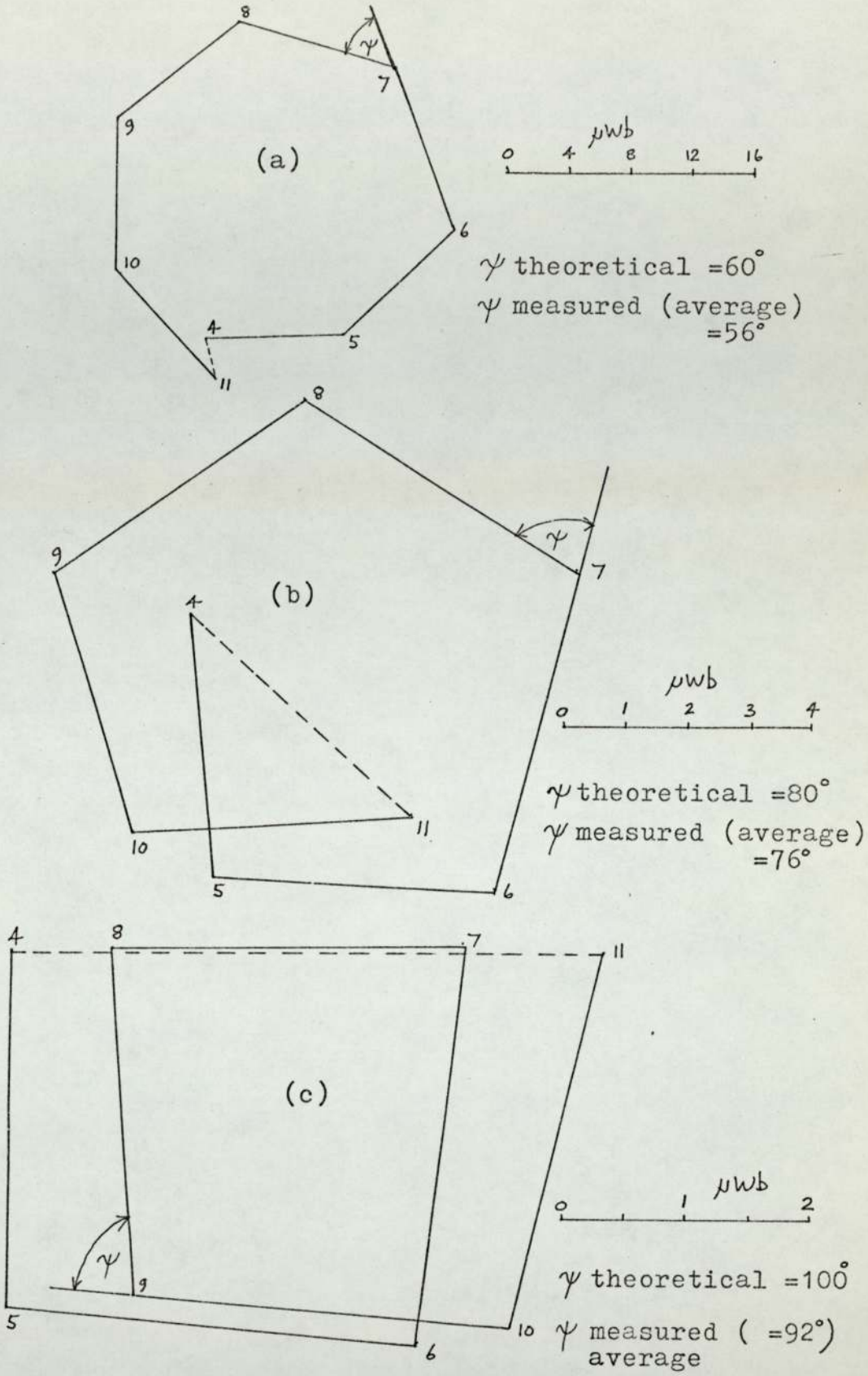

Fig.29

Addition of harmonic fluxes at the tooth surface.

(a) 3rd harmonic flux. (vector diagram drawn
(b) 4th harmonic flux. from measurements on
(c) 5th harmonic flux. the actual machine.)

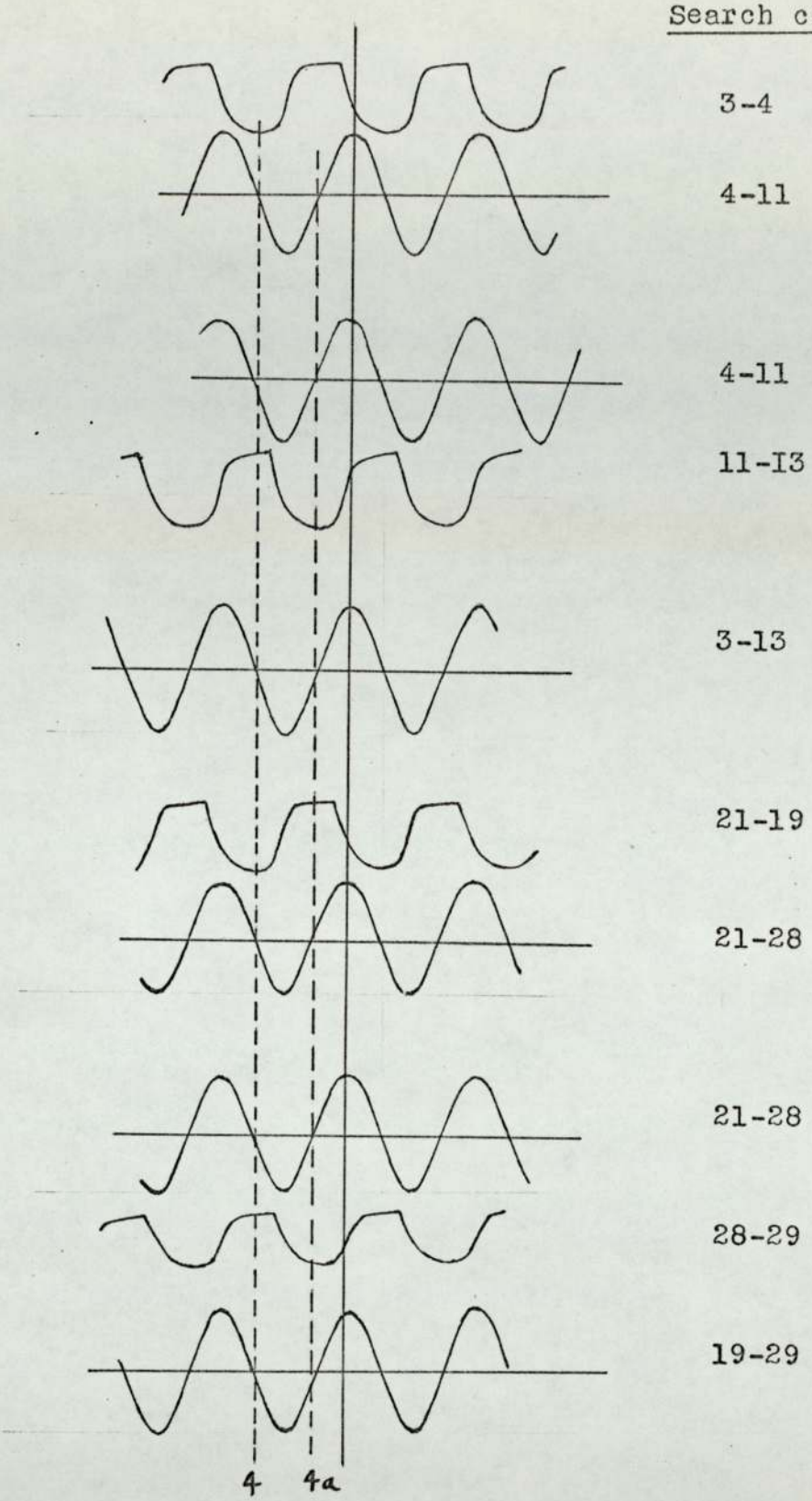

Fig.30

Leakage flux waveforms, 1·0amp field excitation.

(4) -position of symmetry, Fig 14 .

(4a)-position of symmetry, Fig 14 .

Main flux waveforms:- 1cm=450μWb.
Leakage flux waveforms:- 1cm =110·0μWb.

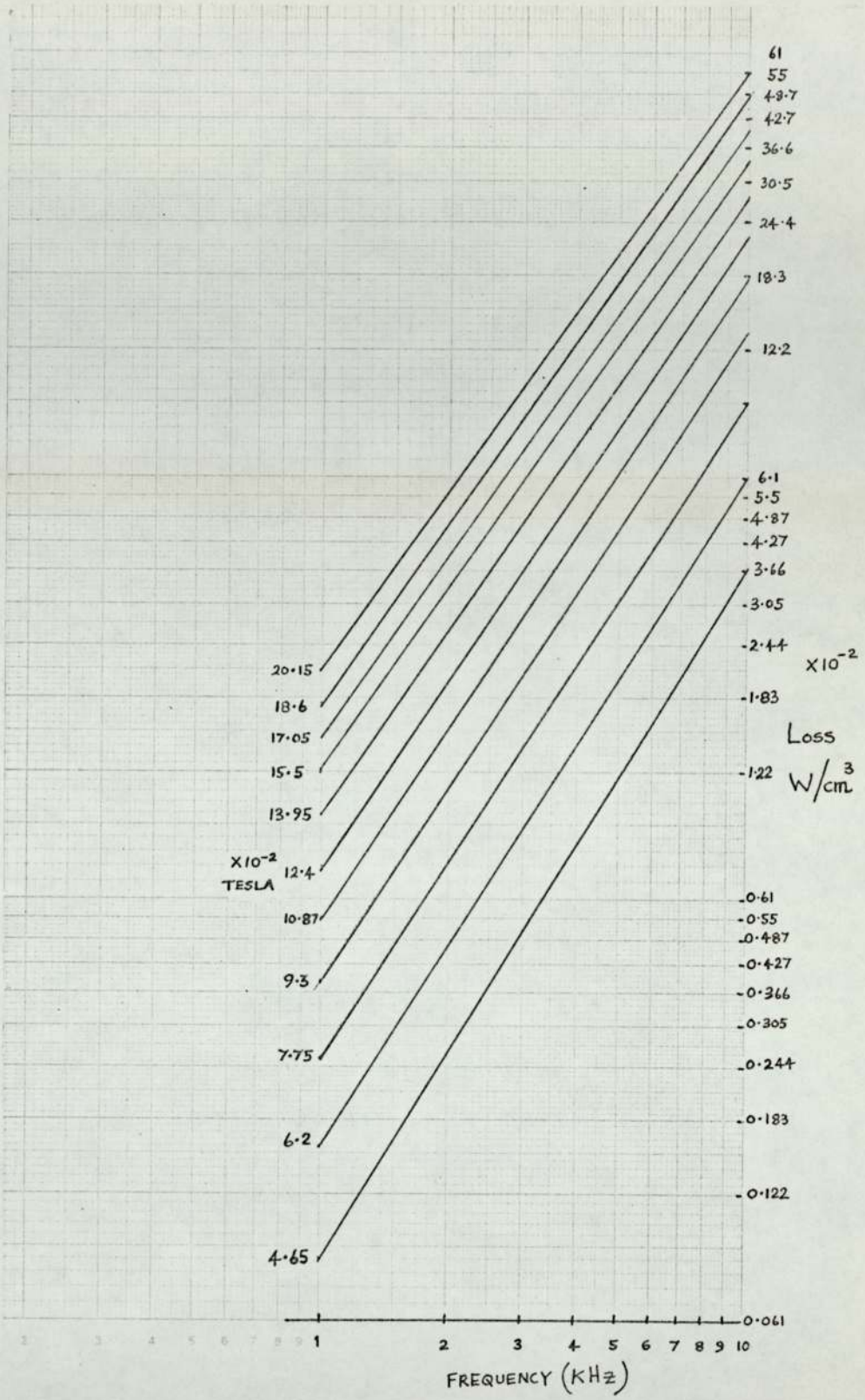

Fig.31

Core loss of MM262 0.0178cm Grade 1100,

for frequency range 1000/10,000 Hz.

Slope at 0.2 Tesla = 1.41 (loss $\propto f^{1.41}$)

Slope at 0.046 Tesla = 1.63 (loss $\propto f^{1.63}$)

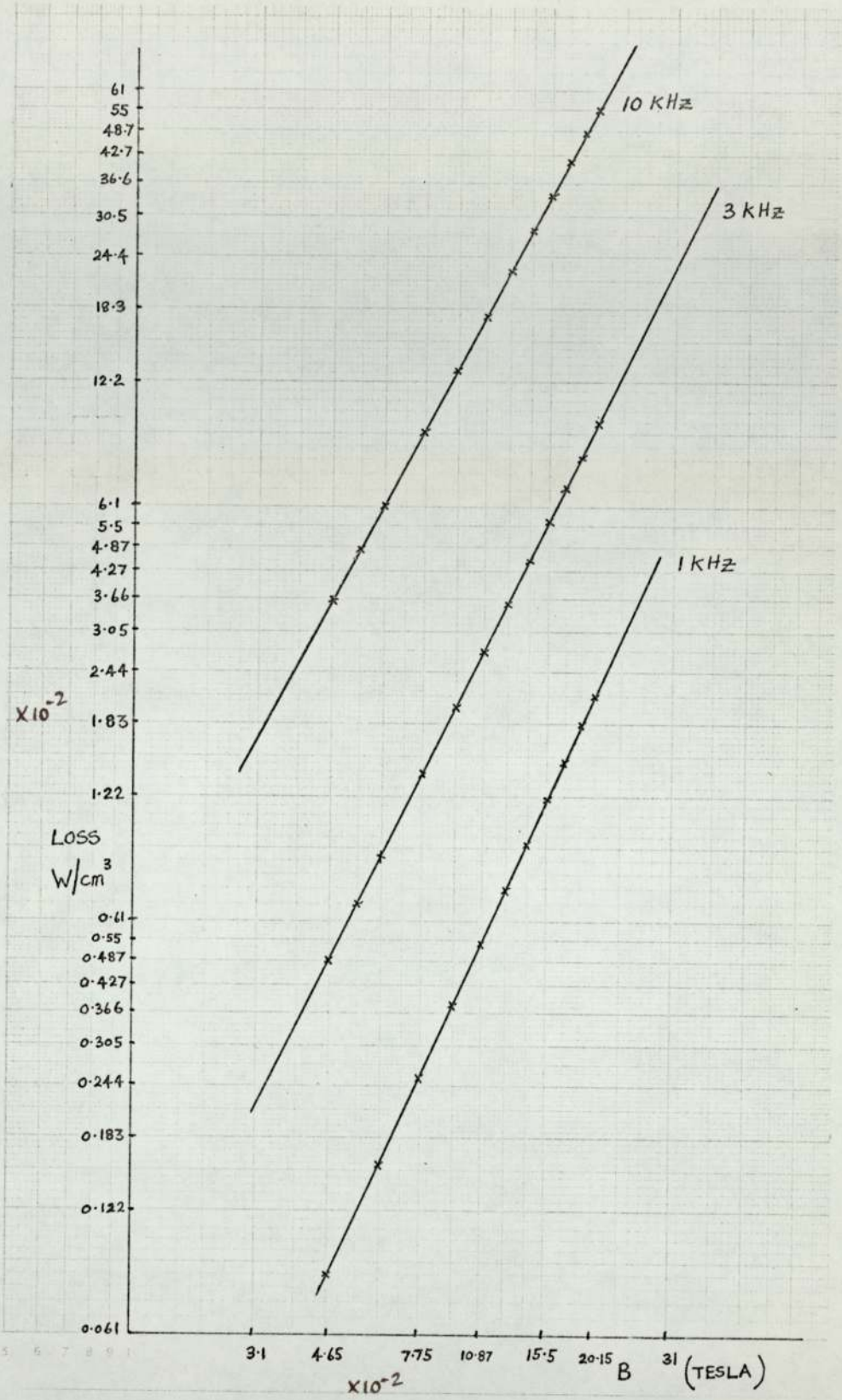

Fig.32

Core loss of MM262 0.0178cm Grade 1100, for frequency range 1000/10,000 Hz.

Slope for 1000 Hz = 2.2 (loss $\propto B^{2.2}$)

Slope for 3 Khz = 2.09 (loss $\propto B^{2.09}$)

Slope for 10 Khz = 1.89 (loss $\propto B^{1.89}$)

Fig.33

Fundamental and second harmonic fluxes in the stator core-no damping.

A-fundamental fluxes.

A1-ϕ_{43-48}, A2-$2\phi_{43-48}$.

A3-ϕAC_{3-4}, A4-ϕ_{58-67}

B&C-second harmonic fluxes.

B1-ϕ_{43-48}, B2-ϕ_{58-67}

C-flux linking the ac coil.

•-measured from actual machine.

x-$2\phi_{49-70}$

▲-vector diagram.

D_1 - ϕAC_{3-4} top damping

D_2 - ϕAC_{3-4} bottom damping.

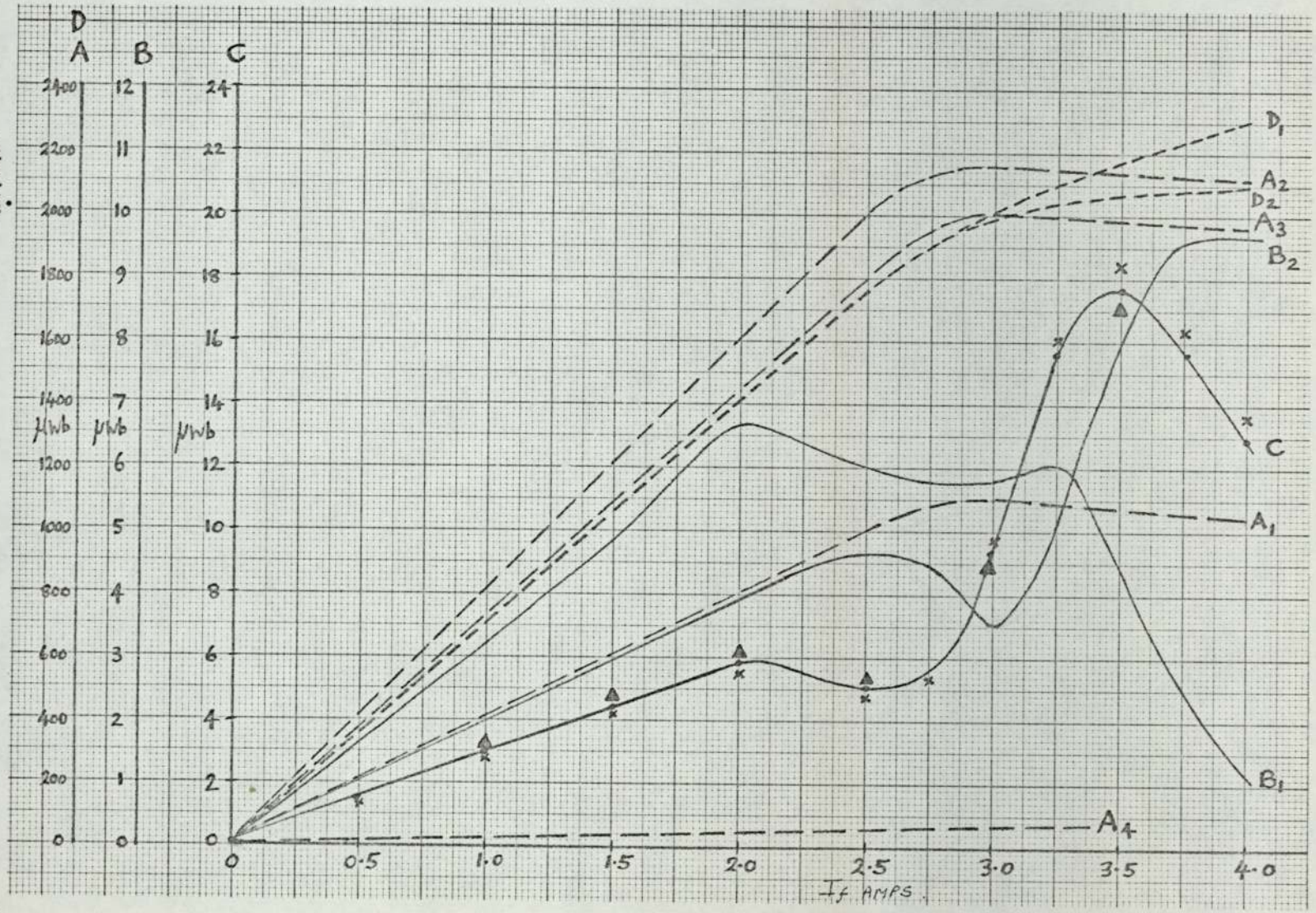

Fig.34

Second harmonic fluxes in the core with bottom and top damping for various values of field excitation.

A1-ϕ_{43-48} bottom damping.

A2-ϕ_{58-67} bottom damping.

A3-ϕ_{49-70} bottom damping.

A4-ϕAC_{3-4} bottom damping. (measured)

▲ ϕAC_{3-4} bottom damping. (vector diagram.)

B1-ϕ_{43-48} top damping.

B2-ϕ_{58-67} top damping.

B3-ϕ_{49-70} top damping.

B4-ϕAC_{3-4} top damping.

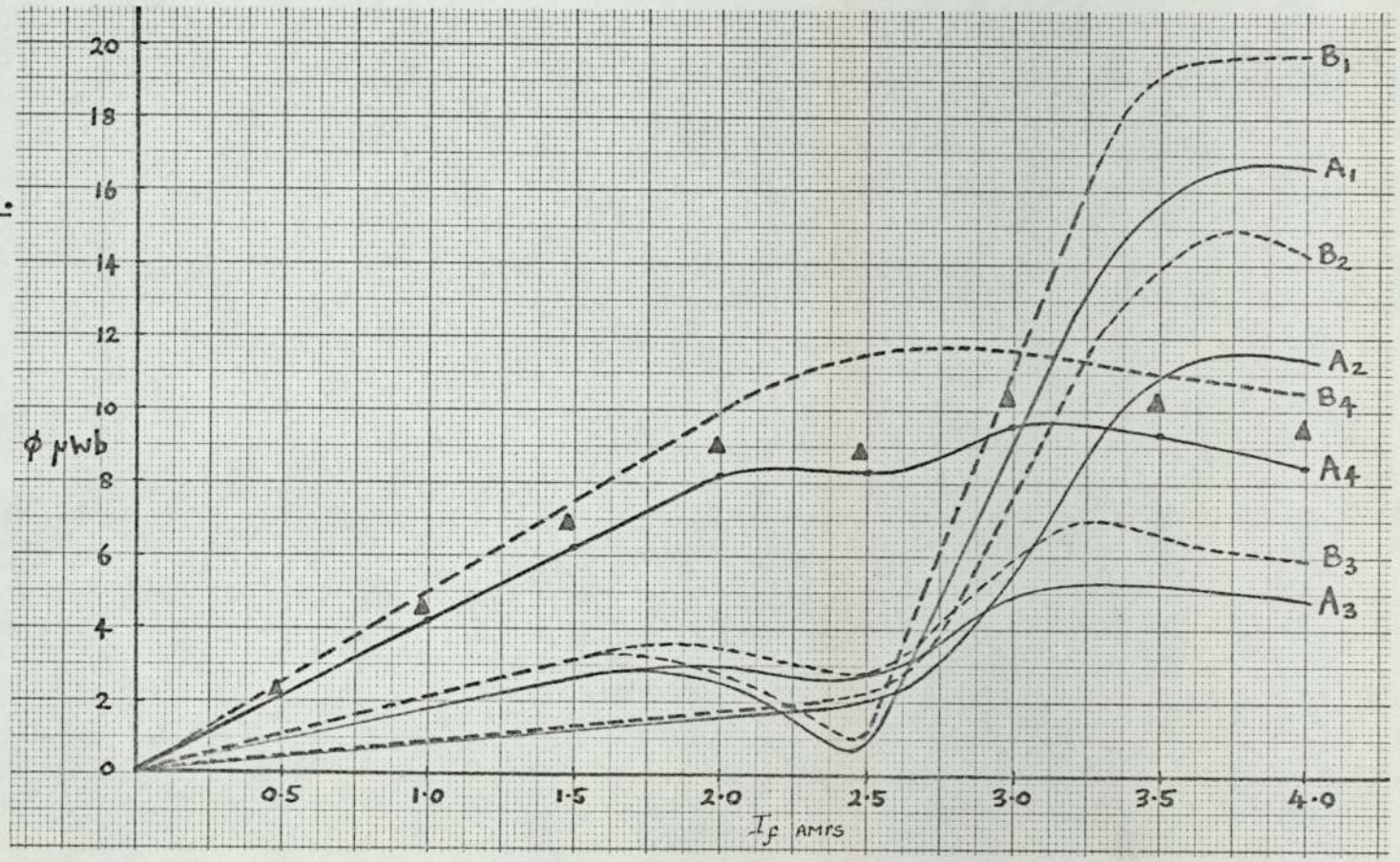

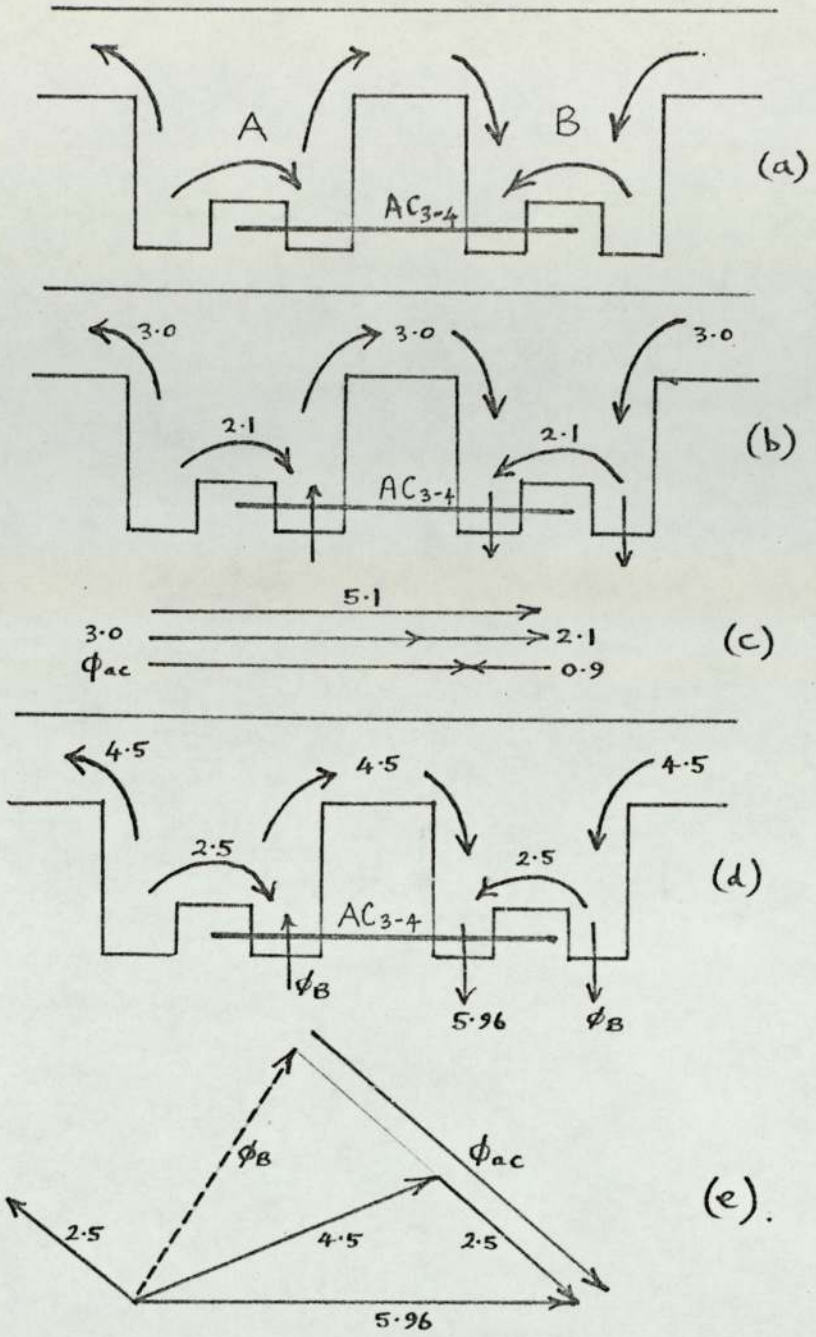

Fig.35

Second harmonic flux paths in the stator core, (no damping.)

(a) second harmonic flux paths.
(AC_{3-4} ac coil linking the search coil area.)

(b) second harmonic flux paths for 1·5 amps field excitation.

(c) phase relationship between ϕ_{49-70}, ϕ_{58-67}, and ϕ_{43-48} for I_f=1·5 amps.

(d) second harmonic flux paths for 2·5 amps field excitation.

(e) phase relationship between ϕ_{49-70}, ϕ_{58-67}, and ϕ_{43-48} for I_f =2·5 amps.

Fig.36

Second harmonic flux distribution in the stator core, open circuit. No damping.

(a) ϕ_{43-44}

(b) ϕ_{44-45}

(c) ϕ_{45-46}

(d) ϕ_{46-47}

(e) ϕ_{47-48}.

Fluxes in μWb, total core length.

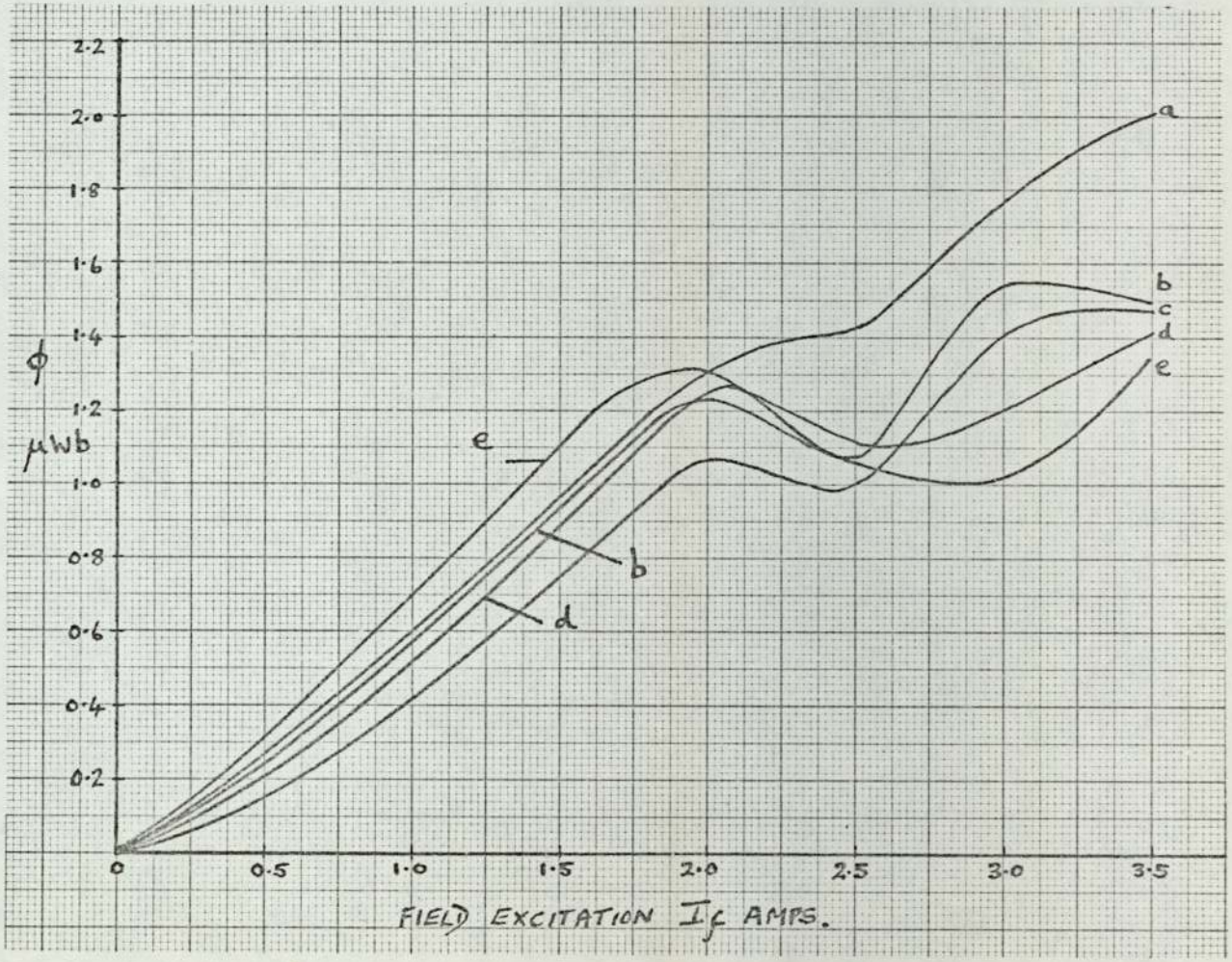

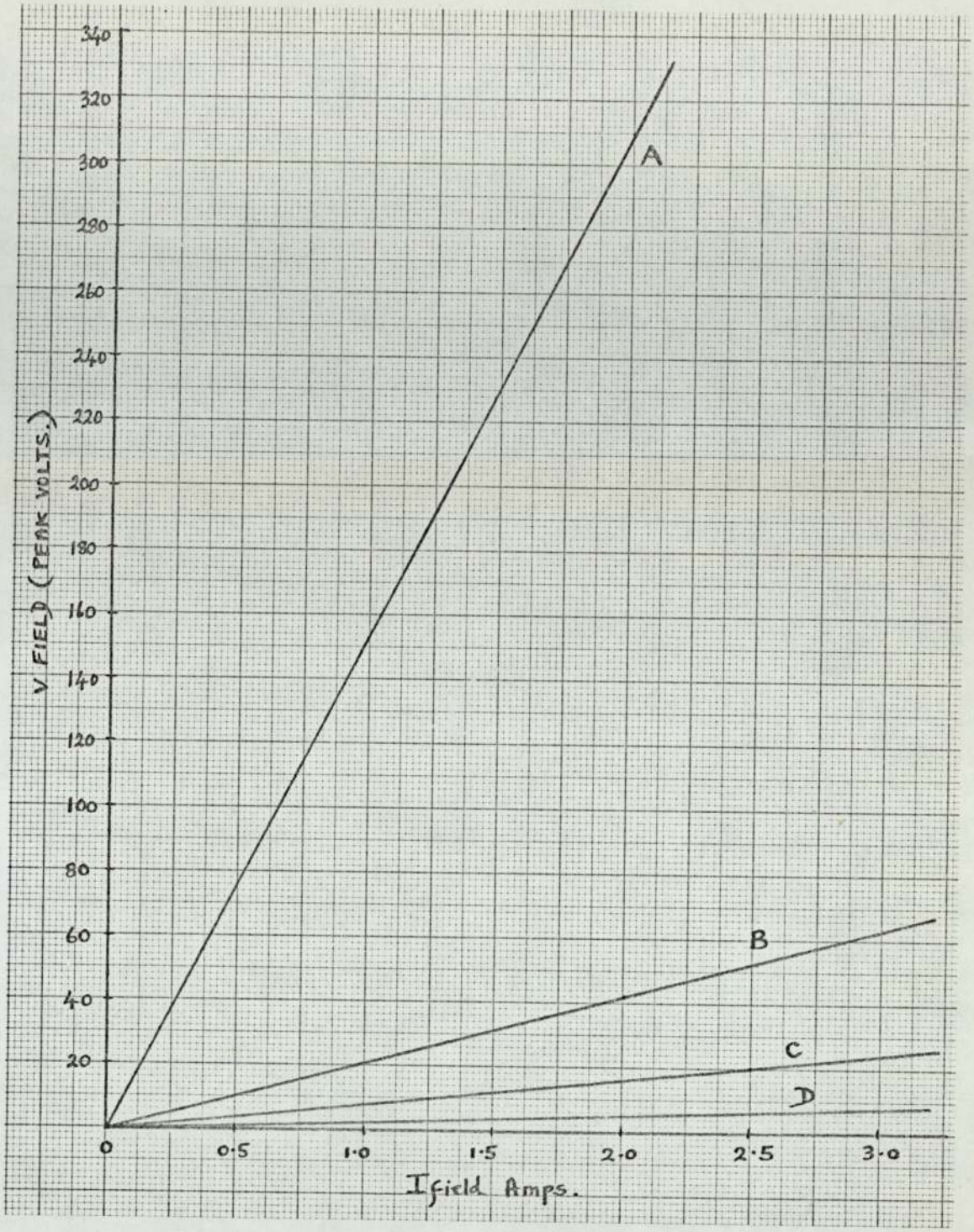

Fig.37

Voltages induced in a field coil with and without damping.

(A) no damping. (B) core damping.

(C) bottom damping. (D) top damping.

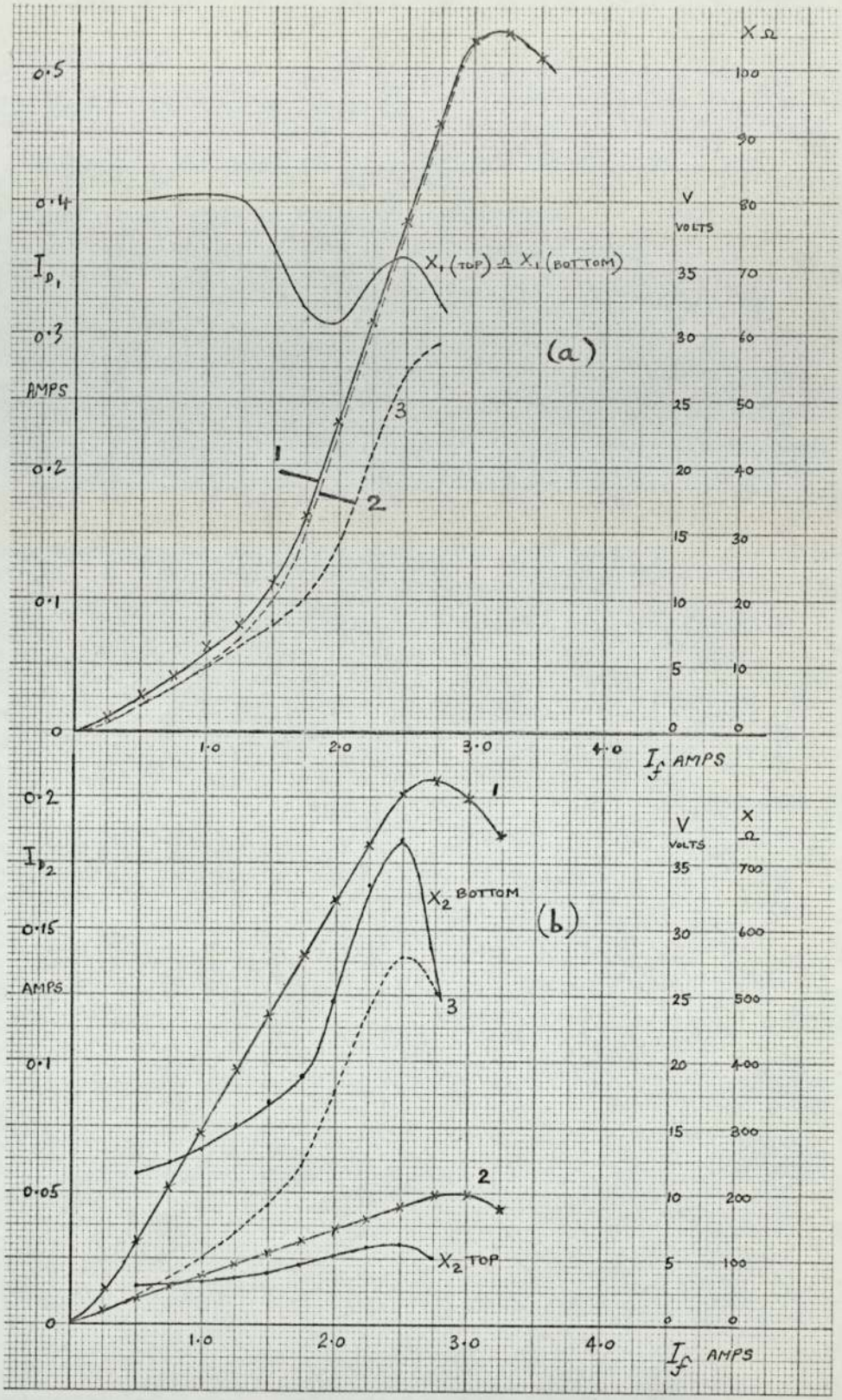

Fig.38

Fundamental and second harmonic damping currents.

(a) Fundamental currents. 1-bottom damping.
2-top damping.

(b) Second harmonic currents. 1-top damping.
2-bottom damping.

3(a)-fundamental voltage induced in damping coil on open-circuit. (no damping)

3(b)- 2nd harmonic voltage induced in damping coil on open-circuit. (no damping)

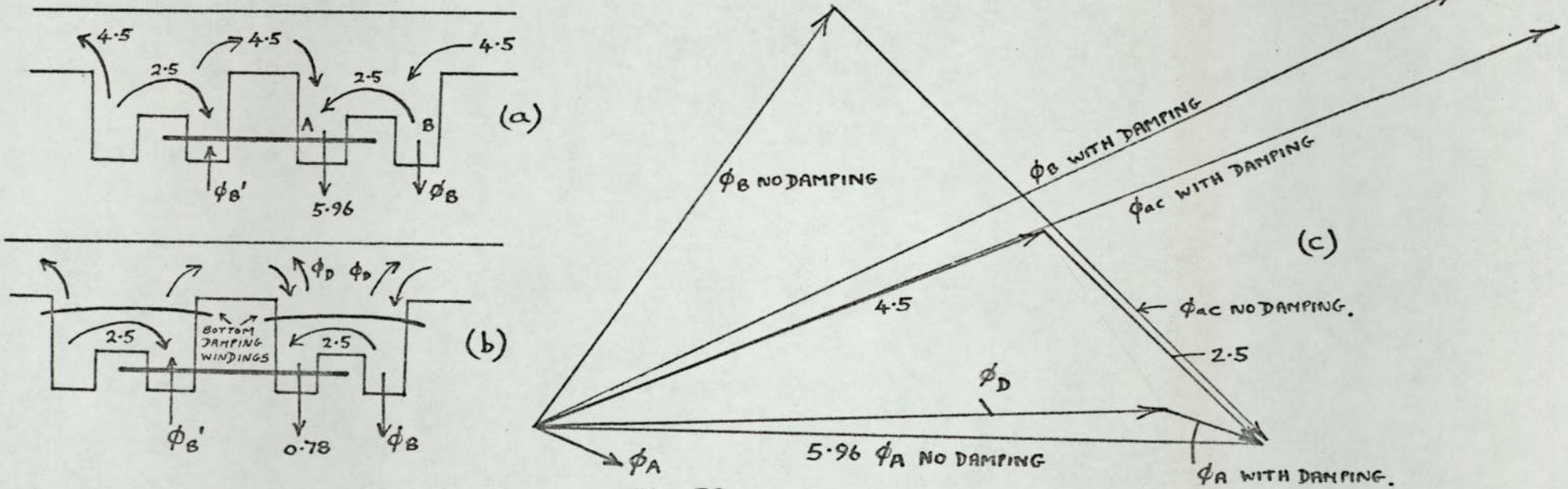

Fig.39

Second harmonic fluxes in the core with damping.

(bottom damping.)

(a) second harmonic fluxes without damping.
(2·5 amps field excitation.)
(b) second harmonic fluxes with damping.
(2·5 amps field excitation.)
(c) ϕ_{ac} from vector diagram showing the flux ϕ_D due to the damping winding.
(2·5 amps field excitation.)

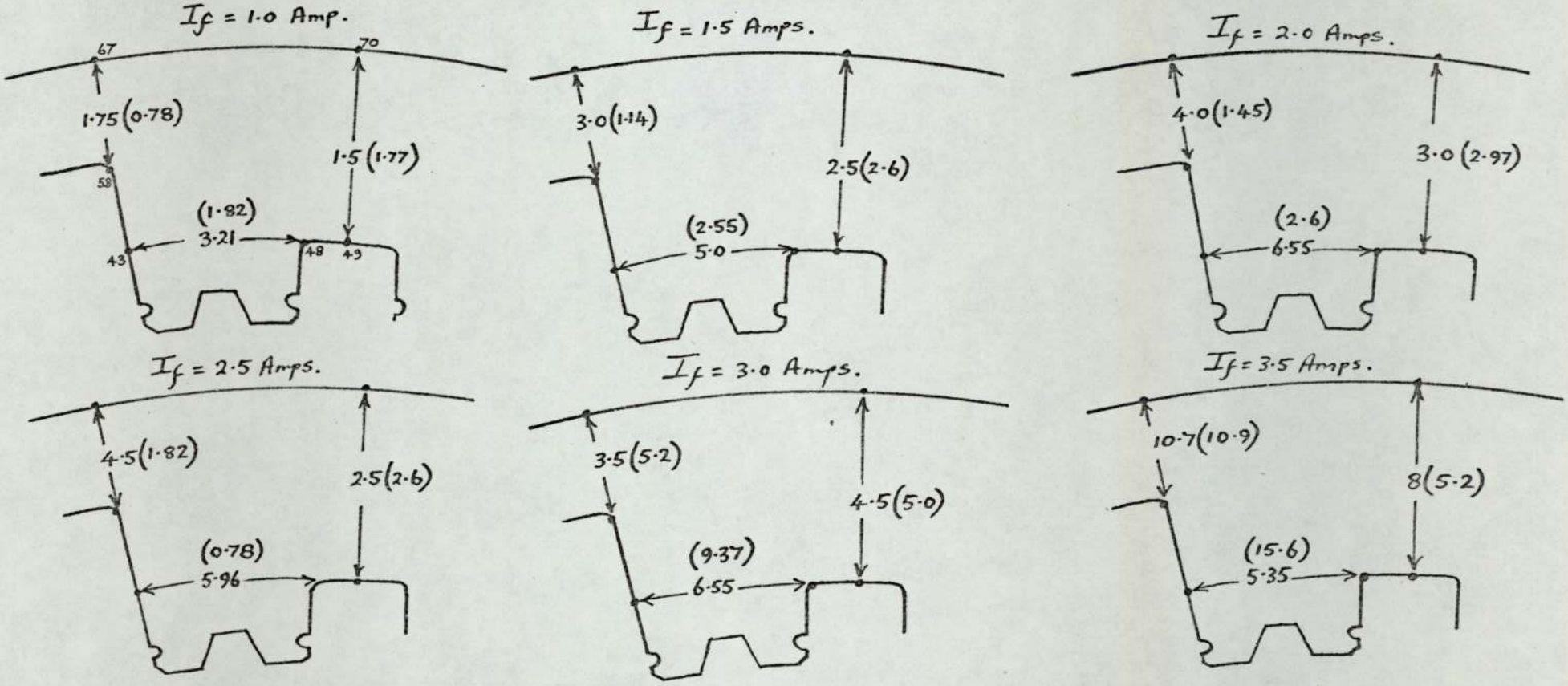

Fig. 40

Second harmonic flux distribution in the stator core.

3·21, 1·5, 1·75, 3·0, etc (no damping.)

(0·78), (1·77), (1·82), etc (bottom damping.)

(all fluxes in μwb, total core length.)

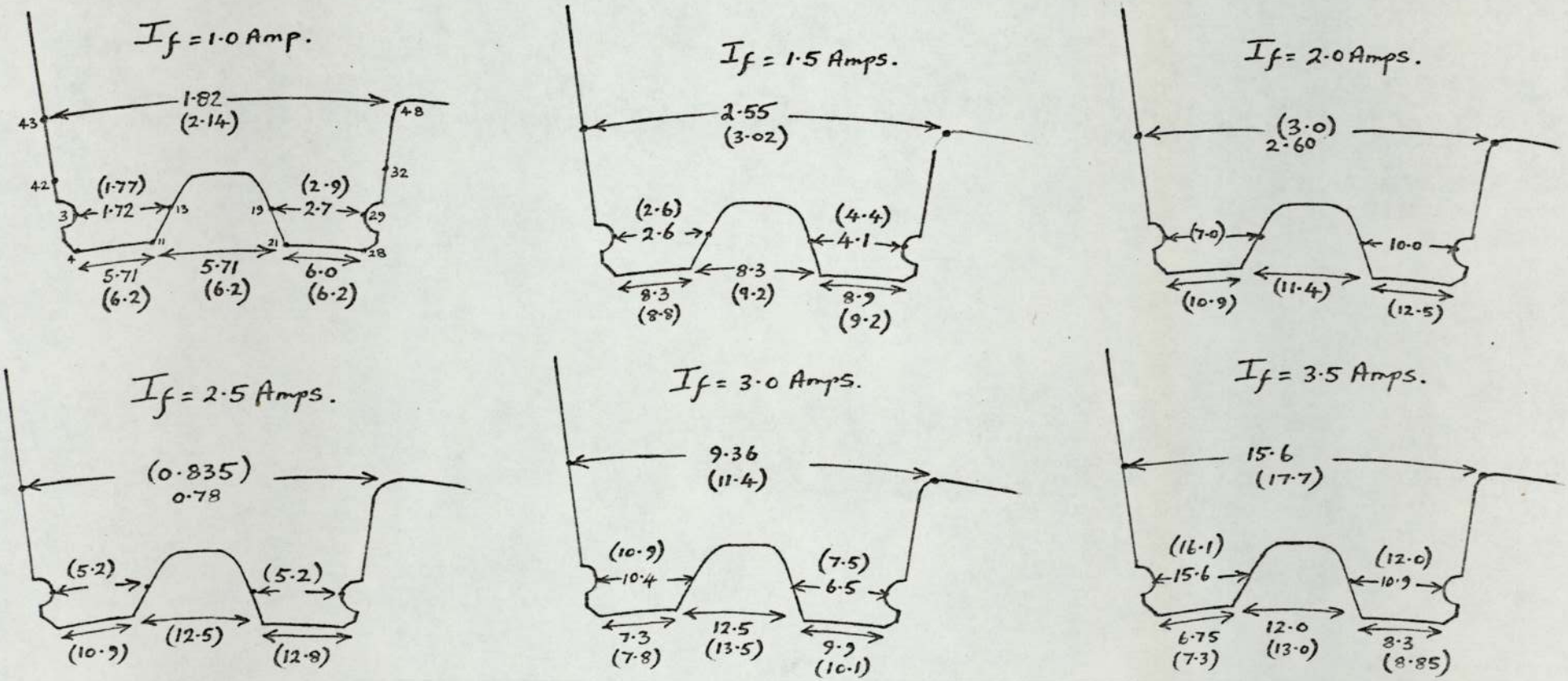

Fig. 41

Second harmonic flux distribution in the stator teeth.

(2·14), (1·77), (2·9) etc bottom damping.

1·82, 2·7, 1·72, etc top damping.
(all fluxes in μWb, total core length.)

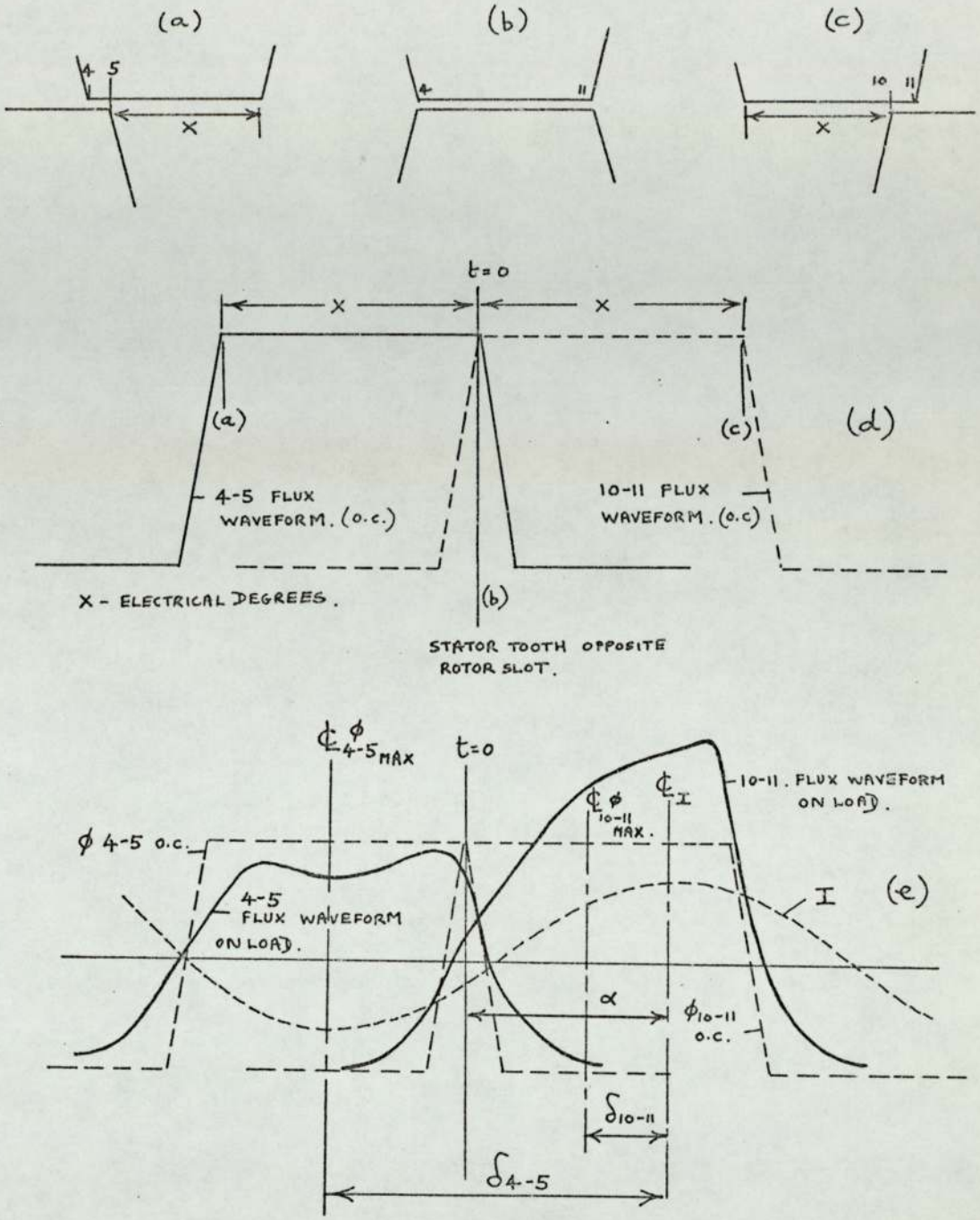

Fig. 42

Phase relationship between flux waveforms in a small section of the tooth surface and the load current waveform.

(a-) flux in section 4-5 just reached a maximum.
(b) flux in section 4-5 still a maximum; just about to decrease.
(b) flux in section 10-11 just reached a maximum.
(c) flux in section 10-11 still a maximum; just about to decrease.
(d) o.c. flux waveforms in sections 4-5 and 10-11.
(e) on load flux waveforms in sections 4-5 and 10-11.

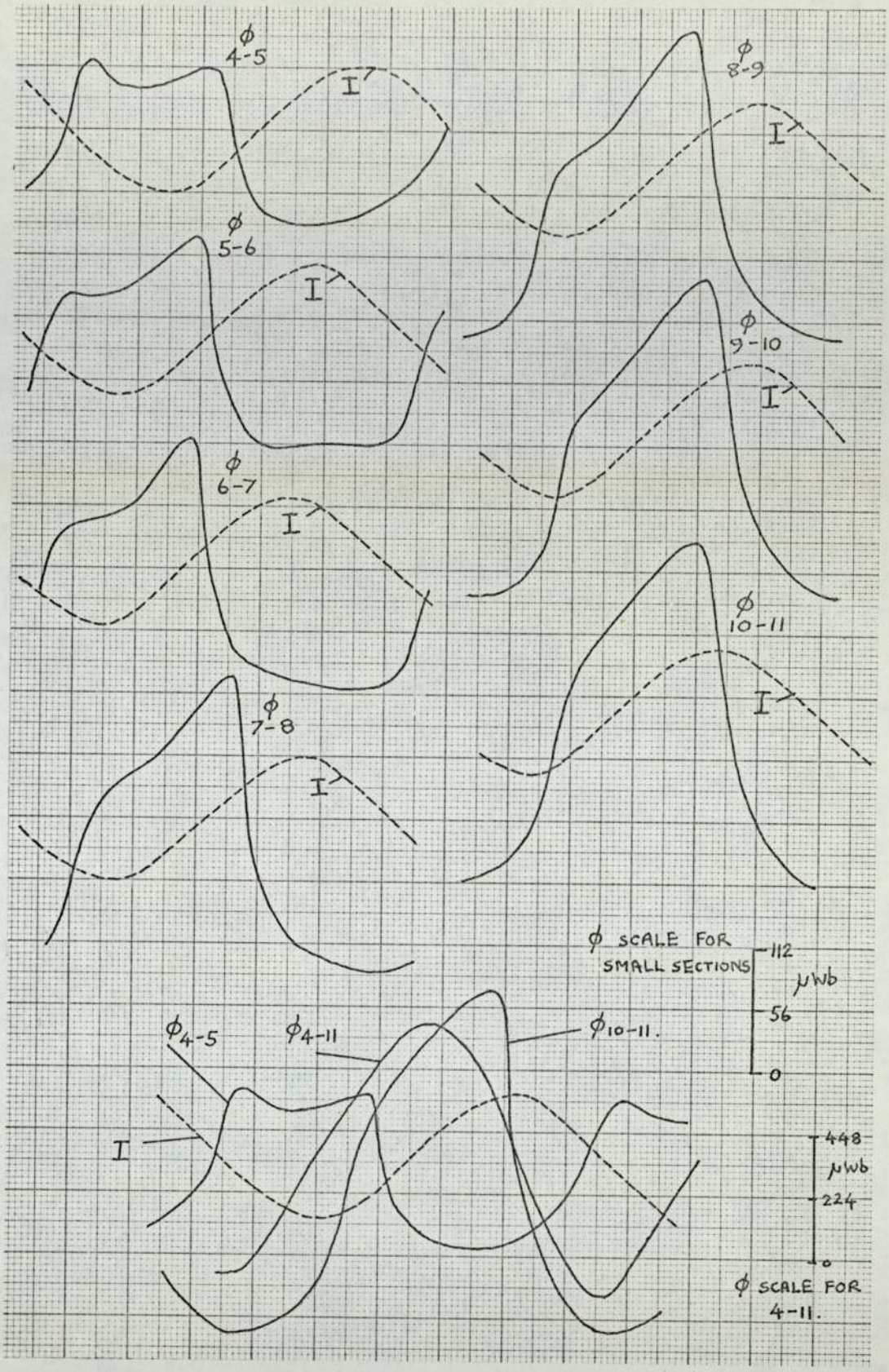

Fig.43

Flux waveforms at the tooth surface under load conditions. Series capacitor =16μF. I_f=3·05 amps. (RATED OUTPUT).

φ 4-5, φ5-6, φ6-7, ...flux waveforms in small sections of the tooth surface.

φ4-11, flux waveform across the total surface.

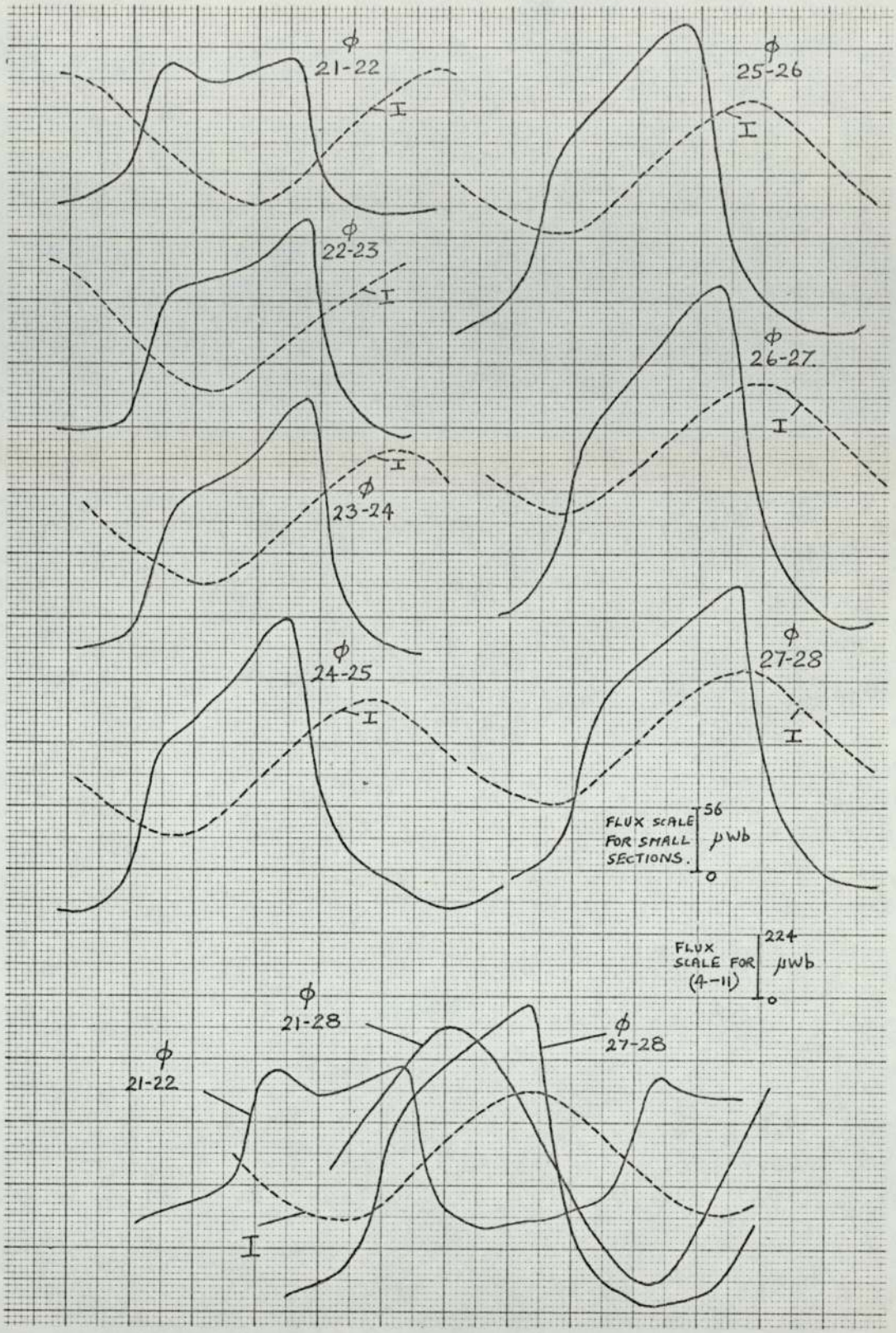

Fig. 44

Flux waveforms at the tooth surface under load conditions. SERIES CAPACITOR . C = 16μF. I_f = 3·05 AMPS. (RATED OUTPUT.)

ϕ21-22, ϕ22-23,---- flux waveforms in small sections of the tooth surface.

ϕ21-28, flux waveform across the total surface.

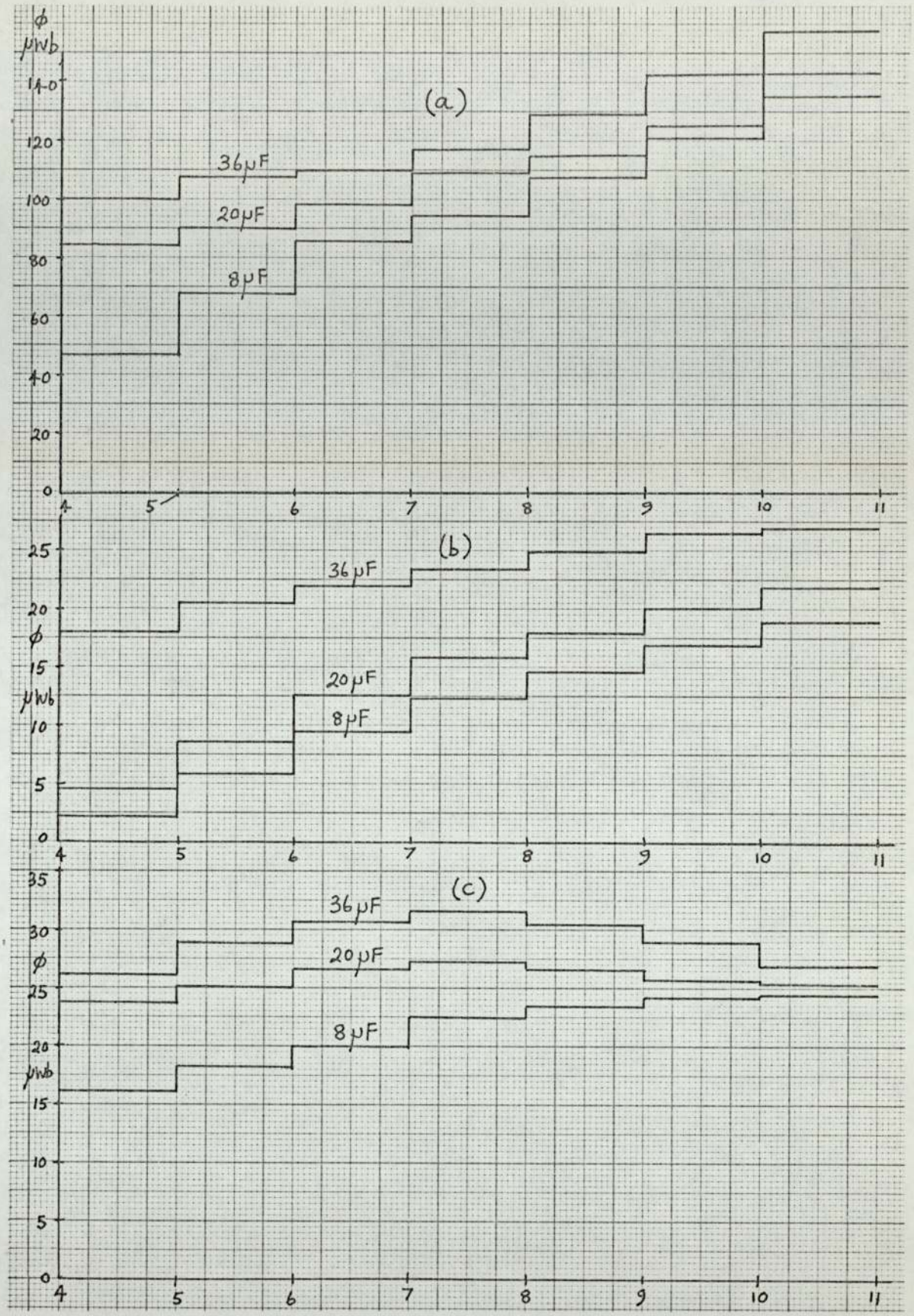

Fig.45

Fluxes at the tooth surface under load conditions for various values of series capacitor.

Rated output, 500volt-load, I_L=88·8 amps.
(a) fundamental flux.
(b) second harmonic flux.
(c) third harmonic flux.

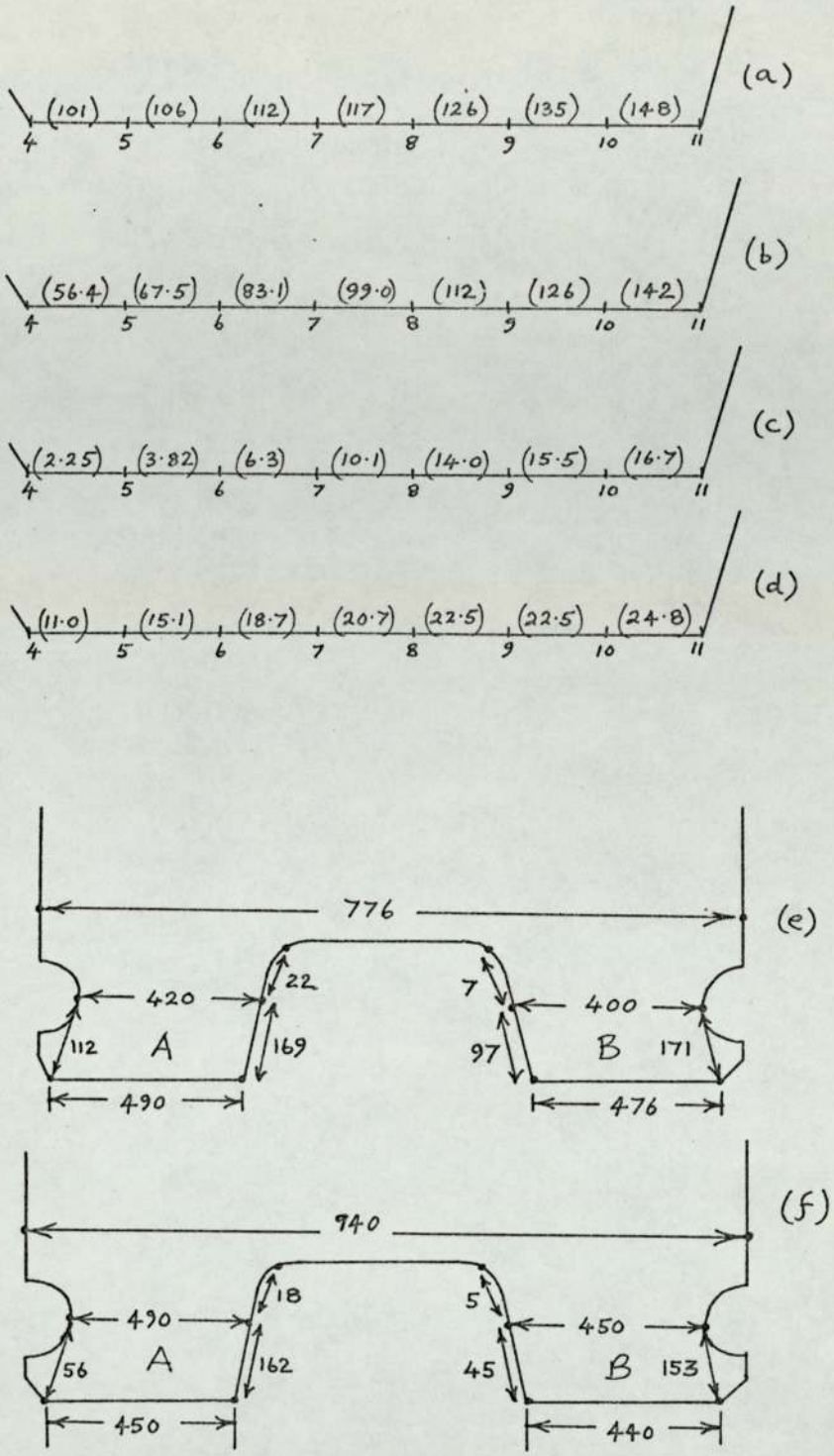

Fig. 46

Fluxes in the small teeth under load conditions.

(a) fundamental fluxes, no series capacitor.
(b) fundamental fluxes, series capacitor C=12μF.
(c) second harmonic fluxes, no series capacitor.
(d) second harmonic fluxes, series capacitor C=12μF.
(e) total fluxes in a small tooth, no series capacitor.
(f) total fluxes in a small tooth, series capacitor, C=12μF. (flux readings in μWb, total core length)

(All flux readings for rated output, 44·4 KVA.)

Fig. 47

Flux waveform in section 4-5 under load conditions.

Rated output, I_L=88·8 amps.
I_f= 3·05 amps. C=16μF.

(a) Open circuit flux waveform.(-dotted lines show approximation to the actual variation.)
(b) actual measured flux waveform on load.
(c) Calculated flux waveform on load.
(d) load current waveform.
Mean flux density on O.C. =0·76 Tesla.
Mean flux density on load =0·635 Tesla.

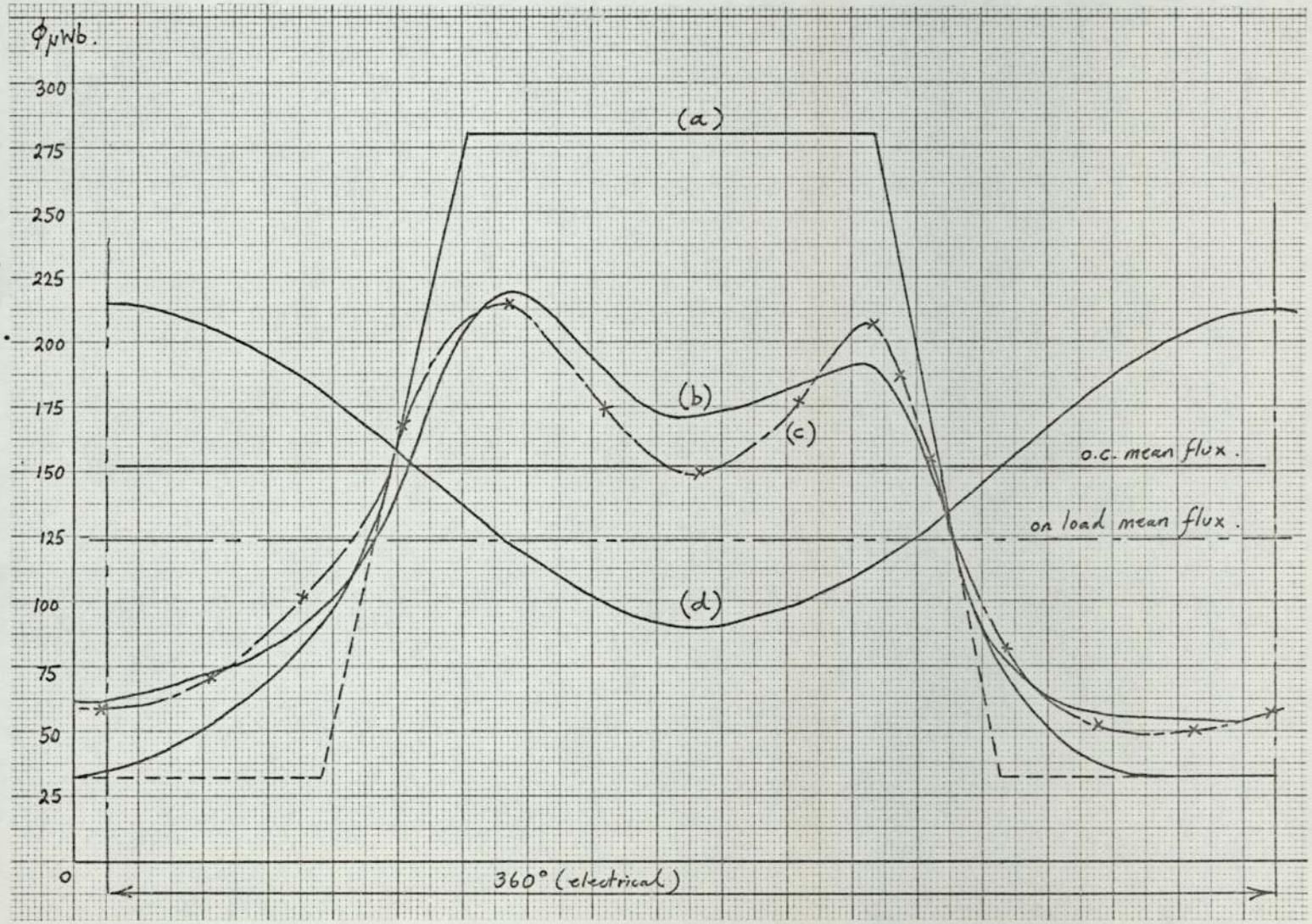

Fig. 48

Flux waveform in section 7-8 on load, C=16 μF.
I_f=3·05 amps.
(a) Open circuit flux waveform.
(b) Measured flux waveform on load.
(c) calculated flux waveform.
(c) calculated flux waveform-(taking into account the distortion of the open circuit waveform)
(d) load current waveform.
Mean flux density on O.C. =0·76 Tesla.
Mean flux density on load =0·69 Tesla.

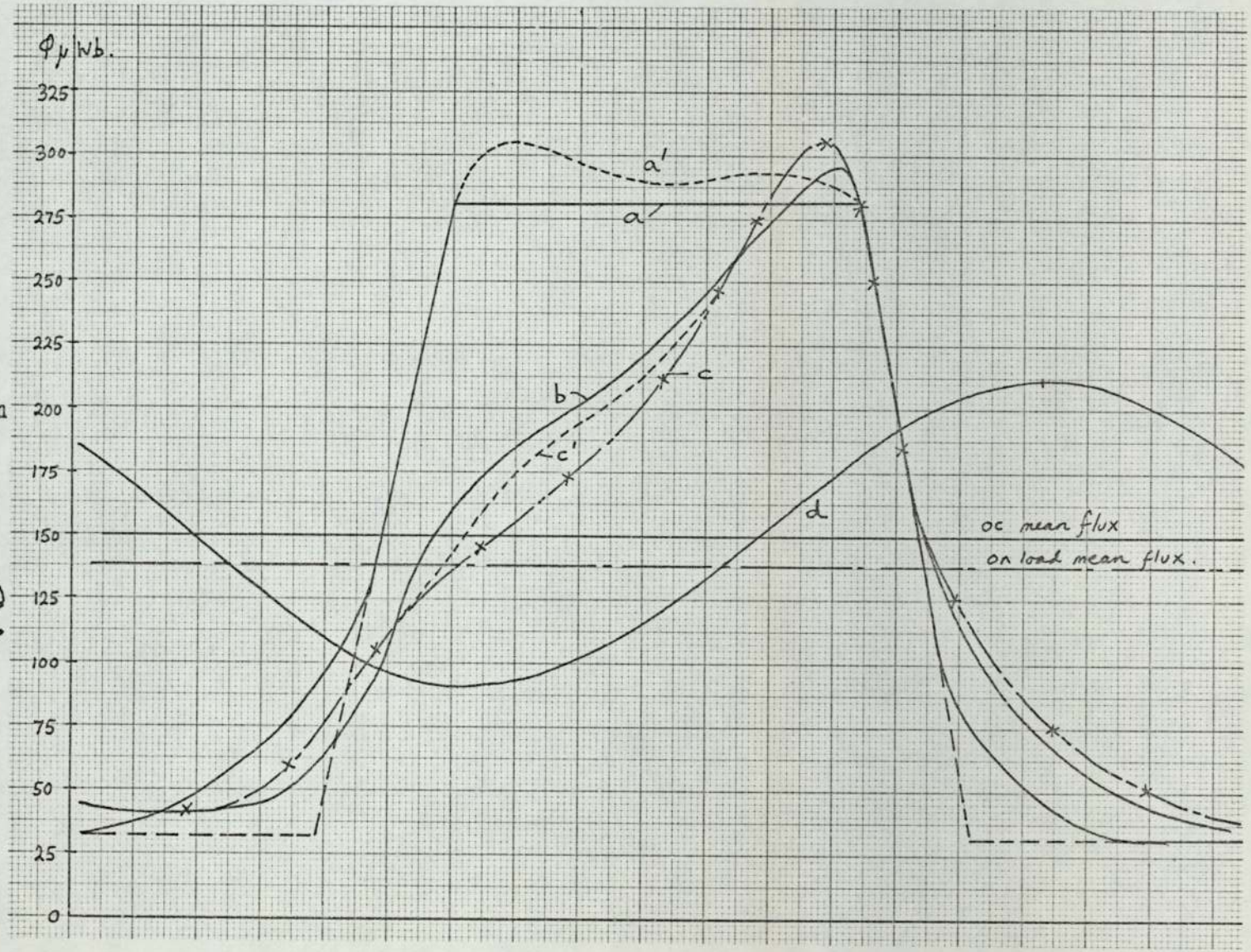

Fig.49

Flux waveform in section 10-11 on load, series capacitor =16μF . Rated output. I_f=3·05 amps.

(a) open circuit flux waveform.
(b) measured flux waveform.
(c) calculated flux waveform.
(d) load current waveform.

Mean flux density on O.C. =0·76 Tesla.
Mean flux density on load =0·78 Tesla.
Measured peak flux density on load=1·8 Tesla.
Calculated peak density =2·0 Tesla.

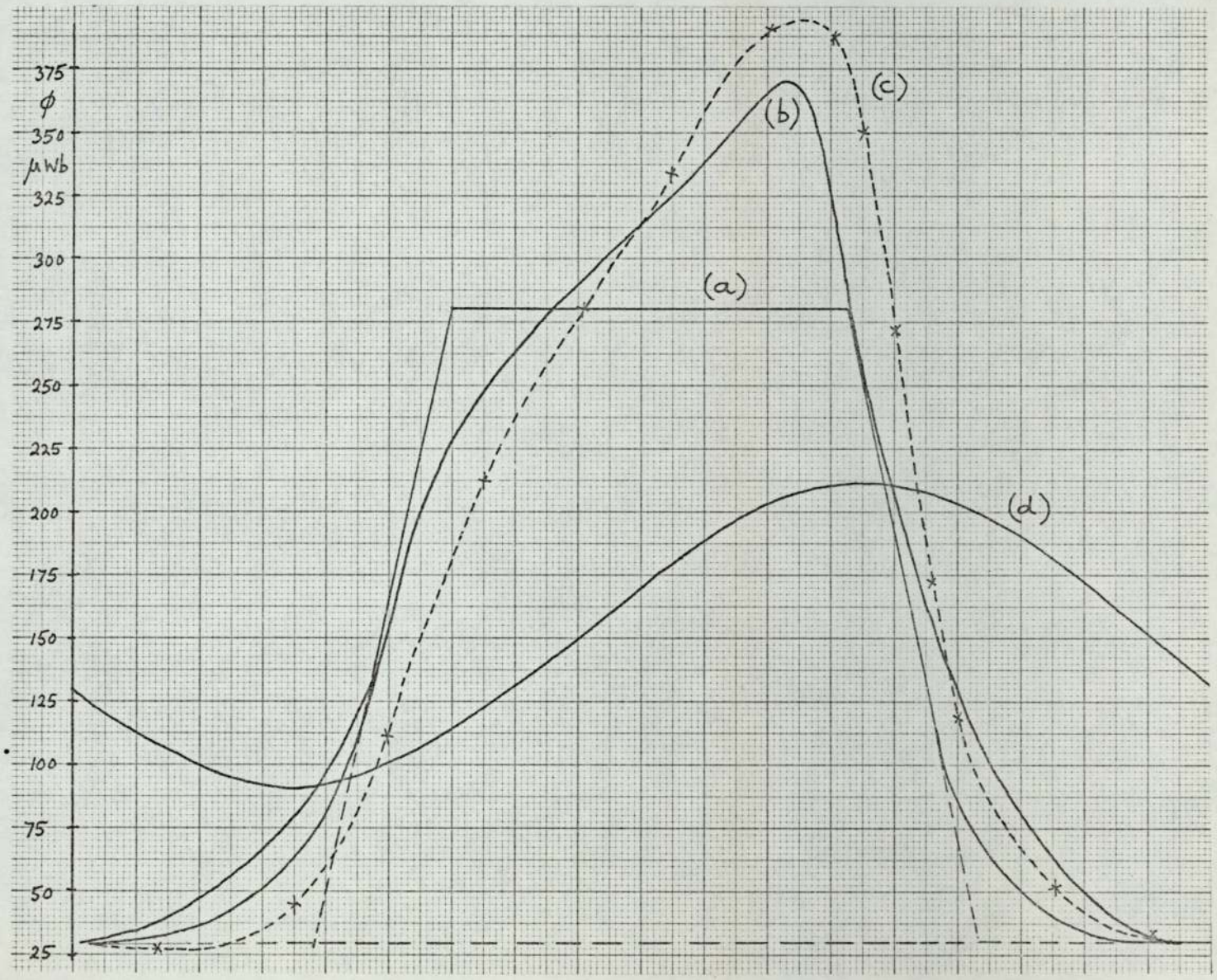

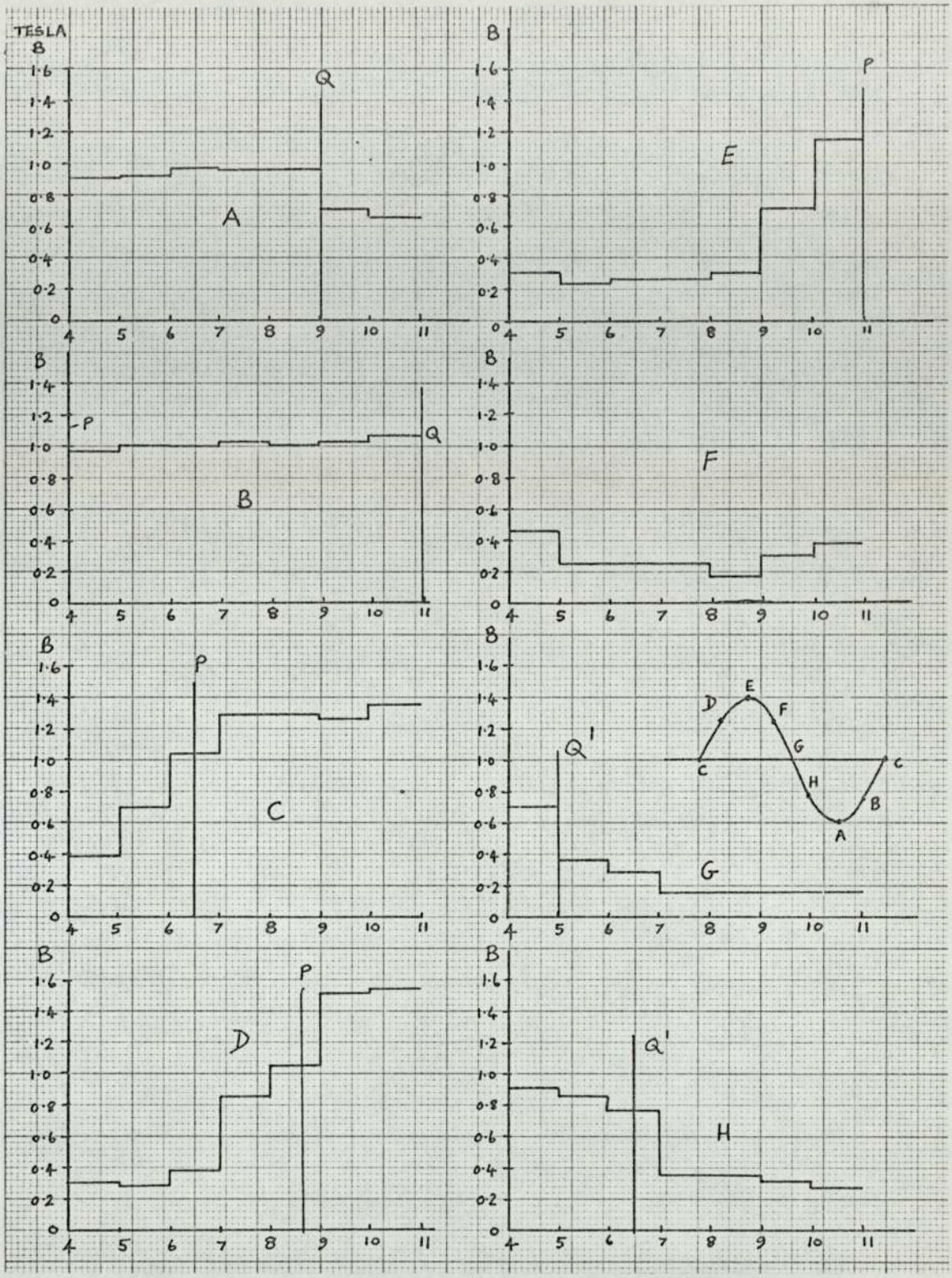

Fig.50

Flux density distribution across the tooth surface for various rotor positions.

Rated output, series capacitor =16μF . I_f=3·05 amps.

Q-leading edge of rotor tooth, P-trailing edge of rotor tooth, Q'- leading edge of adjacent rotor tooth.
Position F-rotor slot opposite stator tooth.
(Flux density in Tesla.)

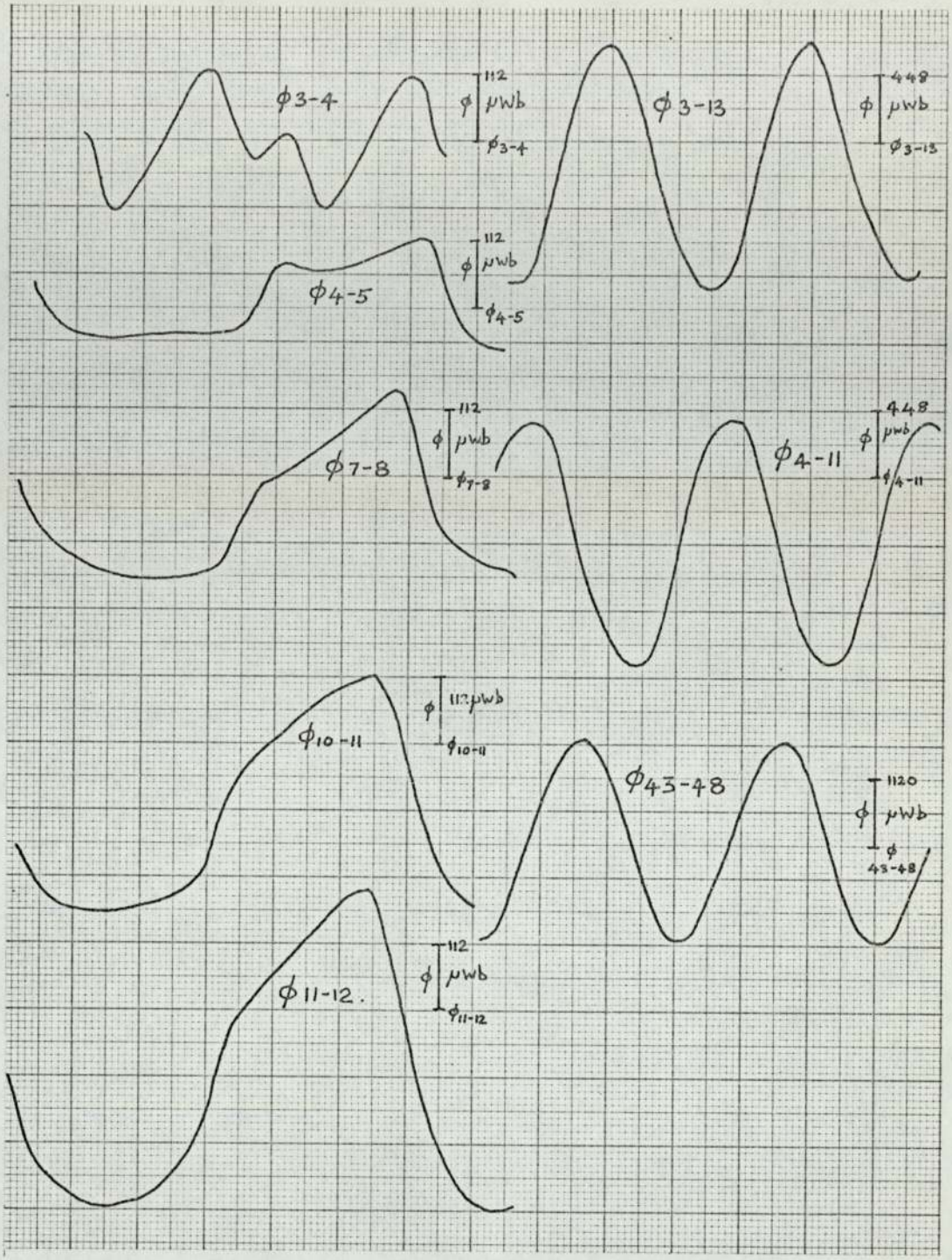

Fig. 51

On load flux waveforms with series capacitor, C=12μF.

φ3-4, leakage flux waveform at the leading edge of the stator tooth.

φ4-5, φ5-6, φ6-7, flux waveforms at the tooth surface.

φ11-12, leakage flux waveform at the trailing edge of the stator tooth.

φ3-13, flux waveform across a small tooth ½ slot depth away from the tooth surface.
φ4-11, flux waveform across the total tooth surface.
φ43-48, flux waveform across a main stator tooth.

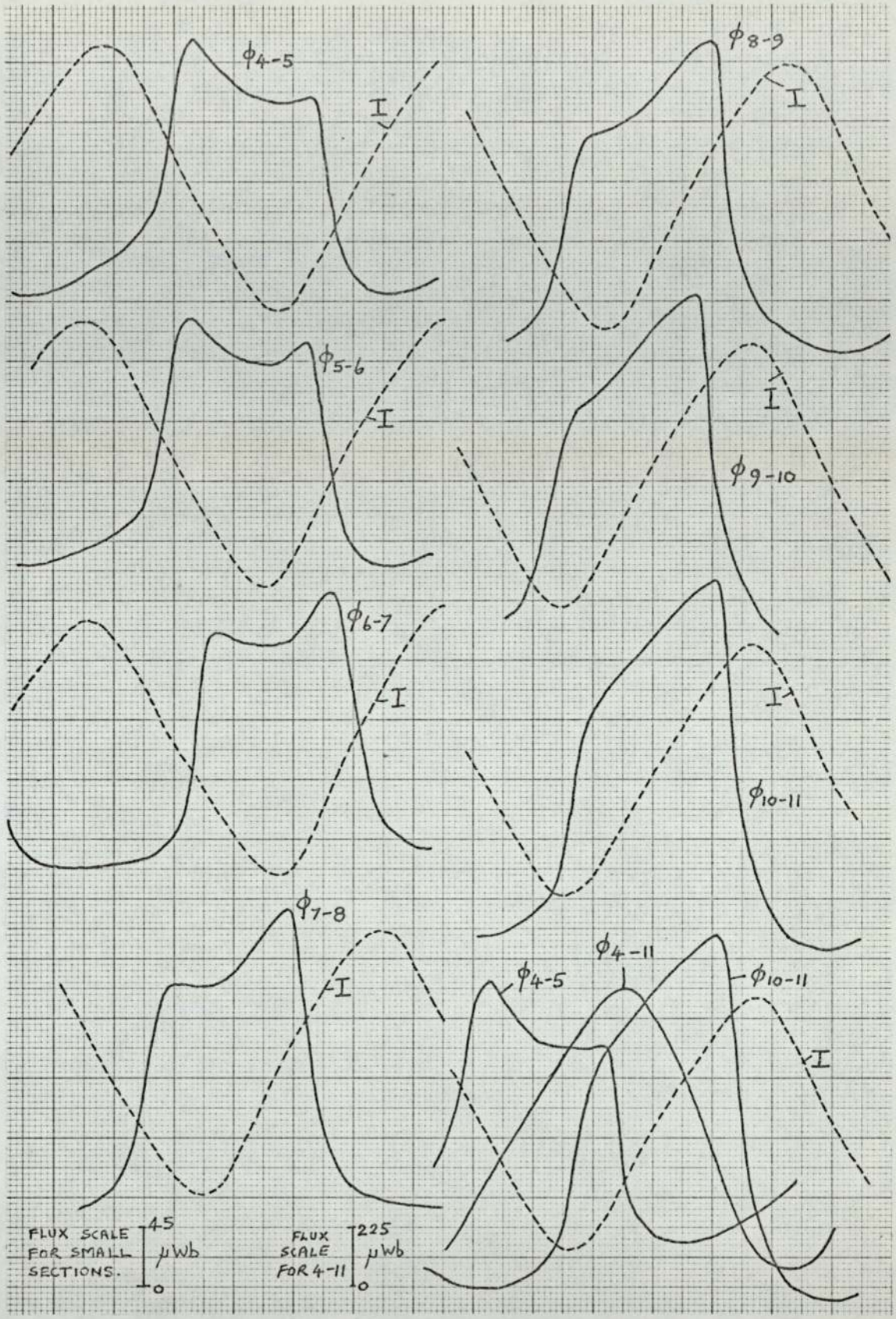

Fig.52

Flux waveforms at the tooth surface under load conditions -no series capacitor, rated output.

ϕ4-5, ϕ5-6, ϕ6-7,.... flux waveforms in small sections of the tooth surface.

ϕ4-11, flux waveform across the total surface.

Fig.53

Flux waveform in section 10-11 on load,-no series capacitor. Rated output.

(a) open circuit flux waveform.

(b) measured flux waveform.

(c) calculated flux waveform.

(d) load current waveform.

I_f=4·05 amps.

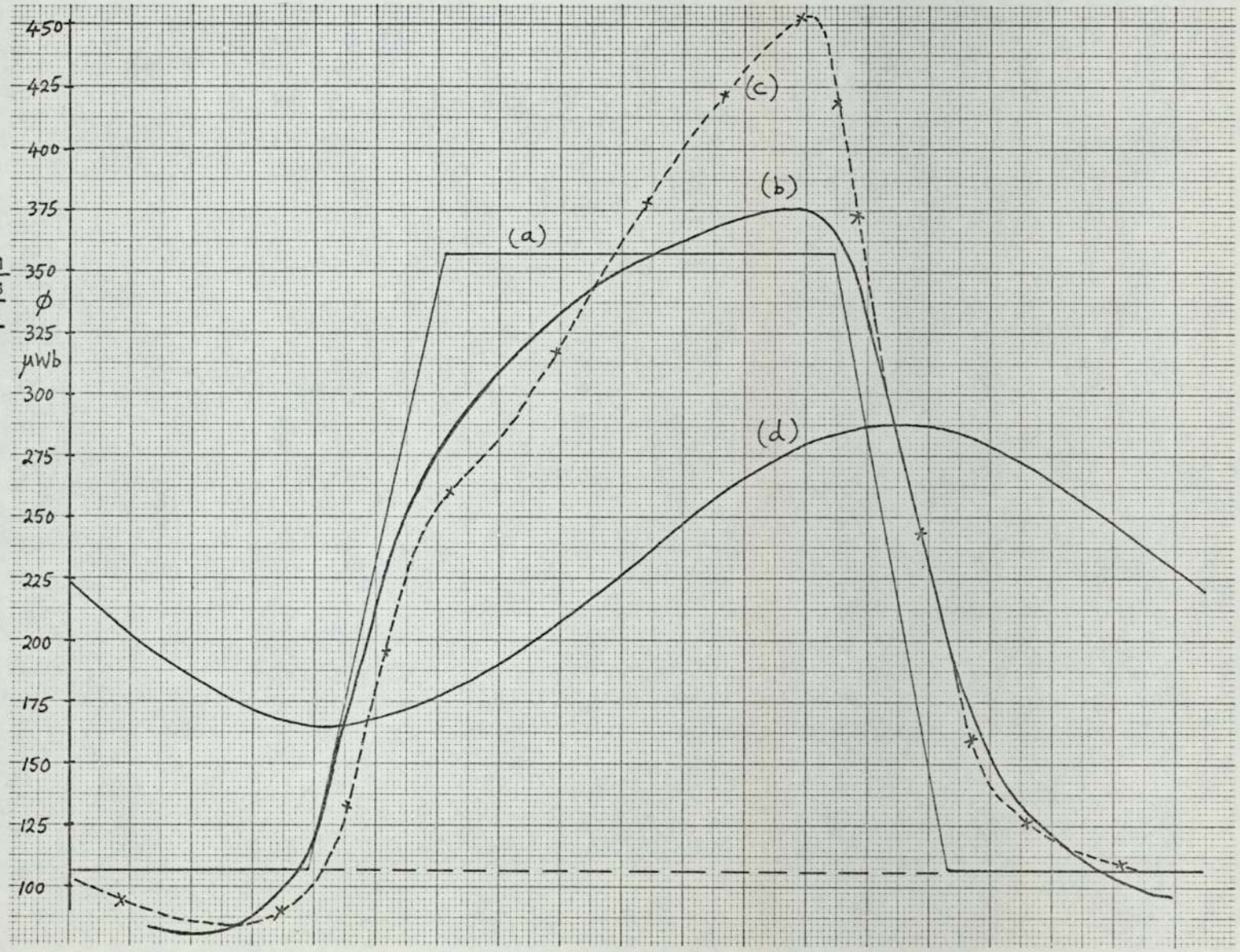

Fig.54

Flux waveform in section 4-5 on load, -no series capacitor. 30kw output.

I_f=3·0 amps.

(a) open circuit flux waveform.

(b) measured flux waveform.

(c) calculated flux waveform.

(d) load current waveform

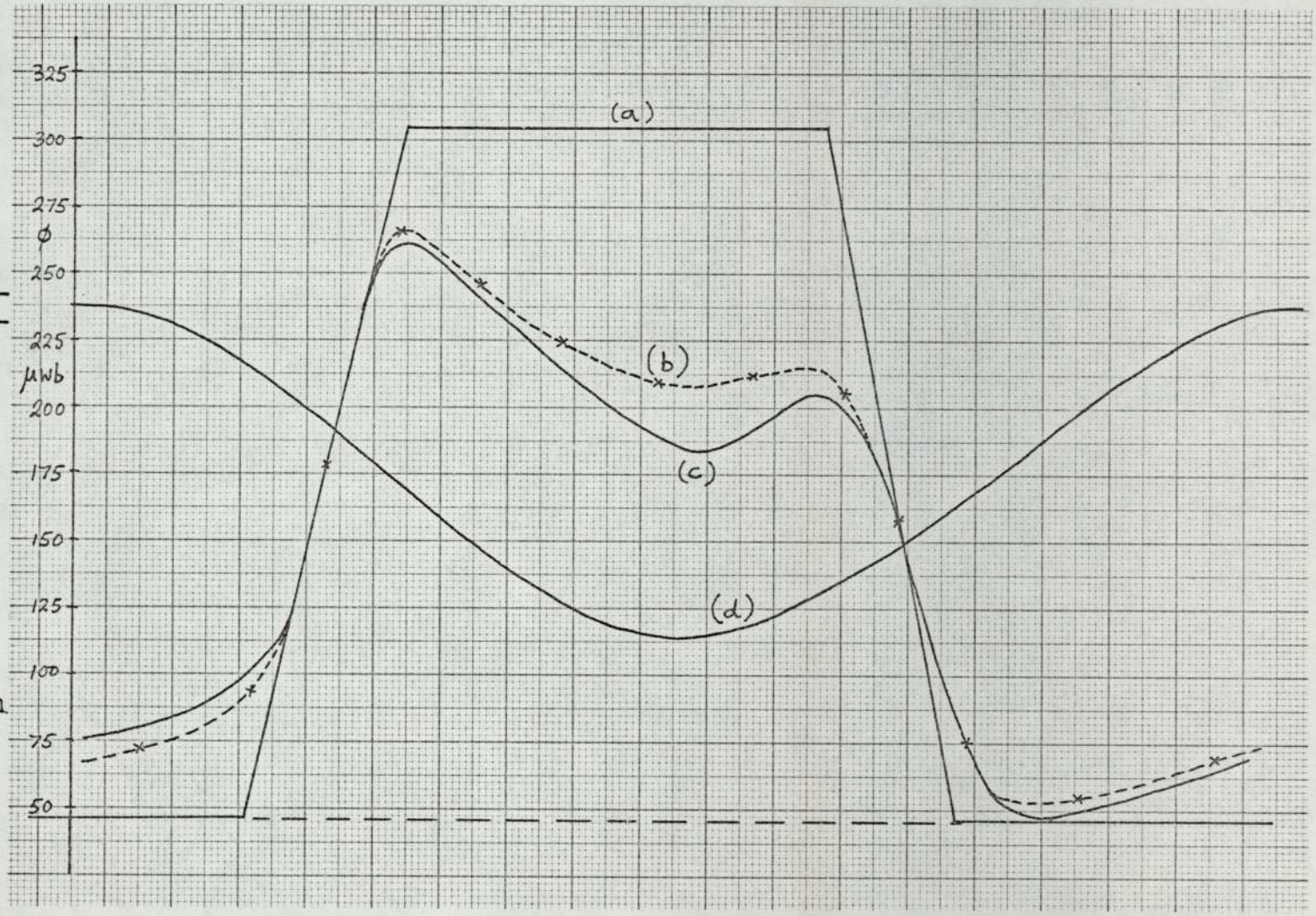

Fig.55

Flux waveform in section 10-11 on load,-no series capacitor. 30kw output.

I_f=3·0 amps.

(a) open circuit flux waveform.

(b) measured flux waveform.

(c) calculated flux waveform.

(d) load current waveform.

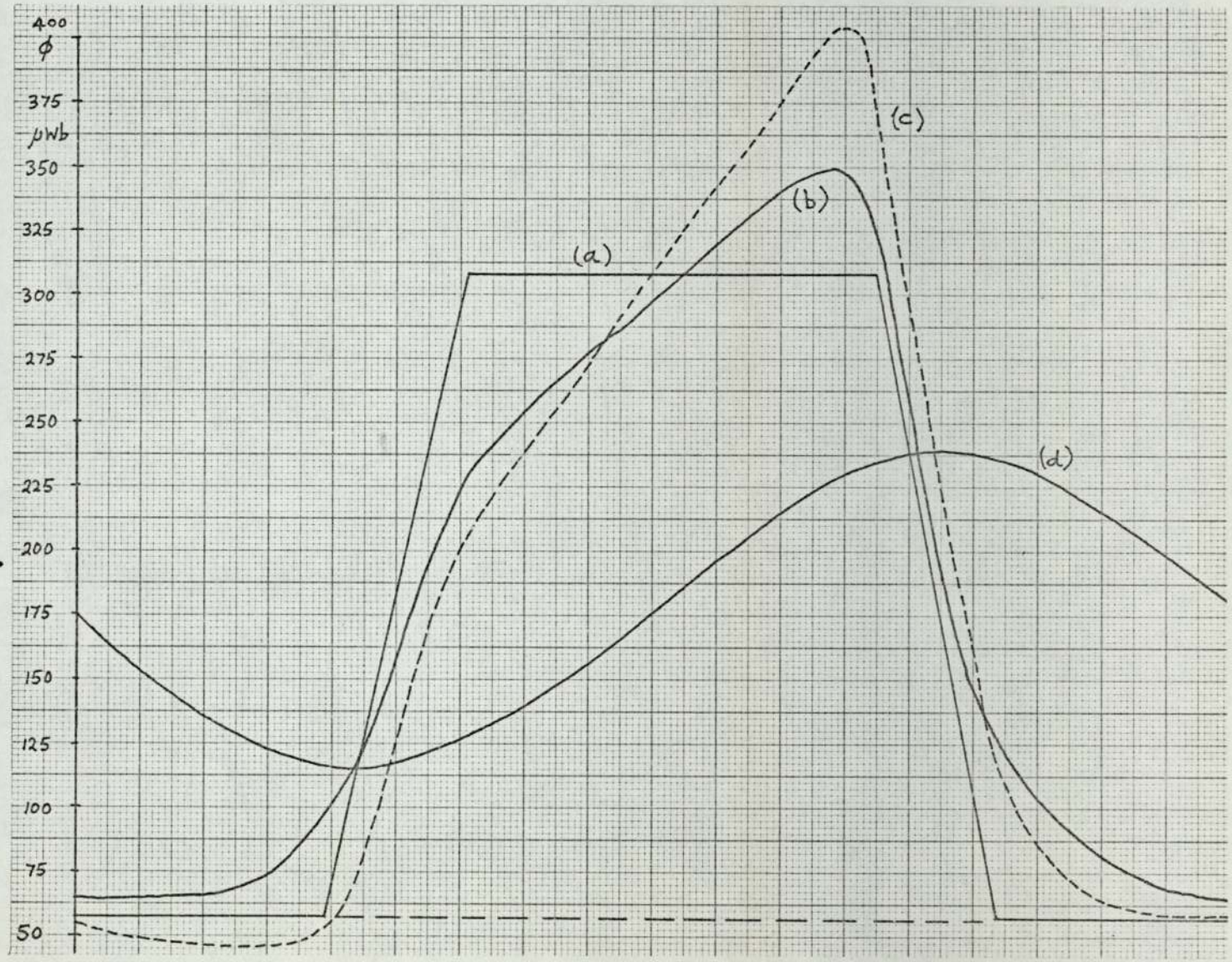

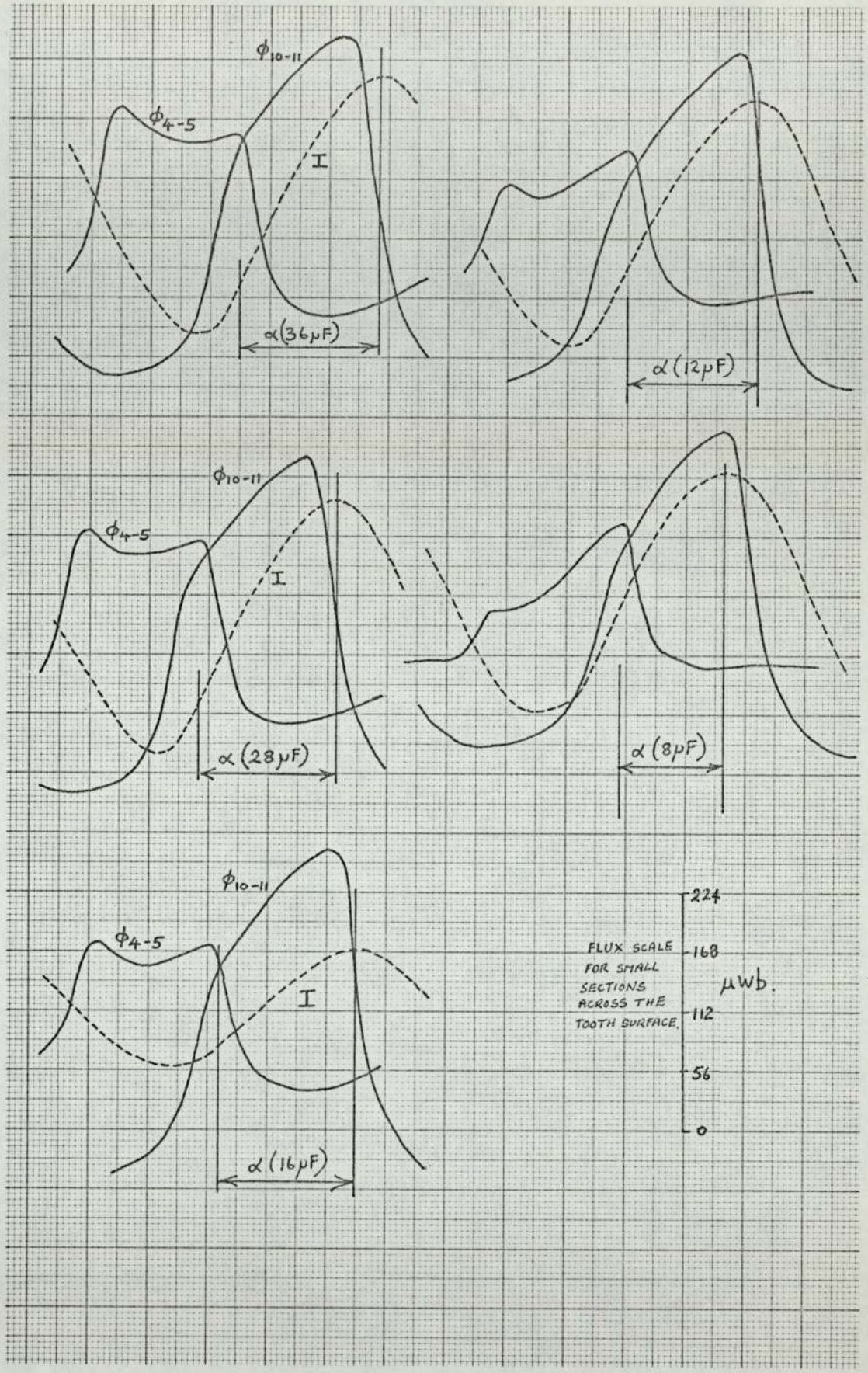

Fig.56

Flux waveforms at the tooth surface for various values of series capacitor.

Rated output, load current =88·8 amps.

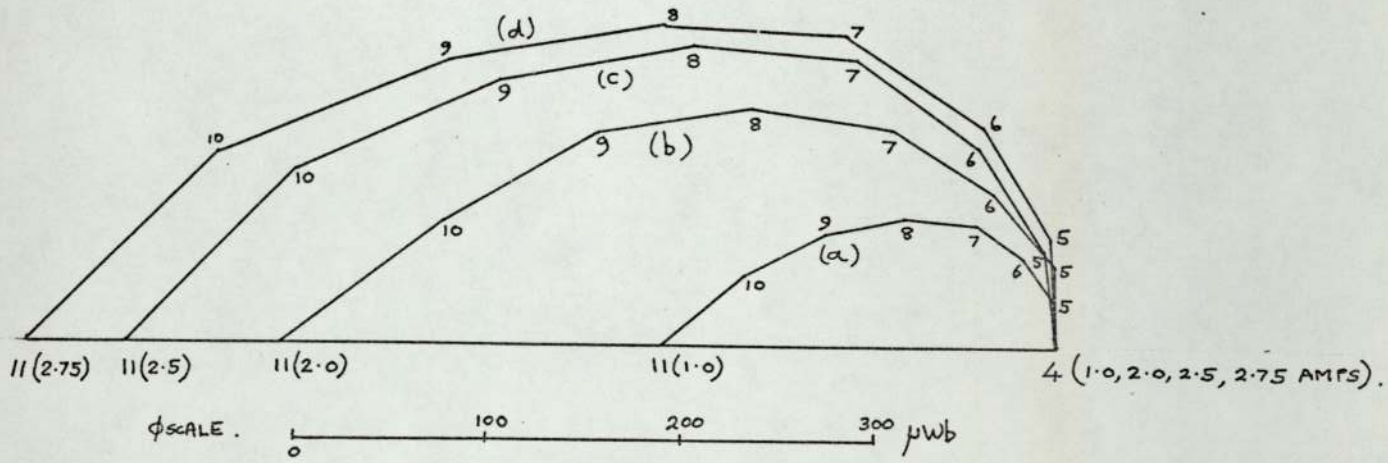

Fig.57

Addition of fundamental fluxes at the tooth surface under load conditions for various values of series capacitor, C=12 μF .

Top damping winding connected.

(a) I_f=1·0 amp.

(b) I_f=2·0 amps.

(c) I_f=2·5 amps.

(d) I_f=2·75 amps.

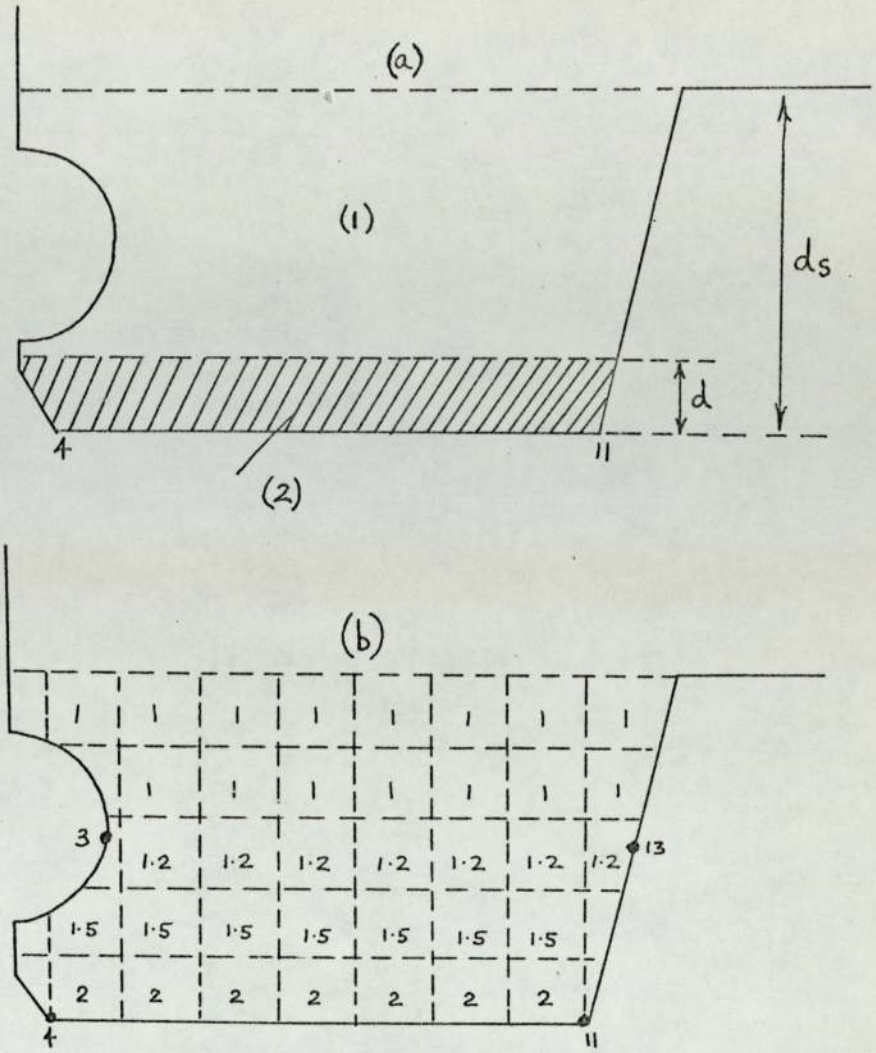

Fig.58

Extra loss factors in a small stator tooth.

(a) (1)- In this region an approximation is made to the extra loss factor depending on the magnitude of k at the surface.

(2)-shaded area: Extra loss factors calculated in this region from the fluxes in the tooth surface. Overall loss factor K_o for this region given by

$$K_o = \left\{ \frac{a k_a + b k_b + c k_c + \text{-------}}{a+b+c+\text{-------}} \right\}$$

(b) For C=12μF , rated output, K_o=2·0.
In the remaining mesh an approximation is made to the extra loss factor.

Average extra loss factor for the small tooth, K_A =1·28.

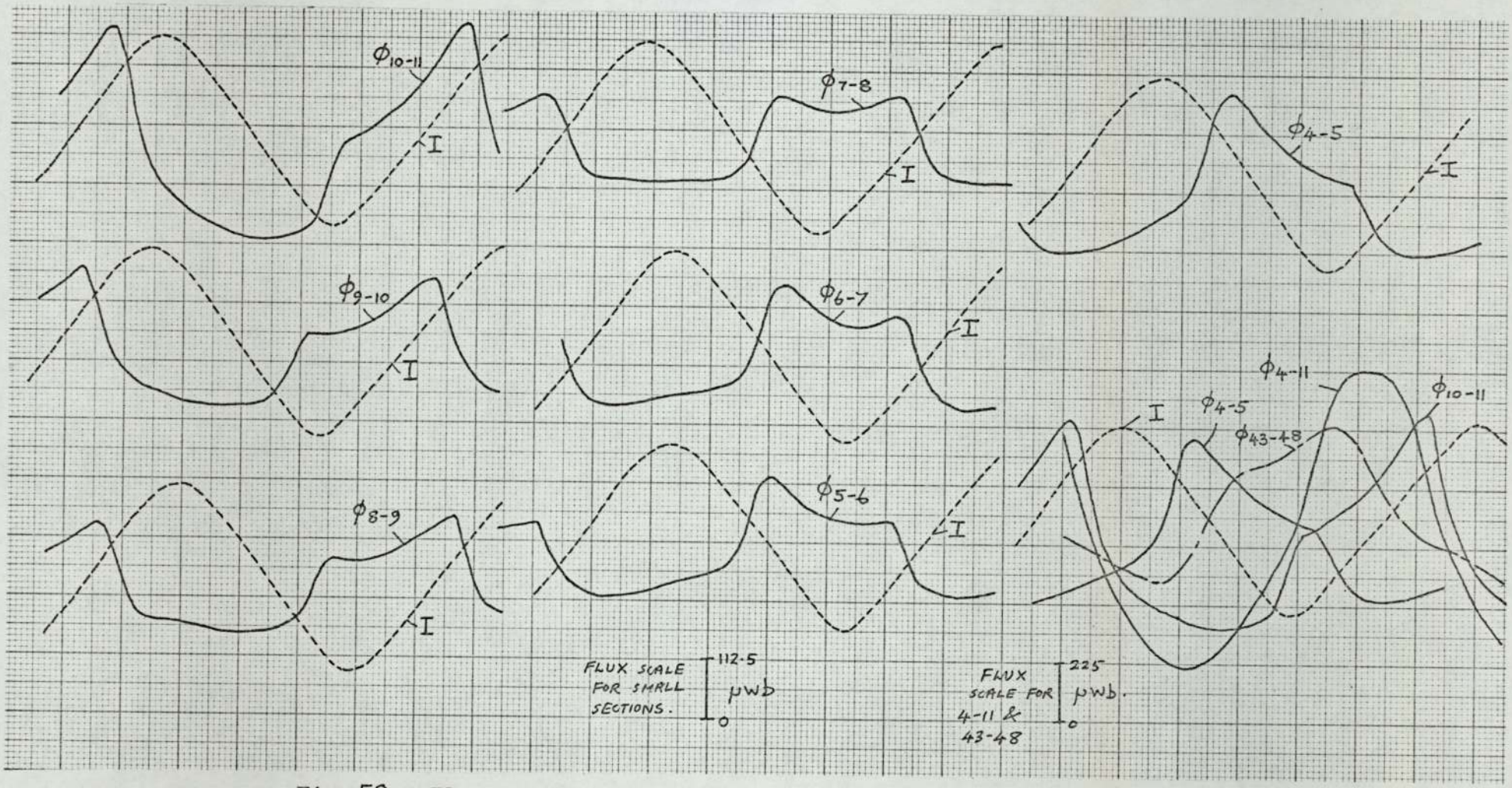

Fig.59 Flux waveforms at the tooth surface under short circuit conditions, no series capacitor, $I_f = 2{\cdot}87$ amps, $I_{sc} = 88{\cdot}8$A.

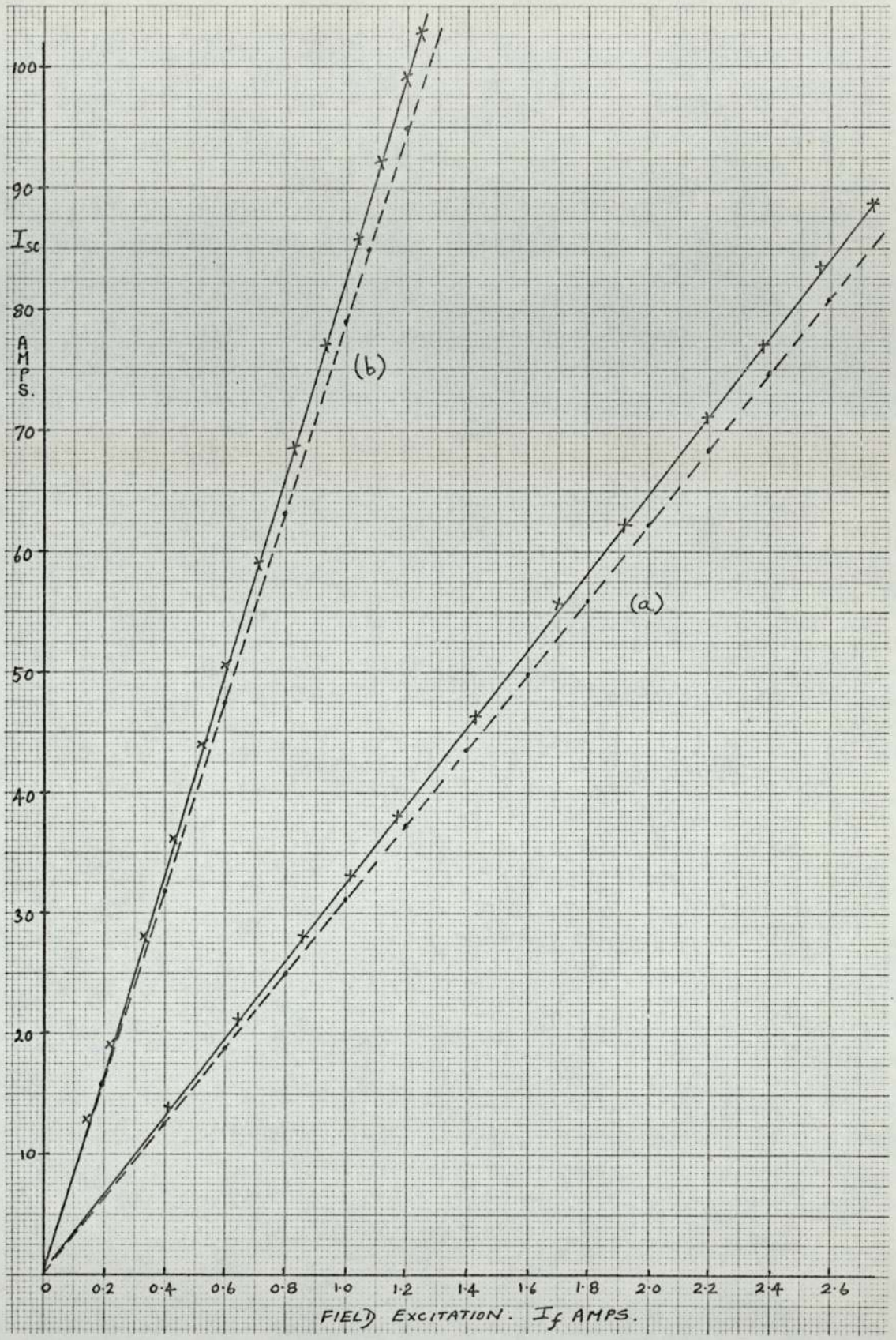

Fig. 60

Short circuit characteristics with and without a series capacitor.

(a)_____ no capacitor (measured)
_ _ _ _ _ _ no capacitor (calculated)

(b)_____ C=12μF . (measured)
_ _ _ _ _ _ C=12μF. (calculated)

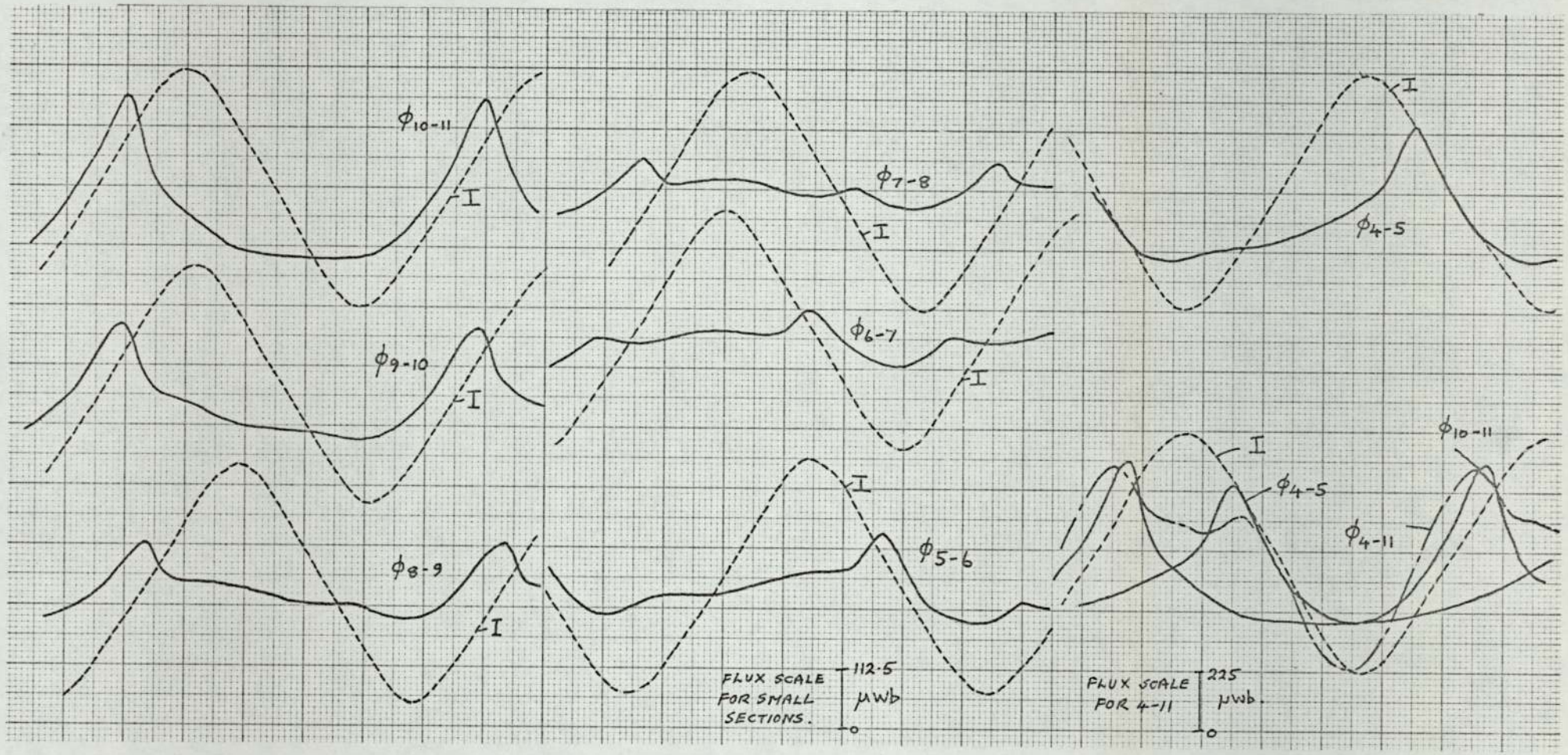

Fig. 61 Flux waveforms at the tooth surface under short circuit conditions, series capacitor, C=12μF . I_f=1·19 amps. I_{sc} = 88·8AMPS.

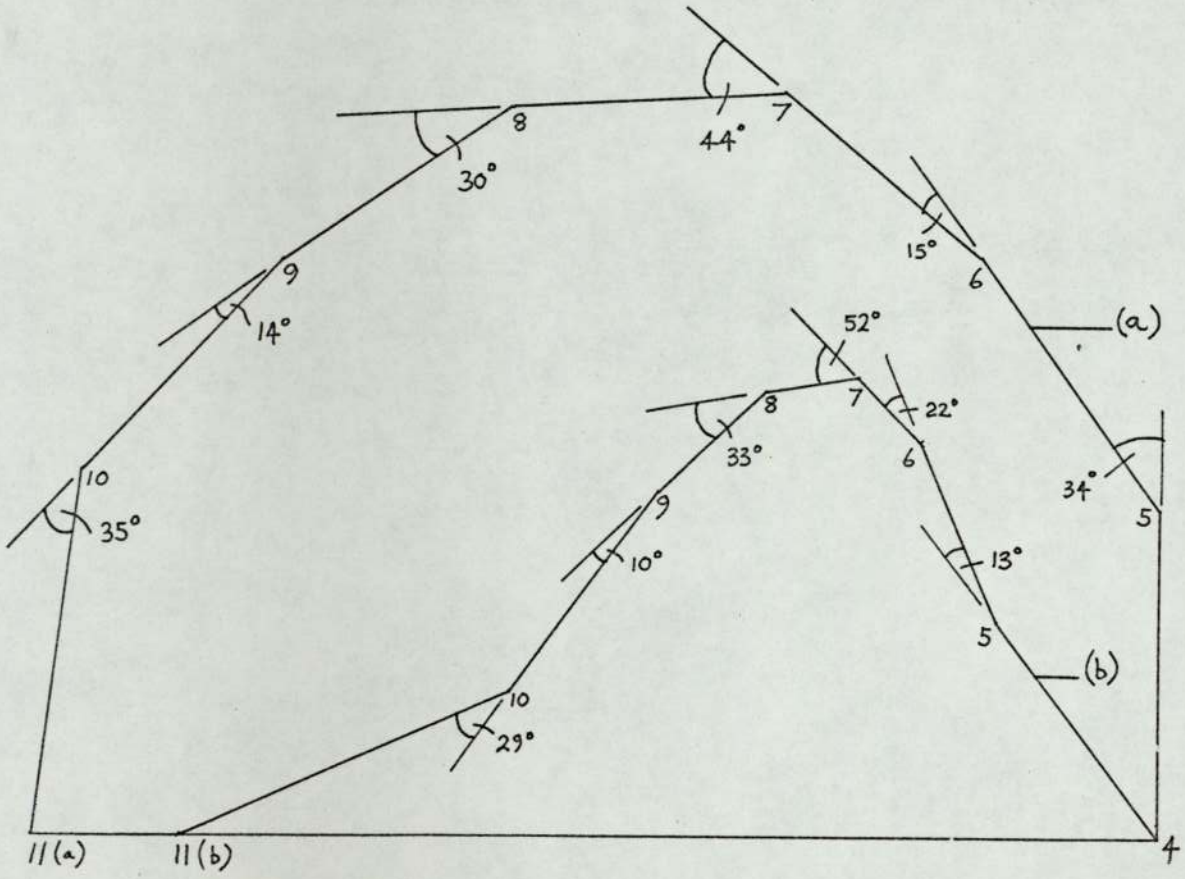

Fig. 62

Fundamental fluxes at the tooth surface under short circuit conditions.

(a) fundamental fluxes at rated load current, -no series capacitor.
I_f = 2·87 amps, -top damping winding connected.
Average ψ angle = 28·6°. K_{D_1} = 0·527.

(b) fundamental fluxes at rated load current, with series capacitor, C = 12 μF. I_f = 1·19 amps.
top damping winding connected.
Average ψ angle = 26·6. K_{D_1} = 0·722.

(Rated load current = 88·8 amps.)

0 22·5 45 67·5 90·0 μWb.
(FLUX SCALE)

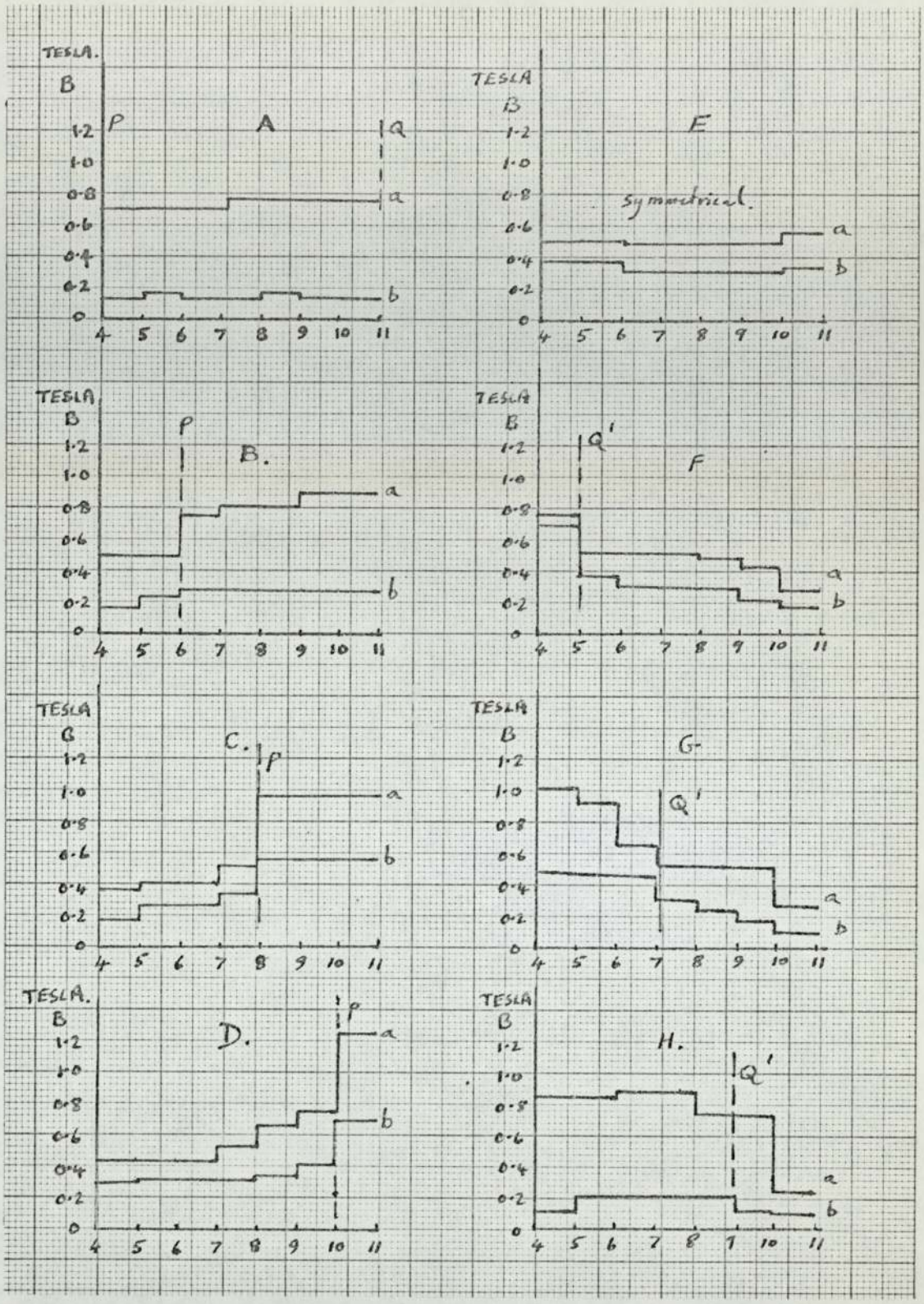

Fig. 63

Flux density distribution across the tooth surface under short circuit conditions.

(a)-no capacitor, I_f = 2·87 amps

(b)-with series capacitor (C=12μF), I_f = 1·19 amps

Q-leading edge of the rotor tooth.
P-trailing edge of the rotor tooth.
Q'-leading edge of adjacent rotor tooth.

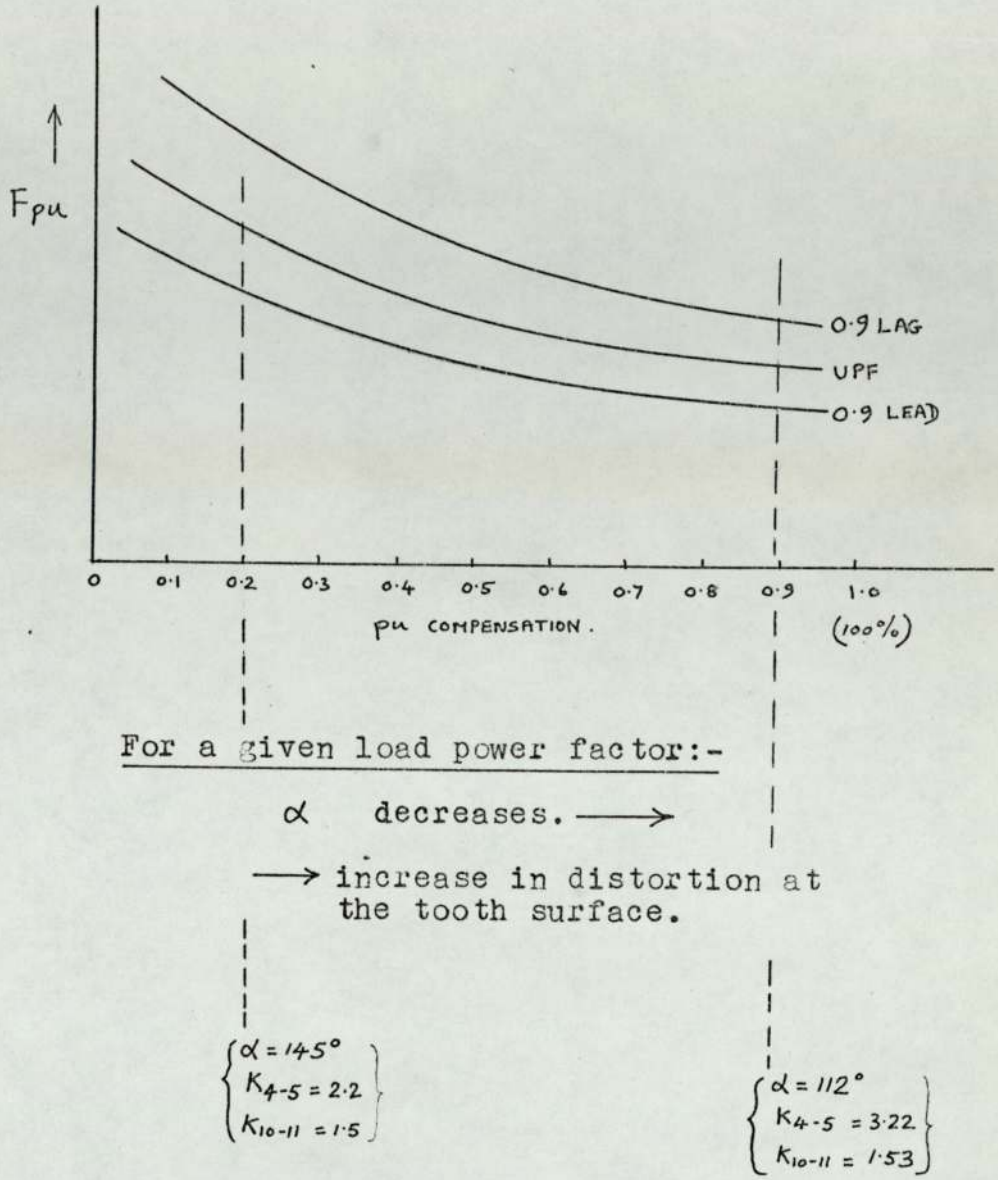

Fig. 64

Relationship between pu field excitation (F_{pu}) and pu compensation at various power factors.

1pu compensation taken for 100% compensation.

Fig. 65

Optimum value for series capacitor.

o-fundamental loss in the tooth surface.

▲- actual loss in the tooth surface.

X- field excitation.

1 pu compensation when $(a+X_L)=X_c$

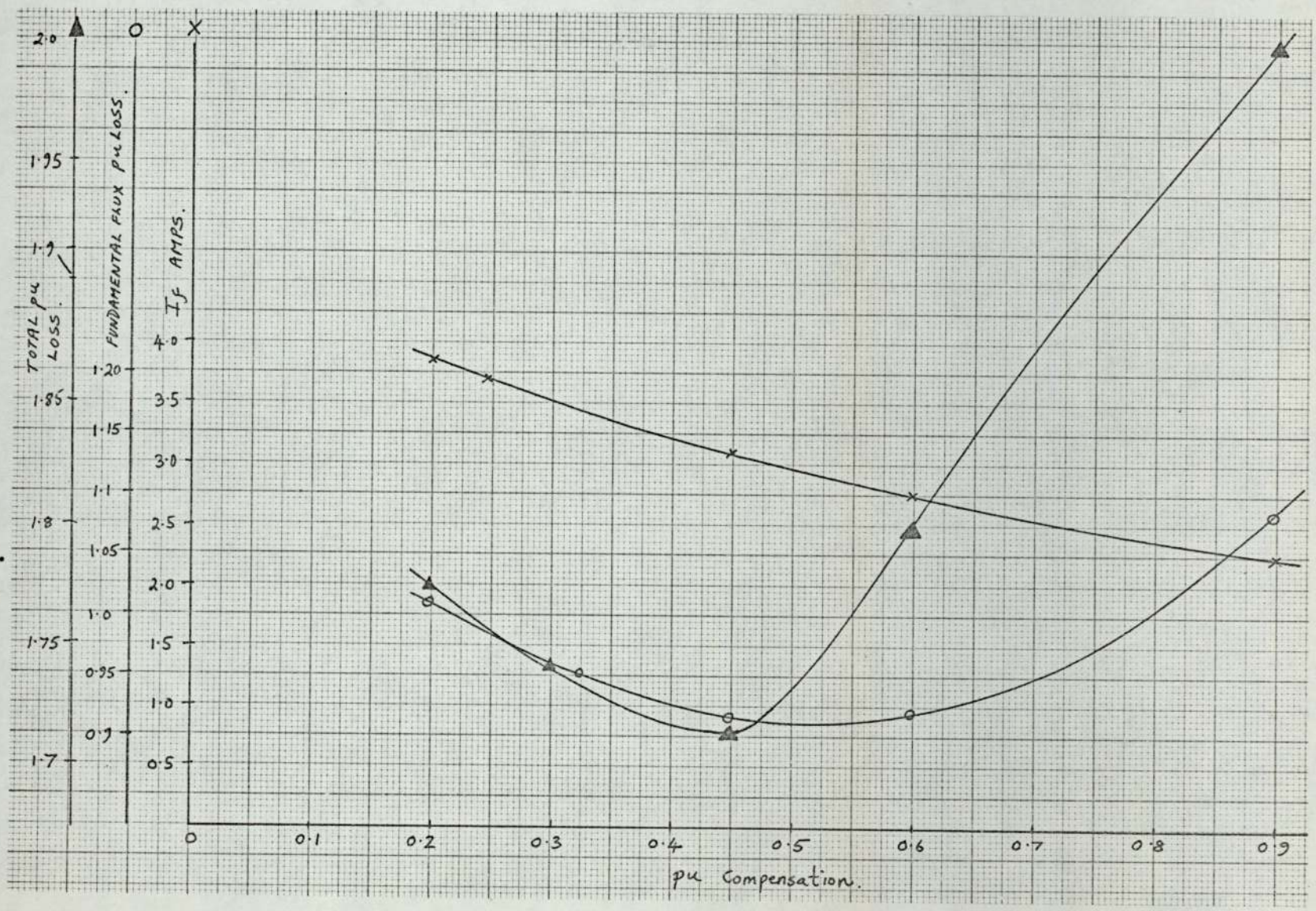

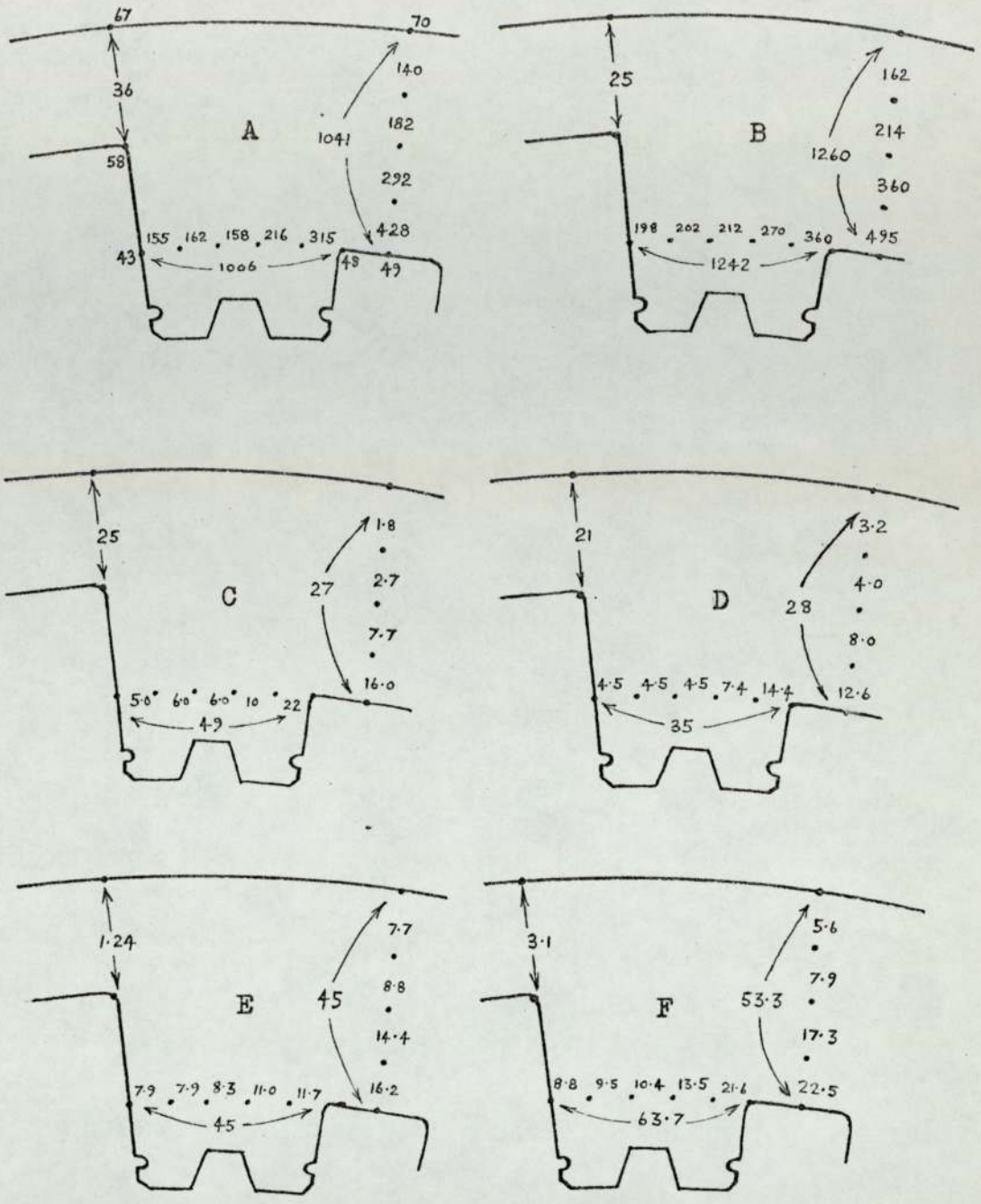

Fig. 66

Harmonic fluxes in the stator core under load conditions Rated output.

A-fundamental flux- zero compensation.
B-fundamental flux- C=12μf.

C-second harmonic flux- zero compensation.
D-second harmonic flux- C=12μf.

E-third harmonic flux- zero compensation.
F-third harmonic flux- C=12μf.

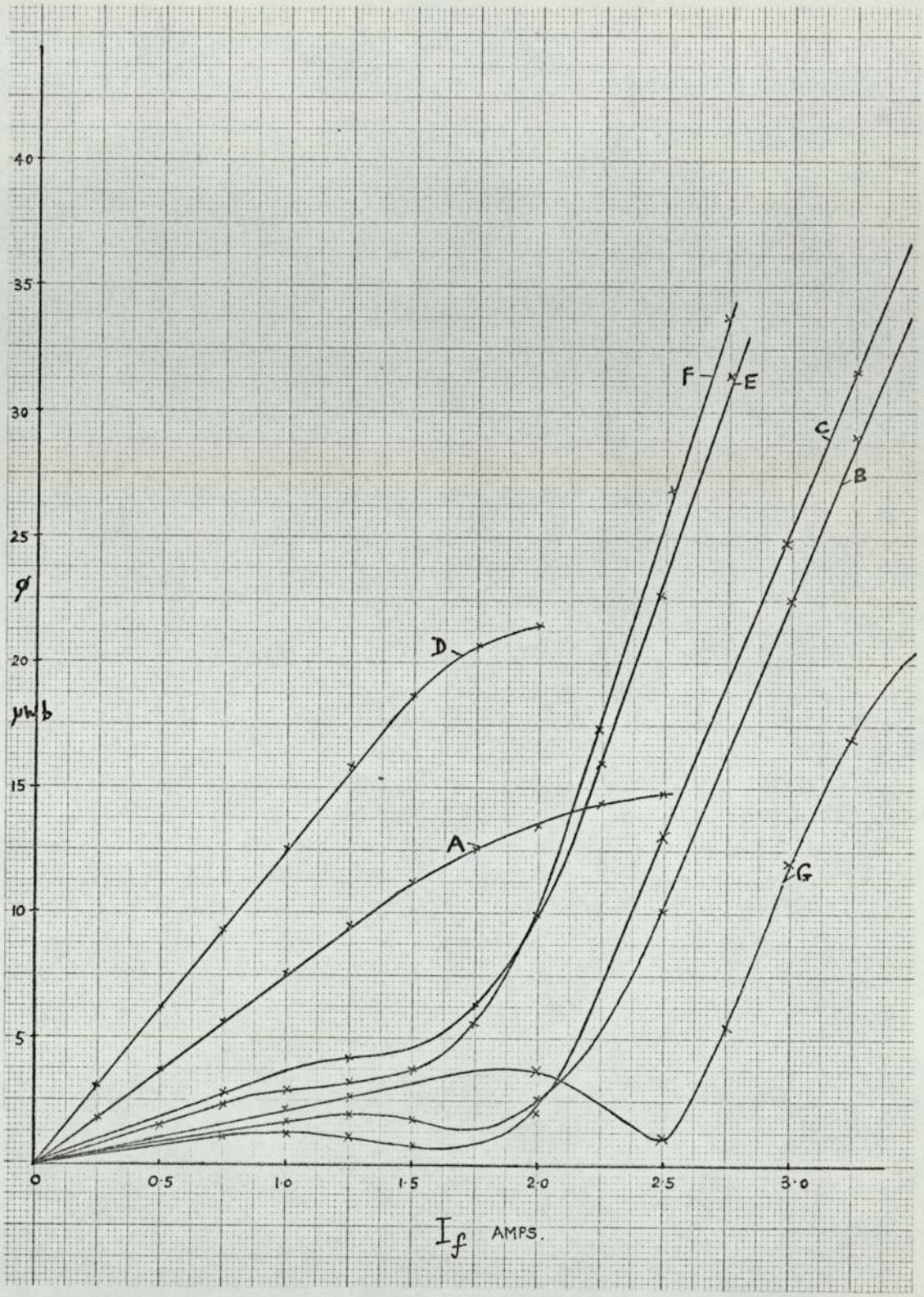

Fig. 67

Second harmonic fluxes in the stator core under load conditions. ϕ_{43-48}.

A-zero compensation- no damping.
B-zero compensation- bottom damping.
C-zero compensation- top damping.
D- series capacitor C=12μF - no damping.
E- series capacitor C=12μF - bottom damping.
F- series capacitor C=12μF - top damping.
G- open circuit- top damping.

Fig.68

Voltage induced in a field coil under load conditions, no series capacitor.

A-no damping. V(rms) [x 10]

B-bottom damping. V(rms)

C-top damping. V(rms)

D-bottom damping. V(peak)

E-top damping. V(peak)

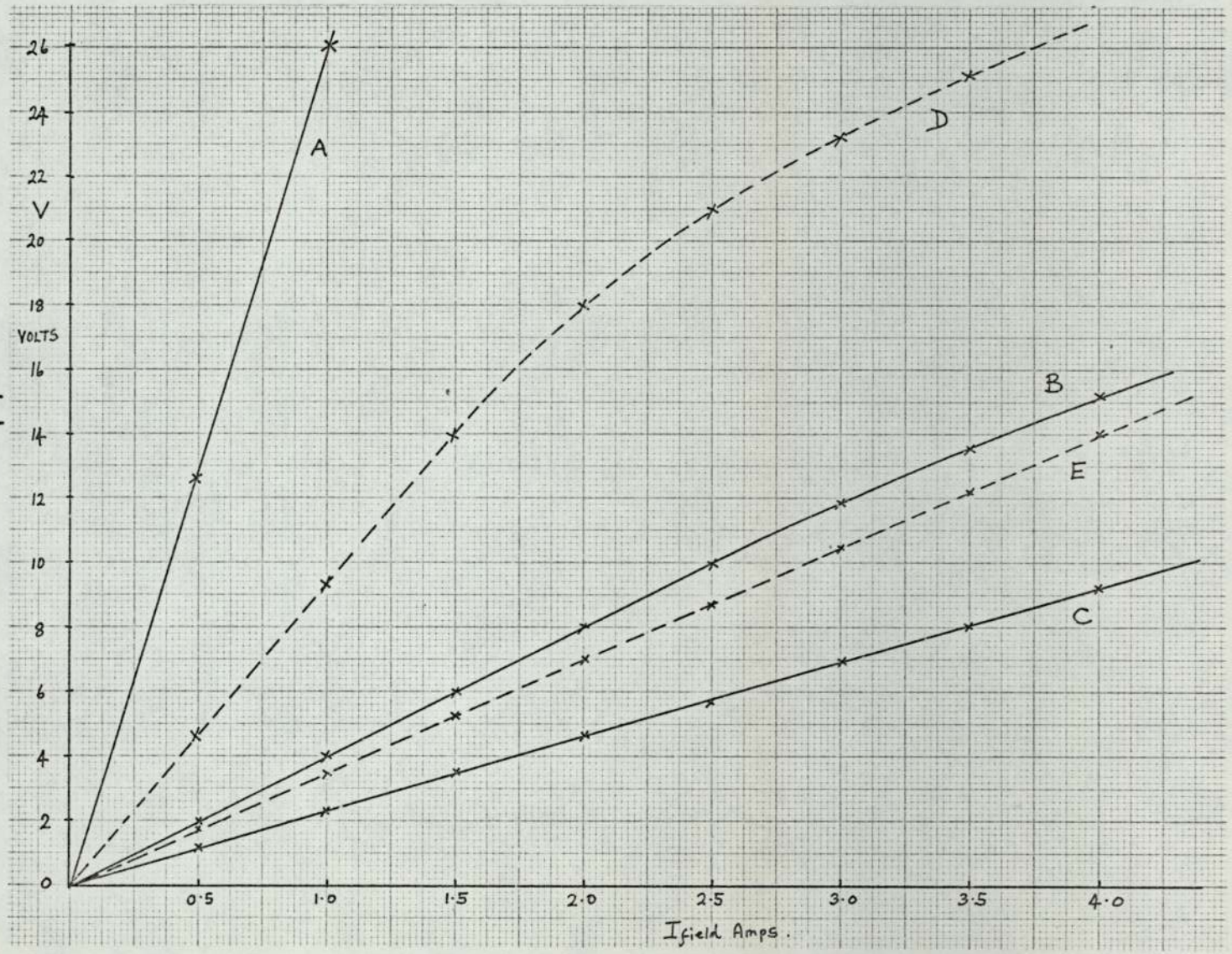

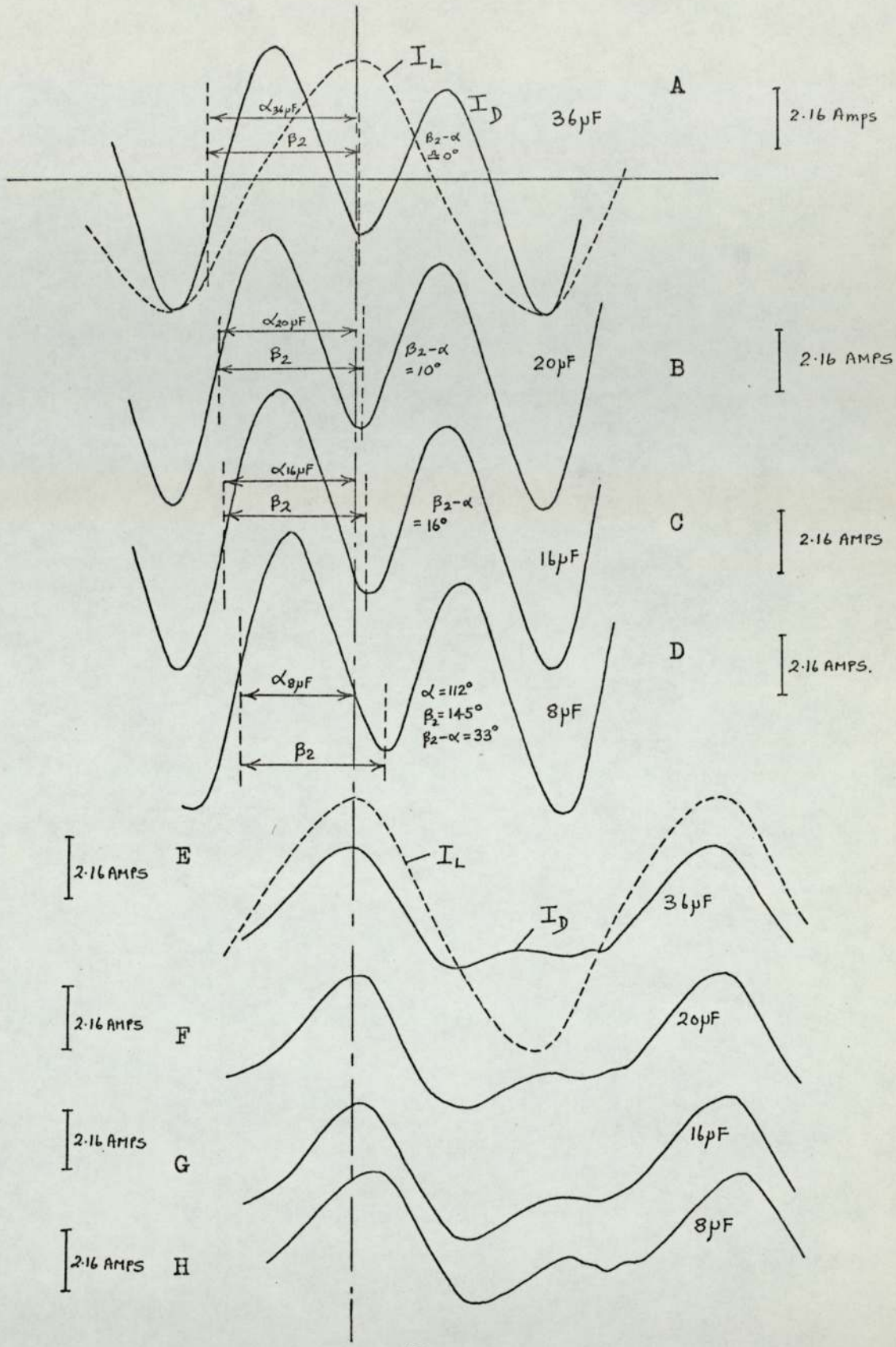

Fig. 69

Damping current waveforms under load conditions for various values of series capacitor, Rated output.

A,B,C,D-top damping: E,F,G,H- bottom damping.
(coils 7-8 top and 7-8 bottom used for measuring damping currents.)

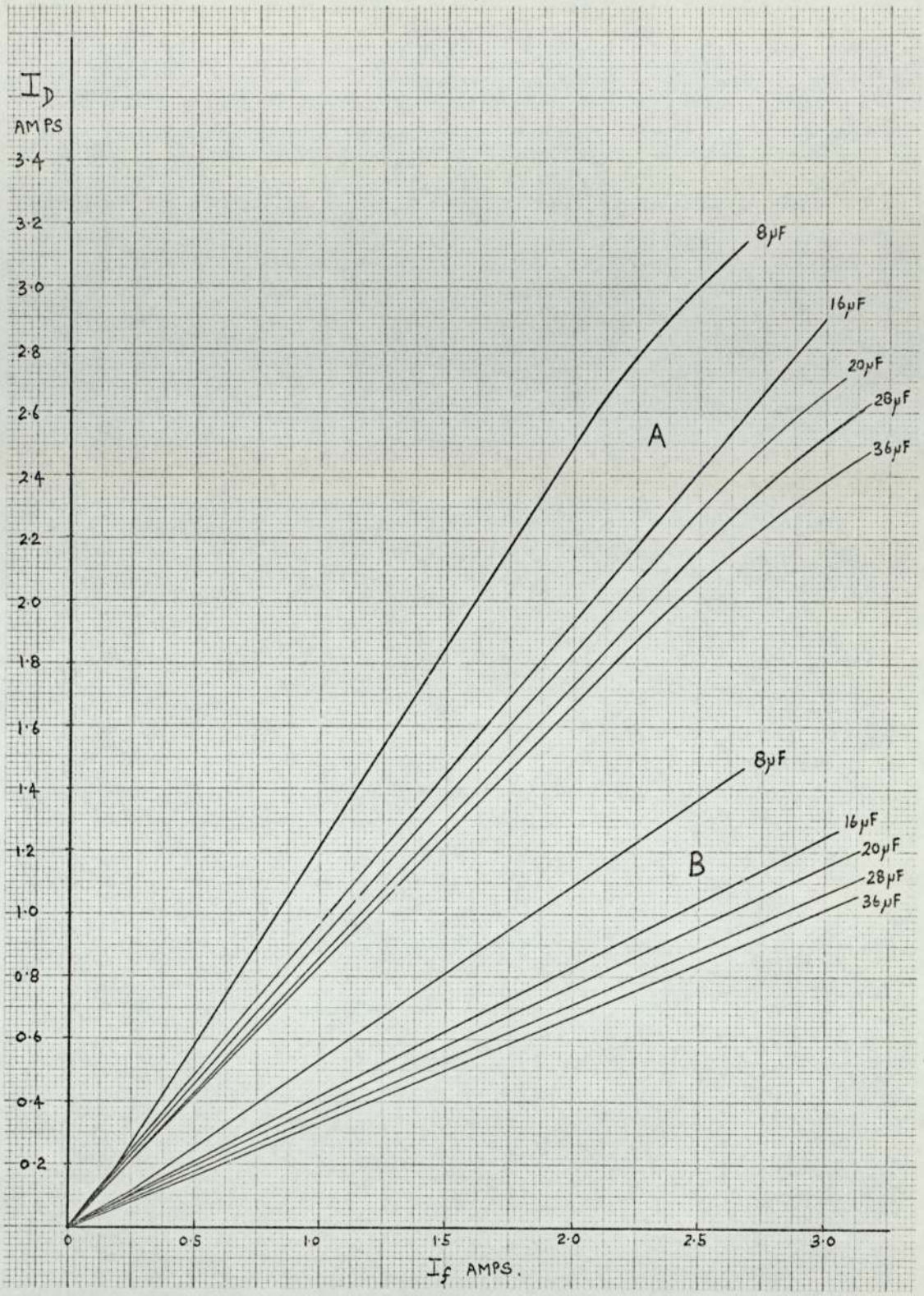

Fig.70

Damping currents under load conditions for various values of series capacitor.

Rated output. Damping coil (9-10).

A- top damping. B- bottom damping.

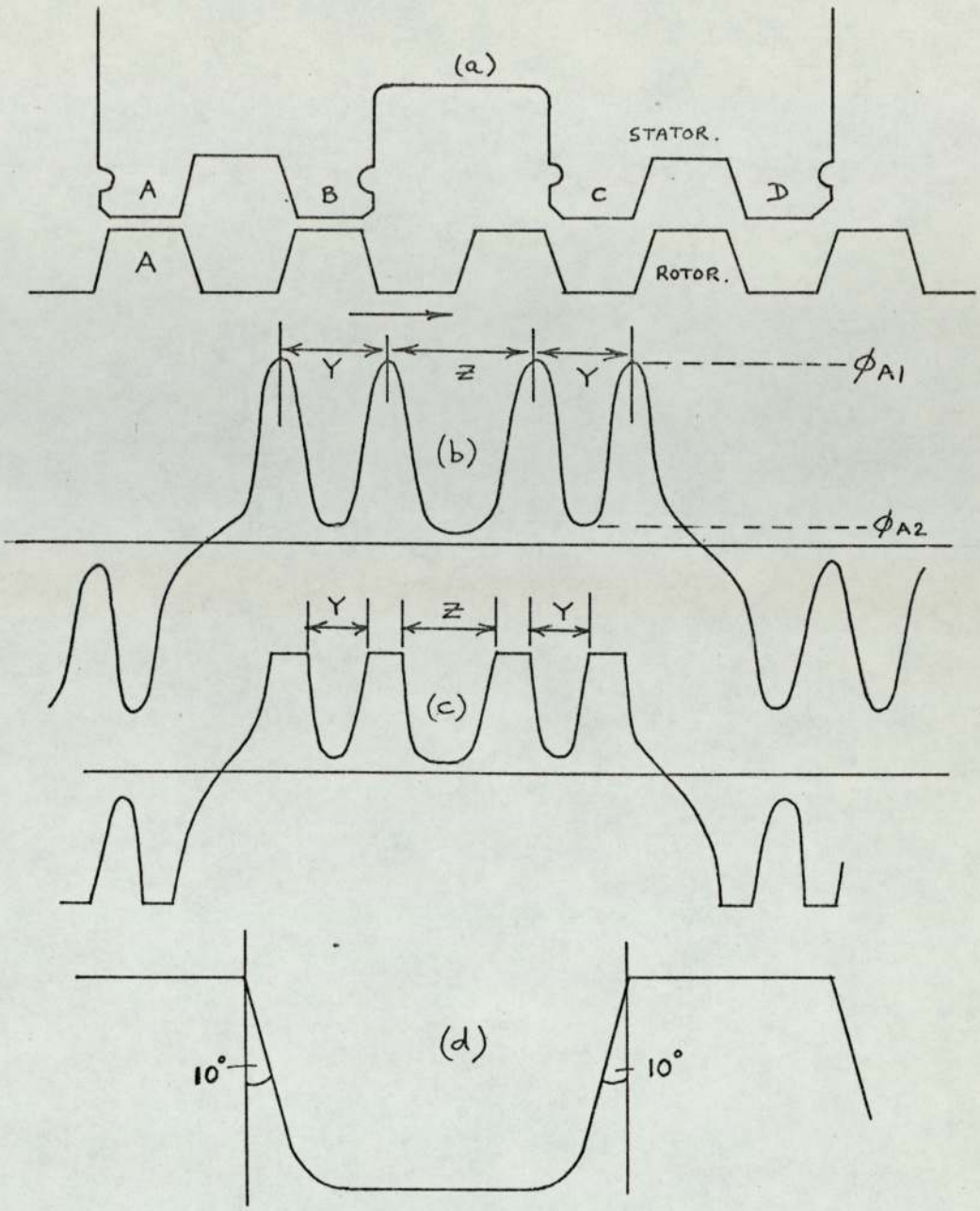

Fig.71

Theoretical flux waveforms in a rotor tooth.

(a) stator and rotor configuration over a dc pole pitch.
(b) theoretical flux waveform across the total rotor tooth surface (rotor tooth A).
(b) Z/Y = ac slot width / small slot width.
ϕ_{A1} - flux passing through tooth A when rotor tooth A is opposite a stator tooth.
ϕ_{A2} - flux passing through tooth A when rotor tooth A is opposite a stator slot.
(c) theoretical flux variation across a small section of the tooth surface.
Z/Y = ac slot width / small slot width.
(d) flux waveform in a small section of the tooth surface.

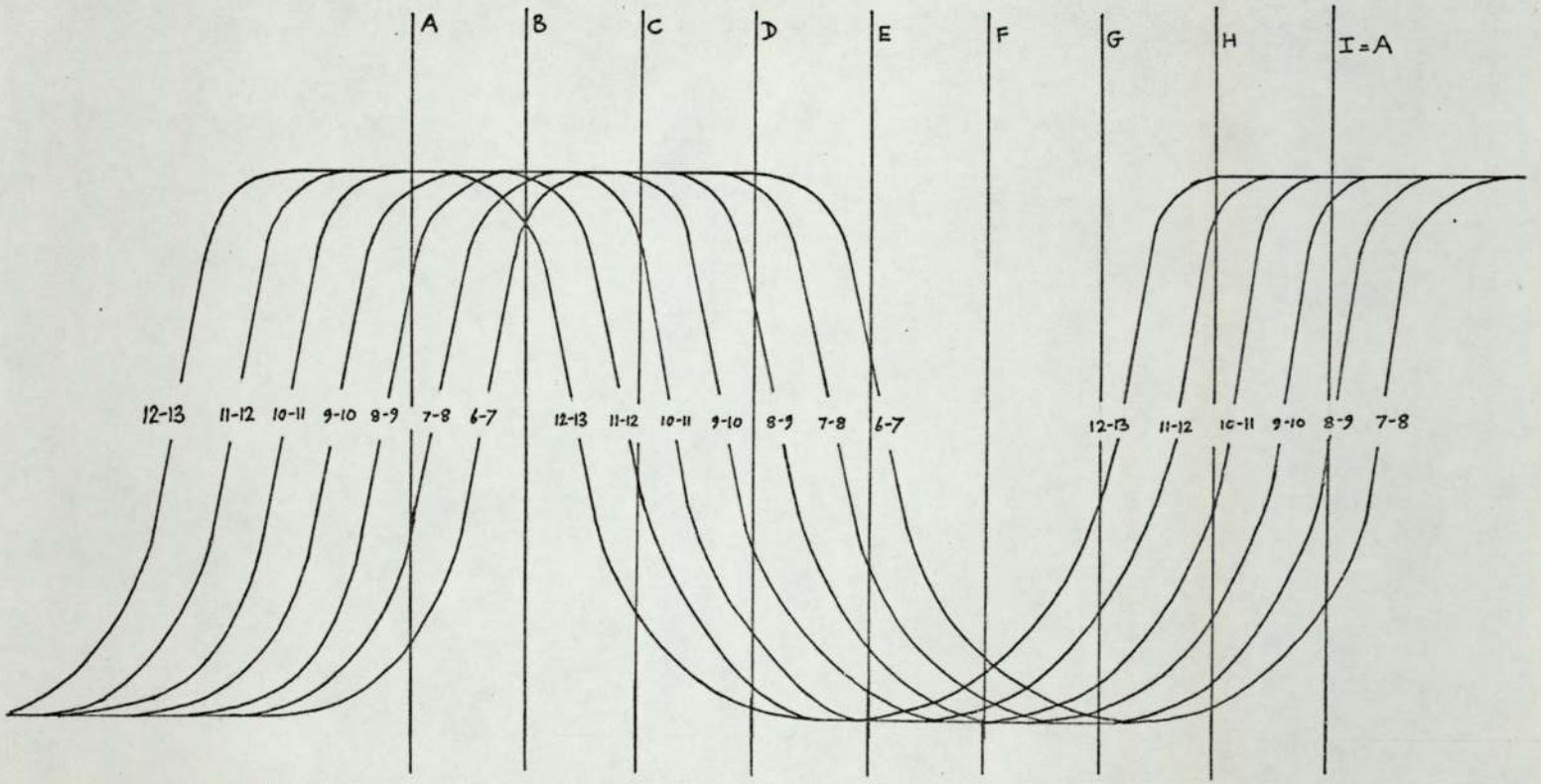

Fig.72 Theoretical displacement of flux waveforms in small sections of the tooth surface for open-circuit conditions.

A,B,C etc represent the position of the rotor tooth A with respect to the stator surface. cond 12-13- leading edge of rotor tooth A. cond 6-7 - trailing edge of rotor tooth A.

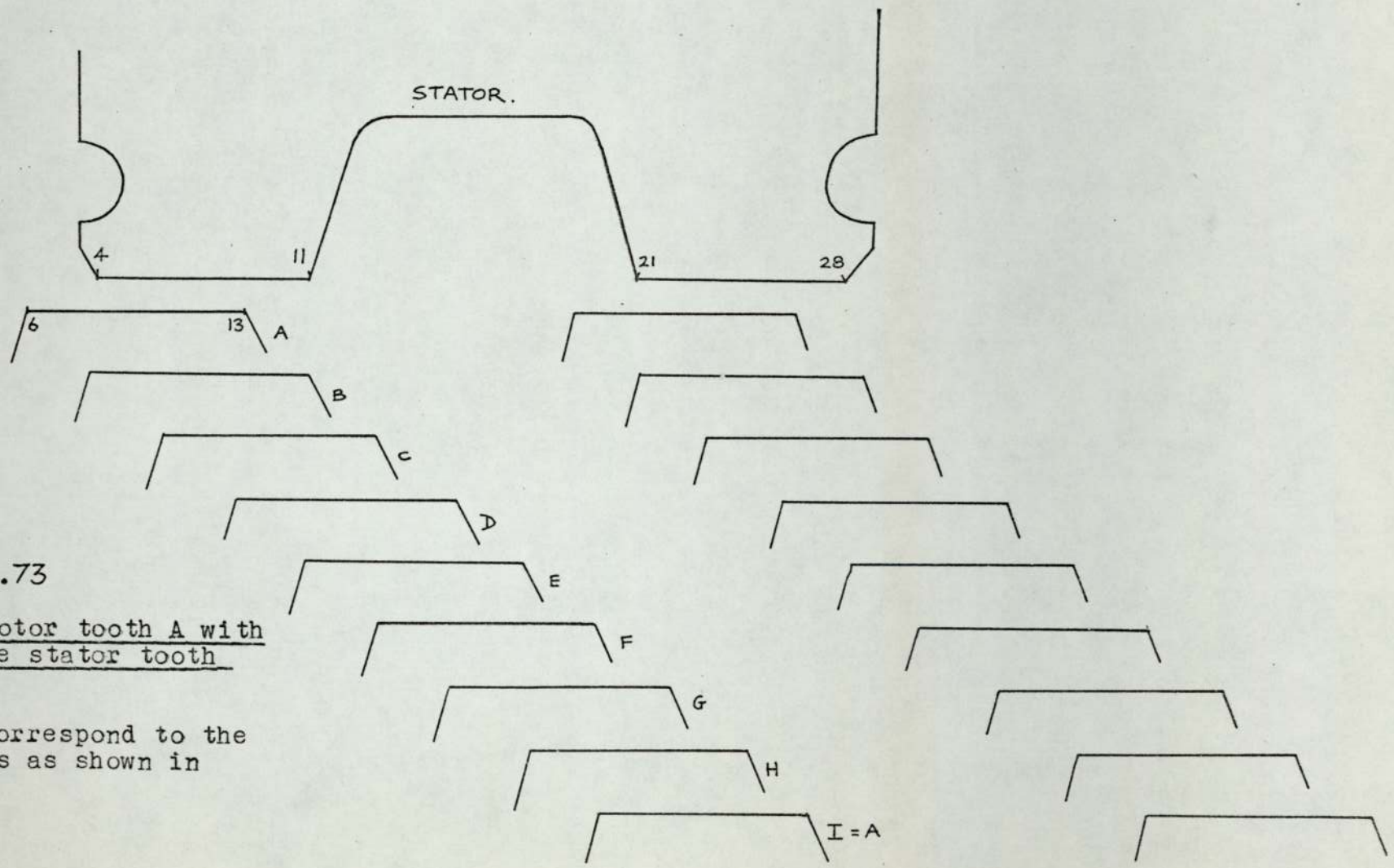

Fig.73

Position of rotor tooth A with respect to the stator tooth surface.

A,B,C,D etc correspond to the flux waveforms as shown in Fig .

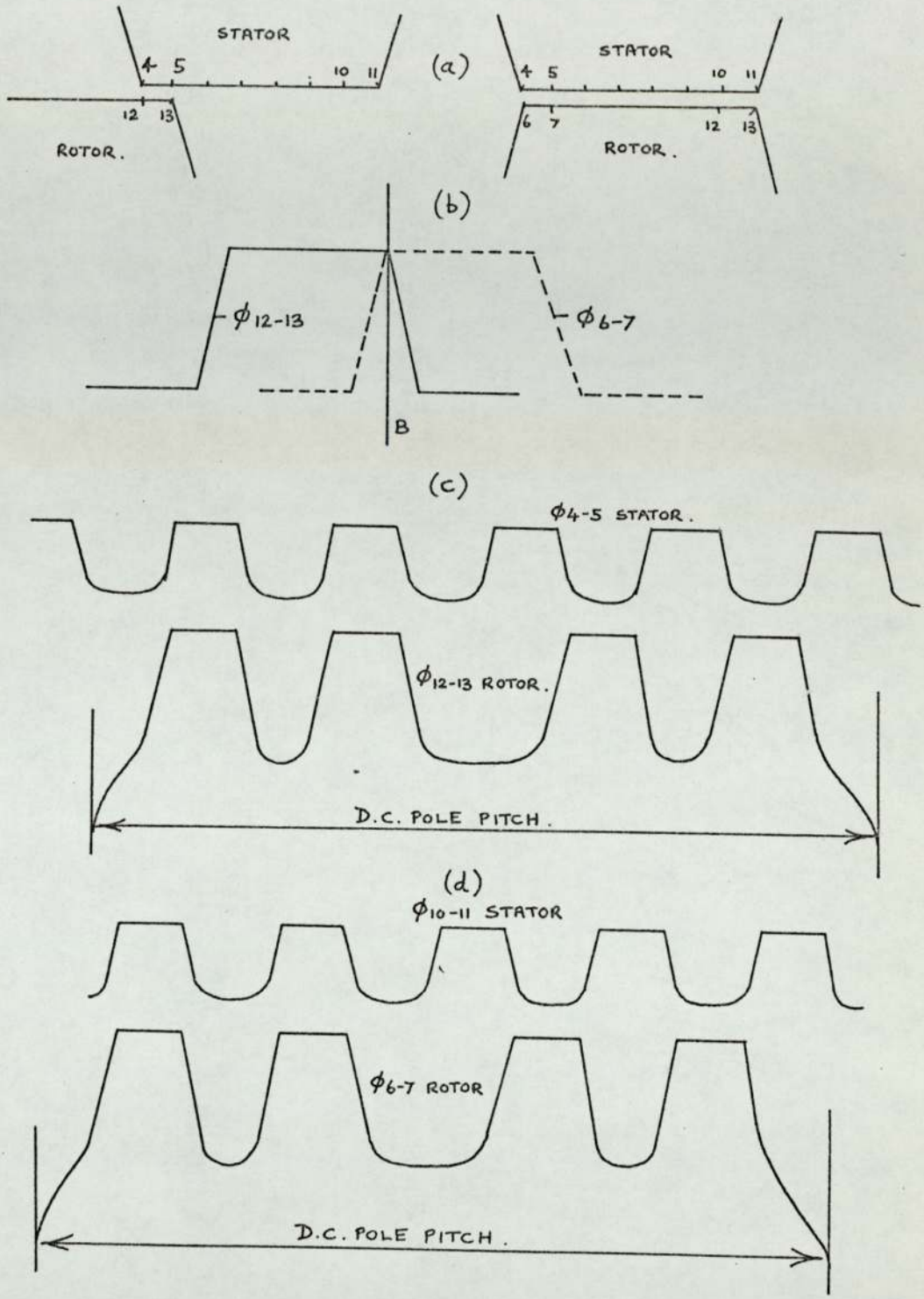

Fig.74

Theoretical flux waveforms in a rotor tooth related to the flux waveforms on the stator surface for open-circuit conditions.

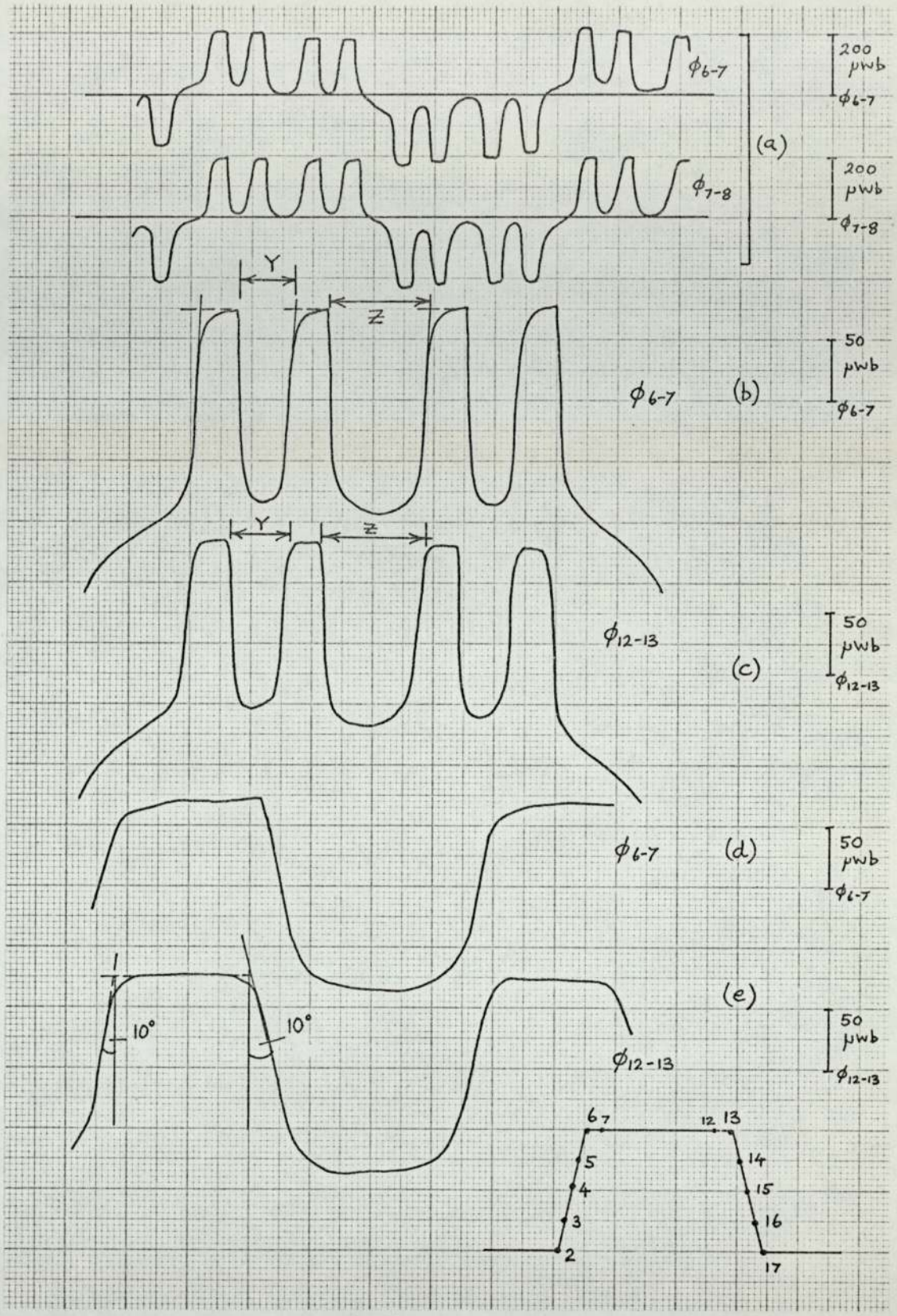

Fig.75

Measured flux waveforms in a rotor tooth under open-circuit conditions.

Rated open circuit voltage. I_f =2·15 amps.

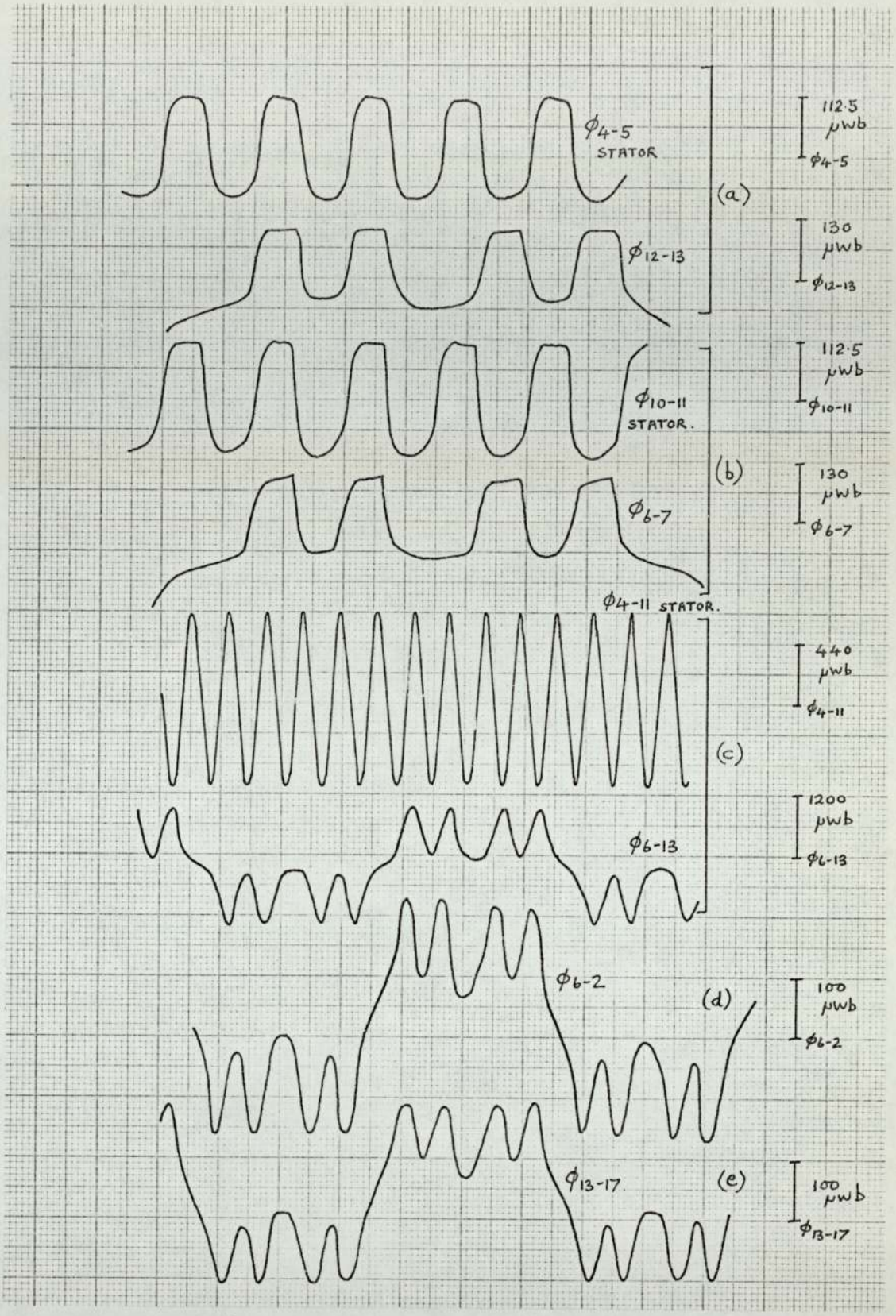

Fig.76

Phase relationship between flux waveforms on the rotor and stator for open circuit conditions.

Rated voltage, I_f=2·15 amps.

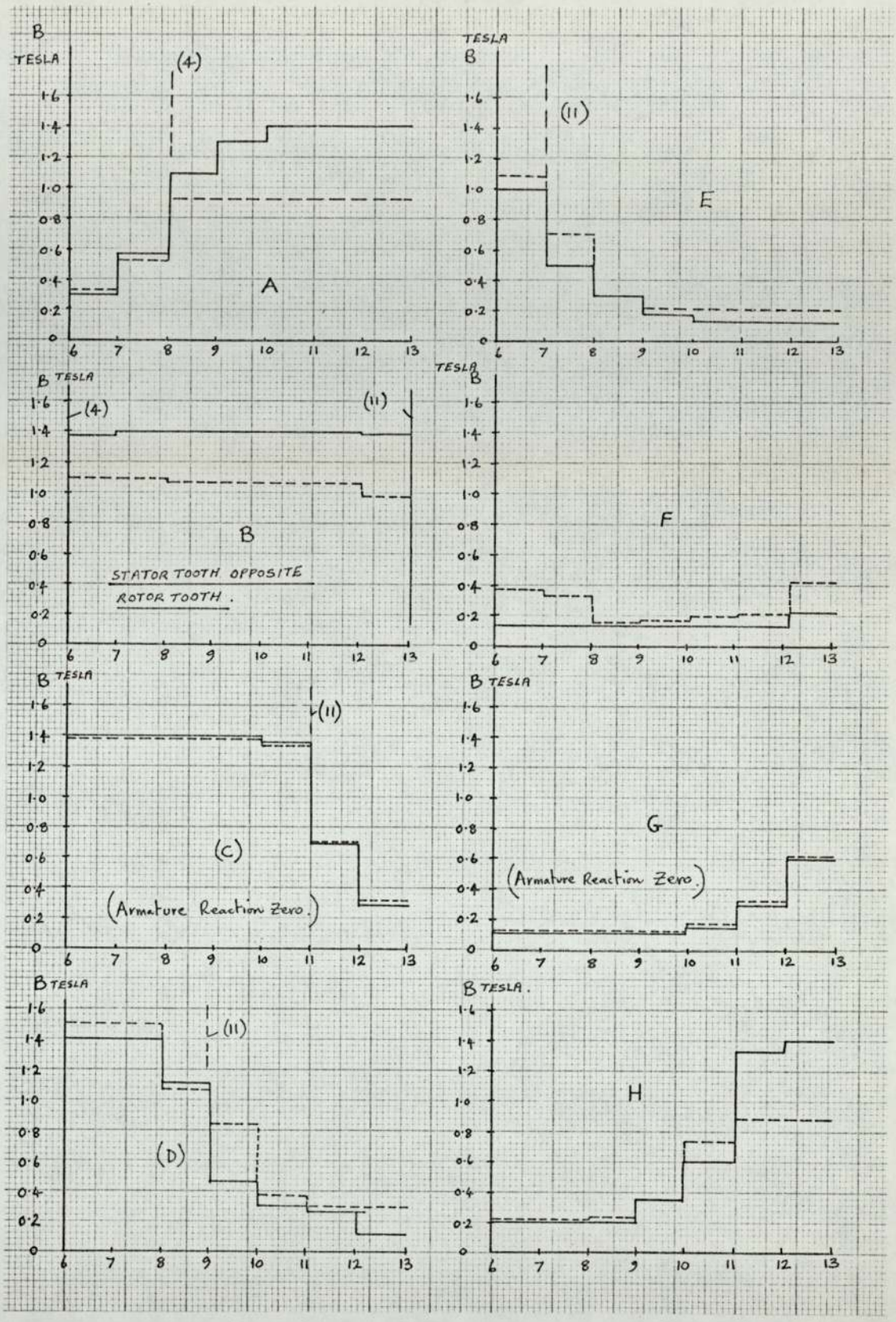

Fig.77

Flux density distribution across the rotor tooth surface under open-circuit and load conditions.

—— open circuit: ----- on load , C=16μF .

4,11,(where shown) represent the conductors on the stator tooth surface (4-11) and their relationship to the rotor tooth position.

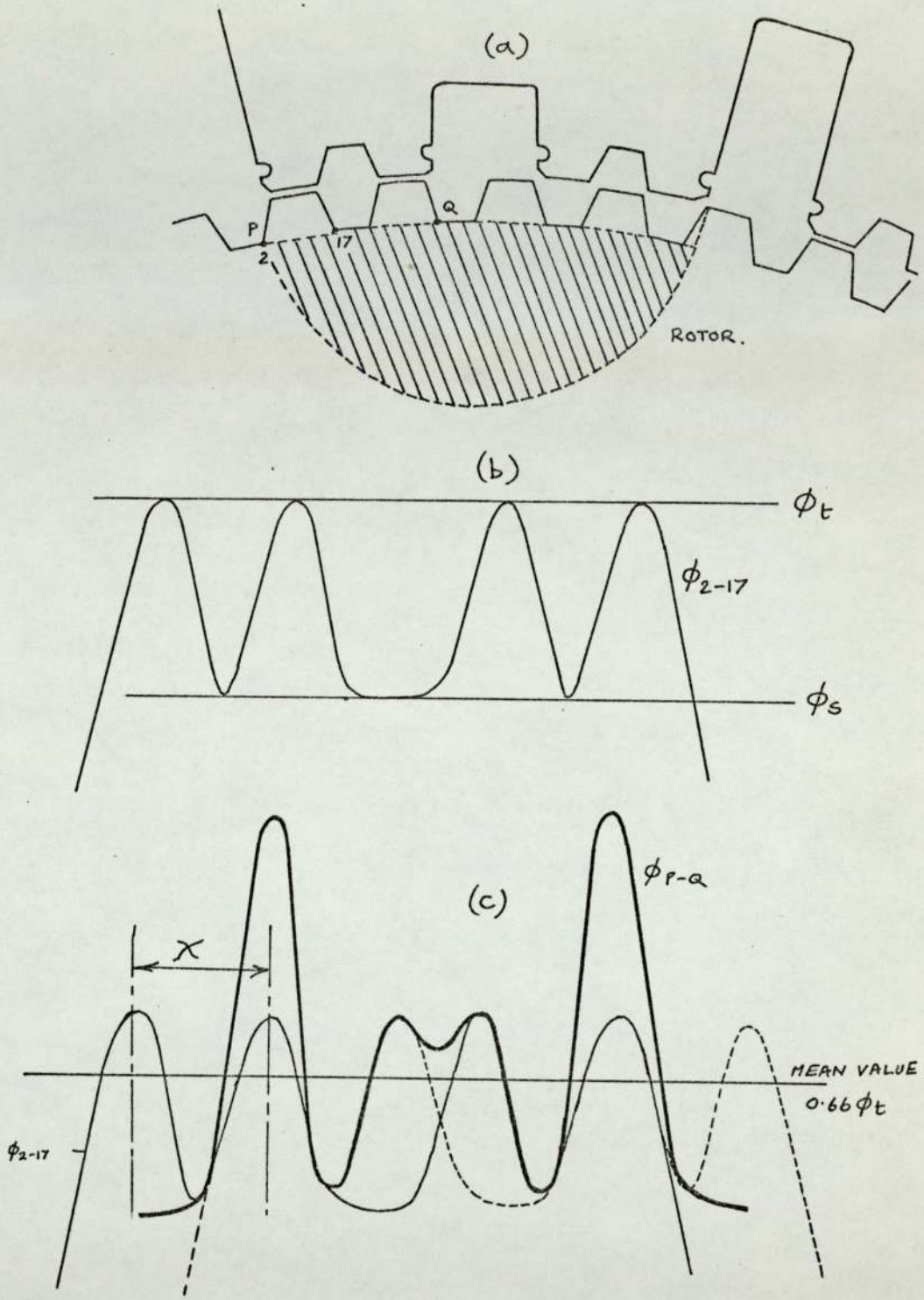

Fig.78

Flux waveforms across two adjacent rotor teeth.

(a) stator and rotor configuration over a dc pole pitch. (shaded area represents the assumed loss region in rotor core.)

(b) flux waveform at the tooth root. (ϕ 2-17 rotor tooth A)
(c) total flux waveform across P-Q.

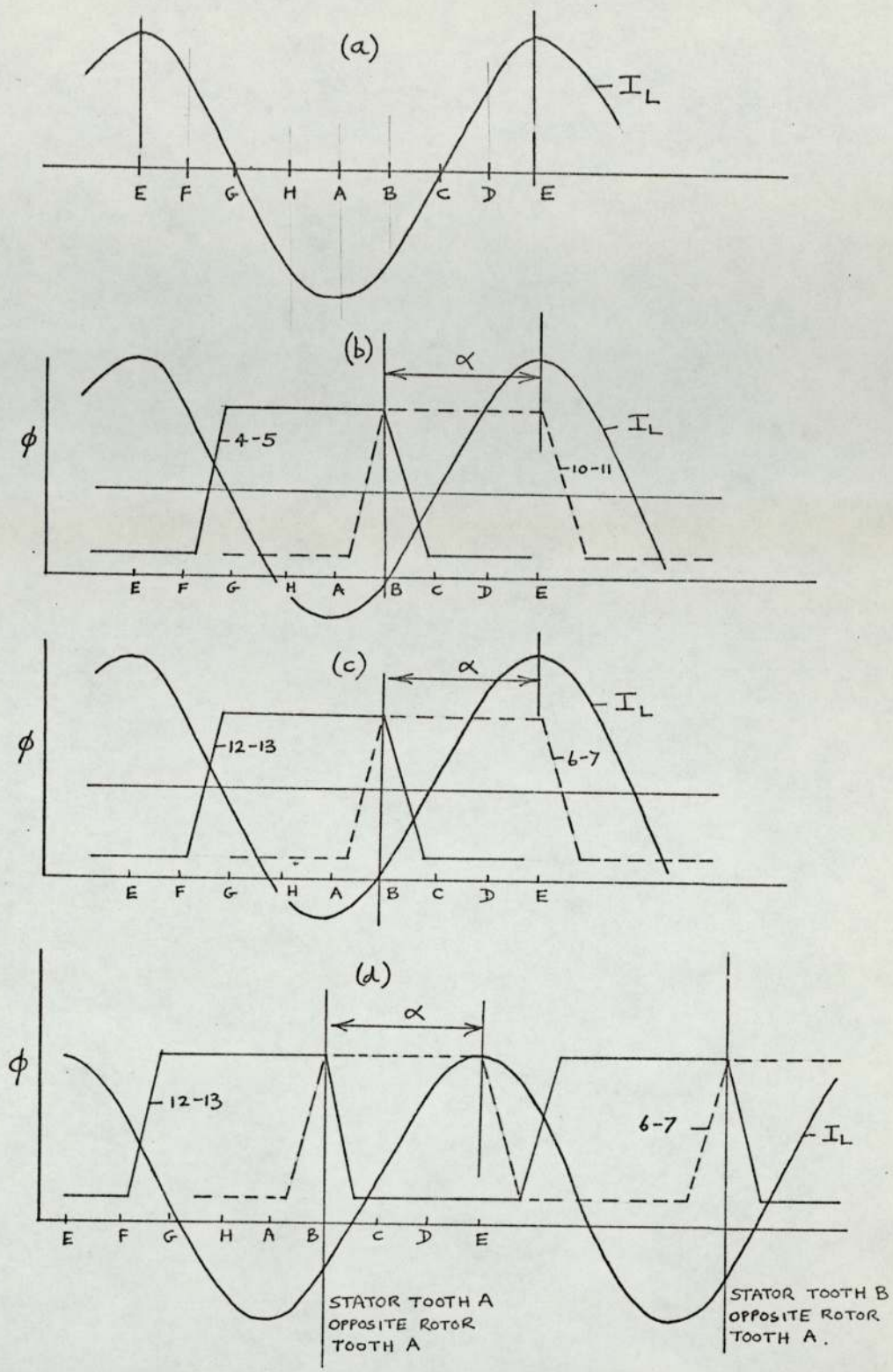

Fig.79

Theoretical phase displacement between the flux waveforms on the stator and rotor and the load current.

(a) load current waveform related to the rotor tooth position for C =16μF.
(b) phase relationship between the load current and the open-circuit φ waveforms on the stator surface.
(c) phase relationship between the load current and the open-circuit φ waveforms on the rotor surface.
(d) phase relationship between the load current and the open-circuit φ waveforms on the rotor surface for tooth A opposite teeth A and B on the stator surface.

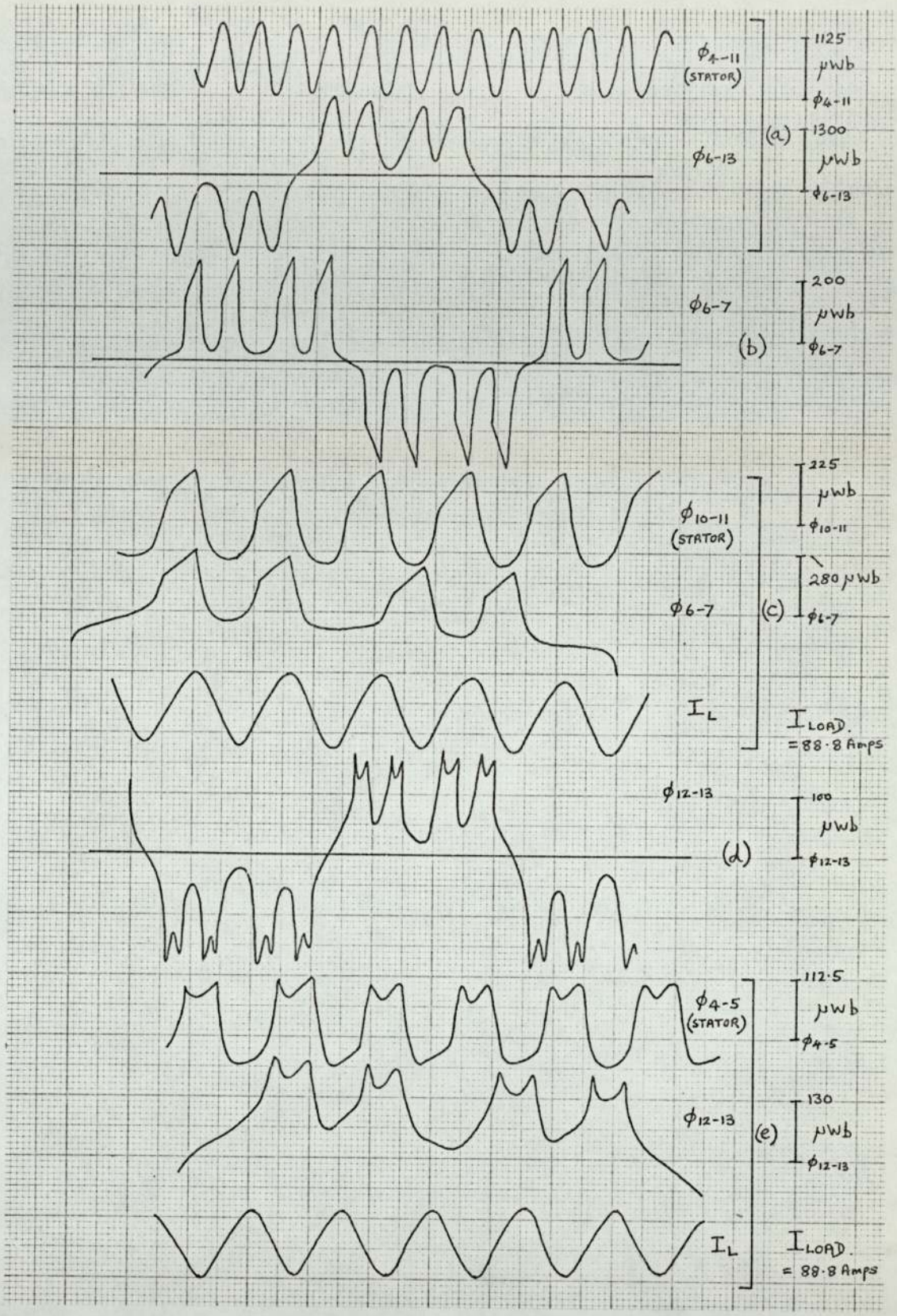

Fig.80

Flux waveforms in a rotor tooth under load conditions.

Series capacitor, C=16μF . Rated output.

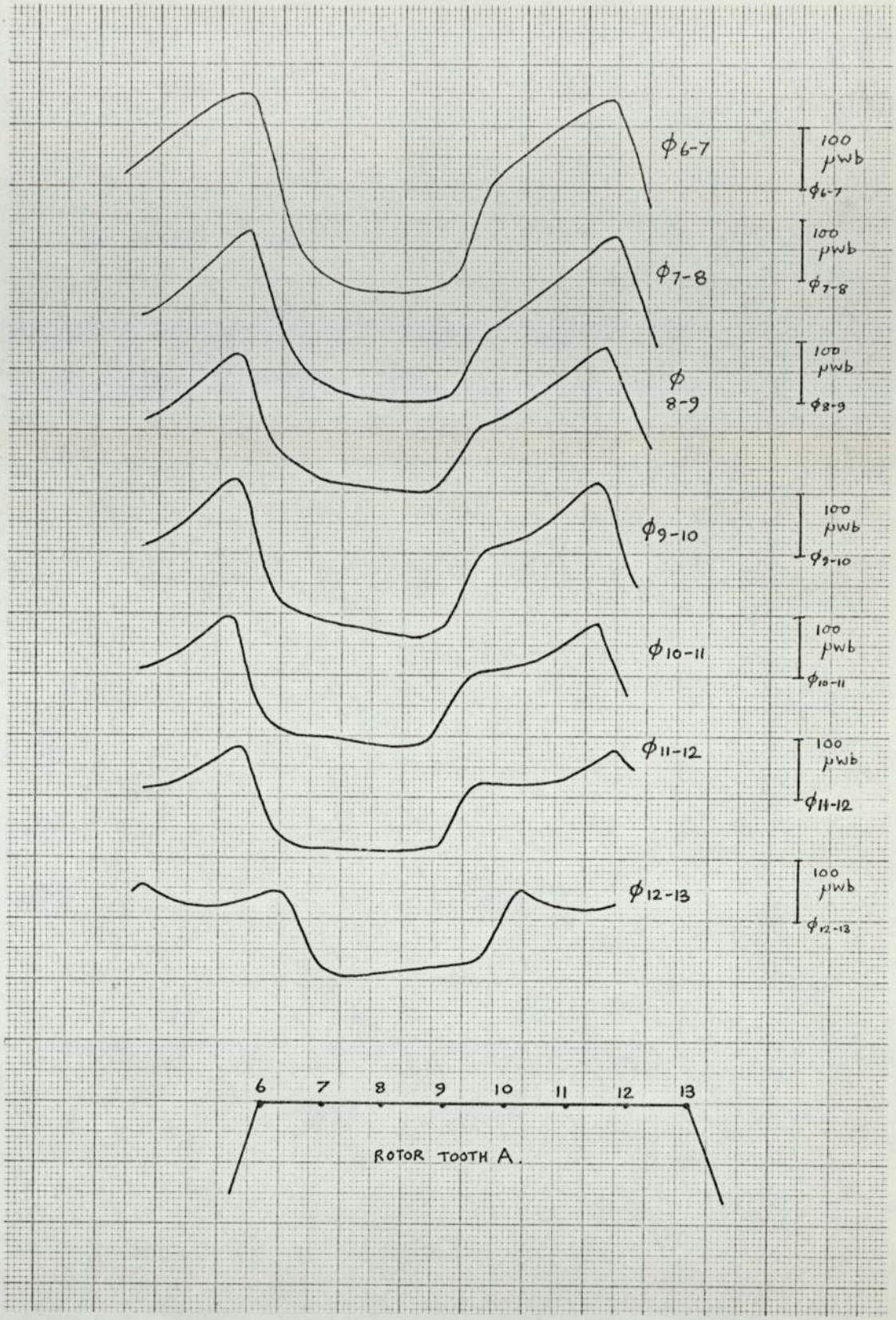

Fig.81

On load flux waveforms across the rotor tooth surface showing the distortion due to armature reaction.

(flux waveforms over a rotor pitch.)

Rated output. I_L =88·8 amps. C= 16μF .

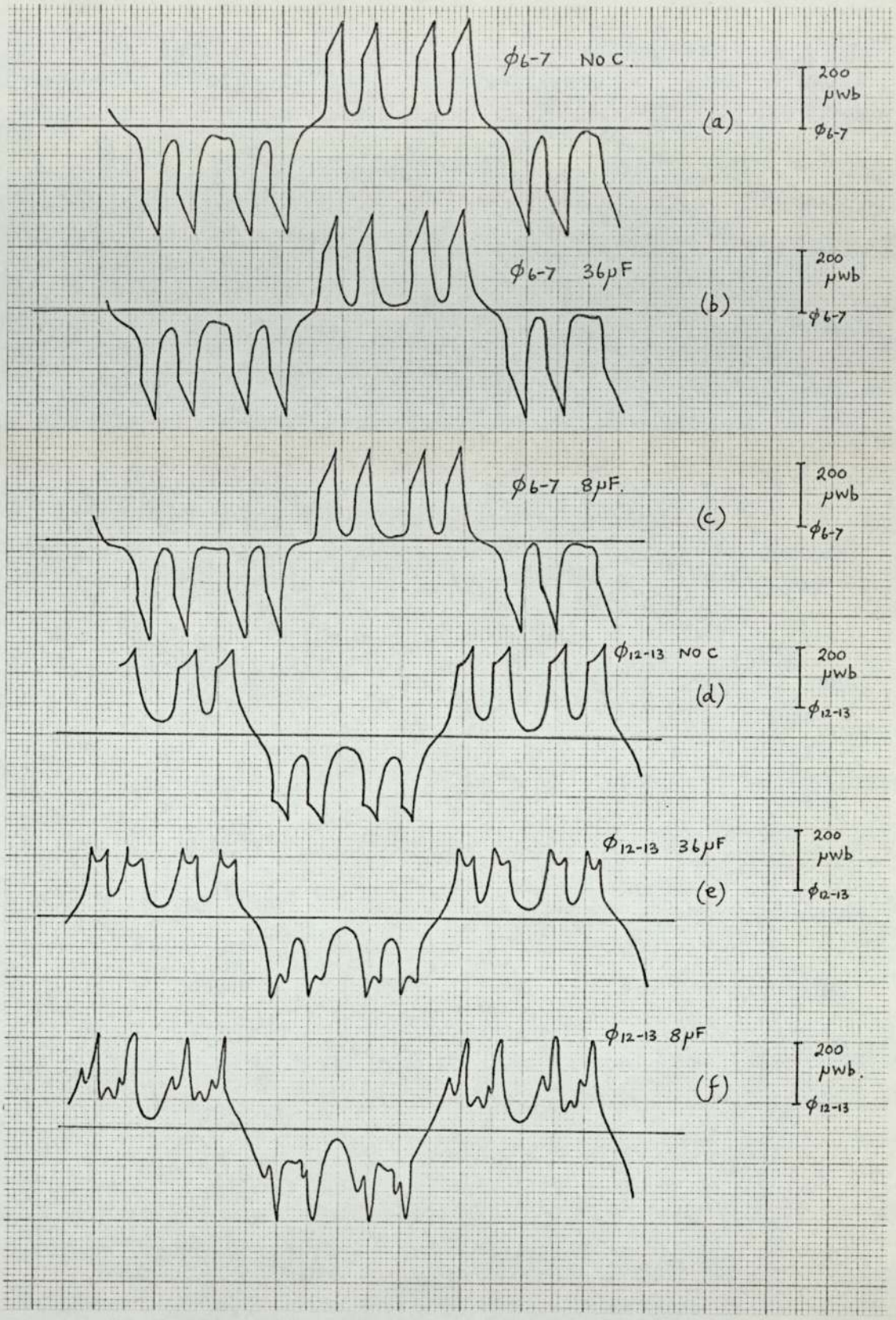

Fig.82

Flux waveforms at the leading and trailing edges of a rotor tooth for various values of series compensation. Rated output. I_L=88·8 amps.

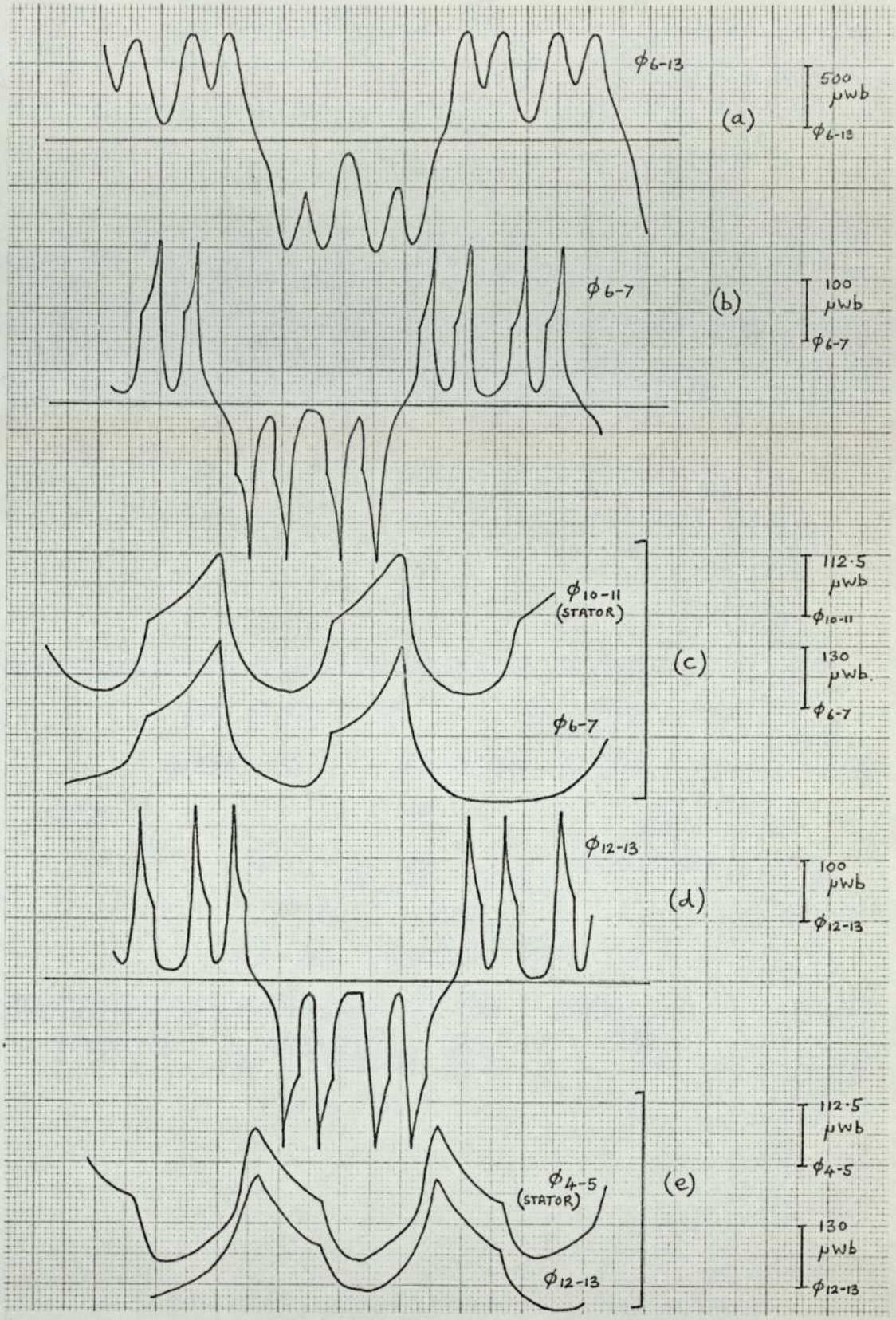

Fig.83

Flux waveforms in a rotor tooth under short circuit conditions.

No series capacitor, I_{sc}=88·8 amps.

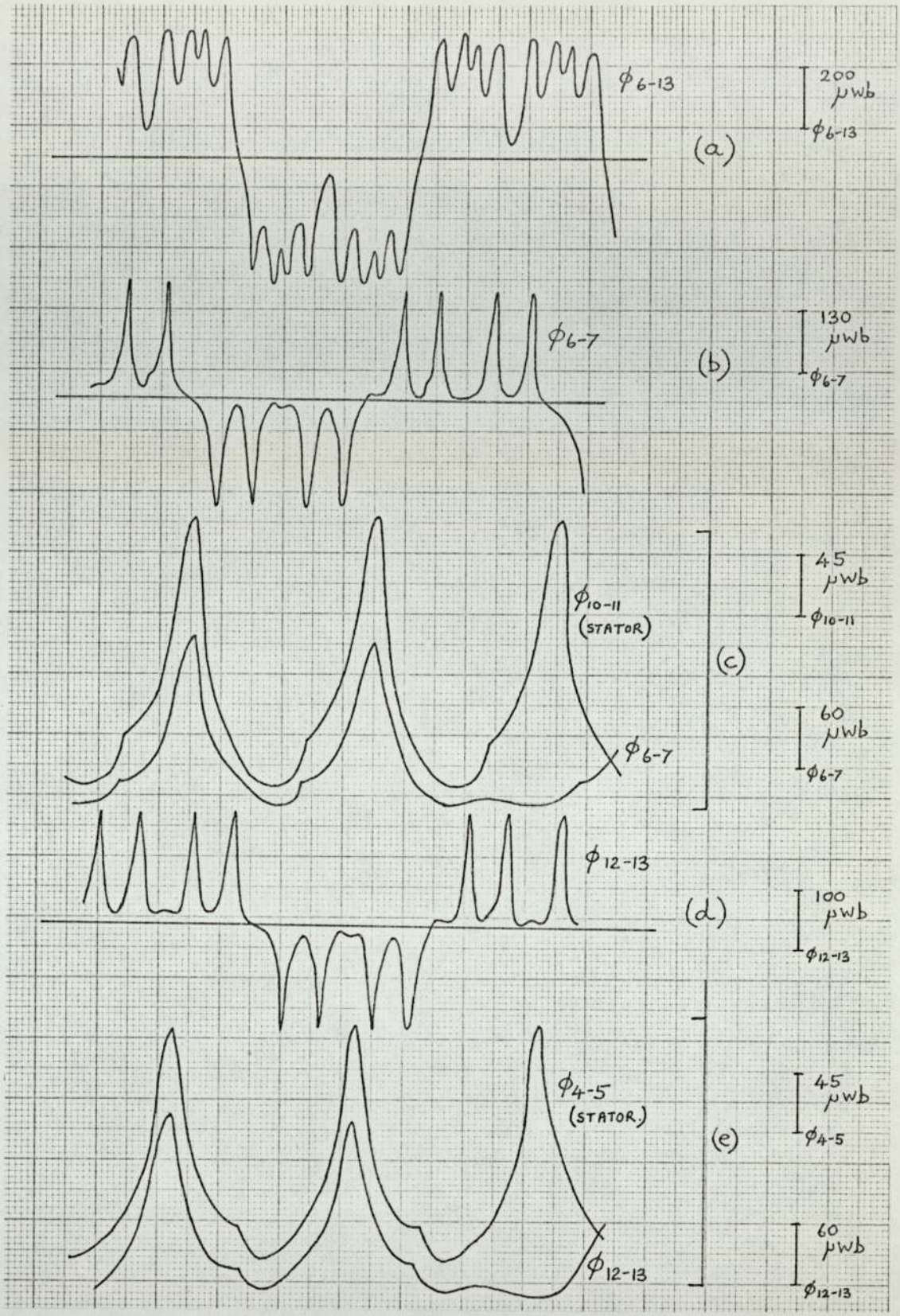

Fig. 84

Flux waveforms in a rotor tooth under short circuit conditions.

Series capacitor, C=16μF . I_{sc}=88·8 amps.

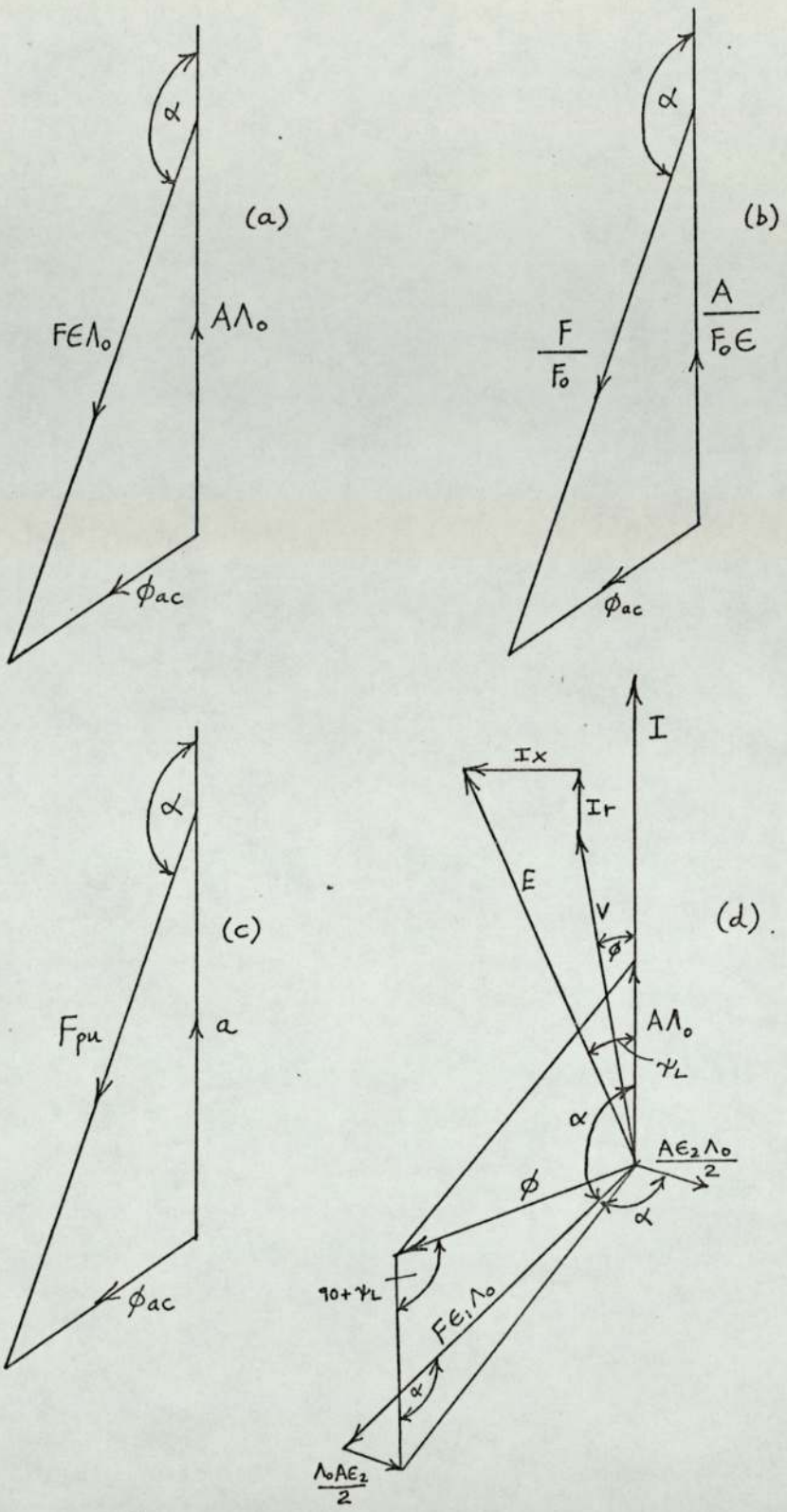

Fig.85

On-load vector diagrams. (Pohl and Raby).

(a) addition of fundamental fluxes to give ϕ_{ac} .

(b),(c) addition of fundamental fluxes to give ϕ_{ac} (pu).

(d) addition of fundamental fluxes- Pohl.

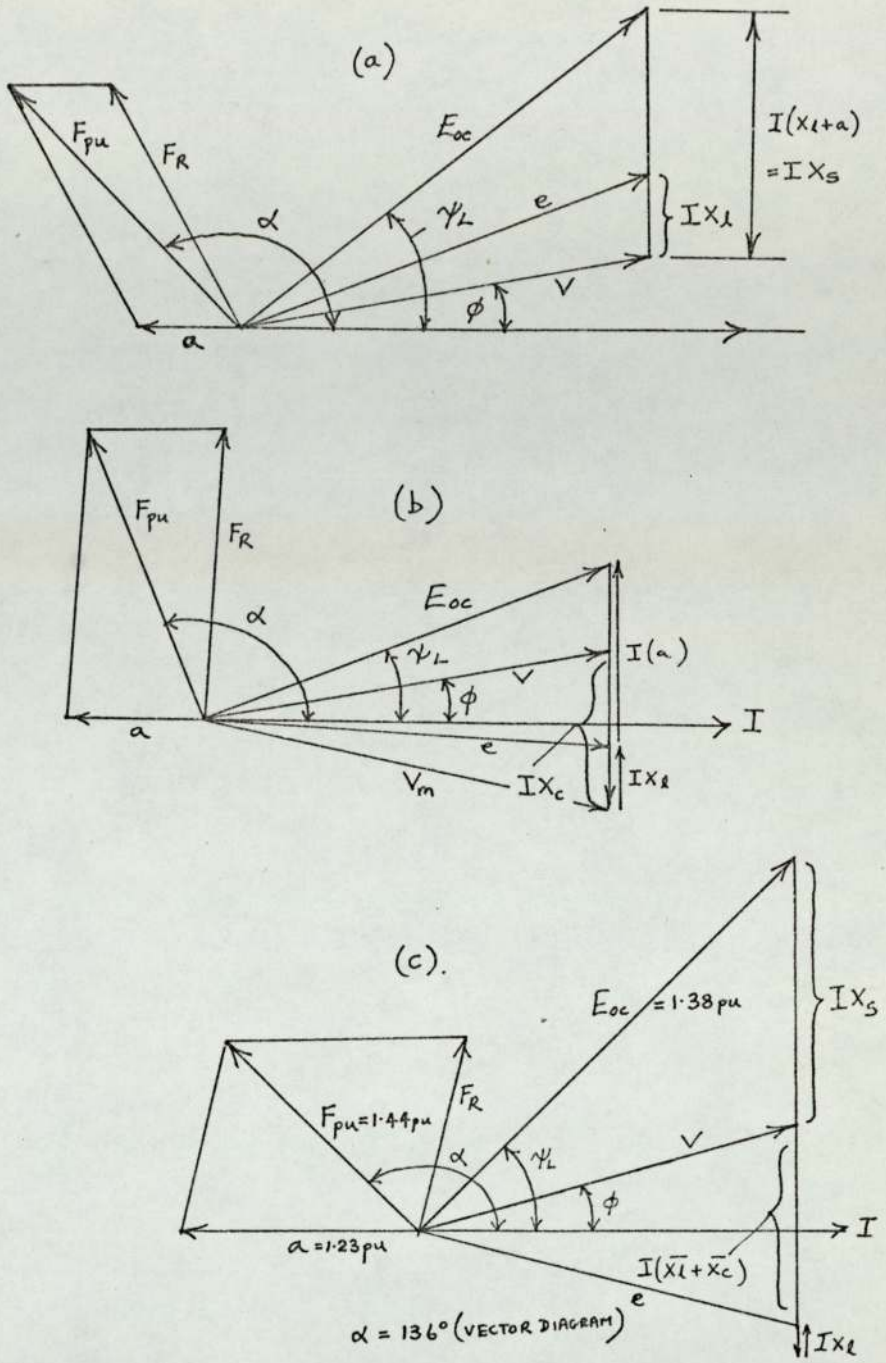

Fig.86

On-load vector diagrams to calculate F_{pu} and α .

(a) - no series capacitor.

(b) - with series capacitor.

(c) - load vector diagram for C=16μF, (rated output)
cos ϕ = 0·962 . I_L= 88·8 amps.

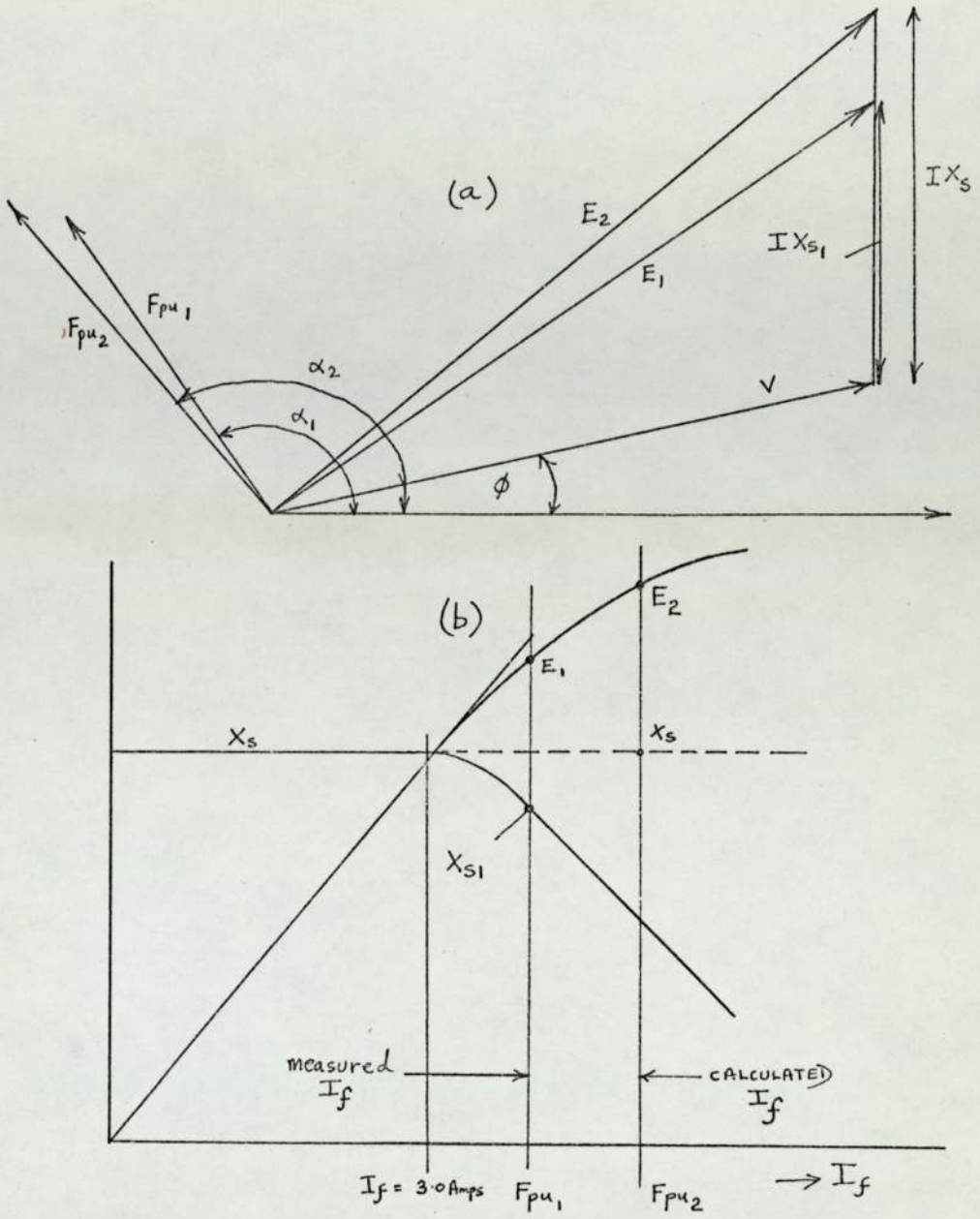

Fig.87

(a) - On-load vector diagram for two values of synchronous reactance, $X_S > X_{S1}$. F_{pu_1} pu field corresponding to E_1 and IX_{S1}. F_{pu_2} pu field corresponding to E_2 and IX_S.

(b) O.C. saturation curve and synchronous reactance

F_{pu_1} measured field current corresponding to E_1,

X_{S1} - saturated value of synchronous reactance.

F_{pu_2} calculated field current assuming that X_S is constant.

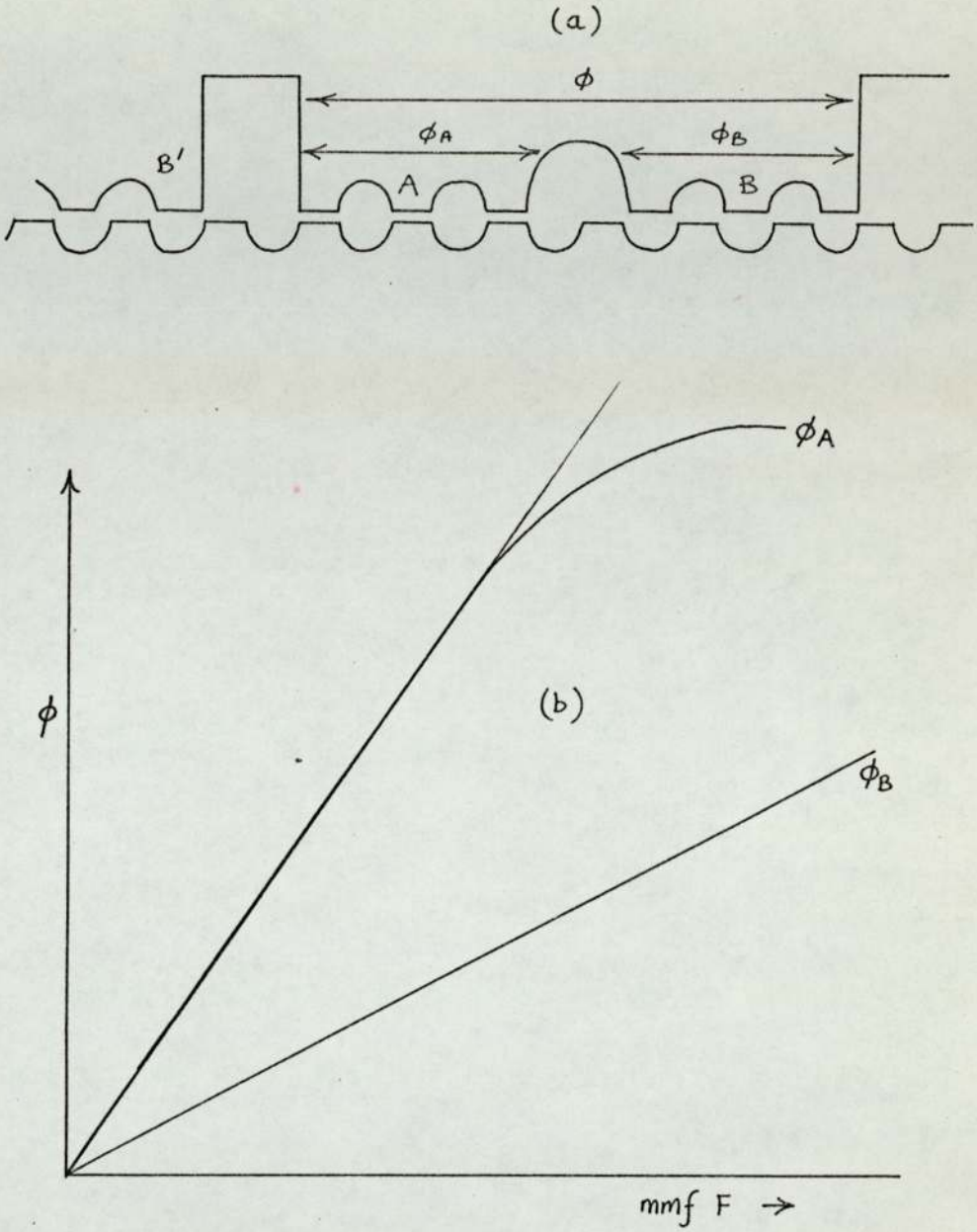

Fig.88

(a) Guy-slotting, (A,B,B′)-symbols used in section 7.2.1.1. and 7.2.1.3.

(b) Open circuit saturation curve. (7.2.1.3.)

ϕ_A -flux in whole stator main tooth A for the rotor position shown in (a).

ϕ_B -flux in whole stator main tooth B for the rotor position shown in (a).

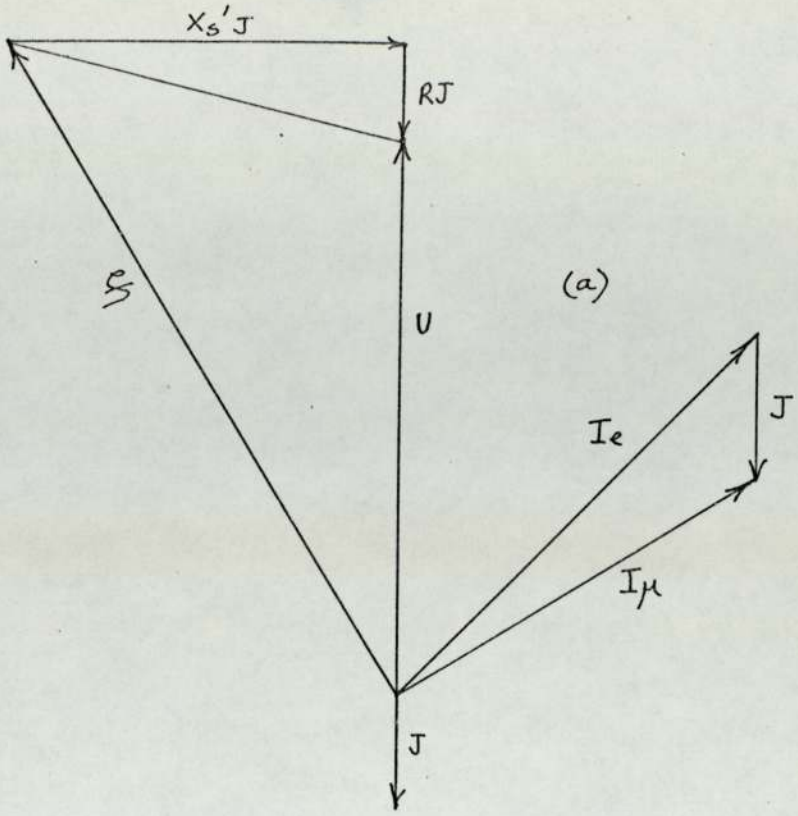

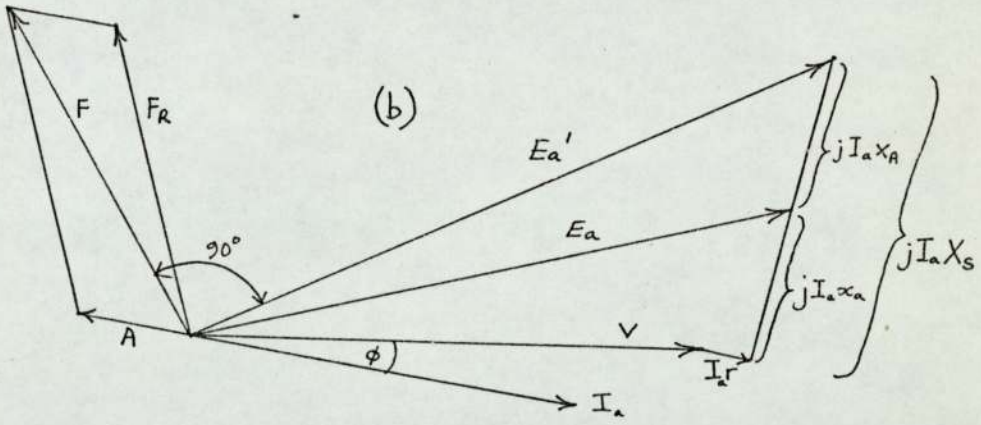

Fig.89

(a) On-load vector diagram (unity power factor) Büssing.

U-terminal voltage, X_s'-leakage reactance.
$\mathcal{E}$-internal voltage, I_μ-field current to give $\mathcal{E}$ referred to the ac winding, J- load current, I_e- total field excitation on load referred to the ac winding.

(b) on-load vector diagram for cylindrical rotor synchronous machine.

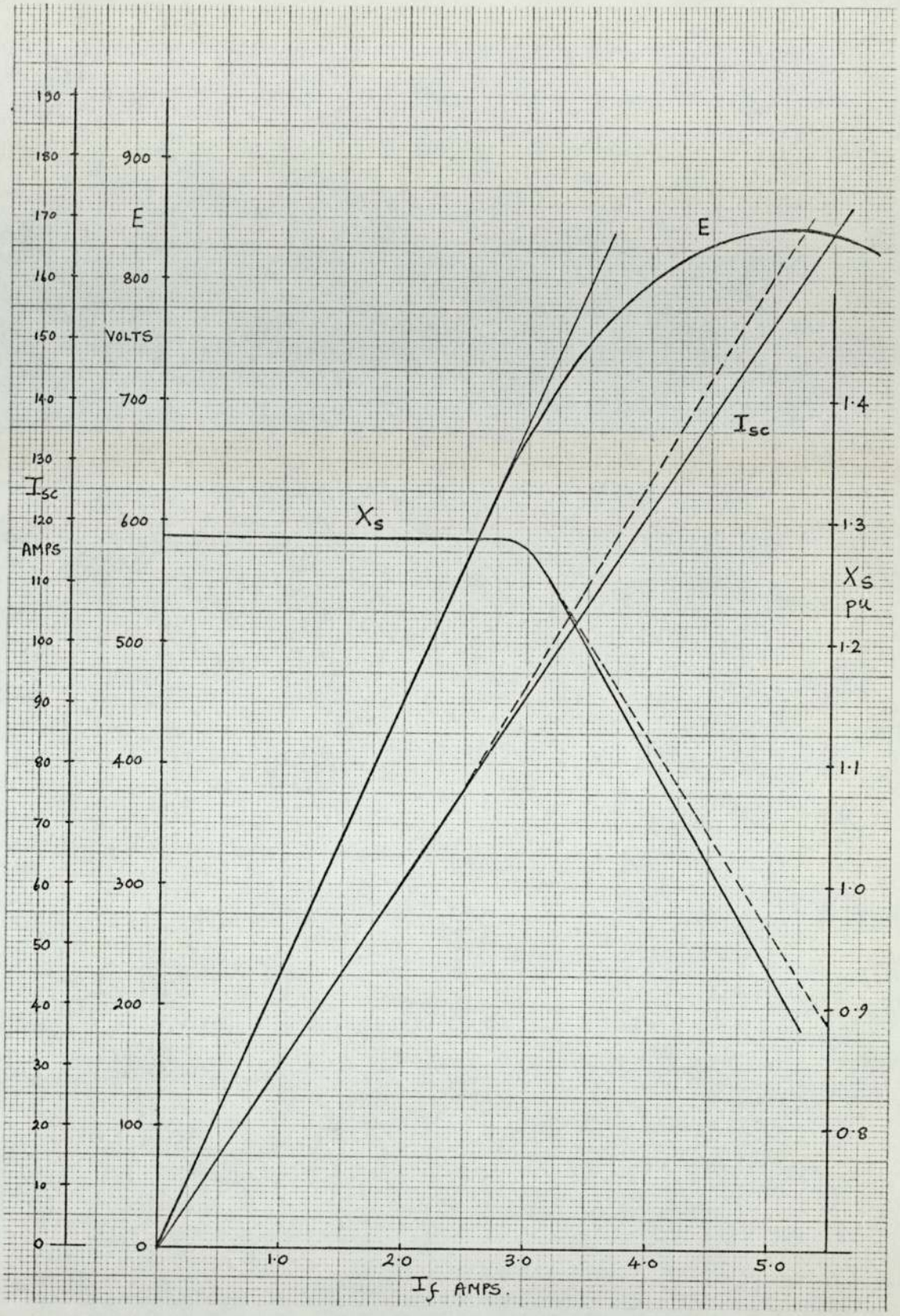

Fig.90

E- open circuit voltage characteristic for the experimental machine.
I_{sc}- short-circuit characteristic for the experimental machine.------ measured, ———— calculated.

X_s synchronous reactance characteristic.
– – – – – – measured ———— calculated.

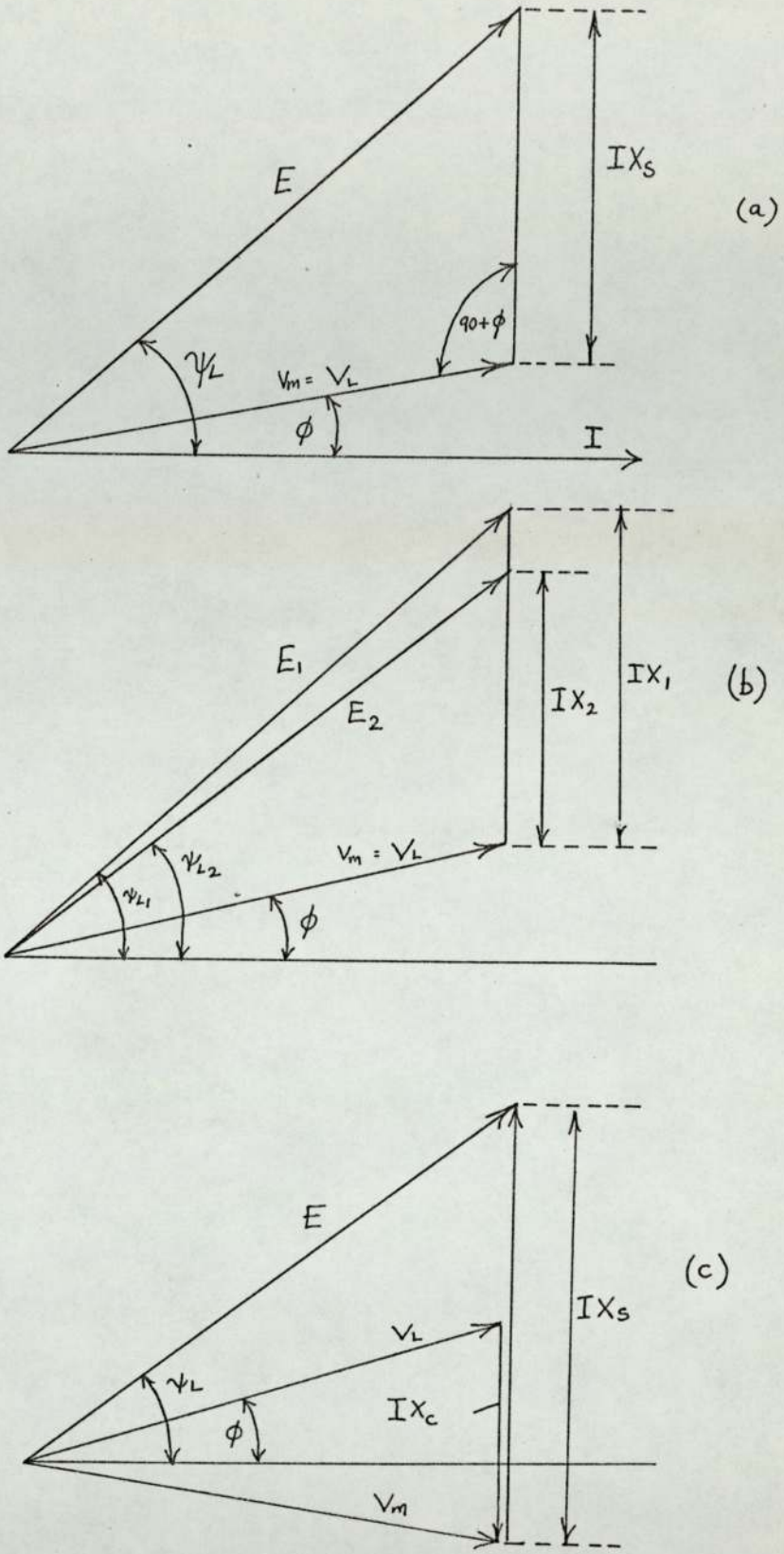

Fig. 91

On-load vector diagrams (7.3.2.)

(a) zero compensation.

(b) vector diagram for different values of x_s .

(c-) with series capacitor.

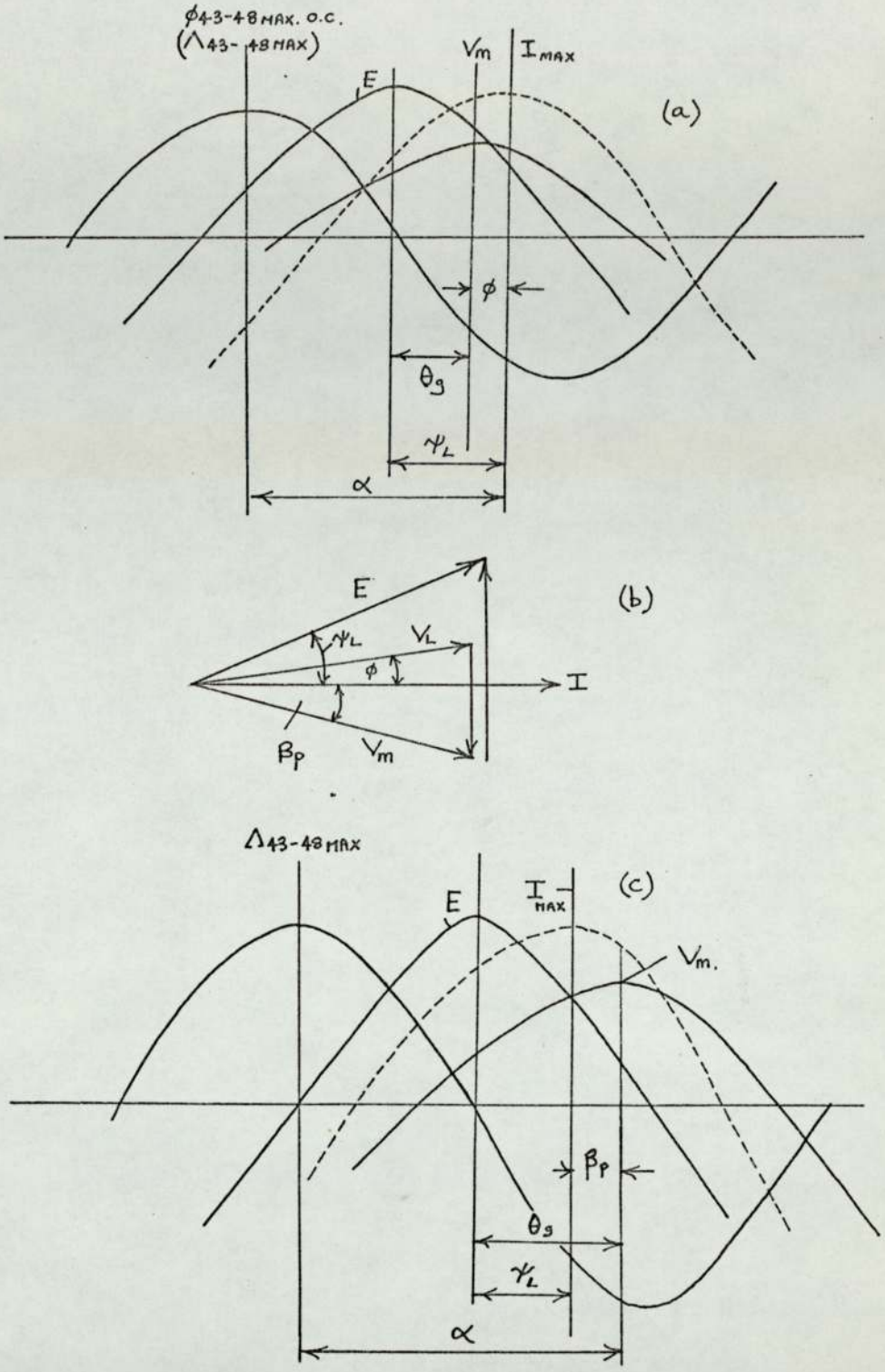

Fig.92

Load angles for the Guy-machine.

(a) zero compensation $\theta_g = \psi_L - \phi$.

(b) vector diagram when series capacitor is used.

(c) with series capacitor $\theta_g = \psi_L + \beta_p$.

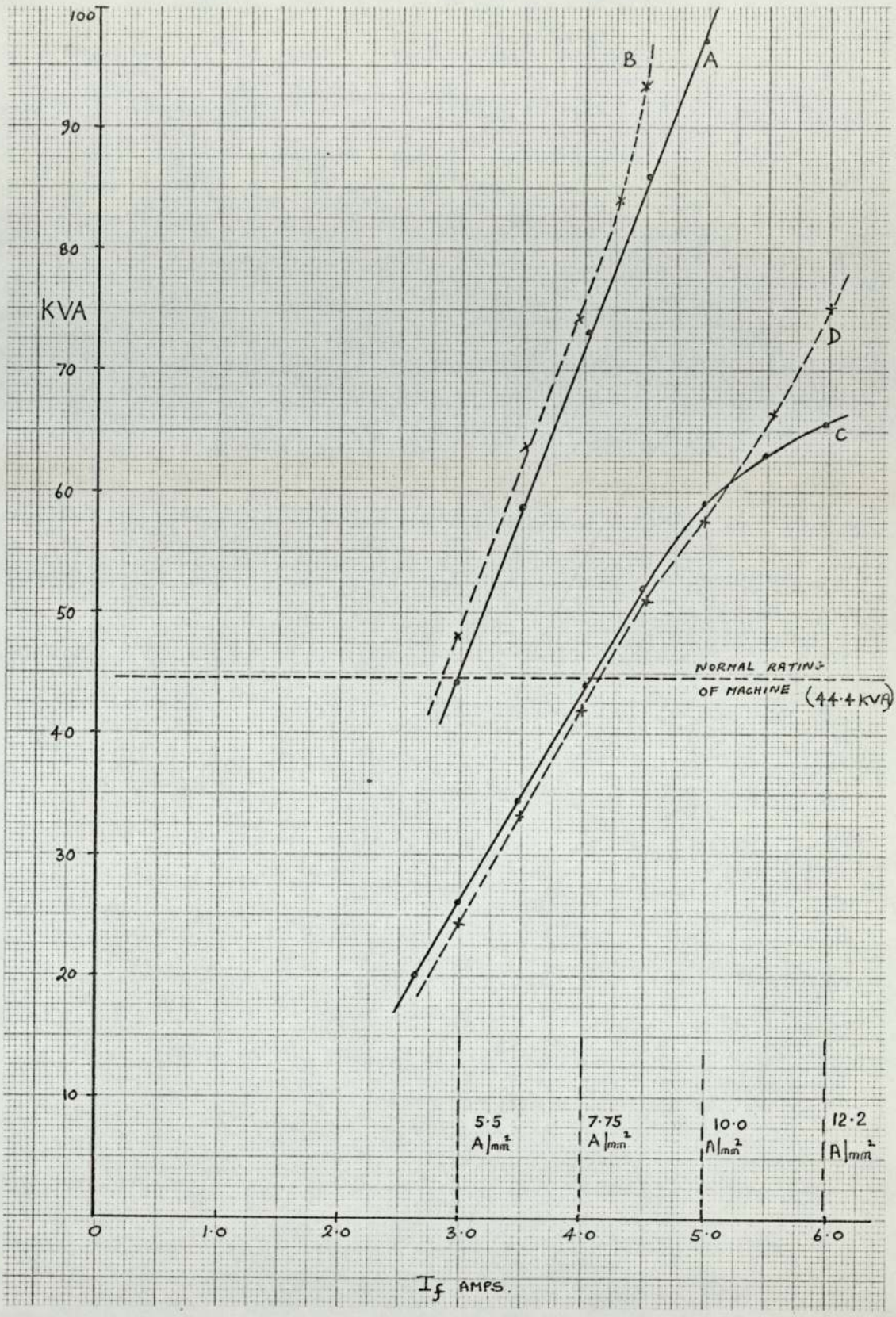

Fig.93

Machine output-I_f curves for zero compensation and C=16μF.

A-16μF (measured) B-16μF (calculated)

C-zero compensation (measured)

D-zero compensation (calculated).

Fig.94

Temp rise in the windings and stator iron, 55 KVA rating.

A- field current.

B- temp rise in field winding.

C- approximate temp rise in field winding (only one damping winding fitted.)

D- temp rise in a.c. winding.

E- temp rise in field winding. (44.4 KVA)

F- temp rise at the back of the core.

G- temp rise in the small teeth.

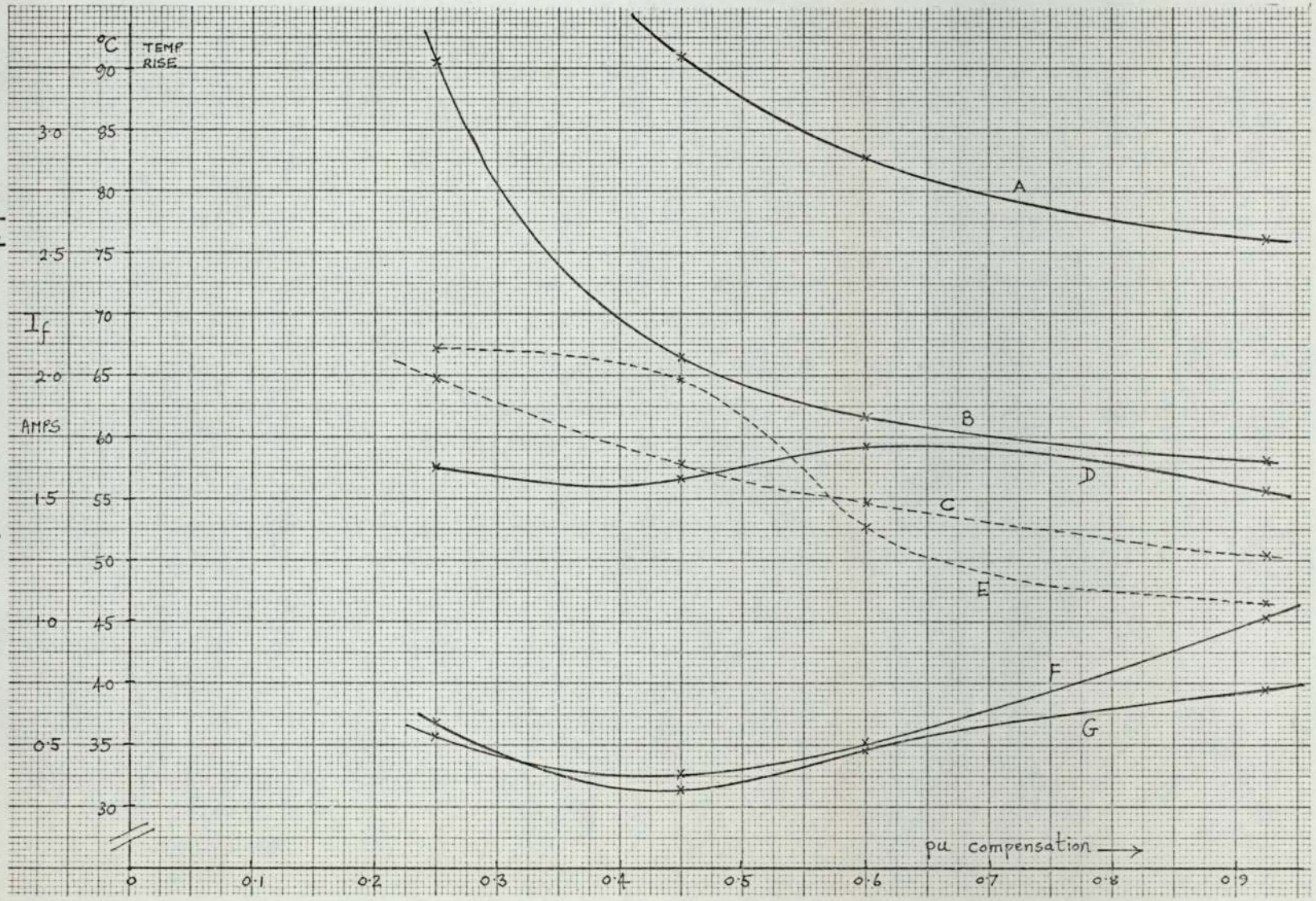

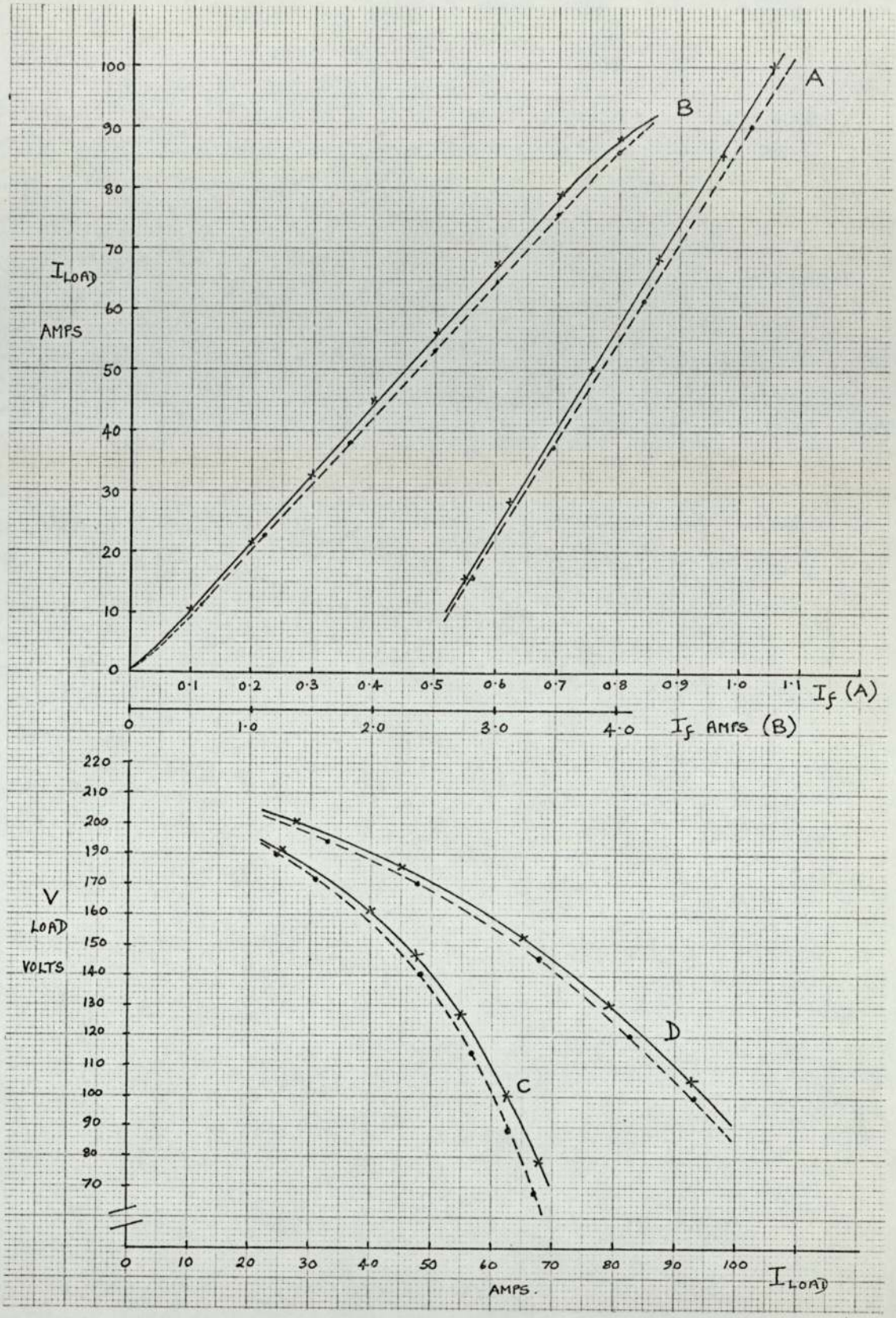

Fig.95

Load characteristics.

A-(V load constant)(variable load and field current)
C=9·6μF.

B- constant impedance test.
C- alternator supplying a variable impedance load
I_f=constant =lamp. C=12μF .
D- alternator supplying a variable impedance load
I_f=constant=lamp C=9·6μF.

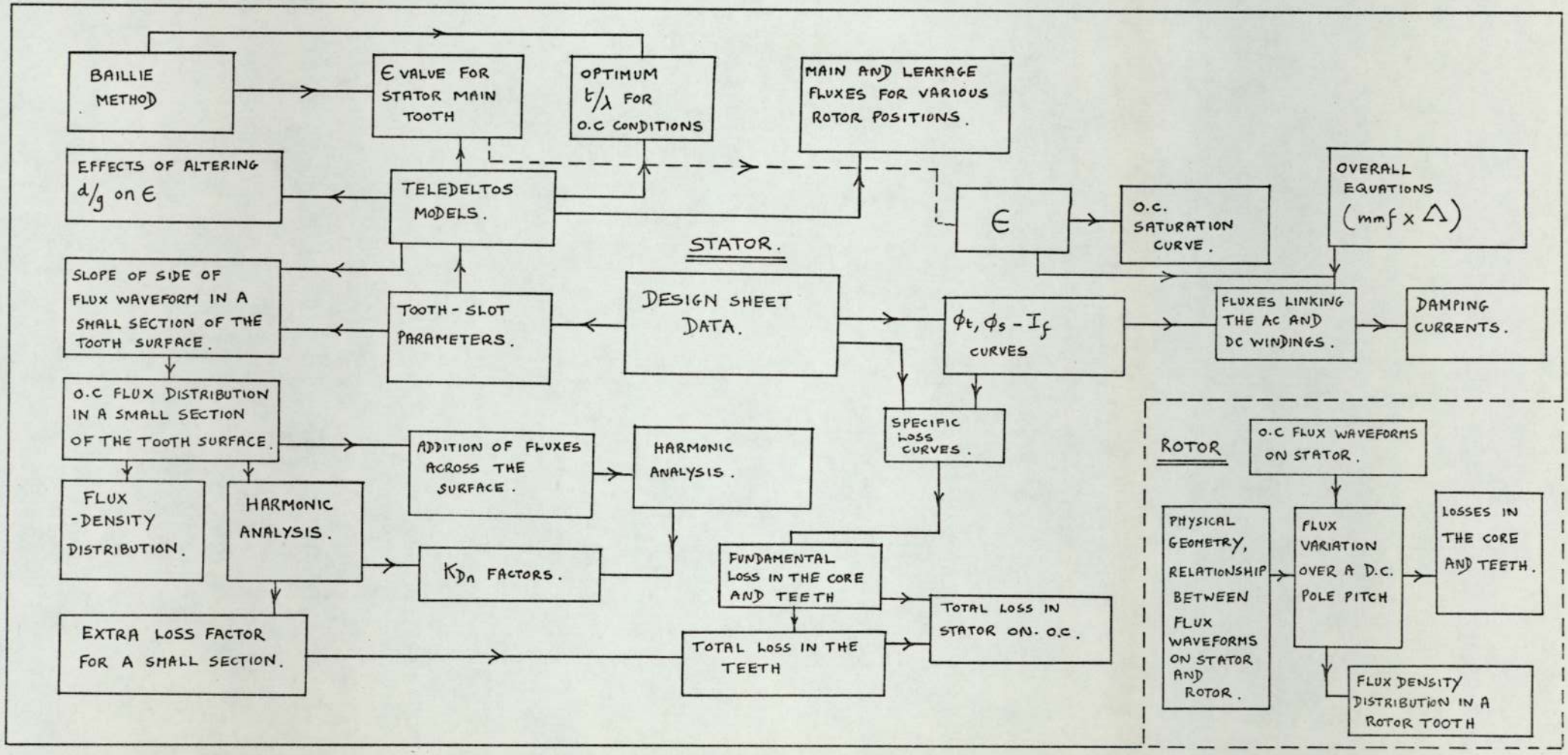

Fig.96 Calculation of fluxes on open-circuit for the rotor and stator.

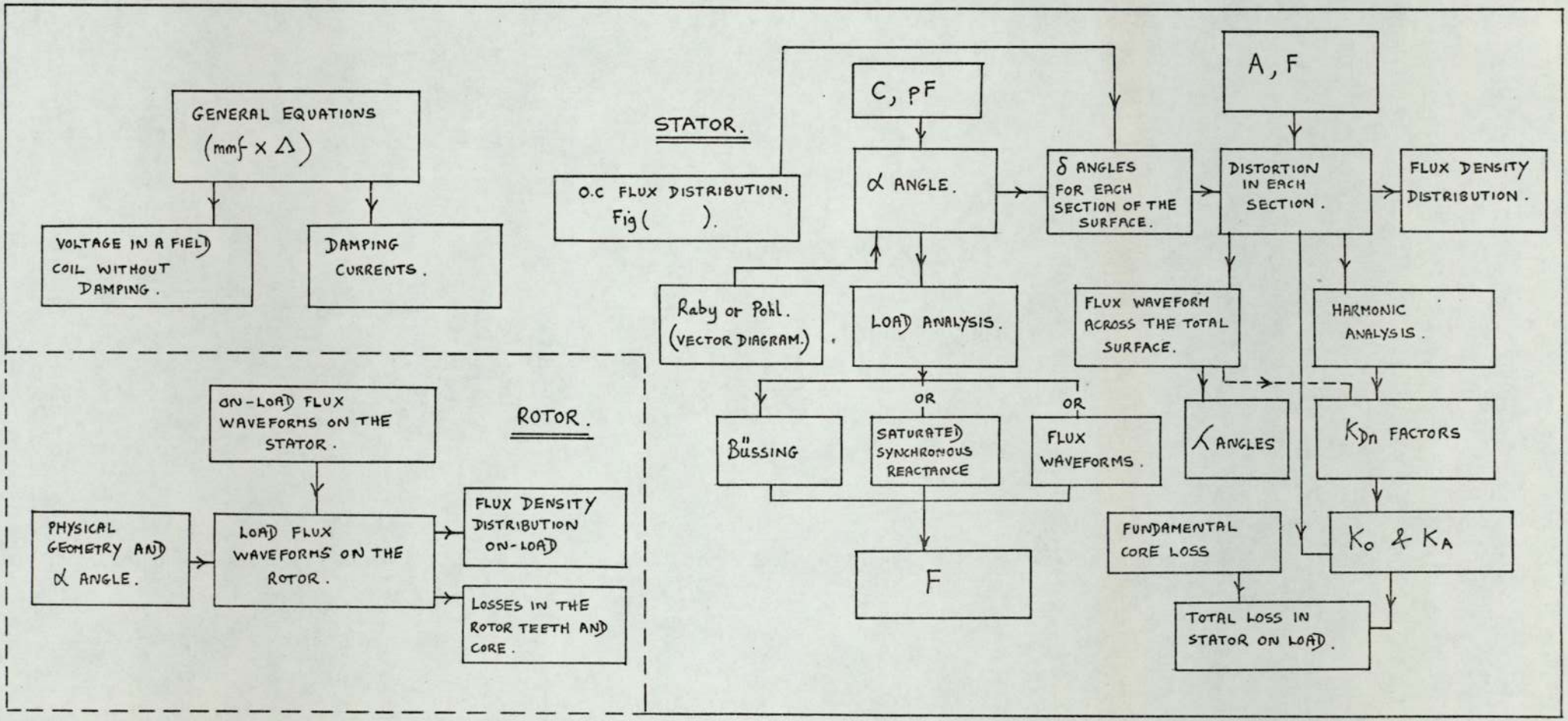

Fig.97 Calculation of fluxes on load for rotor and stator.